

# A quantitative comparison and validation of finite-fault models: The 2011 Tohoku-Oki earthquake

Jeremy Wing Ching Wong<sup>1</sup>, Wenyan Fan<sup>2</sup>, and Alice-Agnes Gabriel<sup>3</sup>

<sup>1</sup>Scripps Institution of Oceanography, University of California San Diego

<sup>2</sup>Scripps Institution of Oceanography, UCSD

<sup>3</sup>Ludwig-Maximilians-Universität München

April 12, 2024

## Abstract

Large earthquakes rupture faults over hundreds of kilometers within minutes. Finite-fault models image these processes and provide observational constraints for understanding earthquake physics. However, finite-fault inversions are subject to non-uniqueness and uncertainties. The diverse range of published models for the well-recorded 2011  $M_w \sim 9.0$  Tohoku-Oki earthquake illustrates this issue, and details of its rupture process remain under debate. Here, we comprehensively compare 32 finite-fault models of the Tohoku-Oki earthquake and analyze the sensitivity of four commonly-used observational data types (geodetic, teleseismic, regional seismic-geodetic, and tsunami) to their slip features. We first project all models to a realistic megathrust geometry and a 1-km subfault size. At this scale, we observe low correlation among the models, irrespective of the data type. However, model agreement improves significantly with increasing subfault sizes, implying that their differences primarily stem from small-scale features. We then forward-compute geodetic and seismic synthetics and compare them with observations available during the earthquake. We find that seismic observations are sensitive to rupture propagation, such as the peak-slip rise time. However, neither teleseismic, regional seismic, nor geodetic observations are sensitive to spatial slip features smaller than  $64 \sim \text{km}$ . In distinction, the seafloor deformation predicted by all models exhibits poor correlation, indicating sensitivity to small-scale slip features. Our findings suggest that fine-scale slip features cannot be unambiguously resolved by remote or sparse observations, such as the four data types tested in this study. However, better resolution may become achievable from dense offshore instrumentation.

# A quantitative comparison and validation of finite-fault models: The 2011 Tohoku-Oki earthquake

Jeremy Wing Ching Wong<sup>1</sup>, Wenyuan Fan<sup>1</sup>, Alice-Agnes Gabriel<sup>1,2</sup>

<sup>1</sup>Scripps Institution of Oceanography, University of California San Diego, La Jolla, CA, USA

<sup>2</sup>Department of Earth and Environmental Sciences, Ludwig-Maximilians-Universität München, Munich , Germany

## Key Points:

- We evaluate 32 finite-fault models of the 2011 Tohoku-Oki earthquake, using realistic slab geometry and varying spatial resolution.
- Models at the 64 km scale agree well with each other, indicating variability stems primarily from small-scale slip features.
- Seismic observations show sensitivity to rupture propagation but not to small-scale slip heterogeneity.

---

Corresponding author: Jeremy Wing Ching Wong, [wcwong@ucsd.edu](mailto:wcwong@ucsd.edu)



## Abstract

Large earthquakes rupture faults over hundreds of kilometers within minutes. Finite-fault models image these processes and provide observational constraints for understanding earthquake physics. However, finite-fault inversions are subject to non-uniqueness and uncertainties. The diverse range of published models for the well-recorded 2011  $M_w$  9.0 Tohoku-Oki earthquake illustrates this issue, and details of its rupture process remain under debate. Here, we comprehensively compare 32 finite-fault models of the Tohoku-Oki earthquake and analyze the sensitivity of four commonly-used observational data types (geodetic, teleseismic, regional seismic-geodetic, and tsunami) to their slip features. We first project all models to a realistic megathrust geometry and a 1-km subfault size. At this scale, we observe low correlation among the models, irrespective of the data type. However, model agreement improves significantly with increasing subfault sizes, implying that their differences primarily stem from small-scale features. We then forward-compute geodetic and seismic synthetics and compare them with observations available during the earthquake. We find that seismic observations are sensitive to rupture propagation, such as the peak-slip rise time. However, neither teleseismic, regional seismic, nor geodetic observations are sensitive to spatial slip features smaller than 64 km. In distinction, the seafloor deformation predicted by all models exhibits poor correlation, indicating sensitivity to small-scale slip features. Our findings suggest that fine-scale slip features cannot be unambiguously resolved by remote or sparse observations, such as the four data types tested in this study. However, better resolution may become achievable from dense offshore instrumentation.

## Plain Language Summary

Large earthquakes often rupture in unexpected ways across extensive areas of geologic faults. Scientists use finite-fault models to resolve these processes in detail. These models use different observations to help us understand earthquakes and plan for future hazard mitigation and risk management. However, these models are not perfect: they are often challenging to resolve, and different models of the same earthquake can show very different results. For example, many different models have been published for the 2011  $M_w$  9.0 Tohoku-Oki earthquake, each showing varying “slip features” of how the megathrust moved during the event. In this study, we compare 32 of these models with each other and with observations in a new and systematic way. The models show coherent features at a scale of 64 km while disagreeing on the smaller, fine-scale details. We find that such fine-scale features cannot be uniquely resolved by the commonly-used remote observations, such as geodetic, regional seismic-geodetic, teleseismic and tsunami data. Our study suggests that to gain a better understanding of large megathrust earthquakes, dense networks of instruments placed directly offshore close to the megathrust are needed for robustly resolving their rupture processes.

## 1 Introduction

Large earthquake rupture can evolve rapidly, propagating hundreds of kilometers in complex ways (Ammon et al., 2005; Ide et al., 2011; Simons et al., 2011). Imaging earthquake rupture processes is vital for understanding earthquake physics and the associated hazards (Tinti, Spudich, & Cocco, 2005; Uchida & Bürgmann, 2021). Finite-fault models characterize the spatiotemporal slip distributions of large earthquakes (Ide, 2007), and these models can be developed using a range of datasets and inversion methods (Hartzell & Heaton, 1983; Ide, 2007; Ji et al., 2002; Jia et al., 2023; S. Minson et al., 2013; Yagi & Fukahata, 2011a). However, finite-fault inversion is often parameterized as an ill-conditioned problem with a large number of unknowns and a simplified, assumed fault configuration (e.g., Fan et al., 2014; Ide, 2007). Moreover, unknown 3D Earth structure leads to inaccurate Green’s functions, further hampering the robustness of finite-fault models (Beresnev,

2003; Gallovič et al., 2015; Wald & Graves, 2001). Dense, near-field geophysical observations can offer critical constraints that help resolve finite-fault models with high fidelity (e.g. Asano & Iwata, 2016; Scognamiglio et al., 2018; Tinti et al., 2016). However, many earthquakes occur in remote regions where observations are scarce, such as in subduction zones. Finite-fault models often significantly differ from each other for the same earthquake (e.g., Mai et al., 2007; Razafindrakoto et al., 2015; Shearer & Bürgmann, 2010; K. Wang et al., 2020), and quantitatively comparing and differentiating these models remains challenging (e.g., Lay, 2018; Mai et al., 2016; K. Wang et al., 2018).

The 2011  $M_w$  9.0 Tohoku-Oki earthquake is one of the best-observed megathrust earthquakes (Lay, 2018). The earthquake ruptured approximately 400 km along-strike and 220 km along-dip offshore the northern Honshu area in Japan (Kodaira et al., 2020). The event was well recorded by a dense and diverse set of observations, including on-shore geodetic data (Sagiya, 2004), offshore acoustic-GNSS (e.g., Kido et al., 2011; M. Sato et al., 2011) and pressure gauge data (e.g., Hino et al., 2011; Y. Ito et al., 2011; Maeda et al., 2011a), regional and global seismic data (e.g., Okada et al., 2004), and tsunami (e.g., Maeda et al., 2011a; Mungov et al., 2013) and seafloor mapping data (Fujiwara et al., 2011; Kodaira et al., 2012). These datasets facilitate the development of many finite-fault models of the Tohoku-Oki earthquake (Sun et al., 2017). However, these models exhibit significant differences in their slip distributions (Lay, 2018; Razafindrakoto et al., 2015). For example, maximum slip estimates at the trench range from 0 m to 80 m for an along-dip cross-section through the hypocenter of 45 published models (Sun et al., 2017). Similar variability exists along the strike direction, particularly regarding the northern rupture extent beyond 39.5°N, which leaves the source of the Sanriku region tsunami a topic under debate (Du et al., 2021; Kodaira et al., 2020; Mori et al., 2011). The discrepancies among the finite-fault models of the Tohoku-Oki earthquake have given rise to several unresolved questions, including the tsunami sources and variability in megathrust and off-fault rheologies (Kodaira et al., 2020; Lay, 2018; Ma, 2023; Sun et al., 2017; Tajima et al., 2013; Uchida & Bürgmann, 2021).

The remainder of this paper is structured as follows. In Section 2, we describe the 32 published finite fault models analyzed in this study and introduce a new reparameterization framework to unify their model parameters for systematic comparison. The model comparison in Section 3 quantitatively identifies their coherent and unique features at varying spatial scales. We quantify the sensitivity of geodetic, teleseismic, regional seismic-geodetic, and tsunami data to the variability in the finite-fault models in Section 4. We discuss controlling factors of model variability and implications of our study as well as future opportunities in Section 5.

## 2 Finite-fault Models of the 2011 Tohoku-Oki Earthquake

We analyze 32 finite-fault slip models of the 2011 Tohoku-Oki earthquake (Figure 1; Text S1). The models have been obtained using various inversion techniques and Green’s functions, which result from the fault parameterization and the Earth’s structure. The finite-fault models are inverted from a wide range of datasets and exhibit a wide range of slip features (Figure 2). Here, we focus on the final slip distribution of each model because a large portion of the models are static. While we do not systematically compare available slip rate histories, we use them to investigate their impact on teleseismic and regional seismo-geodetic observations when available (Sections 4.2.3 and 4.3). We classify the models into five groups based on the datasets used (Figure 1 and 2).

The geodetic finite-fault group (in the following, labeled as “G”) includes nine models that describe the static slip distributions of the Tohoku-Oki earthquake (Diao et al., 2012; Hashima et al., 2016; Iinuma et al., 2012; T. Ito et al., 2011; Pollitz et al., 2011; C. Wang et al., 2012; R. Wang et al., 2013; Xie & Cai, 2018; Zhou et al., 2014). These models are inferred from geodetic measurements, including both onshore and offshore

displacement acquisitions. The regional seismic finite-fault group (“R”) comprises four models (Lee et al., 2011; Suzuki et al., 2011; Wei et al., 2012; Yue & Lay, 2013), which were developed from data of onshore strong ground motion, broadband, and high-rate GNSS (Global Navigation Satellite System) stations. The teleseismic finite-fault group (“S”) contains six models (Ammon et al., 2011; Goldberg et al., 2022; Hayes, 2011; Ide et al., 2011; Kubo & Kakehi, 2013; Yagi & Fukahata, 2011b), primarily derived from teleseismic body waves and surface waves recorded at stations located within the 30° to 90° epicentral distance range. The tsunami finite-fault group (“T”) includes eight models (Fujii et al., 2011; Gusman et al., 2012; Hooper et al., 2013; Kubota et al., 2022; Romano et al., 2014; Satake et al., 2013; Saito et al., 2011; Simons et al., 2011), which are based on tsunami data from near-source pressure gauges, tide gauges, and open-ocean buoys. Six T models are obtained using geodetic data as well, but without using seismic data. Lastly, the joint tsunami seismic and geodetic finite-fault group (“J”) includes five models (Bletery et al., 2014; Melgar & Bock, 2015; S. E. Minson et al., 2014; Yokota et al., 2011; Yamazaki et al., 2018). Models in this last group are required to incorporate geodetic, seismic (regional and/or teleseismic), and tsunami datasets.

## 2.1 Unifying Model Parameterization for Quantitative Comparison

We design a unifying framework to consistently reparameterize the models, ensuring that they share the same geometric and subfault configuration. This unifying procedure allows a quantitative and systematic comparison. We first project the finite-fault models onto the subduction interface using the Slab2.0 model to provide a realistic fault plane geometry (Hayes et al., 2018). Our projection method preserves the seismic potency of each subfault, which is defined as slip times rupture area. We align the shallowest subfault extents of each finite-fault model with the location of the Japan Trench (GEBCO, 2023; Hayes et al., 2018), which is situated approximately 7.65 km below the sea surface. We then project the depth-shifted models onto the subduction interface along the strike-depth plane, as defined by the Slab2.0 model (Hayes et al., 2018), but extending it to the Japan Trench (Figure 3b).

The Slab2.0 model maps the megathrust interface from 10 km to 150 km depth, omitting the shallowest near-trench geometry. Considering that the Tohoku-Oki earthquake likely ruptured all the way to the trench (Lay, 2018; Uchida & Bürgmann, 2021), we here extend the Slab2.0 megathrust to the trench assuming a shallow megathrust dipping angle of 10°. This extension is guided by the near-trench seismic reflection surveys (Y. Ito et al., 2011; Tsuji et al., 2011). We shift the Slab2.0 megathrust geometry to be 0.5 km shallower for a smooth connection with the shallow extension to the trench. This 0.5 km depth shift falls well within the depth uncertainty of the Slab2.0 model (Hayes et al., 2018).

We densify the projected models to a grid with uniformly spaced points, set 1 km apart, following the scheme outlined in Tinti, Fukuyama, et al. (2005). We use a cubic spline interpolation to densify each model to 16 times the original number of subfaults, with four times each along-dip and along-strike direction (Figure 3c). This cubic spline interpolation process assures spatial smoothness without preserving the seismic potency distribution. Therefore, we calculate the sum of the interpolated seismic potency within the area of each original subfault and compare it with that of the original slip distribution to compute the potency ratio per subfault with the ideal ratio as 1. We then use the potency ratio per subfault to scale the original slip for each subfault. We iterate the interpolation with the scaled original slip until the discrepancy in seismic potency between the original and interpolated models falls below a 10% threshold, which typically takes 2–3 iterations. This iterative procedure effectively preserves the seismic potency of the original models while ensuring spatial smoothness in the interpolated models. Without the iterative steps, applying the potency ratio to the interpolated models may result in artificially sharp edges in the upscaled slip distribution due to the coarse param-

eterizations of the original models. We apply this densifying procedure to both the along-strike and along-dip slip to preserve the original rake at each subfault. Finally, we linearly map the densified model to a set of grid points spaced 1 km apart horizontally, and their depths are defined by the megathrust geometry (Figure 3d). We apply this projection-upscaling procedure to all 32 models, leading to a collection of uniformly parameterized models that our following analyses are based on (Figure S1).

Our projection scheme differs from the one outlined in Brown et al. (2015) (hereafter referred to as the Brown method). The Brown method linearly interpolates a finite-fault slip distribution onto a set of dense grids that overlaps with the original finite-fault area, and extrapolates the slip towards the trench using values from the nearest neighbors. In contrast, our projection method adjusts the original subfault locations to align with the realistic megathrust geometry and trench location and interpolates the slip values accordingly (Figure S1). It is important to note that both projection methods could distort the original slip distribution. For example, the Brown method could result in a 20% increase in potency when projecting the planar G7 model onto the Slab 2.0 geometry, whereas our method causes a 2% potency difference compared to the original model (Figure S5). Additionally, the Brown method maps the downdip limit of the original G7 model from 25 km to 38 km due to the increased dipping angle of the megathrust at depth (Figure S5;]hayes2018slab2.

Therefore, the projection choice should be guided by the goal of the analysis. The Brown method prioritizes preserving the original fault location in latitude and longitude, whereas our projection emphasizes the megathrust geometry and subfault depth (Figure S5). The emphasis on realistic geometry is important because of our focus on evaluating data sensitivity including the static deformation comparison (Section 4.1). Differences in near-trench geometry, including depth, dip angle, and planar geometry, could lead to varying and even contrasting crustal deformation patterns (K. Wang et al., 2018). As an example, we compare the onshore and offshore crustal deformation using both projection methods using the 3D velocity structure Green’s function in Figure S6. Because of the extrapolated slip towards the trench, the projected model obtained using the Brown method would lead to a greater overestimation of horizontal displacement compared to the offshore observations (Figure S6). We find that both projection methods perform equally well for most models with 3D geometry (Figure S7). Specifically, both methods can preserve the pattern differences among the models, albeit at varying levels. Therefore, our approach is adequate for identifying the variability in the finite-fault models.

## 2.2 General Features of the Finite-fault Models

The megathrust in the Japan subduction zone extends along the strike from the Ibaraki region to the Sanriku-Oki region. This area can be divided into three main sections along-strike: the northern Sanriku-Oki region (ZN), the central Miyagi-Oki region (ZC), and the southern Ibaraki-Fukushima-Oki region (ZS). Following this geographic along-strike division, we further segment these three sections into six zones, using a depth of 20 km as an along-dip boundary (Figure 4). The 32 finite-fault models exhibit disagreement with respect to their exact rupture extents within these regions. We consider that a respective zone was ruptured during the Tohoku-Oki earthquake if it has  $\geq 10$  m slip.

We summarize the characteristics of each projected slip model according to this six-zone division in Table 1 and indicate the zones for each slip model in Figure S1. During the last 1,500 years, three  $M \geq 8$  earthquakes occurred prior to the 2011 Tohoku-Oki earthquake in the same region. These include the 869 Jyogan  $M$  8.3 earthquake in the central Miyagi-Oki region, and the 1896 Meiji Sanriku  $M$  8.5 tsunami earthquake in the northern Sanriku-Oki region (Tanioka & Sataka, 1996; Imai, 2015) (ZN1, Figure 4). However, no major earthquake with  $M$  8 or larger has been documented in the southern sec-

tion (Satake, 2015) (ZS1, Figure 4). The Tohoku-Oki earthquake was located in the central shallow zone (ZC1, Figure 4) and might have ruptured more than one section or zone. Approximately one-third of the models, including a joint inversion model, J5, show an extended shallow rupture in the Sanriku-Oki region (ZN1, Figure 4d). If true, the Tohoku-Oki earthquake may have re-ruptured the slip area of the 1896 Meiji tsunami earthquake, which may explain the exceptionally high tsunami heights of up to 30 m near the  $39.5^\circ$  coast and the large tsunami runup extending up to 10 km inland (Mori et al., 2011). However, this ZN1-slip feature is not present in all models. In addition, five out of the 32 models suggest that the Tohoku-Oki earthquake penetrated a deeper portion of the megathrust in the Sanriku region (ZN2; Table 1).

All the projected finite-fault models suggest that the Tohoku-Oki earthquake ruptured the central shallow part of the Japan trench megathrust (Figure S1), specifically in the Miyagi-Oki region (ZC1), at a depth of less than 20 km. Bathymetric surveys and acoustic ranging conducted before and after the earthquake identified a horizontal trenchward seafloor displacement of more than 50 m at  $38^\circ\text{N}$  (Y. Ito et al., 2011; Kodaira et al., 2012), providing definitive evidence of significant slip near the trench in the central section. However, the models differ significantly regarding the down-dip rupture extent, with around three-quarters of models indicating deep slip beyond the 20 km depth in the Miyagi-Oki region. Furthermore, the location of the peak slip varies from model to model, with 18 models placing the largest slip at the trench (e.g., G4 and T8 in Figure 4) and 14 models locating the maximum slip away from the trench (e.g., models R3 and J5 in Figure 2). These discrepancies imply contrasting rupture mechanisms and/or variations in the material properties of the very shallow part of the Japan subduction zone (Sun et al., 2017; Ulrich et al., 2022). For example, the role of the shallowest megathrust during the earthquake’s rupture remains debated. The large and shallow slip challenges the previous paradigm that the near-trench rheology would prohibit large slips due to velocity-strengthening fault friction and weak impeding sediments (Kozdon & Dunham, 2013).

The southern extent of the Tohoku-Oki earthquake rupture in the Ibaraki-Fukushima-Oki region remains ambiguous. For example, Bassett et al. (2016) and Liu and Zhao (2018) argued that an altered forearc structure might have controlled the frictional behavior of the megathrust, thus effectively limiting the rupture extent to the shallow Ibaraki-Oki region. In this scenario, the forearc structure at the shallow southern section (ZS1) acts as a barrier to halt southern rupture. However, approximately one-third of the models locate significantly large slip in ZS1, such as model R3 in Figure 4b. Moreover, about one-fourth of the models suggest deeper rupture in the southern section (ZS2; Table 1) in a potentially disconnected secondary slip patch triggered by the main slip in ZC1 (e.g., G4 in Figure 4a).

We derive a median slip model (M) by taking the median slip value at the along-dip and along-strike directions of the 32 finite-fault models at each subfault (Figure 5). The median model has a simple slip distribution with a smooth, circular patch up-dip of the hypocenter (ZC1). The lateral extent of the slip is predominantly confined between  $37^\circ$  to  $39^\circ$  along the strike direction. Regarding the dip direction, the model suggests significant slip extending to the trench, although the maximum slip, valued at 38.0 m, occurs approximately 5 km away from the trench (Figure 5).

The standard deviation of the 32 collected slip distributions highlights the variability among the finite-fault models (Figure 5). The standard deviation peaks at more than 20 m near the trench in ZC1, suggesting that the shallow slip of the Tohoku-Oki earthquake is poorly resolved. Depending on the inversion strategies, some models have likely tapered the slip towards the trench. Therefore, we categorize the models into two groups based on the near-trench slip (Figure 1) and compute their standard deviations separately. We find that the respective standard deviations within each of the two groups remain greater than 15 m near the trench, indicating variations in either the peak-slip



location or the peak-slip amplitude at the trench (Figure 5). The standard deviation distributions and the relative standard deviation (defined as standard deviation over median slip) also suggest widespread slip uncertainties—greater than 2.5 m and 100% median slip—in the northern region up to 40° north, southern region, and down-dip regions up to 60 km depth (Figure 5b and Figure 5d), although the major slip area in the median model has low relative standard deviation (Figure 5d).

### 3 Model Comparison

All finite-fault models suggest large near-trench slip in ZC1 (Figure S1), where a large slip deficit had been estimated prior to the Tohoku-oki earthquake (Hashimoto et al., 2012; Loveless & Meade, 2011). This slip feature is the most consistent attribute among the models, with primary differences arising in secondary features, such as slip distributions in zones away from ZC1 (Lay, 2018). Within zone ZC1, model differences manifest as peak slip locations or variations in the heterogeneity of the slip distributions (Sun et al., 2017). We caution that peak slip may not be well resolved in these finite-fault models due to varying fault parameterization and varying selected Earth structural models (Lay, 2018; K. Wang et al., 2018).

The models obtained using single data types have different limitations, mainly reflecting their sensitivities to offshore slip and network configurations (Lay, 2018; Uchida & Bürgmann, 2021). For example, geodetic models tend to have smooth slip distributions with their peak slip patch located near the hypocentral region (K. Wang et al., 2018). Models using tsunami data may be influenced by spurious seafloor deformation and secondary sources, including inelastic off-fault deformation and possible submarine landslides (Du et al., 2021; Kodaira et al., 2021; Uchida & Bürgmann, 2021; K. Wang et al., 2018). However, tsunami data has an advantage over onshore observations due to its sensitivity to slip near the trench (Lay, 2018; Kodaira et al., 2021). Differential bathymetry and near-trench turbidities can directly constrain the occurrence and amplitude of the near-trench slip, and post-earthquake surveys suggest that the main coseismic slip was limited to the south of 39.2° (Ikehara et al., 2016; Kodaira et al., 2020, 2021). Models obtained from joint inversions using multiple datasets may best represent the various observations of the Tohoku-Oki earthquake (Lay, 2018; Uchida & Bürgmann, 2021). However, the slip distributions of the joint-inversion models are significantly more complex than those of other models. These complexities may be affected by incomplete isolation of the coseismic signals, inaccurate assumptions about signal sources, and the strategies of combining different geophysical datasets (Lay, 2018; K. Wang et al., 2018).

Razafindrakoto et al. (2015) qualitatively compared the overall variability of 21 finite-fault models by computing multi-dimensional scaling statistics, including a grey-scale matrix. Their statistics show large variability among the models, likely reflecting the different underlying dataset types (Razafindrakoto et al., 2015). Specifically, their grey-scale matrix suggests that models obtained using tsunami data are more variable when compared to models developed using other data types (Razafindrakoto et al., 2015). Since their model comparison is drawn from statistical metrics, it is challenging to delineate specific slip features, leaving the spatial differences of the slip distributions unclear. Sun et al. (2017) focused on the near-trench slip characteristics of 45 finite-fault models and compared an along-depth slip profile at 38°N. Their comparison identified a high level of variability among the models (Sun et al., 2017).

In this section, we design a new model-comparison framework to quantitatively extract coherent and unique slip features of the finite-fault models at varying length scales. We also quantify the model variability of the five model groups by examining the wavelength power-spectral densities of their respective median models. Without certainty about the actual rupture process of the Tohoku-Oki earthquake, we consider all models equally feasible since they can explain their respective datasets; we do not rank the models.

### 3.1 Slip Heterogeneity

To investigate variability in smaller-scale heterogeneity of the finite-fault models, we compute the spatial power spectra of each slip distribution. We apply a 2D Fourier transform to obtain a 2D power spectral density. By performing a circular mean over the wave number range ( $k = \sqrt{k_s^2 + k_d^2}$ ,  $k_s$  and  $k_d$  are the along-strike and along-dip wave numbers), we derive a 1D power spectral density of each slip distribution (Goda et al., 2014; Mai & Beroza, 2002). We then compute the respective median spectra for the five model groups. We use these median spectra to evaluate the variations in slip heterogeneity associated with each data type (Figure 6). Their decay rates are related to the smoothness of the slip distributions and reflect the relative heterogeneity in slip distributions at different spatial scales (Mai & Beroza, 2002).

The power spectra density of the slip models show that the spectra variability increases with the wave number, suggesting an increase in model complexities with smaller features (Figure 6). The model spectra show good agreement in the wavelength range below  $1/80 \text{ km}^{-1}$ , which reflects that all models have a significant slip patch approximately 80 km in dimension. However, we find systematic differences in the spectra for different groups in the wave number range of  $1/80$  to  $1/10 \text{ km}^{-1}$  (Figure 6). This variability in spectra results in different spectrum decay rates of the five groups, ranging from -2.1 to -3.0. The tsunami and joint-inversion groups have decay rates around -2.2, indicating that these models are enriched in heterogeneous small-scale features, such as more than one major slip patch or sporadic near-trench slip (Figure 2). In contrast, smooth models, such as those from the geodesy and regional-seismic data groups, are characterized by faster spectra decays with corresponding rates around -3.0 (Figure 6). Models developed from teleseismic data have decay rates of approximately -2.7, reflecting their one or two major smooth patches with few secondary features. Within each group the variability of the spectra varies among different groups, indicating inconsistent model features even when using the same data type.

### 3.2 Model Correlation at Multiple Scales

We quantitatively evaluate the similarity between models by computing a correlation coefficient for each pair of models. This correlation coefficient is the inner dot product of two normalized slip-vector fields, which is the sum of each vector dot product. A slip-vector includes the along-strike and along-dip slip values, and a slip-vector field characterizes the final slip distribution of a finite-fault model. We define the correlation-coefficient  $R_{ij}$ , similar to a Pearson correlation, as:

$$R_{ij} = \frac{\langle \Phi_i, \Phi_j \rangle}{\sqrt{\langle \Phi_i, \Phi_i \rangle \langle \Phi_j, \Phi_j \rangle}} \quad (1)$$

where  $i$  and  $j$  are model indices, and  $\Phi_i$  and  $\Phi_j$  are the corresponding slip models with the unified parameterization configuration. The resulting correlation-coefficient  $R_{ij}$  ranges from -1 to 1: a coefficient of 1 indicates that the two slip-vector fields share an identical spatial pattern, although their absolute values may differ; a coefficient of 0 indicates no correlation between the slip-vectors.

Our unified models all have a subfault size of 1 km, and the model correlation-coefficients range from 0.61 to 0.95 (Figure 7) with an average and median value of 0.79 and 0.79, respectively. This broad range of values indicates clear differences in the slip distribution among the models. Generally, the geodetic group (G) shows the highest coherence among their finite-fault models compared to other groups, with an average and median correlation value of 0.83 and 0.81, respectively. Most of these models consist of a smooth, single slip patch located at the up-dip area near the hypocenter, such as models G3, G5, and G6 (Figure 2), which leads to very high inter-model correlation. Model G2, however, significantly differs from other geodetic models with an average correlation value

of 0.73 with other models. The model suggests a southern slip patch at the up-dip hypocenter region in zone ZC1. The regional seismic group (R) shows high coherence among their finite-fault models compared to other groups. In comparison, the teleseismic group (S) shows a broad range of correlation values, generally lower than those of groups G and R (Figure 2b). Teleseismic models show large variations in secondary slip features, such as the extended slip in different zones.

Intriguingly, models developed using tsunami data, both T and J groups, show considerable variability within their respective groups and when compared to models of other groups. These models comprise a more heterogeneous slip distribution with complex slip features in their distribution and values, causing the observed low correlation values. We find that the median model, M, highly correlates with all other models, with a median correlation value of 0.89. This high correlation reflects that the main feature of the median model—the slip in ZC1—is captured by all models. The results also suggest that the dominant slip area likely centers around a single slip patch in ZC1, since more complex slip features of the models do not impact the correlation values very much.

Our 1-km model parameterization is much smaller than the typical subfault sizes used in finite-fault inversion (Ide, 2007). Subfault dimensions are often set to be around 16, 32, and 64 km for geodetic, seismic, and tsunami finite-fault inversions, respectively (e.g. Inuma et al., 2012; Wei et al., 2012; Satake et al., 2013). Therefore, we downscale the slip models to increase the subfault sizes from 1 km to 16, 32, and 64 km and then compare the variability of slip features at different length scales (Figure 8). We apply a 2D discrete wavelet transform to the slip distributions using the Daubechies' first wavelet (Daubechies, 1990). The wavelet transform allows us to isolate slip features at varying spatial scales by filtering out higher-order wavelets (Figure 8). For example, inversely transforming a low-pass filtered wavelet spectrum results in a lower-resolution slip distribution. This wavelet transform process is similar to an image compression technique using Daubechies' first wavelet group (Daubechies, 1990). Importantly, our downscaling process preserves the overall moment, moment centroid location, and spatial distribution of the slip features at the selected wavelength scale.

We apply the downscaling procedure to each 1 km subfault-size model to 16, 32, and 64 km subfault sizes, and process the slip distributions of the along-strike and along-dip directions separately (Figure S2–S4). The 64 km length scale approximates the wavelength of a 10 s period crustal P wave at subduction zones, and the displacements of these 10 s period P waves are commonly used in teleseismic finite-fault inversions (e.g. Ammon et al., 2005; Kubo & Kakehi, 2013; Yue et al., 2014). As an example, Figure 8 shows the slip distribution of model S3 and the median model at scales of 1, 16, 32, and 64 km. The original S3 model consists of two major along-strike slip patches shallower than 20 km, along with complex small-scale patches at around 40 km depth. These deeper patches have spatial scales of less than 32 km, and the 64 km scale model primarily retains the dominant, large-scale shallow slip features. Thus, our wavelet-based downscaling procedure effectively removes the small length-scale features of the finite-fault models.

The correlation coefficients between the models increase as the subfault size increases, confirming that the model variability primarily originates from small-scale features (Figure 9a–c). At the 64 km scale, the median and average correlation-coefficients are 0.89 and 0.88, respectively. This coherent pattern is present in all model pairs, regardless of the datasets used (Figure 9c). Much like at the 1-km scale, all models show a high correlation with the median model at larger scales (Figure 9d). Our results reveal a coherent pattern emerging among all the projected models: a primary slip patch that occurred up-dip of the hypocenter around 10 km depth during the Tohoku-Oki earthquake. However, the model features are inconsistent at the 16 and 32 km length scales, either in their locations or amplitudes. The correlation results from 1 km to 16 km scales largely remain the same (Figure 7,9), indicating that the original model resolutions were limited to around 16 km.



## 4 Model Validation

Previous model-comparison studies primarily focused on identifying coherent and unique slip features (e.g., Ide, 2007; Razafindrakoto et al., 2015; K. Wang et al., 2018, 2020). Here, we systematically examine the sensitivity of four commonly-used datasets to the variability in the finite-fault models (Figures 10–16), including geodetic (Section 4.1), teleseismic (Section 4.2), regional seismic-geodetic (Section 4.3), and tsunami data (Section 4.4). We compute synthetics for all models using the same Green’s functions. Then, we compare the synthetics with observations using the correlation-coefficient and variance-reduction metrics. We test the models not only by comparing their respective data types used in obtaining the models but also by inspecting the fit to datasets not included in their finite-fault inversions.

Our comparison evaluates both the data sensitivity to model variability and the data capability to resolve smaller-scale features. We examine the data sensitivity to the slip features identified in Section 3, including the contrasting rupture extent in different zones. Additionally, we compare synthetics with observations, as well as with each other, using slip distributions at varying scales.

### 4.1 Onshore and Offshore Geodetic Data

We test the geodetic data type using both onshore and offshore static-displacement measurements. We compute the synthetic static displacements for each site using Green’s functions from Hori et al. (2021), applied to models at the 16, 32, and 64 km spatial scales. These Green’s functions are numerically computed using a 3D velocity structural model and realistic topography at approximately 1 km resolution of the Japan region. Specifically, we compute the synthetics for the onshore GEONET network, which includes 365 stations, and the eight offshore GNSS-A sites (Table S1; M. Sato et al., 2011; Kido et al., 2011). Additionally, we examine vertical displacement data recorded by six pressure gauges operated by Tohoku University (Hino et al., 2011; Y. Ito et al., 2011) and the University of Tokyo (Maeda et al., 2011b). Our primary focus are the correlation-coefficients between the synthetics and observations instead of the variance reduction metric. The variance reduction metric is strongly influenced by synthetic amplitudes, which depend on the assumed velocity models and the finite-fault parameterization. For example, using a 3D velocity structure to compute synthetics from models obtained using 1D structures may reduce the overall amplitudes (K. Wang et al., 2018). The correlation-coefficient, on the other hand, evaluates the coherence between synthetic and observed displacement fields and is better suited to compare slip distributions with large spatial heterogeneities. However, the variance reduction metric can be a useful tool for differentiating models as long as the models are resolved using the same Green’s function for an objective comparison (e.g., Figure S8).

We find that neither the onshore nor the offshore geodetic observations can distinguish between the slip models at the same scale (Figure 10). For example, the four models in Figure 10 at the 16 km scale, including the median model (M), can all explain the observed displacement fields well, with correlation-coefficients greater than 0.91 between their synthetics and the observations. The median model has a simple distribution with only one slip patch in ZC1 (Figure 10d), while the other three models have distinct, incoherent features, such as model R3 ruptures in ZS1 (Figure 10e), model J5 ruptures in ZN1 (Figure 10f), and model S3 ruptures in ZC2 (Figure 10a), respectively. For the onshore stations, the limited data resolution likely results from the 150 km distance between the epicenter of the offshore earthquake and the nearest coastal station of the GEONET network. Even for models with significant down-dip slip in ZC2, the coastal GEONET stations remain too far to resolve the down-dip slip features conclusively due to the increasing depth of the megathrust (Figure S9).

The offshore geodetic network, consisting of GNSS-A and pressure gauge stations, cannot resolve the differences in the slip distributions or the peak-slip locations (Figures 10h, S9–S10). For example, models G3 to G6 can all generate synthetics with correlation-coefficients  $\geq 0.97$ . However, some models locate the peak slip near the trench (G4), whereas others place the peak slip around the hypocenter (G3, G5, and G6). Additionally, secondary slip features, such as slip in ZS1 and ZN1, do not impact the offshore synthetics significantly. The median model and model J5 can explain the offshore displacements equally well, while model J5 is remarkably more heterogeneous than the median model. The limited resolution of the offshore geodetic network is likely due to the fact that most of its stations are located in the central Miyagi-Oki section. Only 13 stations were deployed in this 150 km by 150 km area prior to the earthquake. This offshore network configuration determines that the offshore observations were primarily controlled by the slip directly beneath these stations. Given that all projected models coherently resolve a large slip patch in ZC1, they can all reasonably explain the offshore observations. We emphasize that the location of the offshore geodetic network covered the center of the Tohoku-Oki earthquake rupture area, playing a critical role in resolving the largest slip patch, although its sparse configuration limited its capability in resolving secondary slip features.

We find negligible differences in the geodetic synthetics among the same models at the 16, 32, and 64 km scales. The correlation values between the observations and the synthetics remain consistently high ( $> 0.90$ ) for all models across all scales, for both onshore and offshore geodetic data (Figure 10). These results suggest that the resolution of the geodetic dataset is likely lower than 64 km for the offshore slip distribution and that the data cannot differentiate slip features at smaller scales. For example, the synthetic onshore-geodetic static displacements from model S3 show no differences across the three scales (Figure 10a–c, synthetics in red and observations in black). The offshore synthetics show similar patterns, suggesting marginal resolution differences across scales, even though all models inverted from geodetic datasets included part or all of the offshore data and their original models have subfault sizes much smaller than the 64 km scale.

We compute the variance reductions for the finite-fault models with respect to the geodetic datasets (Figure S8). The variance reduction metric shows a higher sensitivity to slip distribution variability than the correlation coefficient. Most of the models have  $\geq 80\%$  variance reduction, with the exception of four models. The variance reduction pattern of the onshore geodetic data shows a similar pattern as the model correlation with the median model (Figure 9d). This suggests that onshore geodetic data can generally well-resolve slip features at the 64 km spatial scale. In addition, there is a difference in variance reduction for offshore data between the 32 and 64 km scales for most models. However, these differences in variance reduction are negligible when comparing the same models at the 16 and 32 km scales. These results show that the amplitudes of offshore displacement under the present conditions are sensitive to localized slip features, suggesting that the offshore geodetic data might have higher spatial resolution than 64 km when evaluated using the variance reduction metric.

## 4.2 Teleseismic Data

Teleseismic waves are one of the most commonly used observations to invert finite-fault models of large earthquakes (e.g., Ji et al., 2002; Yagi & Fukahata, 2011a; Okuwaki et al., 2020). They have relatively simple waveforms and can effectively characterize the temporal evolution of earthquake rupture processes (Okuwaki & Fan, 2022). Different from computing geodetic synthetics, both the slip distribution and slip-rate functions are required for synthesizing teleseismic waveforms. Slip-rate functions characterize the temporal moment release for each individual subfault (Ide, 2007). To focus on comparing the slip distribution variability, we first test, validate, and identify a slip-rate func-

tion type. We assume a single-time-window slip-rate function with a uniform duration for all subfaults. We test a range of slip-rate functions, such as the cosine and Yoffe functions, and then apply the best-performing one to all models to compute teleseismic synthetics. The best-performing slip-rate function is defined as the one resulting in the highest variance reduction in fitting teleseismic P waves. With this replaced uniform slip-rate function, our comparison focuses on the impact of the slip distribution variability. The slip-rate function is paired with the peak-slip-rate time (PSRT) distribution from model S3 to synthesize teleseismic seismic waves, including both body and surface waves. The peak-slip-rate time distribution of model S3 is used because the model is obtained using the single-time window method and inverted from both body waves and surface waves. We justify the procedure in Sections 4.2.1–4.2.3.

We compute teleseismic synthetic displacement waveforms using Instaseis (van Driel et al., 2015). This method uses pre-computed Green’s function databases, calculated using the anisotropic version of the Preliminary Reference Earth Model (PREM) and the AxiSEM method up to 2 s period band (Dziewonski & Anderson, 1981; Nissen-Meyer et al., 2014). The teleseismic synthetics are compared with three-component broadband records at 40 stations from the II and IU networks, located within an epicentral range of 30° to 90° and covering all azimuths (Figure 11a; see Open Research for details). We remove the instrument response from the observations, integrate velocity waveforms into displacement waveforms, and decimate the data to a 1 Hz sampling rate. Both the observations and synthetics are filtered using a 4<sup>th</sup>-order Butterworth band-pass filter to the appropriate period band before the comparison: body waves are filtered in the 10–150 s period band and surface waves are filtered in the 100–200 s period band. We compare the windowed body waves from -20 to 230 s relative to their PREM-predicted arrival times and surface waves from 500s to 3300 s relative to the Tohoku-Oki earthquake origin time. These frequency ranges are comparable to the teleseismic analysis used in the S models, as well as in teleseismic finite-fault models of the  $M_w$  8.8 Maule earthquake and the  $M_w$  9.1 Sumatra earthquake (e.g. Ammon et al., 2005; Kubo & Kakehi, 2013; Yue et al., 2014). Before comparing the waveforms, we cross-correlate the synthetics with the observations and apply an empirical time correction to account for the arrival time uncertainty due to the 3D Earth structure. We adopt the same correlation value metric to compare the waveforms and use the median correlation value for each wave type as a representative metric to compare the finite-fault models.

#### 4.2.1 Geometric Effects

We explore and validate the effects of fault geometry on teleseismic synthetics. We use model S3 as an example and compare the synthetics obtained from the original multi-planar fault configuration and the projected S3 model onto a realistic megathrust geometry. The projected model has the same number of subfaults as the original model, and the slip-rate functions of the subfaults remain the same. The synthetics from both models are nearly identical, leading to almost the same correlation coefficients of 0.90 with the observations. For example, the P wave synthetics (blue) using the realistic megathrust geometry, those from the original configuration (red), and the observed P waves (black) share a high resemblance, as illustrated in Figure S17. We conclude that the projection scheme does not significantly impact the teleseismic synthetics (Table S2). This exercise validates the idealized planer parameterization in most finite-fault models of the Tohoku-Oki earthquake. The results suggest that the 2011 Tohoku-Oki teleseismic waves are not very sensitive to geometry changes, likely due to that the majority of the observations are located far away from the nodal planes with down-going rays (Figure S14). We expect insignificant geometric effects on geodetic observations as well because all the models can explain the observed offsets equally well with high correlation values (Figure 10).

#### 4.2.2 Slip-rate Function Effects

The original model S3 uses a cosine function as its slip-rate function, with rise times varying from 6 to 24 s and durations ranging from 12 to 48 s. We replace these original slip-rate functions of the projected S3 model with a regularized Yoffe function (Tinti, Fukuyama, et al., 2005; Yoffe, 1951), characterized by a rise time of 16 s and a duration of 40 s for all subfaults to compute teleseismic synthetics. The rest of the finite-fault parameters remain the same to isolate the effects of a chosen slip-rate function. We select the regularized Yoffe function as the slip-rate function because it is compatible and consistent with the traction and slip evolution of the dynamic propagation of earthquake ruptures (Tinti, Spudich, & Cocco, 2005). The varying rise time and decay rates of the Yoffe function resemble the results from both dynamic simulations and laboratory experiments (Ohnaka & Yamashita, 1989; Tinti, Spudich, & Cocco, 2005).

The two sets of synthetics are nearly identical, and they both can satisfactorily explain the observations (Figure S18). The synthetics obtained using the replaced slip-rate function have fewer high-frequency signals compared to the synthetics using the original model (Figure S18), likely due to the absence of rise-time variations. Nonetheless, the model adopting the replaced slip-rate function can fit the observed seismograms with a median correlation coefficient of 0.84 for P waves (Table S2). Similarly, the SH and SV waves with the uniform slip-rate function can fit the observed seismograms with a median correlation of 0.77 and 0.81. These findings validate our proposed strategy of computing teleseismic synthetics.

We explore a range of slip-rate functions, including cosine, triangular, and different Yoffe slip-rate functions with durations of 40 and 55 s (Text S2; Figure S16). The teleseismic synthetics are insensitive to these variations, and the median correlation coefficients are all greater than 0.82 for the P waves (Table S2). Furthermore, we test varying durations for the suite of slip-rate functions and find that the slip-rate duration does not significantly impact the synthetic amplitudes as long as the duration is less than 40 s for the given subfault parameterization (Figure S18 and S20). For longer durations, the associated synthetic body waves have lower amplitudes than those using slip-rate functions with shorter durations (Figure S21). With the same spatial configuration, the variation in duration relates to the variation in the apparent rupture-front propagation, the effects of which will be evaluated in the next Section 4.2.3. Overall, the results confirm that the chosen regularized Yoffe function, with a rise time of 16 s and a duration of 40 s, can effectively represent the slip-rate functions for computing and comparing teleseismic synthetics from the set of finite-fault models.

#### 4.2.3 Rupture Propagation Effects

The earthquake rupture propagation significantly impacts teleseismic synthetics (Figure S19). To evaluate this effect, we vary the rupture propagation parameters to compute the onset times of each slip-rate function and corresponding teleseismic synthetics and keep the remaining finite-fault setup the same as the original model S3. We first assume a constant rupture velocity, resulting in a circular rupture front as shown in Figure S14c. With an assumed rupture speed of 2 km/s, the synthetic P waves cannot explain the observed waveforms between 30 to 80 s (Figure S19), and the median correlation value drops to 0.65 for P waves (Table S2). We then assume a slower speed of 1.5 km/s for the first 100 km of rupture propagation and a rupture speed of 2 km/s for the remaining rupture process, following finite-fault inversion schemes used in some of the teleseismic models (e.g., Ammon et al., 2011; Lay et al., 2011; Shao et al., 2011). Teleseismic synthetics obtained using this two-step rupture propagation cannot explain the observations either, resulting in a median correlation value of 0.65 for P waves (Figure S19).

In our experiment in Section 4.2.2, we use a single, regularized Yoffe function constrained by the S3 onset time distribution for computing teleseismic synthetics. Here,

we align the onset times of the slip-rate functions with the peak-slip-rate times (PSRT) in model S3 for each subfault. The associated synthetics are nearly identical to those from the original S3 model, with correlation-coefficient differences less than 0.02 (Table S2). The PSRT configuration improves the data fitting to the observed waveforms more than the original onset time configuration when using the uniform, single slip-rate function approach (Figure S18). Specifically, the PSRT synthetics can produce the high-frequency waveforms that is missing in the onset-time synthetics (Figure S18).

We validate our approach using slip distributions and peak-slip-rate times from other finite-fault models. To test the effects of different PSRT distributions, we also apply the PSRT approach to models S6 and J3 using their respective distributions (Figure S23). This analysis yields satisfactory P-wave data fitting with correlation coefficients of 0.75 and 0.75 for the two models (Figure S24), respectively, while synthetics from their original models have correlation coefficients of 0.71 and 0.73 with the observations, respectively. We then use the S3 PSRT and slip distributions from models S6 and J3 at the 16 km scale to generate teleseismic synthetics (Figure S22). The synthetics can explain the observations with correlation coefficients of 0.77 and 0.76 (Table S2), which are around 0.05 different from those of the model S3 synthetics at the same scale (Table S2). This validation demonstrates that the model S3 PSRT distribution can be used to pair with other slip distributions to compute teleseismic synthetics. Therefore, we use the model S3 PSRT distribution and the selected single Yoffe slip-rate function to compute teleseismic synthetics for all 32 finite-fault models. We note that our analysis does not consider complex rupture propagation effects, such as multiple slip episodes inferred from multiple time-window slip inversion (Lee et al., 2011; Melgar & Bock, 2015; Yue & Lay, 2013) or in dynamic rupture scenario simulations informed from local strong ground motions (Galvez et al., 2016, 2020).

#### 4.2.4 Sensitivity of Teleseismic Data to Finite-fault Model Variation

We compute teleseismic synthetic waveforms using the final slip distributions at the 16, 32, and 64 km scales of all models. We employ the same procedure, using the model S3 PSRT distribution and a regularized Yoffe slip-rate function with a rise time of 16 s and a duration of 40 s, to compute the synthetic waveforms. When generating teleseismic synthetics with spatial scales greater than 16 km, the 32 or 64 km size subfault are divided into 16 km subfaults and each 16 km subfault has the same slip as the 32 or 64 km size subfault. We then use the same slip-rate and PRST distribution with this slip distribution to generate synthetic waveforms. The synthetics include both body and surface waves. As an example, Figure 11 shows the resulting synthetic teleseismic waveforms from 16 km scale models at the IL.BRVK, IU.COR, and IU.HNR stations, representing azimuths of  $312^\circ$ ,  $51^\circ$ , and  $158^\circ$ , respectively. Figure S11 and S12 show the resulting synthetic teleseismic waveforms from 32 km and 64 km scale models. For a quantitative comparison, we compute correlation coefficients between the synthetics and the observed waveforms for five wave types from each model, including the P, SH, SV, Rayleigh, and Love waves (Figure 12).

We find that none of the five types of teleseismic waveforms is sensitive to variations in the slip distribution (Figure 11c). Synthetic seismograms for the same stations are highly coherent with each other (red lines in Figure 11c,d). For example, Figure 11c shows body wave synthetics from all 32 finite-fault models and the median model at the 16 km scale at stations IL.BRVK, IU.COR, and IU.HNR, which are nearly identical to each other. These synthetics can all satisfactorily explain the body wave phases, such as fitting the complex P wave phases correctly. It is worth noting that these synthetics can achieve comparable misfit reductions (waveform fittings) to other teleseismic finite-fault inversion studies (e.g. Kubo & Kakehi, 2013; Yoshida et al., 2011). The S wave synthetics have similar correlation coefficients with those of P waves (Figure 12), and the two phases do not show distinctive sensitivities. Similarly, the surface wave synthetics



from different models are coherent with each other and can all explain the observations (Figure 11d and 12). These synthetic surface waves tend to have higher amplitudes than real observations, likely due to our simplistic 1D Green's functions. In addition, we also find that the associated moment-rate functions of the models share a similar function shape (Figure 11b). We further compare the teleseismic synthetics with 32 and 64 km scales in Figure S2 and S3 and observe similar waveform fits. The synthetics of the five types of teleseismic waves show minor variations with different slip models. Our results reveal that with the same temporal evolution of the rupture propagation, variations in the slip distributions do not significantly impact the moment-rate function or teleseismic synthetics.

We further quantify the sensitivity of teleseismic waves to the same slip models at the 16, 32, and 64 km scales. For each model, we compute the synthetics using three different length scales and correlate the synthetics with the observations to examine their sensitivities (Figure 12). We find little difference in the synthetic waveforms for different scales, and they all correlate well with the observations. For example, the P wave synthetics have consistent correlation values around 0.70–0.80 for the same models at all scales. Similarly, the S waves and surface waves cannot resolve slip models at finer scales either (Figure 11). These results indicate that teleseismic finite-fault models likely have a spatial resolution of around 64 km for the Tohoku-Oki earthquake.

### 4.3 Regional Seismic and Geodetic Data

The 2011 Tohoku-Oki earthquake was recorded by densely distributed regional strong ground motion seismic and high-rate geodetic stations. Using regional seismic and geodetic data often led to finite-fault models with a higher degree of rupture complexity, including multiple rupture episodes near the hypocenter (e.g., Lee et al., 2011; Melgar et al., 2013; Bletery et al., 2014). We follow the same setup as used in Section 4.2 to compute the regional seismic and geodetic synthetics and evaluate the sensitivity of the regional data to rupture propagation and slip distribution variations. We focus on 30 high-rate GNSS time series (Figure 13) from the GEONET network of the Geospatial Information Authority (GSI) of Japan and 25 K-NET and KiK-net three-component strong motion stations (Figure 14) from the National Research Institute for Earth Science and Disaster Prevention (NIED) data center. All stations are located within 350 km of the epicenter of the 2011 Tohoku-Oki earthquake.

We first validate our projection method by comparing the synthetics resulting from the original and projected model J4 (Supplementary Text S3). We find that the original and projected synthetics agree well when using the J4 original slip-rate functions, with the strong ground motion comparison in Figure S35 and high-rate GNSS comparison in Figure S39. This exercise validates the projection procedure for examining the two regional data types.

To compare to high-rate GNSS data, we focus on horizontal components and low-pass filter the GNSS time series at 10 seconds. We compute high-rate GNSS synthetics following the same procedure as for obtaining the teleseismic synthetics (see Supplementary Text S3). We use the regularized Yoffe slip-rate function and the model S3 PSRT distribution (Section 4.2). This procedure is applied to each of the 33 slip models at the 16, 32, and 64 km scales, respectively (e.g., Figure 13). The high-rate GNSS synthetics from different models share similar waveforms but have different amplitudes, including different static offsets. The amplitudes of the synthetic static offsets, here using the Instaseis method with a 1D velocity model (van Driel et al., 2015), are comparable to the results computed using the 3D Green's function in Section 4.1. For example, Figures S38 and S39 illustrate the agreement between the 1D and 3D synthetic offsets as well as between the observed and synthetic offsets for model J4. Figure S40 compares the variance reduction for static offsets at the 30 GNSS stations for all models at 16, 32,

and 64 km scales using 1D and 3D synthetics. We find that the variance reduction metrics are different for the 33 models, although the correlation values are largely comparable.

The static-offset differences between synthetics from the 33 models are highlighted in Figure 13. These synthetics correlate well with the observations with correlation coefficients exceeding 0.9 on average. However, when their amplitudes are normalized, the high-rate GNSS synthetics are almost identical (Figure S41). This result indicates that the high-rate GNSS data may not be able to distinguish the small-scale spatial variability among the slip models. The amplitude differences primarily result from the variations in the total seismic moment and in slip in the down-dip regions (e.g., ZC2). Models with larger moments lead to higher static offsets in the synthetics (Figure S9). We note that the similarity between the normalized synthetics stems from using the same set of slip rate functions and PSRT distribution.

We find that regional strong ground motion data may be more sensitive to the details of earthquake rupture propagation than other regional observations. The coastal strong ground motion records have complex waveforms, and the vertical seismograms cannot be easily explained by the assumed, simplified model. In the 10-to-100-second period band, the original model J4 that includes re-rupturing episodes near the hypocenter can explain the three-component displacement records at the 25 strong motion stations. The corresponding vertical synthetics have an average correlation value of 0.86 with the observations (Figure S35). In contrast, the assumed, simplified model using the J4 slip distribution, the S3 rupture propagation without re-activation, and the regularized Yoffe slip-rate functions leads to an average correlation value of 0.65 between the associated synthetics and vertical observations (Figure S36). In distinction, the horizontal component strong motion data can be explained by the assumed, simplified model with an average correlation coefficient of 0.7, including stations MYGH03, MYGH08, and FK031 that are close to the earthquake epicenter (Figure 14).

To isolate the sensitivity of strong ground motions to the slip distribution variability, we compute three-component synthetics (10-to-100-second period band) using the same simplified rupture propagation and the slip distributions of the 33 models at the 16, 32, and 64 km scales (e.g., Figure 14, Figure S43 and Figure S44), and then compare the synthetics with those from the median model (M). At the same spatial scales, the three-component synthetics have similar waveforms to those from the median model (Figure 14d). For example, models J3 and J4 have distinct slip complexities (Figure S3 and Figure S4), but they generate similar synthetic waveforms. Additionally, the horizontal synthetics can match the observed displacement waveforms in the same period band. We find that the same slip models at 16, 32, and 64 km scales result in similar synthetic waveforms, with correlation values exceeding 0.9 on average (Figure 14d, Figure S36 and S37). These synthetic waveform tests indicate that the strong-ground motion records are less sensitive to small-scale variability in the slip models (Figure 14d).

Our analysis implies that strong motion stations within 200 km of the 2011 Tohoku-Oki earthquake are likely most valuable in resolving both the earthquake rupture propagation and slip distribution. When comparing the synthetics with observations at different distances, we find that the sensitivity of regional strong motion records decreases with increasing epicentral distance (Figure 15). The observations can be well explained by the synthetics obtained assuming the simplified rupture propagation model once the epicentral distance is larger than 300 km, with their correlation coefficients greater than 0.7 on average, including the vertical components. These waveforms are less complex, comparable to those of teleseismic observations (Figure 14). In contrast, waveforms at stations within 200 km epicentral distance are complex and are challenging to model even when multiple rupture episodes are permitted, such as in the original model J4. While this model is obtained using the regional seismic observation and the multi-time-window method, its synthetic waveforms have an average correlation value of 0.71 for the ver-

tical component observations in comparison to a value of 0.95 for the east component (Figure S35).

#### 4.4 Tsunamigenic Seafloor Uplift

The Tohoku-Oki earthquake generated a devastating and far-reaching tsunami across the Pacific Ocean. Tsunami data has a unique sensitivity to seafloor displacement, and the data recorded by offshore bottom-pressure gauges, Global Positioning System (GPS) wave gauges, and DART buoys are commonly used to invert for seafloor uplift models, which are then used to invert for earthquake slip distributions (e.g., M. Sato et al., 2011; Maeda et al., 2011a; Saito et al., 2011; Hossen et al., 2015; Dettmer et al., 2016; Jiang & Simons, 2016). This two-step procedure decouples the observed tsunami data from the assumed fault geometry and Earth structures, allowing the inverted seafloor displacement to be validated by other independent geophysical observations (Fujiwara et al., 2011; Kodaira et al., 2012).

We take advantage of a published seafloor uplift model obtained using tsunami data (Jiang & Simons, 2016) and compute synthetics from the collection of slip models to compare with the smoothed uplift model of Jiang and Simons (2016). This model is obtained by inverting data from ocean bottom pressure gauges, seafloor cable pressure gauges and GPS gauges, and three open ocean DART tsunami meters. We use the smooth version of the seafloor uplift model (referred to as model SJS hereinafter) because of its reported lower uncertainty. This model shows a broad uplift region at the major slip area shown in the median model, albeit with a more heterogeneous spatial pattern (Figure 16a). Using the procedure outlined in Section 4.1, we compute the vertical seafloor displacement at the same set of model grid points as in Jiang and Simons (2016). The displacements are obtained using the same Green's functions from Hori et al. (2021) as we used for computing the onshore and offshore geodetic synthetics. We then compare the seafloor uplift synthetics with model SJS by calculating their correlation-coefficients. We apply the comparison procedure to finite-fault models at the 16, 32, and 64 km scales for all 32 models and the median model.

The seafloor-uplift synthetics show clear differences among the finite-fault models, suggesting that seafloor uplift observations can distinguish their major features. For example, seafloor-uplift synthetics from five models in Figure 16 at the 16 km scale have large variations, reflecting the variations in their corresponding slip distributions (Figures 16 and 2). In addition, models at different spatial scales would cause different seafloor-uplift fields, indicating that this type of data may have a spatial resolution of 32 km for the 2011 Tohoku-Oki earthquake, such as the model J5 example in Figure 16. However, seafloor-uplift fields cannot distinguish the secondary features of the slip models, such as the contrasting shallow and deep rupture patches in the southern section of models R3 and G4, respectively (Figures 4 and 16). The southern secondary slips of both models exceed 10 m. However, the corresponding seafloor uplifts are less than 2 m, an uplift amplitude within the absolute uncertainty range of model SJS (Jiang & Simons, 2016).

Despite the seafloor-uplift synthetics showing a clear distinction among different slip models, the synthetics do not correlate well with model SJS, with an average correlation-coefficient of 0.6. These low correlation-coefficients stem from the variability of the finite-fault models and may also reflect significant uncertainties in the tsunami-inferred seafloor uplift (Jiang & Simons, 2016). The variations in synthetics lead to a large range of corresponding correlation coefficients comparable to the variations in the slip models. Our synthetic analyses also indicate that a well-resolved seafloor uplift field has the potential to determine finite-fault slip distributions at a 32 km scale, a higher resolution than those of the teleseismic or geodetic datasets.



## 5 Discussion

### 5.1 What Controls the Finite-fault Model Variability?

We quantitatively compare the collection of finite-fault models for the Tohoku-Oki earthquake and find that they share a consistent feature regarding the location of the largest slip patch, updip of the hypocenter in the Miyagi-Oki shallow region (ZC1). At a spatial scale of 64 km, these models have an average correlation coefficient of 0.88. We generate a static net slip median model that effectively captures this coherent slip feature, with correlation-coefficients  $\geq 0.80$  compared with other models at all spatial scales, from 1 to 64 km (Figure 9d). Furthermore, the median model does not have secondary features in other zones, and its 10 m slip contour only extends 220 km along the strike direction. Our data validation analyses show that the median model can explain the on-shore and offshore geodetic observations (Figure 10). The model can also explain teleseismic observations when paired with an appropriate PSRT distribution (Figure 11–16). The excellent performance of the median model results from the averaging procedure, which can reduce both model-induced and data-induced errors (S. Minson et al., 2013). The averaging procedure is particularly effective when a large set of models obtained from a diverse set of datasets is available (Twardzik et al., 2012), as the Green’s functions linearly connect the model to the data.

Our model comparisons reveal considerable variability in secondary slip features among the models. Specifically, slip features with spatial extents less than 64 km are distinctive across different models. We find that the degree of variability seems to correlate with the types of data used in developing the models. Most models in groups R and S are characterized by one or two large slip patches in ZC1 without significant secondary features. This characteristic is reflected in the model correlation-coefficient histograms in Figure 7b, which display smaller spreads than other groups. Models in group G can vary greatly, leading to two separate subgroups, as shown in Figure 7b. Models in group T are highly heterogeneous, and their secondary features do not agree with each other, leading to nearly uniform correlation-coefficient distributions within the group and with other groups (Figure 7b). Models in group J are inverted from a variety of datasets, but they all have included tsunami and seismic data. These models show the least coherence within their group or compared to models of other groups (Figure 7b). As shown in Section 4, the available geodetic and seismic observations can constrain the models to approximately a 64 km scale, while the tsunami data might provide sensitivity at a spatial scale of 32 km. This discrepancy in sensitivity may contribute to the observed complexities in the models developed using tsunami data, which is also reflected in the power spectra of the slip models in Figure 6.

The rupture extent of the models differs among the five groups. The G, R and S groups have an average along-strike extent of 250 km for the 10 m slip contour, whereas the rest of the groups show rupture extents up to 300 km for the same slip contour range along the strike direction. The extended slip areas are shown as secondary slip features in models from the T, and J groups. The limited sensitivity of geodetic, regional seismic and teleseismic data to these small-scale features may account for these differences. However, secondary slip features in the T, and J group models disagree, and no consistent rupture extent can be extracted from these models, even within the same model group. Even though tsunami observations may have higher sensitivities to smaller slip patches, the inconsistent model features cannot support the notion that they are superior to those from the geodetic, regional seismic, or teleseismic data. Joint inversion of multiple datasets may balance the complementary sensitivities of different datasets to resolve more accurate finite-fault models. However, the localized, small-scale features in the J models are notably different from those of models from other groups, casting doubt on their reliability in capturing small-scale features.

The sensitivity of tsunami data to small-scale features likely results from the slow propagation speed of tsunamis. Assuming a tsunami wave speed of 200 m/s, a 32 km separation of slip patches would lead to an 1800-second separation in the recorded tsunami waves for an instantaneous rupture scenario. This temporal separation in the record would allow the tsunami data to record small-scale slip features. However, due to the space-time trade-offs for large earthquakes, the number and azimuth distribution of tsunami observations have critical controls in determining the seafloor displacement, which could cause model disparities when the observations are sparse.

In addition, the inversion of tsunami data often involves multiple steps, which include translating the recorded tsunamis into seafloor deformations, followed by inverting slip at the megathrust interface using the deformation estimates. For example, Hossen et al. (2015) and Dettmer et al. (2016) demonstrate that tsunami dispersion effects and accounting for source kinematics may lead to differences in the imaged seafloor uplift, notably in the northern region with extended uplift near the trench. Other timing discrepancies in the tsunami far-field may stem from solid Earth elasticity and ocean water compressibility (Tsai et al., 2013). Differences in model setup, effectively different Green's functions, have strong controls in the seafloor deformation response, consequently resulting in discrepancies in the inverted slip distributions. K. Wang et al. (2018) underscores the influence of model assumption in the slip models, and the poorly constrained near-trench fault geometry and bathymetry would lead to large uncertainties in the modeled seafloor deformation.

Another potential factor that may cause the large variability in models obtained using tsunami data is the possible existence of unaccounted secondary sources, such as submarine landslides, localized off-fault deformation, or splay fault slip, which can amplify coseismic seafloor displacements and contribute to generating tsunamis (Y. Ito et al., 2011; Ide et al., 2011; Tsuji et al., 2011; Ma & Nie, 2019; van Zelst et al., 2022; Biemiller et al., 2023; Ma, 2023). The collection of finite-fault models assumes that all geophysical signals are solely stemming from earthquake slip across the megathrust. If submarine landslides or other events occurred during or shortly after coseismic rupture, they may bias the inferred slip models. In this case, strong additional sources would yield coherent secondary slip features in the models derived from the tsunami data. However, our analyses show that the T and J groups contain the least coherent models at small scales. This observation does not appear to confirm the secondary source hypothesis.

In addition to the data types, finite-fault inversion methods have a strong impact on the resulting models. For example, the collection of models shows pronounced differences in slip distribution near the trench. Some models feature tapered slips near the trench, potentially due to no-slip boundary conditions employed during the inversion. The peak-slip location is influenced by boundary conditions. For example, Zhou et al. (2014) demonstrated that the peak-slip location would shift away from the trench if a no-slip boundary condition is imposed during the inversion. For example, models T1 and S3 demonstrate strong taper slips to zero near the trench. Conversely, a free-slip boundary condition would lead to the peak-slip location being placed near the trench, including models G4 and G7 (e.g., Figure 1). Inversion techniques also influence the model variability (Figure 2). Particularly, models from full Bayesian methods without employing smoothness or spatial correlation priors are more heterogeneous, such as models T1 and J2 in Figure 2, and averaging ensemble models does not equal to a smoothness prior (D. S. Sato et al., 2022; Yagi & Fukahata, 2011b; Zhou et al., 2014).

The finite-fault model configuration, such as the fault geometry and subfault parameterization, and the adopted velocity structures directly impact the model variability (K. Wang et al., 2018). Our analysis assumes a fixed fault geometry from Slab2.0 and uses a 1D velocity structure to compute Green's function. This procedure allows us to explore the data sensitivity to different slip distributions but does not examine model-induced uncertainties, which may have contributed to the model variability (e.g., Bletery

et al., 2015; Funning et al., 2014; K. Wang et al., 2018; Ragon et al., 2018; Halló & Gallovič, 2020; Agata et al., 2021).

## 5.2 What Does the Variability Imply?

The exact rupture extent of the Tohoku-Oki earthquake has both scientific and societal implications, particularly the extent and amplitude of potential secondary slip features in the northern and southern sections. Based on the rupture extents of historical earthquakes, the Japan subduction zone was estimated to be capable of generating earthquakes of a maximum magnitude of 8.2 prior to the Tohoku-oki earthquake (Uchida & Bürgmann, 2021). Ten of the 32 finite-fault models suggest that the Tohoku-oki earthquake ruptured into zone ZN1 in the Sanriku-Oki region, which may have hosted the large tsunamigenic 1611 M8.5 Sanriku earthquake (Kawakatsu & Seno, 1983; Imai, 2015). Rupture in ZN1 has important implications for our understanding of the recurrence pattern of large earthquakes in the region. In the southern section, contrasting frictional and material behaviors of the upper plate may act as rupture barriers and limit the rupture extent to the shallow Ibraki-Oki region (ZS1) (e.g. Bassett et al., 2016; Liu & Zhao, 2018). Subducted seamounts leading to a rough subduction interface at around 36°N may also terminate the southern rupture (K. Wang & Bilek, 2014). However, 7 out of 32 finite-fault models show extended southern extended deep rupture (ZS2), and 11 finite-fault models show extended shallow rupture in the southern section (ZS1). The varying southern deep extended rupture may also penetrate the three 1936, 1937, and 1978 M7 or above Fukushima Shioya-Oki earthquake rupture areas (Abe, 1977; Yamanaka & Kikuchi, 2004; Simons et al., 2011; Nakata et al., 2016). Given the variability and uncertainty of the finite-fault models, and a lack of certainty of the mechanics of how earthquakes arrest (e.g., Kammer et al., 2015; Galis et al., 2017), physical controls of megathrust earthquake rupture extents are yet to be confirmed in the Japan subduction zone and globally.

The scale and distribution of slip heterogeneity may reflect fault-zone heterogeneities, including in the pre-earthquake stress distribution, fault frictional properties, fault geometry and roughness, pore fluid pressure or fault zone materials (Bassett & Watts, 2015; Gallovič et al., 2019; Moore et al., 2015; Madden et al., 2022; Tinti et al., 2021; K. Wang & Bilek, 2014). The observed slip complexities in the suite of models, if true, suggest that the seismogenic zone composes of a wide range of heterogeneity with spatial scales reaching tens of kilometers. Specifically, the J models suggest highly complex slip behavior in the hypocentral and near trench regions, which would require either very high initial stress build-up, strong co-seismic weakening, or other mechanisms to sustain the nucleation and dynamic rupture propagation (e.g., Goldsby & Tullis, 2011; Di Toro et al., 2011; Viesca & Garagash, 2015). However, we show that these small features cannot be confidently confirmed by the commonly used datasets. Future physics-based dynamic rupture or seismic cycling simulations are needed to explore these features in a self-consistent way.

## 5.3 How to Better Evaluate Finite-Fault Models?

Even though the collection of models suggests a variety of slip distributions, their moment-release distributions may bear a higher resemblance with each other (Lay et al., 2011). Slip distributions are impacted by the Green's functions used in the finite-fault inversion, and there are trade-offs between the assumed velocity structure and the final slip distributions (Gallovič et al., 2015). The moment-release distribution is a composite model that includes both the slip distribution and the local velocity structures, and it is better resolved in finite-fault inversions. Lay et al. (2011) compared two contrasting slip distributions, one obtained with and the other without shallow, weak sediments (a low shear modulus layer) near the trench. The model obtained with a low shear modulus layer has a significantly larger slip near the trench, an effect confirmed in 3D megathrust dynamic rupture simulations (Sallarès & Ranero, 2019; Ulrich et al., 2022). How-

ever, the moment-release distributions of the two models are almost identical. Comparisons based on the moment-release distributions may lead to more consistent interpretations of the rupture process. However, such comparisons would require detailed documentation of not only the finite-fault models but also the associated Green's functions and near-source velocity structures.

Our investigation of both the teleseismic and regional seismic synthetics shows that the spatial complexity in the final slip distribution does not significantly impact the waveform fitting (Figures 12 and 14). However, the temporal evolution of the rupture front plays a critical role in explaining the data, and it cannot be approximated as a smooth propagation with one or two rupture speeds for the Tohoku-Oki earthquake. Specifically, we find that both regional seismic and teleseismic observations are highly sensitive to the peak-slip-rate-time distribution. We find that the peak-slip-rate-time distributions from different kinematic models agree on major slip episodes when using similar teleseismic datasets. For example, Figures S14 and S15 show that peak-slip-rate-time from models S3, S6, and J3 can explain the teleseismic observations equally well. These peak-slip-rate-time distributions can also be represented as slip-rate snapshots in kinematic finite-fault models, and Gallovič and Ampuero (2015) reported similar findings: finite-fault models developed using seismic data agree well on their spatiotemporal evolution, even when the final slip distributions are distinctively different. Additionally, regional seismic observations, particularly the vertical component of the strong motion records of the 2011 Tohoku-Oki earthquake, are also sensitive to the slip-rate functions. A simplified rupture propagation model with a single-time-window slip-rate function is insufficient to reproduce the observed strong motion waveforms.

#### 5.4 Future Opportunities

Our seafloor uplift synthetics suggest that the seafloor displacement field can resolve megathrust slip distributions at a spatial scale of 32 km. The resolution can discern detailed slip patterns, which can provide critical insights into rupture dynamics and faulting conditions. Although the offshore geodetic measurements during the Tohoku-Oki earthquake can provide the most accurate displacement measurements, their sparse distribution limits their resolutions to less than 64 km.

The Seafloor Observation Network for Earthquakes and Tsunamis along the Japan Trench (S-net) has the potential to resolve future megathrust earthquakes in great detail (Nishikawa et al., 2019). The S-net was developed after the Tohoku-Oki earthquake and it covers the entire Japan subduction zone with 150 colocated pressure gauges and accelerograms with a nominal inter-station interval between 30 and 60 km (Mochizuki et al., 2018). It is a cabled network and transmits data back to onshore in real-time. The network configuration suggests a high sensitivity to megathrust slip distributions. We conduct a synthetic analysis following the procedure outlined in Section 4.1 to compute static displacements at each S-net station. Specifically, we calculate the vertical uplift synthetics using all slip models at different scales and compare the synthetics to those from the median model at the corresponding scales. The correlation coefficients of the synthetics show the sensitivity of S-net data to variations in slip features relative to the median model.

We find that S-net can distinguish variability in the slip distributions (Figure 17). The seafloor uplift synthetics in Figure 17 show clear differences among six example models at the 16 km scale. The synthetics can directly contour slip areas with slips of 5 m or above. This resolution can accurately resolve secondary slip features that do not significantly impact the geodetic or teleseismic synthetics. The synthetics vary for the same model at different scales (e.g., Figure 17), suggesting a possible resolving ability of 16 km. This resolution results from both the dense spatial coverage and the uplift amplitude sensitivity of the instruments. Our synthetic experiment shows that large-scale, dense off-

shore networks are critical to constraining megathrust slips and mitigating the associated hazards.

We find that teleseismic data are highly sensitive to the spatiotemporal rupture process, such as the peak-slip-rate-time distribution. However, the data seems to have limited resolvability for small-scale slip features. This apparently paradoxical sensitivity is likely due to the fact that the observed teleseismic displacement P-wave waveforms are dominated by signals in the 20–30 s period band. In this case, the characteristic wavelength of the waveforms would be around 120–180 km, and such long wavelengths limit the data resolution. Therefore, higher frequency teleseismic observations may better constrain the spatial-temporal evolution of megathrust earthquakes. Specifically, velocity P-wave waveforms have higher frequency signals than displacement records, and they may potentially resolve the small-scale slip features at higher resolutions (Yagi & Fukahata, 2011b). To explore this hypothesis, we conduct a similar teleseismic validation exercise using velocity waveforms at the same set of stations (Figures S23-S24 and Text S3). We find that the synthetics do not correlate with the teleseismic velocity records as well as the displacement records, suggesting a possible higher sensitivity to variations in the finite-fault models. Similarly, we find that regional strong motion seismic records are sensitive to the earthquake rupture propagation, and exploiting these observations, particularly observations within 200 km epicentral distance may yield finite-fault models with an improved resolution.

## 6 Conclusion

We quantitatively compare and validate 32 finite-fault models of the 2011 Tohoku-Oki earthquake. We first design a reparameterization framework to unify the models using a realistic megathrust geometry while preserving potency distribution at a 1 km scale. We then downscale the models to 16, 32, and 64 km scales to compare their coherent and unique features. We find that the models agree well at the 64 km scale but do not agree on small-scale features, either regarding their locations or amplitudes. All unified models suggest that the Tohoku-Oki earthquake ruptured the updip megathrust near the hypocenter in the Miyagi-Oki region, and large slip occurred near or at the trench. This coherent feature is reflected in the median model, obtained by averaging the collection of models. We examine the sensitivity of the commonly used geodetic, teleseismic, regional seismic and geodetic, and tsunami seafloor uplift datasets to the variability in the finite-fault models. Our results suggest that geodetic, regional seismic, and teleseismic data have a spatial resolution of 64 km for the final slip distribution, while the tsunami data might have a higher sensitivity to slip features at 32 km scales. We find that both regional seismic and teleseismic observations are highly sensitive to the earthquake rupture process. However, teleseismic data are less sensitive to the slip-rate functions at each subfault. We calculate synthetic vertical uplifts at the S-net offshore in Japan, and the results suggest that the network can resolve megathrust earthquake slip distribution at a high spatial resolution of 16 km. Our results show that near-field and uniformly gridded dense offshore instrumentation networks are crucial for resolving complex earthquake rupture processes and assessing their associated hazards.

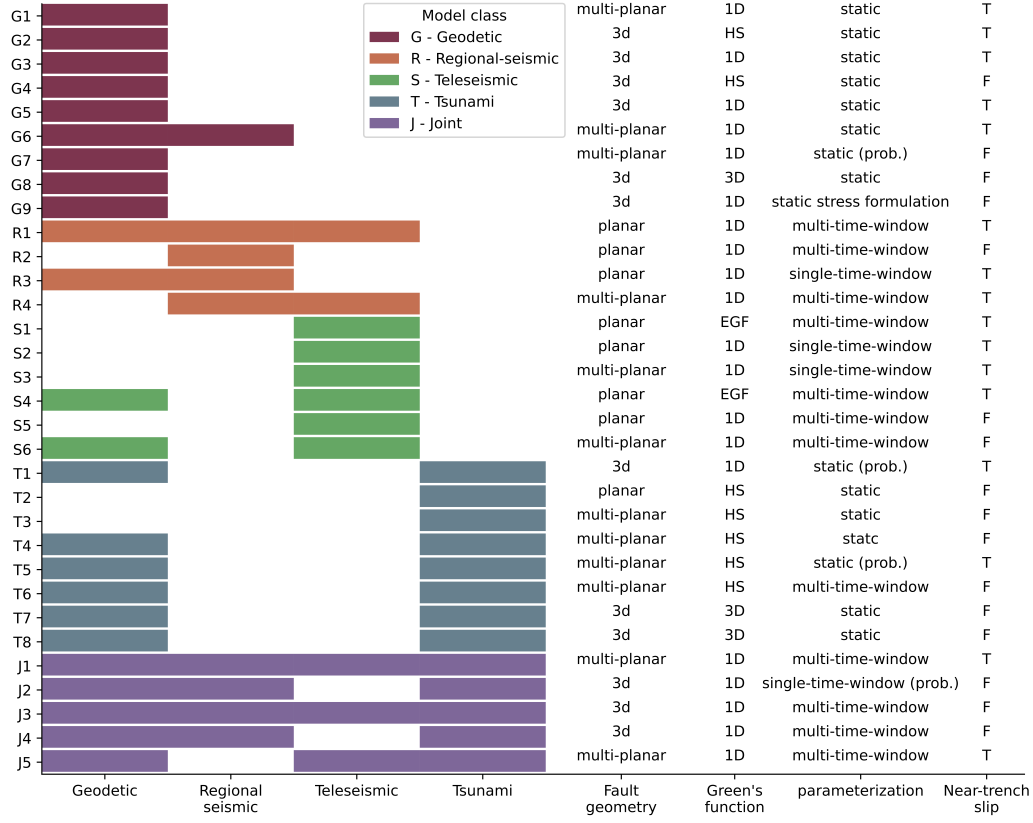


**Figure 1.** Thirty-two finite fault models used in our analysis, arranged by dataset type and publication date (see Text S1 for details). Color blocks in the left-four columns indicate datasets used to obtain each finite fault model with the color indicating the five model groups. Right-four columns describe the fault geometry, Green's function (HS: halfspace model, 1D: one-dimensional velocity model, 3D: three-dimensional velocity model, EGF: empirical Green's function), parameterization used and near-trench slip features (T: tapered slip, F: free slip to trench) of each finite fault model, respectively.



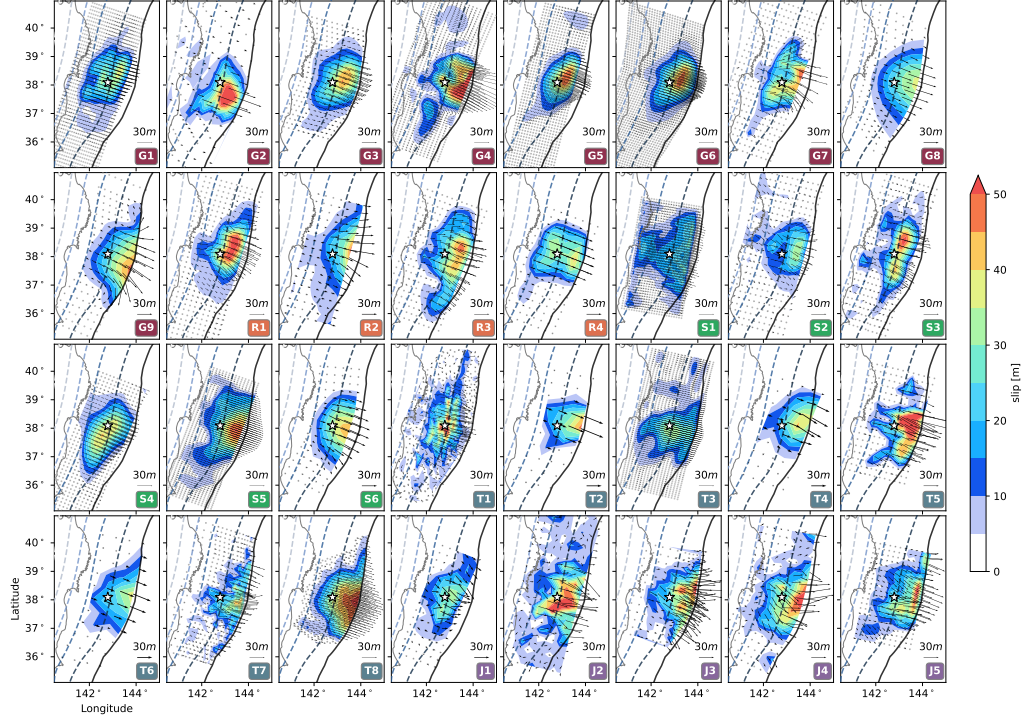


**Figure 2.** Slip distributions of the 32 finite fault models. Slip distributions and slip directions are shown as color contours and vectors, respectively. Grey dots indicate the centers of each model's subfaults. USGS hypocenter location is shown as a white star. Slab2.0 megathrust geometry from Hayes et al. (2018) is shown as dotted contours with a 20 km depth interval. Japan trench is shown as a black solid line and the Japanese coastline is shown as a grey solid line. All model acronyms are defined in Figure 1 and detailed in Text S1.

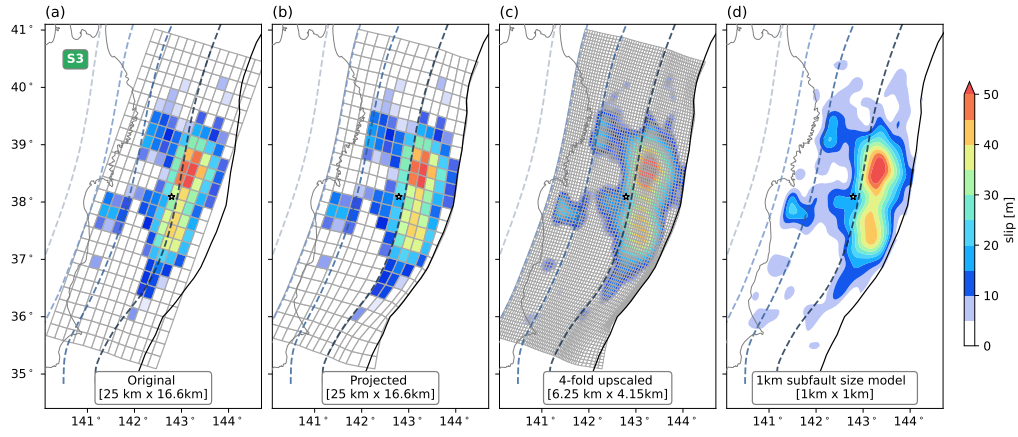


**Figure 3.** Illustration of the upscaling and projection scheme for an exemplary finite-fault model, S3. (a) Original slip distribution and subfault parameterization of the planar fault geometry. (b) Projected model using the slab 2.0 megathrust geometry. (c) Up-scaled slip distribution with densified subfault along dip and along strike four times respectively. (d) Final projected and up-scaled slip distribution at a 1 km spatial scale. Numbers on the legend indicate the subfault size.



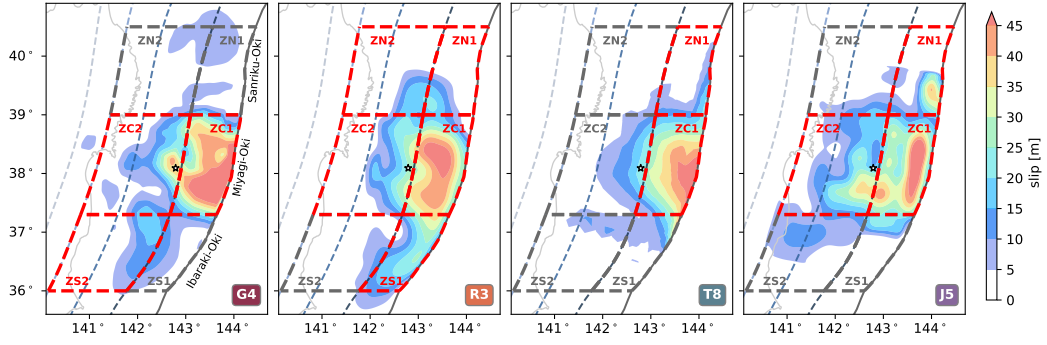


**Figure 4.** Division of the Japan megathrust into six zones and zone categorizations of four example finite-fault models. Zones with  $\geq 10$  m slip features are highlighted using red dashed contours. Table 1 summarizes the models with respect to their major slip features in each associated zone.

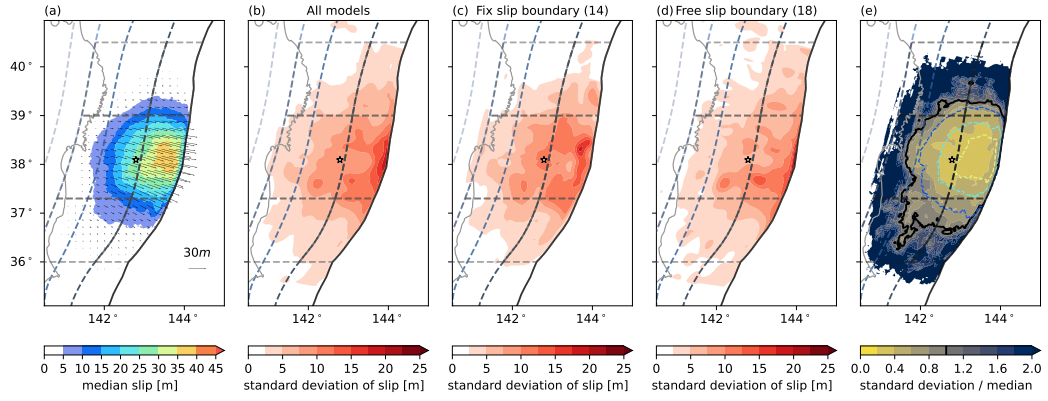


**Figure 5.** Median and standard deviations of the 32 finite-fault models. (a) Median model slip distribution at 1 km spatial scale. (b) Standard deviation of slip distribution for all models. (c) Standard deviation of slip distribution for models with tapered slip towards the trench. (d) Standard deviation of slip distribution for models with a free-slip boundary condition at the trench. Number of models included in the groups are shown in subtitle parentheses. (e) Standard deviation over median of the slip distributions. Solid black line delineates the region below 1. Colored dotted lines indicate a 10m contour of the median slip distribution. Artifacts in the standard deviation distributions are due to the original coarse fault parameterization of the finite-fault models. Grey dotted lines indicate the zones listed in Figure 4. Similar averaging finite-fault models approach are also applied in K. Wang et al. (2018) .

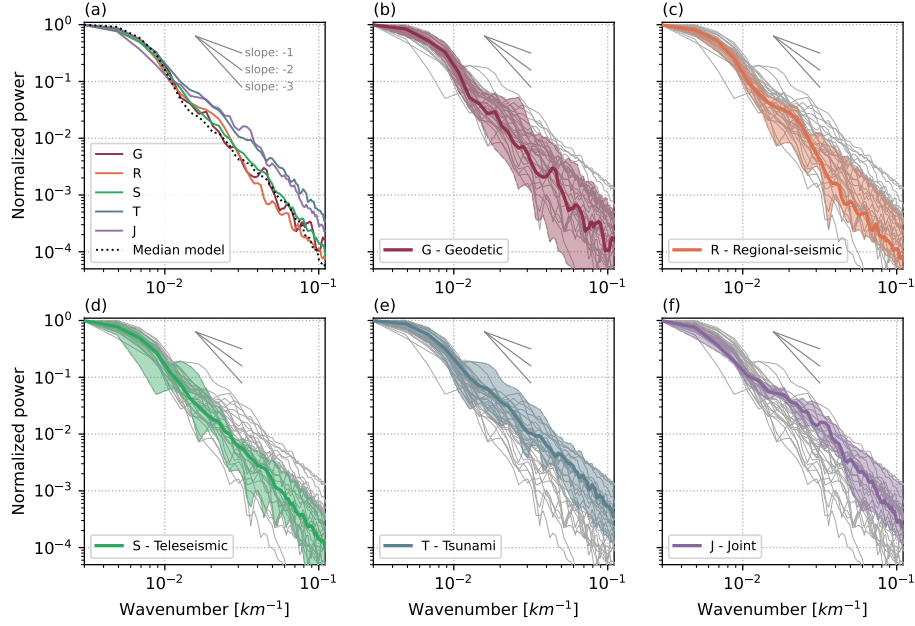


**Figure 6.** Normalized wavenumber ( $k$ ) power spectra of the 32 finite-fault models and the median model. (a) Color solid lines are the respective median spectra of each five model groups and the grey dotted line is the spectrum of the median model (Figure 5). Power spectra of the (b) geodetic group, (c) regional seismic group, (d) teleseismic group, (e) tsunami group and (f) joint-inversion group. Color-shaded areas are the range of the minimum and maximum respective spectra of the models in each group. Solid colored line is the median spectra of each model group. Grey lines represent the spectra of all 33 slip models. Decay rates of the models range from -2.0 to -4.0, with -3.0 for the geodetic group median, -3.0 for the regional-seismic group median, -2.8 for the teleseismic group median, -2.3 for the tsunami group median, and -2.1 for the joint-inversion group median.

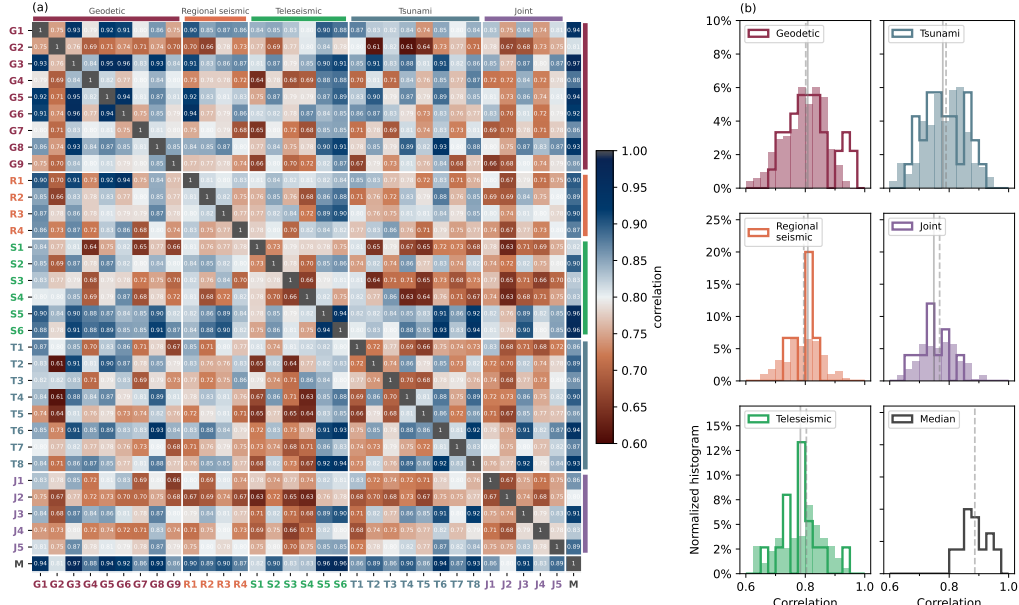


**Figure 7.** Correlation coefficients for finite-fault models at a 1 km scale. (a) Correlation coefficients matrix of the 32 finite-fault models and the median model, with each entry representing the correlation coefficient between two respective models. Background color of each entry indicates the correlation coefficient value. Matrix rows follow the same sorting order as in Figure 1 with the last row added+ for the median model (M). (b) Correlation coefficient histograms of the five model groups and the median model: solid lines show the correlation coefficient distribution of models within the group; filled histograms show the correlation coefficient distribution of models with other model groups. Light grey solid lines indicate the median value of the correlation coefficients within the respective group and dashed grey lines indicate the median value of the correlation coefficients with other model groups. Median model histogram shows its correlation with the 32 finite-fault models. Median values of the correlation coefficients within the groups: Geodetic (G), 0.81; Regional seismic (R), 0.81; Teleseismic (S), 0.78; Tsunami (T), 0.78; Joint (J): 0.75. Median value of the correlation coefficients with the median model is 0.89.

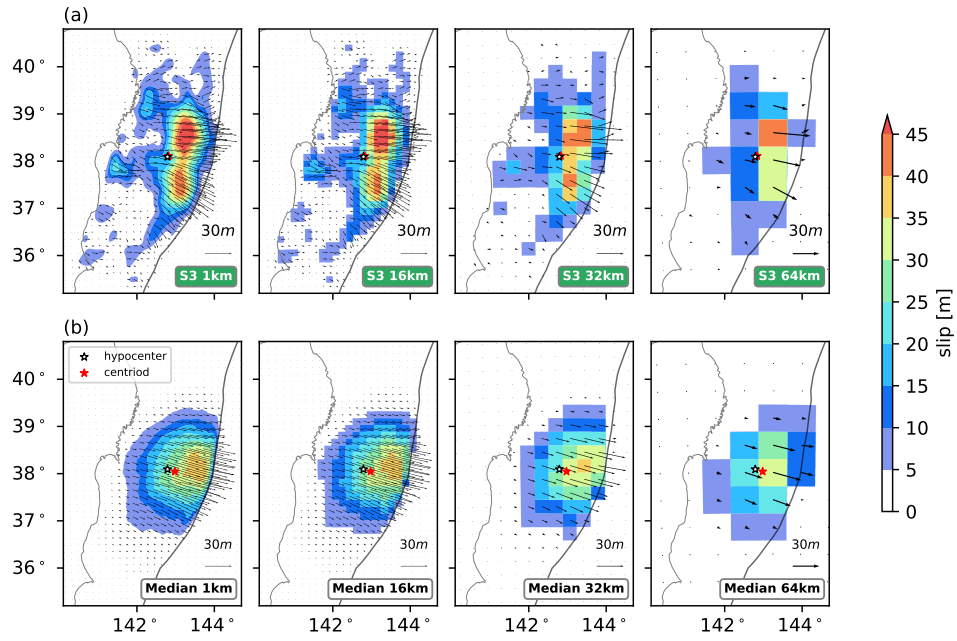


**Figure 8.** Example slip models at the 1, 16, 32, and 64 km spatial scales. (a) Model S3 at the four spatial scales. (b) Median model at the four spatial scales. Models at larger spatial scales lose fine-scale features, but the centroid locations are preserved. Hypocenter and centroid locations are indicated as white and red stars, respectively.

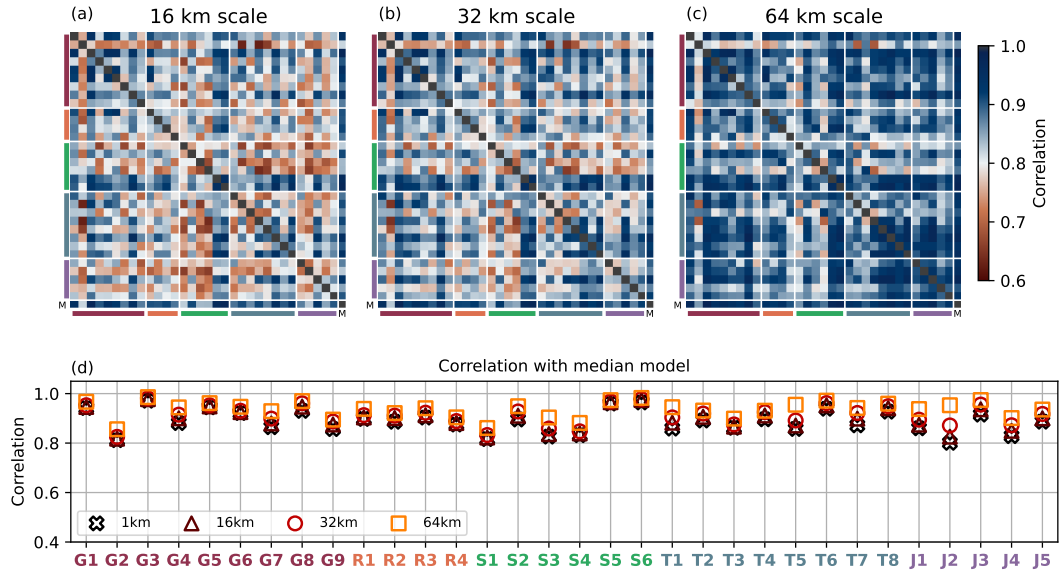


**Figure 9.** Correlation coefficients of models at the (a) 16, (b) 32, and (c) 64 km scales. Legends are similar to that in Figure 7. (d) Correlation coefficients of the 32 models with the median model at the 1, 16, 32, and 64 km scales. Median and standard deviation of models at the 16, 32, and 64 km scales are 0.81 and 0.07, 0.84 and 0.06, and 0.89 and 0.05, respectively.

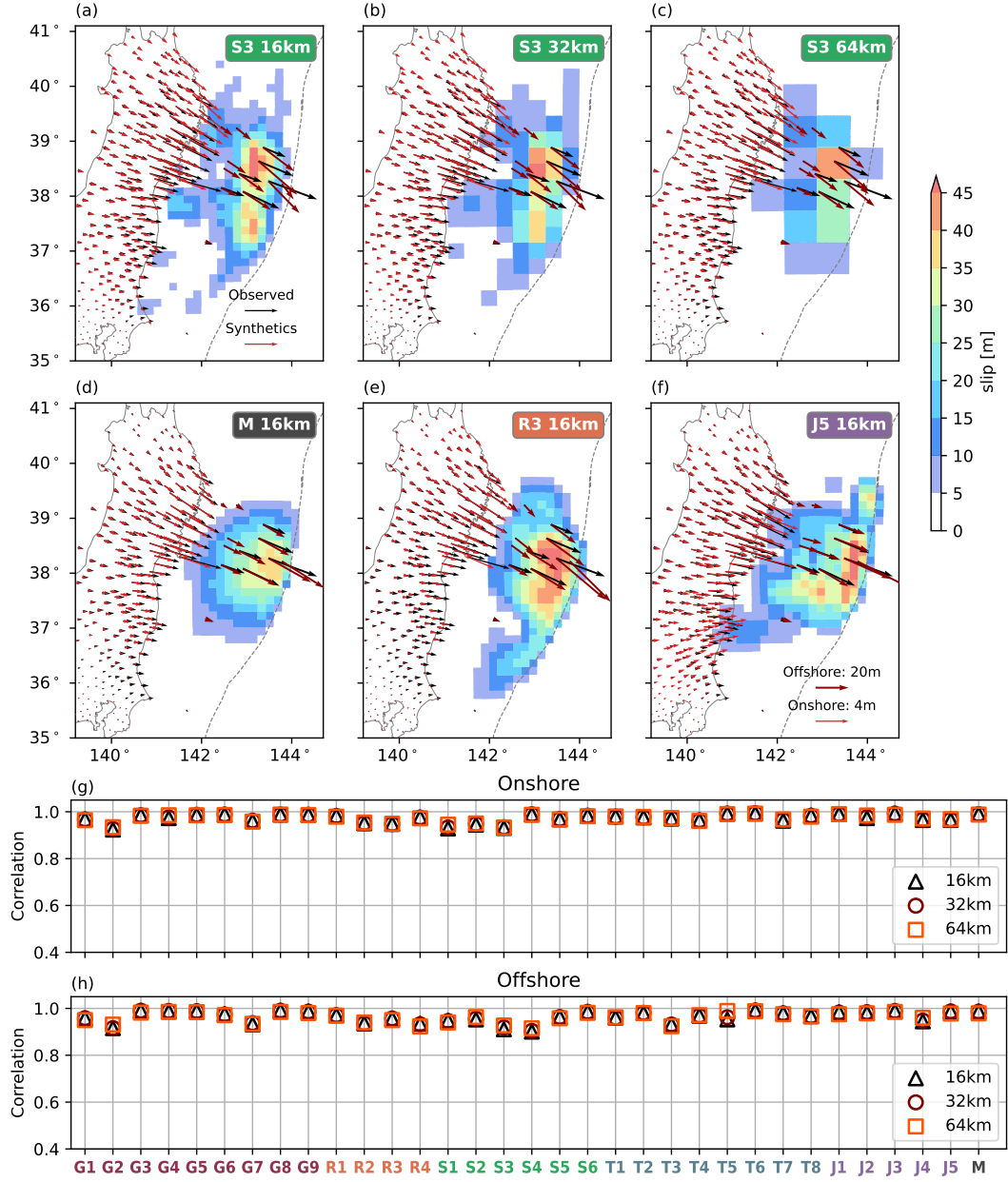


**Figure 10.** Onshore and offshore horizontal geodetic displacement observations (black arrows) and synthetics (red arrows), and their correlation coefficient values. (a)–(c) synthetic (black) and observed (red) horizontal geodetic displacements of model S3 at the 16 (a), 32 (b), and 64 km (c) scales. (d)–(f) Geodetic synthetics and observations of model M (d), R3 (e), J5 (f) at the 16 km scale. (g) Correlation coefficient values between the onshore geodetic synthetics and observations at the 16, 32, and 64 km scales. (h) Correlation coefficient values between the offshore geodetic synthetics and observations at the 16, 32, and 64 km scales.

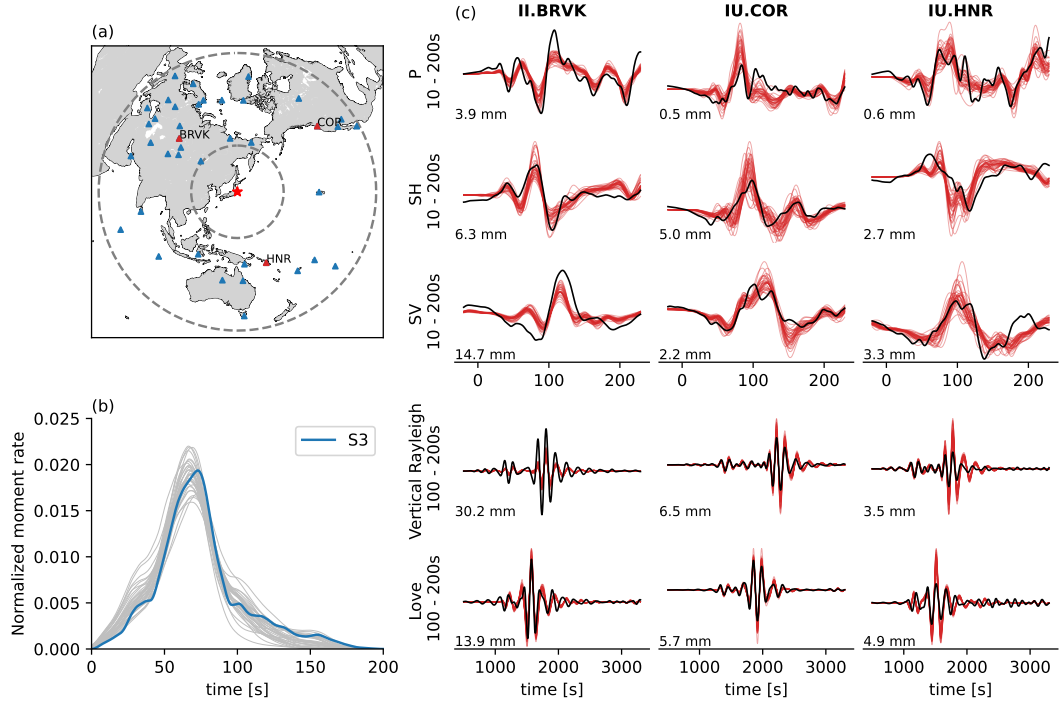


**Figure 11.** Comparison of teleseismic observations and synthetics at 16 km slip model scale. (a) Map view of 40 II and IU stations used in the analysis. Red triangles are the stations in (c). Dotted circles show epicentral distances of 30° and 90°, respectively. (b) Normalized moment rate functions of the original S3 model (blue), the 32 unified finite-fault models, and median model (grey). (c) Synthetic and observed teleseismic waveforms. Black lines are the observed waveforms; red lines are the synthetic waveforms from the 32 finite-fault models and the median model. Five rows are P wave, SH wave, SV wave, Rayleigh wave, and Love wave, respectively. Amplitudes of the observed waveforms are labeled at the lower-left corner of each waveform plot.



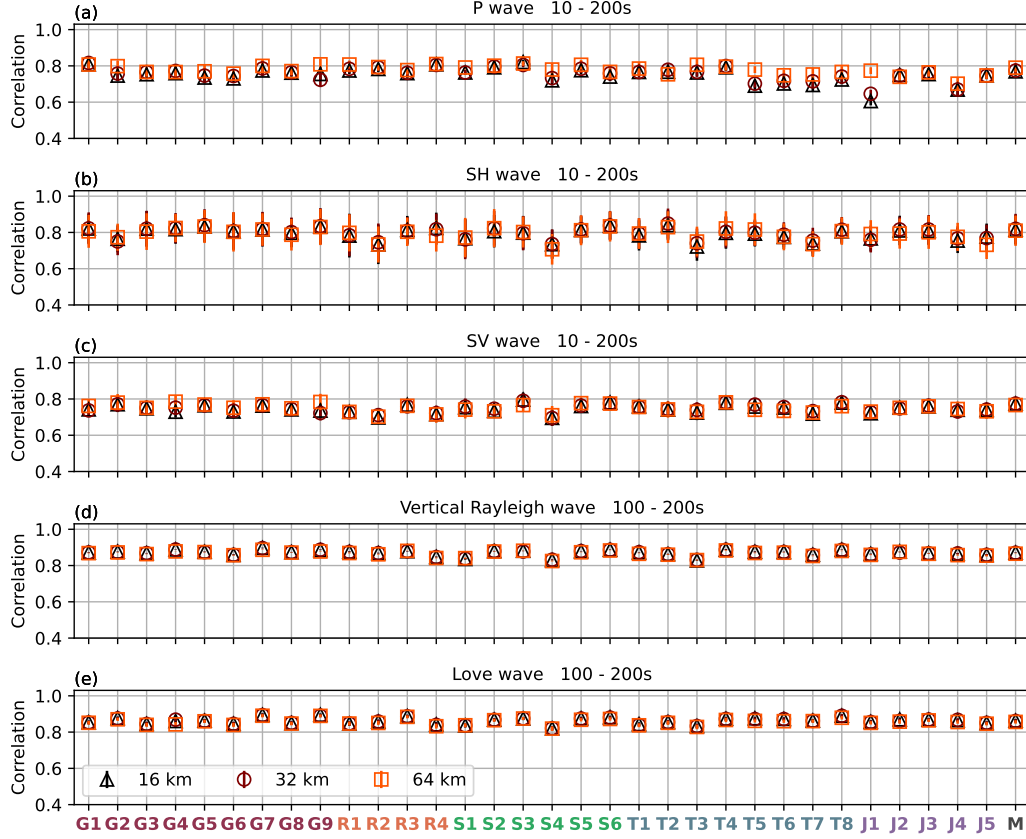


**Figure 12.** Correlation coefficient values between the teleseismic observations and synthetics at the 16, 32, and 64 km scales. (a) P wave. (b) SH wave. (c) SV wave. (d) Rayleigh wave. (e) Love wave. Median correlation values between the synthetic and observed teleseismic waveforms at the 40 teleseismic stations are taken as the characteristic correlation coefficient values for each model. Three markers indicate the characteristic median values for models at the 16, 32, and 64 km scales. Error bars represent the associated standard deviation of correlation coefficient values of the 40 stations.

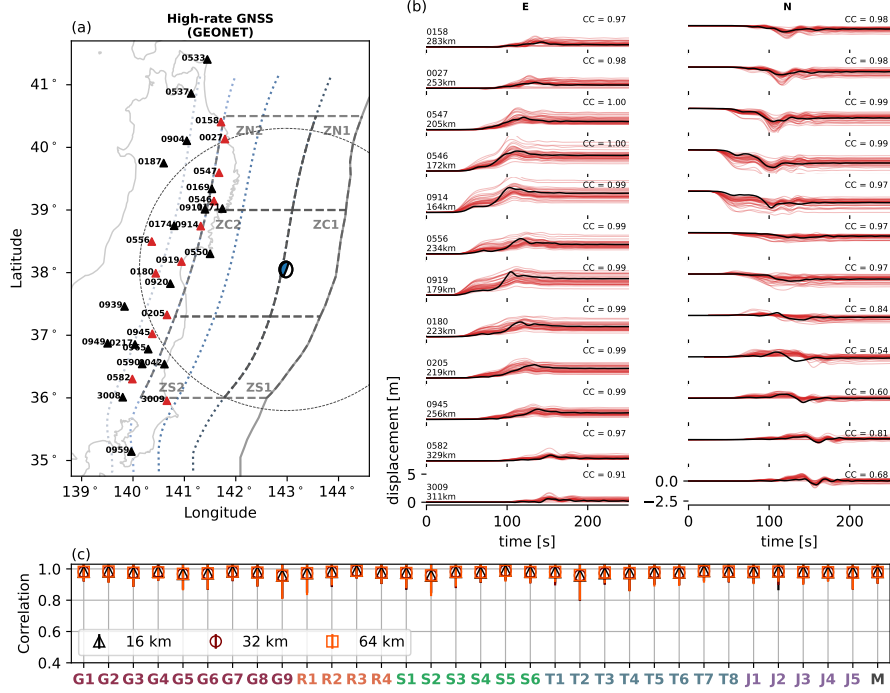


**Figure 13.** Comparison of high-rate GNSS observations and synthetics at 16 km slip model scale. (a) Map view of the GEONET stations used in the study. Red triangles are the stations in (b). Beach-ball focal mechanism represents the centroid location of the median model. Dotted circles show the centroid distance of 250 km (b) Synthetics and observed waveforms. Black lines are the observed waveforms; Red lines are the synthetics from the 32 finite-fault models and the median model at the 16 km scale. (c) Correlation coefficient values between the observations and synthetics at the 16, 32, and 64 km scale. Markers indicate the median correlation values of all stations, with an error bar indicating the associated standard deviation.

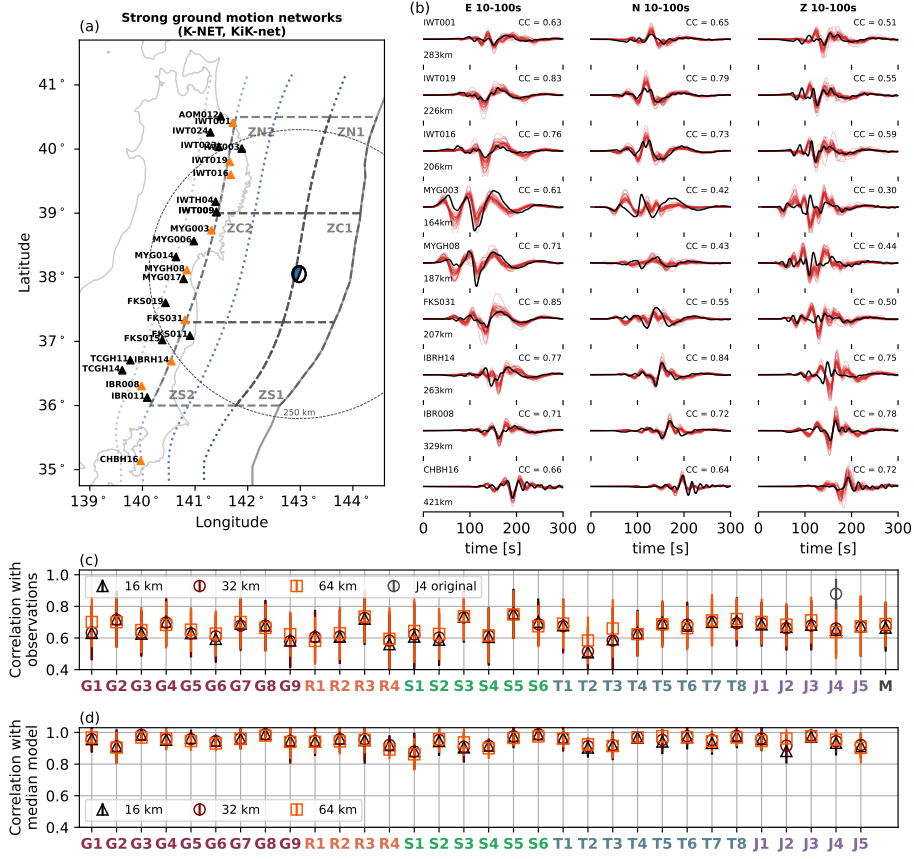


**Figure 14.** Comparison of regional strong-ground motion records (displacement) with synthetics at 16 km slip model scale. (a) Map view of the strong-ground motion stations used in the study. Red triangles are the stations in (b). The beachball focal mechanism represents the centroid location of the median model. Dotted circles show the centroid distance of 250 km (b) Synthetics and observed waveforms. Black lines are the observed waveforms; Red lines are the synthetics from the 32 finite-fault models and the median model at 16 km scale. (c) Correlation coefficient between the observations and synthetics at the 16, 32, and 64 km scale. (d) Correlation coefficients between the median synthetics and all models at 16, 32 and 64 km scale. Markers indicate the median correlation values of all stations, with an error bar indicating the associated standard deviation.

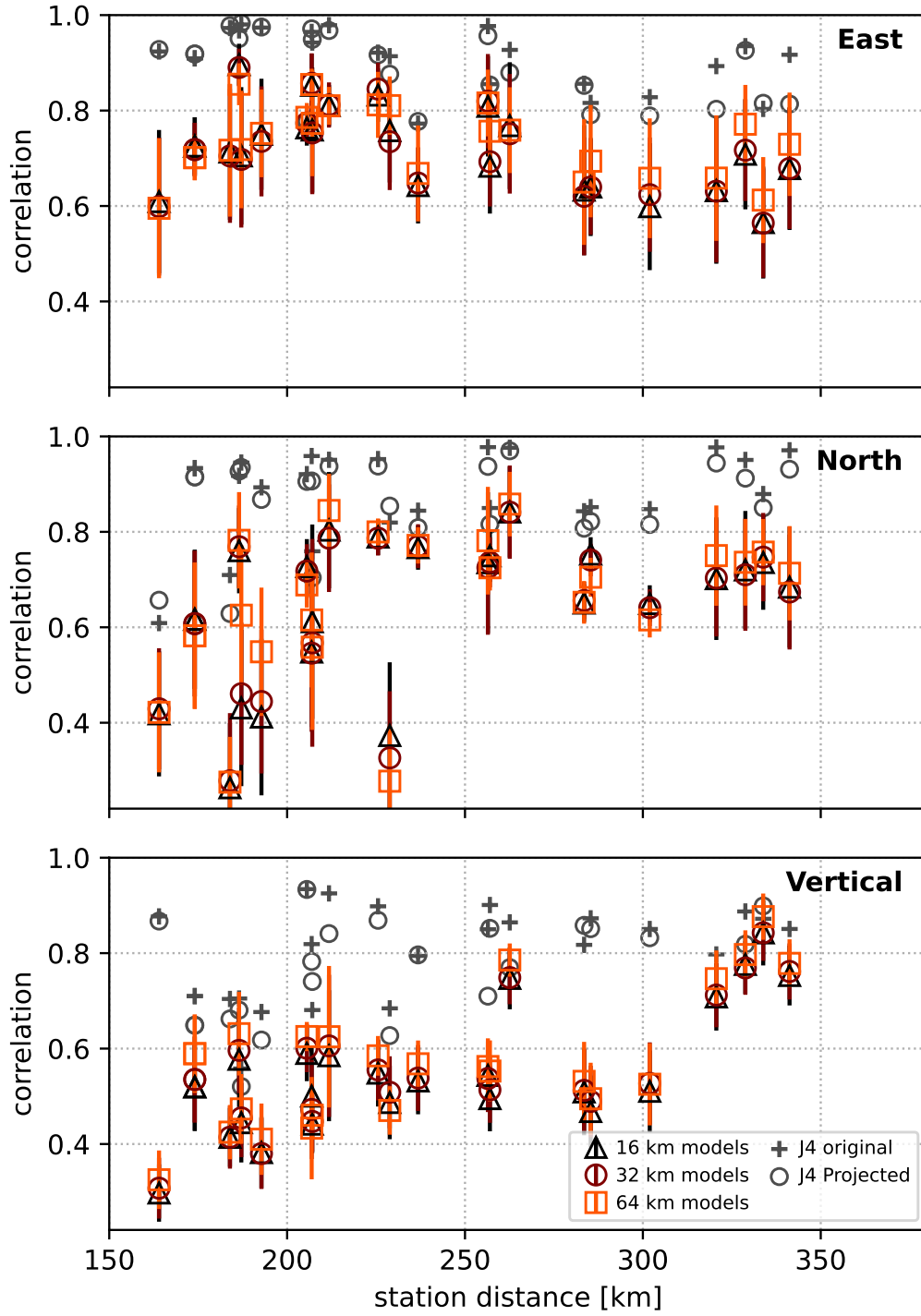


**Figure 15.** Strong ground motion synthetics correlation with respect to station distance. Synthetics correlation at (a) East component, (b) north component, and (c) vertical component. Colored error bars represent the median value and standard deviation of the correlation coefficient of all 33 model synthetics at each station. Cross and circle grey scatters are the correlation coefficients of the J4 model original synthetics and projected geometry synthetics.

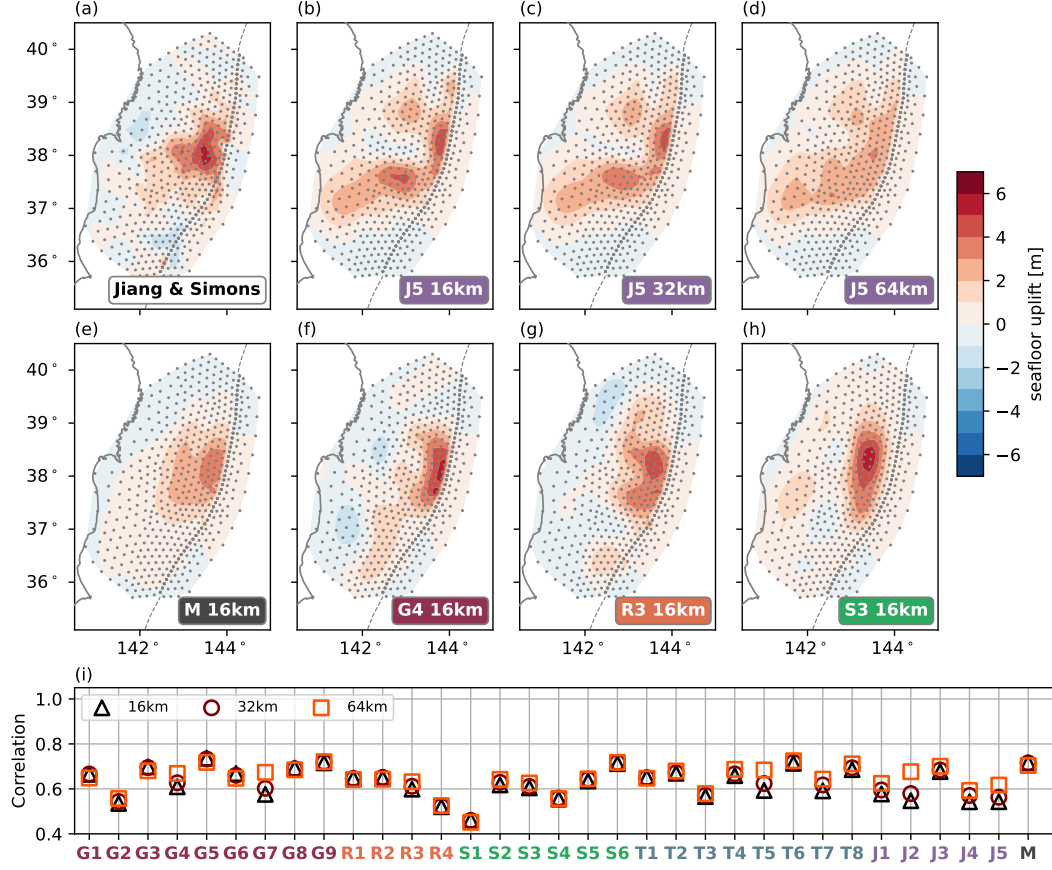


**Figure 16.** Seafloor uplift model of Jiang and Simons (2016) (model SJS), seafloor uplift synthetics from the finite-fault models, and their correlation coefficient values between the synthetics with model SJS. Grey dots show the modeled grid points. (a) Model SJS. (b)–(d) Synthetic seafloor uplift of model J5 model at the 16 (b), 32 (c), and 64 km (d) scales, respectively. (e)–(h) Synthetic seafloor uplift of the median slip model, models G5, R4, and S3 at a 16 km scale. (i) Correlation coefficient values between model SJS and synthetics of the 32 finite-fault models and the median model at the 16, 32, and 64 km scales.

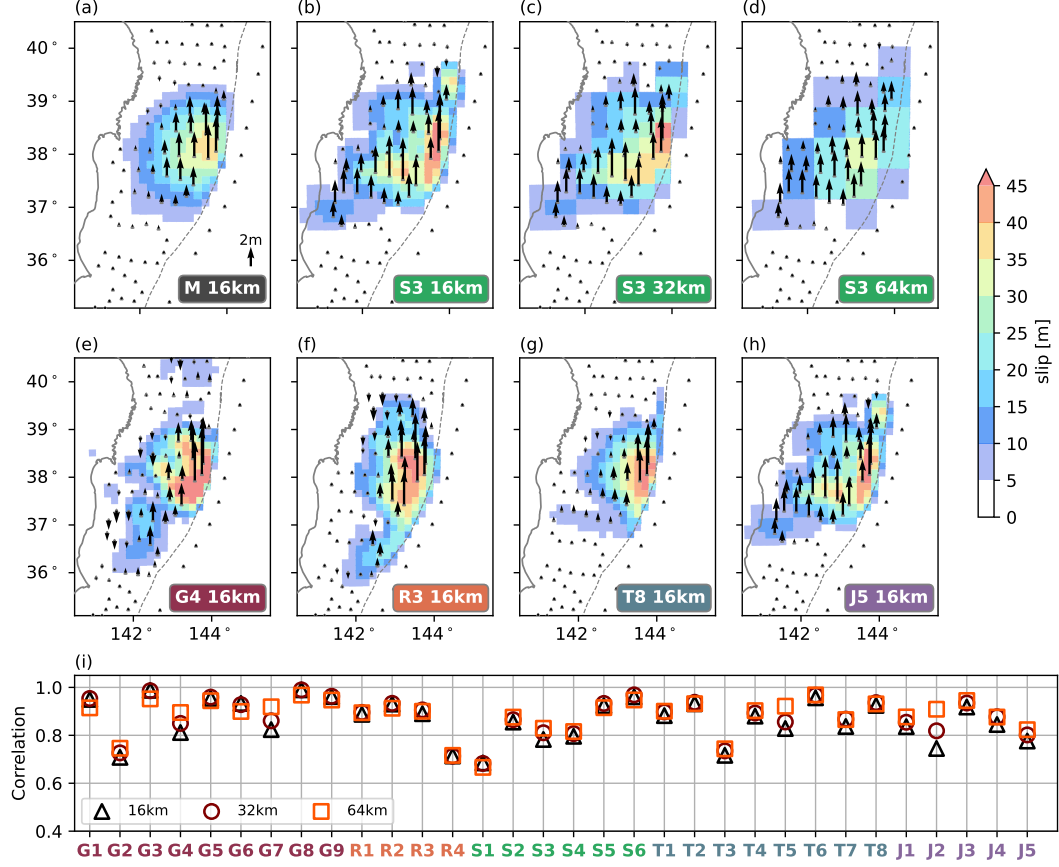


**Figure 17.** S-net seafloor uplift synthetics and their correlation coefficient values with the synthetics of the median model. S-net stations are shown as grey dots (Mochizuki et al., 2018). (a) Synthetic coseismic seafloor uplifts of the median slip model at the 16 km scale. (b)–(d) Synthetics seafloor uplifts of model S3 at the 16, 32, and 64 km scales. (e)–(h) Synthetics seafloor uplifts of models G5, R4, T8, and S3 at the 16 km scale. (i) Correlation coefficient values between synthetics of the median model and the 32 finite-fault models at the 16, 32, and 64 km scales.



**Table 1.** Finite-fault model features in rupture zones

Zone (counts)	Models
ZN1: Sanriku - shallow (10)	R1, R2, R3, T5, T6, T8, J1, J2, J4, J5
ZN2: Sanriku - deep (4)	G7, R4, S3, T1
ZC1: Miyagi - shallow (32)	All models
ZC2: Miyagi - deep (26)	G1, G2, G4, G6, G7, R1, R3, R4, S1, S2, S3, S4, S5, S6, T1, T2, T3, T5, T6, T7, T8, J1, J2, J3, J4, J5
ZS1: Ibaraki-Fukushima - shallow (11)	G9, R1, R3, S3, T1, T5, T7, T8, J2, J3, J4
ZS2: Ibaraki-Fukushima - deep (7)	G4, R5, S2, S4, T1, T5, J2

## 7 Open Research

The 32 finite-fault models are retrieved from a subset of Sun et al. (2017) collected models, the SRCMOD database (Mai & Thingbaijam, 2014), online datasets shared with referenced papers, and from authors sharing them directly. The GEONET GNSS data was provided by the Geospatial Information Authority (GSI) (Sagiya, 2004). We compared the teleseismic synthetics with the teleseismic data obtained from the Federation of Digital Seismic Networks (FDSN) through the Incorporated Research Institutions for Seismology (IRIS). Figures are generated with the python Matplotlib package (Hunter, 2007). We use SimModeler of the Simmetrix Simulation Modeling Suite to create the geometry of the slab interface. We use Python throughout the analysis (Van Rossum & Drake Jr, 1995). The median slip model is shared as Data Set S1.

The Green’s function library for subduction zones are provided by Hori et al. (2021), which was created by JAMSTEC’s own modification of a computer program under development by Earthquake Research Institute, The University of Tokyo. The library includes data modified from Japan Integrated Velocity Structure Model version 1 (JIVSM) (Koketsu et al., 2009, 2012) and the Earth Gravitational Model 2008 (Pavlis et al., 2012).

## Acknowledgments

We thank Editor Satoshi Ide, the Associate Editor, Kelin Wang, and an anonymous reviewer for helpful comments. We thank Tianhaozhe Sun, Shiann-Jong Lee, Quentin Bletery, Akinori Hashima, and Thorsten Becker for sharing their Tohoku-Oki earthquake finite-fault models and Yuji Yagi and Ryo Okuwaki for insightful discussions. We thank Dorian Golriz and Yehuda Bock for sharing the processed GEONET data. The project was supported by NSF grants EAR-2143413 and EAR-2121568. AAG acknowledges additional support from NASA (grant No. 80NSSC20K0495), NSF (grants EAR-2225286, OAC-2139536, OAC-2311208), the European Union’s Horizon 2020 Research and Innovation Programme (grant No. 852992), Horizon Europe (grant No. 101093038, 101058129, and 101058518) and the Southern California Earthquake Center (SCEC awards 22135, 23121). Computing resources were provided by the Institute of Geophysics of LMU Munich (Oeser et al., 2006).

## References

- Abe, K. (1977). Tectonic implications of the large shioya-Oki earthquakes of 1938. *Tectonophysics*, 41(4), 269–289.
- Agata, R., Kasahara, A., & Yagi, Y. (2021). A bayesian inference framework for fault slip distributions based on ensemble modelling of the uncertainty of underground structure: with a focus on uncertain fault dip. *Geophysical Journal International*, 225(2), 1392–1411.

- Ammon, C. J., Ji, C., Thio, H.-K., Robinson, D., Ni, S., Hjorleifsdottir, V., . . . others (2005). Rupture process of the 2004 sumatra-andaman earthquake. *science*, 308(5725), 1133–1139.
- Ammon, C. J., Lay, T., Kanamori, H., & Cleveland, M. (2011). A rupture model of the 2011 off the Pacific coast of Tohoku earthquake. *Earth, Planets and Space*, 63(7), 693–696.
- Asano, K., & Iwata, T. (2016). Source rupture processes of the foreshock and mainshock in the 2016 Kumamoto earthquake sequence estimated from the kinematic waveform inversion of strong motion data. *Earth, Planets and Space*, 68(1), 1–11.
- Bassett, D., Sandwell, D. T., Fialko, Y., & Watts, A. B. (2016). Upper-plate controls on co-seismic slip in the 2011 magnitude 9.0 Tohoku-Oki earthquake. *Nature*, 531(7592), 92–96.
- Bassett, D., & Watts, A. B. (2015). Gravity anomalies, crustal structure, and seismicity at subduction zones: 1. seafloor roughness and subducting relief. *Geochemistry, Geophysics, Geosystems*, 16(5), 1508–1540.
- Beresnev, I. A. (2003). Uncertainties in finite-fault slip inversions: to what extent to believe?(a critical review). *Bulletin of the Seismological Society of America*, 93(6), 2445–2458.
- Biemiller, J., Gabriel, A.-A., & Ulrich, T. (2023). Dueling dynamics of low-angle normal fault rupture with splay faulting and off-fault damage. *Nature Communications*, 14(1), 2352.
- Bletery, Q., Sladen, A., Delouis, B., & Mattéo, L. (2015). Quantification of tsunami bathymetry effect on finite fault slip inversion. *Pure and Applied Geophysics*, 172, 3655–3670.
- Bletery, Q., Sladen, A., Delouis, B., Vallée, M., Nocquet, J.-M., Rolland, L., & Jiang, J. (2014). A detailed source model for the  $M_w$  9.0 Tohoku-Oki earthquake reconciling geodesy, seismology, and tsunami records. *Journal of Geophysical Research: Solid Earth*, 119(10), 7636–7653.
- Brown, L., Wang, K., & Sun, T. (2015). Static stress drop in the  $M_w$  9 Tohoku-Oki earthquake: Heterogeneous distribution and low average value. *Geophysical Research Letters*, 42(24), 10–595.
- Daubechies, I. (1990). The wavelet transform, time-frequency localization and signal analysis. *IEEE transactions on information theory*, 36(5), 961–1005.
- Dettmer, J., Hawkins, R., Cummins, P. R., Hossen, J., Sambridge, M., Hino, R., & Inazu, D. (2016). Tsunami source uncertainty estimation: The 2011 Japan tsunami. *Journal of Geophysical Research: Solid Earth*, 121(6), 4483–4505.
- Diao, F., Xiong, X., & Zheng, Y. (2012). Static slip model of the m w 9.0 Tohoku (Japan) earthquake: Results from joint inversion of terrestrial GPS data and seafloor GPS/acoustic data. *Chinese Science Bulletin*, 57, 1990–1997.
- Di Toro, G., Han, R., Hirose, T., De Paola, N., Nielsen, S., Mizoguchi, K., . . . Shimamoto, T. (2011). Fault lubrication during earthquakes. *Nature*, 471(7339), 494–498.
- Du, Y., Ma, S., Kubota, T., & Saito, T. (2021). Impulsive tsunami and large runup along the sanriku coast of Japan produced by an inelastic wedge deformation model. *Journal of Geophysical Research: Solid Earth*, 126(8), e2021JB022098.
- Dziewonski, A. M., & Anderson, D. L. (1981). Preliminary reference earth model. *Physics of the earth and planetary interiors*, 25(4), 297–356.
- Fan, W., Shearer, P. M., & Gerstoft, P. (2014). Kinematic earthquake rupture inversion in the frequency domain. *Geophysical Journal International*, 199(2), 1138–1160.
- Fujii, Y., Satake, K., Sakai, S., Shinohara, M., & Kanazawa, T. (2011). Tsunami source of the 2011 off the Pacific coast of Tohoku earthquake. *Earth, planets and space*, 63(7), 815–820.
- Fujiwara, T., Kodaira, S., No, T., Kaiho, Y., Takahashi, N., & Kaneda, Y. (2011).

- The 2011 Tohoku-Oki earthquake: Displacement reaching the trench axis. *Science*, 334(6060), 1240–1240.
- Funning, G. J., Fukahata, Y., Yagi, Y., & Parsons, B. (2014). A method for the joint inversion of geodetic and seismic waveform data using abic: application to the 1997 manyi, tibet, earthquake. *Geophysical Journal International*, 196(3), 1564–1579.
- Galis, M., Ampuero, J. P., Mai, P. M., & Cappa, F. (2017). Induced seismicity provides insight into why earthquake ruptures stop. *Science advances*, 3(12), eaap7528.
- Gallovič, F., & Ampuero, J.-P. (2015). A new strategy to compare inverted rupture models exploiting the eigenstructure of the inverse problem. *Seismological Research Letters*, 86(6), 1679–1689.
- Gallovič, F., Imperatori, W., & Mai, P. M. (2015). Effects of three-dimensional crustal structure and smoothing constraint on earthquake slip inversions: Case study of the  $M_w$ 6.3 2009 L’Aquila earthquake. *Journal of Geophysical Research: Solid Earth*, 120(1), 428–449.
- Gallovič, F., Valentová, L., Ampuero, J.-P., & Gabriel, A.-A. (2019). Bayesian dynamic finite-fault inversion: 2. application to the 2016  $M_w$  6.2 amatrice, italy, earthquake. *Journal of Geophysical Research: Solid Earth*, 124(7), 6970–6988.
- Galvez, P., Dalguer, L. A., Ampuero, J.-P., & Giardini, D. (2016). Rupture reactivation during the 2011 m w 9.0 Tohoku earthquake: Dynamic rupture and ground-motion simulations. *Bulletin of the Seismological Society of America*, 106(3), 819–831.
- Galvez, P., Petukhin, A., Irikura, K., & Somerville, P. (2020). Dynamic source model for the 2011 Tohoku earthquake in a wide period range combining slip reactivation with the short-period ground motion generation process. *Pure and Applied Geophysics*, 177, 2143–2161.
- GEBCO. (2023). *Gebco 2023 grid* [dataset]. doi: 10.5285/f98b053b-0cbc-6c23-e053-6c86abc0af7b
- Goda, K., Mai, P. M., Yasuda, T., & Mori, N. (2014). Sensitivity of tsunami wave profiles and inundation simulations to earthquake slip and fault geometry for the 2011 Tohoku earthquake. *Earth, Planets and Space*, 66, 1–20.
- Goldberg, D., Barnhart, W., & Crowell, B. (2022). Regional and teleseismic observations for finite-fault product. *US Geol. Surv. Data Release*.
- Goldsby, D. L., & Tullis, T. E. (2011). Flash heating leads to low frictional strength of crustal rocks at earthquake slip rates. *Science*, 334(6053), 216–218.
- Gusman, A. R., Tanioka, Y., Sakai, S., & Tsushima, H. (2012). Source model of the great 2011 Tohoku earthquake estimated from tsunami waveforms and crustal deformation data. *Earth and Planetary Science Letters*, 341, 234–242.
- Halló, M., & Gallovič, F. (2020). Bayesian self-adapting fault slip inversion with green’s functions uncertainty and application on the 2016 mw7. 1 kumamoto earthquake. *Journal of Geophysical Research: Solid Earth*, 125(3), e2019JB018703.
- Hartzell, S. H., & Heaton, T. H. (1983). Inversion of strong ground motion and teleseismic waveform data for the fault rupture history of the 1979 Imperial Valley, California, earthquake. *Bulletin of the Seismological Society of America*, 73(6A), 1553–1583.
- Hashima, A., Becker, T. W., Freed, A. M., Sato, H., & Okaya, D. A. (2016). Co-seismic deformation due to the 2011 Tohoku-Oki earthquake: influence of 3-D elastic structure around Japan. *Earth, Planets and Space*, 68(1), 1–15.
- Hashimoto, C., Noda, A., & Matsuura, M. (2012). The m w 9.0 northeast Japan earthquake: total rupture of a basement asperity. *Geophysical Journal International*, 189(1), 1–5.
- Hayes, G. P. (2011, 09). Rapid source characterization of the 2011  $M_w$  9.0 off the Pacific coast of Tohoku earthquake. *Earth, Planets and Space*, 63(7), 529–534.

- Hayes, G. P., Moore, G. L., Portner, D. E., Hearne, M., Flamme, H., Furtney, M., & Smoczyk, G. M. (2018). Slab2, a comprehensive subduction zone geometry model. *Science*, *362*(6410), 58–61.
- Hino, R., Ito, Y., Suzuki, K., Suzuki, S., Inazu, D., Inuma, T., ... Kaneda, Y. (2011). Foreshocks and mainshock of the 2011 Tohoku earthquake observed by ocean bottom seismic/geodetic monitoring. In *AGU Fall Meeting Abstracts*.
- Hooper, A., Pietrzak, J., Simons, W., Cui, H., Riva, R., Naeije, M., ... Socquet, A. (2013). Importance of horizontal seafloor motion on tsunami height for the 2011  $M_w=9.0$  Tohoku-Oki earthquake. *Earth and Planetary Science Letters*, *361*, 469–479.
- Hori, T., Agata, R., Ichimura, T., Fujita, K., Yamaguchi, T., & Inuma, T. (2021). High-fidelity elastic green's functions for subduction zone models consistent with the global standard geodetic reference system. *Earth, Planets and Space*, *73*.
- Hossen, M. J., Cummins, P. R., Dettmer, J., & Baba, T. (2015). Tsunami waveform inversion for sea surface displacement following the 2011 Tohoku earthquake: Importance of dispersion and source kinematics. *Journal of Geophysical Research: Solid Earth*, *120*(9), 6452–6473.
- Hunter, J. D. (2007). Matplotlib: A 2d graphics environment. *Computing in Science & Engineering*, *9*(3), 90–95. doi: 10.1109/MCSE.2007.55
- Ide, S. (2007). Slip inversion. *Earthquake seismology*, *4*, 193–223.
- Ide, S., Baltay, A., & Beroza, G. C. (2011). Shallow dynamic overshoot and energetic deep rupture in the 2011  $M_w$  9.0 Tohoku-Oki earthquake. *Science*, *332*(6036), 1426–1429.
- Inuma, T., Hino, R., Kido, M., Inazu, D., Osada, Y., Ito, Y., ... others (2012). Co-seismic slip distribution of the 2011 off the Pacific Coast of Tohoku earthquake ( $M9.0$ ) refined by means of seafloor geodetic data. *Journal of Geophysical Research: Solid Earth*, *117*(B7).
- Ikehara, K., Kanamatsu, T., Nagahashi, Y., Strasser, M., Fink, H., Usami, K., ... Wefer, G. (2016). Documenting large earthquakes similar to the 2011 Tohoku-Oki earthquake from sediments deposited in the Japan trench over the past 1500 years. *Earth and Planetary Science Letters*, *445*, 48–56.
- Imai, K. (2015). Paleo tsunami source estimation by using combination optimization algorithm—Case study of the 1611 Keicho earthquake tsunami. *Tohoku Journal of Natural Disaster Science*, *51*, 139.
- Ito, T., Ozawa, K., Watanabe, T., & Sagiya, T. (2011). Slip distribution of the 2011 off the Pacific coast of Tohoku earthquake inferred from geodetic data. *Earth, planets and space*, *63*(7), 627–630.
- Ito, Y., Tsuji, T., Osada, Y., Kido, M., Inazu, D., Hayashi, Y., ... Fujimoto, H. (2011). Frontal wedge deformation near the source region of the 2011 Tohoku-Oki earthquake. *Geophysical Research Letters*, *38*(7).
- Ji, C., Wald, D. J., & Helmberger, D. V. (2002). Source description of the 1999 Hector Mine, California, earthquake, part i: Wavelet domain inversion theory and resolution analysis. *Bulletin of the Seismological Society of America*, *92*(4), 1192–1207.
- Jia, Z., Jin, Z., Marchandon, M., Ulrich, T., Gabriel, A.-A., Fan, W., ... others (2023). The complex dynamics of the 2023 kahramanmaraş, turkey, m w 7.8-7.7 earthquake doublet. *Science*, *381*(6661), 985–990.
- Jiang, J., & Simons, M. (2016). Probabilistic imaging of tsunamigenic seafloor deformation during the 2011 Tohoku-Oki earthquake. *Journal of Geophysical Research: Solid Earth*, *121*(12), 9050–9076.
- Kammer, D. S., Radiguet, M., Ampuero, J.-P., & Molinari, J.-F. (2015). Linear elastic fracture mechanics predicts the propagation distance of frictional slip. *Tribology letters*, *57*, 1–10.
- Kawakatsu, H., & Seno, T. (1983). Triple seismic zone and the regional variation

- of seismicity along the northern Honshu arc. *Journal of Geophysical research: Solid Earth*, 88(B5), 4215–4230.
- Kido, M., Osada, Y., Fujimoto, H., Hino, R., & Ito, Y. (2011). Trench-normal variation in observed seafloor displacements associated with the 2011 Tohoku-Oki earthquake. *Geophysical Research Letters*, 38(24).
- Kodaira, S., Fujiwara, T., Fujie, G., Nakamura, Y., & Kanamatsu, T. (2020). Large coseismic slip to the trench during the 2011 Tohoku-Oki earthquake. *Annual Review of Earth and Planetary Sciences*, 48, 321–343.
- Kodaira, S., Iinuma, T., & Imai, K. (2021). Investigating a tsunamigenic megathrust earthquake in the Japan trench. *Science*, 371(6534), eabe1169.
- Kodaira, S., No, T., Nakamura, Y., Fujiwara, T., Kaiho, Y., Miura, S., . . . Taira, A. (2012). Coseismic fault rupture at the trench axis during the 2011 Tohoku-Oki earthquake. *Nature Geoscience*, 5(9), 646–650.
- Koketsu, K., Miyake, H., & Suzuki, H. (2012). Japan integrated velocity structure model version 1. In *Proceedings of the 15th world conference on earthquake engineering* (Vol. 1, p. 4).
- Koketsu, K., Miyake, H., Tanaka, Y., et al. (2009). A proposal for a standard procedure of modeling 3-d velocity structures and its application to the Tokyo metropolitan area, Japan. *Tectonophysics*, 472(1-4), 290–300.
- Kozdon, J. E., & Dunham, E. M. (2013). Rupture to the trench: Dynamic rupture simulations of the 11 March 2011 Tohoku earthquake. *Bulletin of the Seismological Society of America*, 103(2B), 1275–1289.
- Kubo, H., & Kakehi, Y. (2013). Source process of the 2011 Tohoku earthquake estimated from the joint inversion of teleseismic body waves and geodetic data including seafloor observation data: source model with enhanced reliability by using objectively determined inversion settings. *Bulletin of the Seismological Society of America*, 103(2B), 1195–1220.
- Kubota, T., Saito, T., & Hino, R. (2022). A new mechanical perspective on a shallow megathrust near-trench slip from the high-resolution fault model of the 2011 Tohoku-Oki earthquake. *Progress in Earth and Planetary Science*, 9(1), 1–19.
- Lay, T. (2018). A review of the rupture characteristics of the 2011 Tohoku-Oki  $M_w$  9.1 earthquake. *Tectonophysics*, 733, 4–36.
- Lay, T., Ammon, C. J., Kanamori, H., Xue, L., & Kim, M. J. (2011, 09). Possible large near-trench slip during the 2011  $M_w$  9.0 off the Pacific coast of Tohoku earthquake. *Earth, Planets and Space (Online)*, 63(7), 687–692.
- Lee, S.-J., Huang, B.-S., Ando, M., Chiu, H.-C., & Wang, J.-H. (2011). Evidence of large scale repeating slip during the 2011 Tohoku-Oki earthquake. *Geophysical Research Letters*, 38(19).
- Liu, X., & Zhao, D. (2018). Upper and lower plate controls on the great 2011 Tohoku-Oki earthquake. *Science advances*, 4(6), eaat4396.
- Loveless, J. P., & Meade, B. J. (2011). Spatial correlation of interseismic coupling and coseismic rupture extent of the 2011  $M_w$  = 9.0 Tohoku-Oki earthquake. *Geophysical Research Letters*, 38(17).
- Ma, S. (2023). Wedge plasticity and a minimalist dynamic rupture model for the 2011  $M_w$  9.1 Tohoku-Oki earthquake and tsunami. *Tectonophysics*, 869, 230146.
- Ma, S., & Nie, S. (2019). Dynamic wedge failure and along-arc variations of tsunamigenesis in the Japan trench margin. *Geophysical Research Letters*, 46(15), 8782–8790.
- Madden, E. H., Ulrich, T., & Gabriel, A.-A. (2022). The state of pore fluid pressure and 3-D megathrust earthquake dynamics. *Journal of Geophysical Research: Solid Earth*, 127(4), e2021JB023382.
- Maeda, T., Furumura, T., Sakai, S., & Shinohara, M. (2011a). Significant tsunami observed at ocean-bottom pressure gauges during the 2011 off the Pacific coast



- of Tohoku earthquake. *Earth, Planets and Space*, 63, 803–808.
- Maeda, T., Furumura, T., Sakai, S., & Shinohara, M. (2011b, 09). Significant tsunami observed at ocean-bottom pressure gauges during the 2011 off the Pacific coast of Tohoku earthquake. *Earth, Planets and Space (Online)*, 63(7), 803–808.
- Mai, P. M., & Beroza, G. C. (2002). A spatial random field model to characterize complexity in earthquake slip. *Journal of Geophysical Research: Solid Earth*, 107(B11), ESE–10.
- Mai, P. M., Burjanek, J., Delouis, B., Festa, G., Francois-Holden, C., Monelli, D., ... Zahradnik, J. (2007). Earthquake source inversion blindtest: Initial results and further developments. In *AGU Fall Meeting Abstracts* (Vol. 2007, pp. S53C–08).
- Mai, P. M., Schorlemmer, D., Page, M., Ampuero, J.-P., Asano, K., Causse, M., ... others (2016). The earthquake-source inversion validation (SIV) project. *Seismological Research Letters*, 87(3), 690–708.
- Mai, P. M., & Thingbaijam, K. (2014). SRCMOD: An online database of finite-fault rupture models. *Seismological Research Letters*, 85(6), 1348–1357.
- Melgar, D., & Bock, Y. (2015). Kinematic earthquake source inversion and tsunami runup prediction with regional geophysical data. *Journal of Geophysical Research: Solid Earth*, 120(5), 3324–3349.
- Melgar, D., Crowell, B. W., Bock, Y., & Haase, J. S. (2013). Rapid modeling of the 2011  $M_w$  9.0 Tohoku-Oki earthquake with seismogeodesy. *Geophysical Research Letters*, 40(12), 2963–2968.
- Minson, S., Simons, M., & Beck, J. (2013). Bayesian inversion for finite fault earthquake source models i—theory and algorithm. *Geophysical Journal International*, 194(3), 1701–1726.
- Minson, S. E., Simons, M., Beck, J., Ortega, F., Jiang, J., Owen, S., ... Sladen, A. (2014). Bayesian inversion for finite fault earthquake source models—ii: the 2011 great Tohoku-Oki, Japan earthquake. *Geophysical Journal International*, 198(2), 922–940.
- Mochizuki, M., Uehira, K., Kanazawa, T., Kunugi, T., Shiomi, K., Aoi, S., ... others (2018). S-net project: Performance of a large-scale seafloor observation network for preventing and reducing seismic and tsunami disasters. In *2018 OCEANS-MTS/IEEE Kobe Techno-Oceans (OTO)* (pp. 1–4).
- Moore, J. C., Plank, T. A., Chester, F. M., Polissar, P. J., & Savage, H. M. (2015). Sediment provenance and controls on slip propagation: Lessons learned from the 2011 Tohoku and other great earthquakes of the subducting northwest Pacific plate. *Geosphere*, 11(3), 533–541.
- Mori, N., Takahashi, T., Yasuda, T., & Yanagisawa, H. (2011). Survey of 2011 Tohoku earthquake tsunami inundation and run-up. *Geophysical research letters*, 38(7).
- Mungov, G., Eblé, M., & Bouchard, R. (2013). DART® tsunameter retrospective and real-time data: A reflection on 10 years of processing in support of tsunami research and operations. *Pure and Applied Geophysics*, 170, 1369–1384.
- Nakata, R., Hori, T., Hyodo, M., & Ariyoshi, K. (2016). Possible scenarios for occurrence of  $M \sim 7$  interplate earthquakes prior to and following the 2011 Tohoku-Oki earthquake based on numerical simulation. *Scientific reports*, 6(1), 25704.
- Nishikawa, T., Matsuzawa, T., Ohta, K., Uchida, N., Nishimura, T., & Ide, S. (2019). The slow earthquake spectrum in the Japan trench illuminated by the S-net seafloor observatories. *Science*, 365(6455), 808–813.
- Nissen-Meyer, T., van Driel, M., Stähler, S. C., Hosseini, K., Hempel, S., Auer, L., ... Fournier, A. (2014). AxiSEM: broadband 3-D seismic wavefields in axisymmetric media. *Solid Earth*, 5(1), 425–445.

- Oeser, J., Bunge, H.-P., & Mohr, M. (2006). Cluster design in the earth sciences tethys. In M. Gerndt & D. Kranzlmüller (Eds.), *High-performance computing and communications* (pp. 31–40). Springer Berlin Heidelberg.
- Ohnaka, M., & Yamashita, T. (1989). A cohesive zone model for dynamic shear faulting based on experimentally inferred constitutive relation and strong motion source parameters. *Journal of Geophysical Research: Solid Earth*, *94*(B4), 4089–4104.
- Okada, Y., Kasahara, K., Hori, S., Obara, K., Sekiguchi, S., Fujiwara, H., & Yamamoto, A. (2004). Recent progress of seismic observation networks in Japan—Hi-net, F-net, K-Net and KiK-net. *Earth, Planets and Space*, *56*, xv–xxviii.
- Okuwaki, R., & Fan, W. (2022). Oblique convergence causes both thrust and strike-slip ruptures during the 2021 M 7.2 Haiti earthquake. *Geophysical Research Letters*, *49*(2), e2021GL096373.
- Okuwaki, R., Hirano, S., Yagi, Y., & Shimizu, K. (2020). Inchworm-like source evolution through a geometrically complex fault fueled persistent supershear rupture during the 2018 Palu Indonesia earthquake. *Earth and Planetary Science Letters*, *547*, 116449.
- Pavlis, N. K., Holmes, S. A., Kenyon, S. C., & Factor, J. K. (2012). The development and evaluation of the earth gravitational model 2008 (egm2008). *Journal of geophysical research: solid earth*, *117*(B4).
- Pollitz, F. F., Bürgmann, R., & Banerjee, P. (2011). Geodetic slip model of the 2011 M9.0 Tohoku earthquake. *Geophysical Research Letters*, *38*(7).
- Ragon, T., Sladen, A., & Simons, M. (2018). Accounting for uncertain fault geometry in earthquake source inversions—i: theory and simplified application. *Geophysical Journal International*, *214*(2), 1174–1190.
- Razafindrakoto, H. N., Mai, P. M., Genton, M. G., Zhang, L., & Thingbaijam, K. K. (2015). Quantifying variability in earthquake rupture models using multidimensional scaling: Application to the 2011 Tohoku earthquake. *Geophysical Journal International*, *202*(1), 17–40.
- Romano, F., Trasatti, E., Lorito, S., Piromallo, C., Piatanesi, A., Ito, Y., ... Cocco, M. (2014). Structural control on the Tohoku earthquake rupture process investigated by 3d FEM, tsunami and geodetic data. *Scientific reports*, *4*(1), 1–11.
- Sagiya, T. (2004). A decade of geonet: 1994–2003 the continuous GPS observation in Japan and its impact on earthquake studies. *Earth, planets and space*, *56*(8), xxix–xli.
- Saito, T., Ito, Y., Inazu, D., & Hino, R. (2011). Tsunami source of the 2011 Tohoku-Oki earthquake, Japan: Inversion analysis based on dispersive tsunami simulations. *Geophysical Research Letters*, *38*(7).
- Sallarès, V., & Ranero, C. R. (2019). Upper-plate rigidity determines depth-varying rupture behaviour of megathrust earthquakes. *Nature*, *576*(7785), 96–101.
- Satake, K. (2015). Geological and historical evidence of irregular recurrent earthquakes in Japan. *Philosophical Transactions of the Royal Society A: Mathematical, Physical and Engineering Sciences*, *373*(2053), 20140375.
- Satake, K., Fujii, Y., Harada, T., & Namegaya, Y. (2013). Time and space distribution of coseismic slip of the 2011 Tohoku earthquake as inferred from tsunami waveform data. *Bulletin of the seismological society of America*, *103*(2B), 1473–1492.
- Sato, D. S., Fukahata, Y., & Nozue, Y. (2022). Appropriate reduction of the posterior distribution in fully bayesian inversions. *Geophysical Journal International*, *231*(2), 950–981.
- Sato, M., Ishikawa, T., Ujihara, N., Yoshida, S., Fujita, M., Mochizuki, M., & Asada, A. (2011). Displacement above the hypocenter of the 2011 Tohoku-Oki earthquake. *Science*, *332*(6036), 1395–1395.



- Scognamiglio, L., Tinti, E., Casarotti, E., Pucci, S., Villani, F., Cocco, M., ...  
 Dreger, D. (2018). Complex fault geometry and rupture dynamics of the  
 $M_w$  6.5, 30 october 2016, Central Italy earthquake. *Journal of Geophysical  
 Research: Solid Earth*, 123(4), 2943–2964.
- Shao, G., Li, X., Ji, C., & Maeda, T. (2011). Focal mechanism and slip history of  
 the 2011  $M_w$  9.1 off the Pacific coast of Tohoku earthquake, constrained with  
 teleseismic body and surface waves. *Earth, planets and space*, 63(7), 559–564.
- Shearer, P., & Bürgmann, R. (2010). Lessons learned from the 2004 sumatra-  
 andaman megathrust rupture. *Annual Review of Earth and Planetary Sci-  
 ences*, 38, 103–131.
- Simons, M., Minson, S. E., Sladen, A., Ortega, F., Jiang, J., Owen, S. E., ... oth-  
 ers (2011). The 2011 magnitude 9.0 Tohoku-Oki earthquake: Mosaicking the  
 megathrust from seconds to centuries. *science*, 332(6036), 1421–1425.
- Sun, T., Wang, K., Fujiwara, T., Kodaira, S., & He, J. (2017). Large fault slip peak-  
 ing at trench in the 2011 Tohoku-Oki earthquake. *Nature communications*,  
 8(1), 14044.
- Suzuki, W., Aoi, S., Sekiguchi, H., & Kunugi, T. (2011). Rupture process of the  
 2011 Tohoku-Oki mega-thrust earthquake ( $M_0$ ) inverted from strong-motion  
 data. *Geophysical Research Letters*, 38(7).
- Tajima, F., Mori, J., & Kennett, B. L. (2013). A review of the 2011 Tohoku-Oki  
 earthquake ( $M_w$  9.0): Large-scale rupture across heterogeneous plate coupling.  
*Tectonophysics*, 586, 15–34.
- Tanioka, Y., & Sataka, K. (1996). Fault parameters of the 1896 sanriku tsunami  
 earthquake estimated from tsunami numerical modeling. *Geophysical research  
 letters*, 23(13), 1549–1552.
- Tinti, E., Casarotti, E., Ulrich, T., Taufiqurrahman, T., Li, D., & Gabriel, A.-A.  
 (2021). Constraining families of dynamic models using geological, geodetic  
 and strong ground motion data: The  $M_w$  6.5, october 30th, 2016, norcia earth-  
 quake, italy. *Earth and Planetary Science Letters*, 576, 117237.
- Tinti, E., Fukuyama, E., Piatanesi, A., & Cocco, M. (2005). A kinematic source-  
 time function compatible with earthquake dynamics. *Bulletin of the Seismolog-  
 ical Society of America*, 95(4), 1211–1223.
- Tinti, E., Scognamiglio, L., Michelini, A., & Cocco, M. (2016). Slip heterogeneity  
 and directivity of the  $M_l$  6.0, 2016, Amatrice earthquake estimated with rapid  
 finite-fault inversion. *Geophysical Research Letters*, 43(20), 10–745.
- Tinti, E., Spudich, P., & Cocco, M. (2005). Earthquake fracture energy inferred  
 from kinematic rupture models on extended faults. *Journal of Geophysical Re-  
 search: Solid Earth*, 110(B12).
- Tsai, V. C., Ampuero, J.-P., Kanamori, H., & Stevenson, D. J. (2013). Estimating  
 the effect of earth elasticity and variable water density on tsunami speeds.  
*Geophysical Research Letters*, 40(3), 492–496.
- Tsuji, T., Ito, Y., Kido, M., Osada, Y., Fujimoto, H., Ashi, J., ... Matsuoka, T.  
 (2011). Potential tsunamigenic faults of the 2011 off the Pacific coast of To-  
 hoku earthquake. *Earth, planets and space*, 63, 831–834.
- Twardzik, C., Madariaga, R., Das, S., & Custódio, S. (2012). Robust features of the  
 source process for the 2004 parkfield, california, earthquake from strong-motion  
 seismograms. *Geophysical Journal International*, 191(3), 1245–1254.
- Uchida, N., & Bürgmann, R. (2021). A decade of lessons learned from the 2011  
 Tohoku-Oki earthquake. *Reviews of Geophysics*, 59(2), e2020RG000713.
- Ulrich, T., Gabriel, A.-A., & Madden, E. H. (2022). Stress, rigidity and sediment  
 strength control megathrust earthquake and tsunami dynamics. *Nature Geo-  
 science*, 15(1), 67–73.
- van Driel, M., Krischer, L., Stähler, S. C., Hosseini, K., & Nissen-Meyer, T. (2015).  
 Instaseis: Instant global seismograms based on a broadband waveform  
 database. *Solid Earth*, 6(2), 701–717.

- Van Rossum, G., & Drake Jr, F. L. (1995). *Python tutorial* (Vol. 620). Centrum voor Wiskunde en Informatica Amsterdam, The Netherlands.
- van Zelst, I., Rannabauer, L., Gabriel, A.-A., & van Dinther, Y. (2022). Earthquake rupture on multiple splay faults and its effect on tsunamis. *Journal of Geophysical Research: Solid Earth*, *127*(8), e2022JB024300.
- Viesca, R. C., & Garagash, D. I. (2015). Ubiquitous weakening of faults due to thermal pressurization. *Nature Geoscience*, *8*(11), 875–879.
- Wald, D. J., & Graves, R. W. (2001). Resolution analysis of finite fault source inversion using one-and three-dimensional green’s functions: 2. combining seismic and geodetic data. *Journal of Geophysical Research: Solid Earth*, *106*(B5), 8767–8788.
- Wang, C., Ding, X., Shan, X., Zhang, L., & Jiang, M. (2012). Slip distribution of the 2011 Tohoku earthquake derived from joint inversion of GPS, InSAR and seafloor GPS/acoustic measurements. *Journal of Asian Earth Sciences*, *57*, 128–136.
- Wang, K., & Bilek, S. L. (2014). Invited review paper: Fault creep caused by subduction of rough seafloor relief. *Tectonophysics*, *610*, 1–24.
- Wang, K., Dreger, D. S., Tinti, E., Bürgmann, R., & Taira, T. (2020). Rupture process of the 2019 Ridgecrest, California  $M_w$  6.4 foreshock and  $M_w$  7.1 earthquake constrained by seismic and geodetic data. *Bulletin of the Seismological Society of America*, *110*(4), 1603–1626.
- Wang, K., Sun, T., Brown, L., Hino, R., Tomita, F., Kido, M., . . . Fujiwara, T. (2018). Learning from crustal deformation associated with the m9 2011 tohoku-oki earthquake. *Geosphere*, *14*(2), 552–571.
- Wang, R., Parolai, S., Ge, M., Jin, M., Walter, T. R., & Zschau, J. (2013). The 2011  $M_w$  9.0 Tohoku earthquake: Comparison of GPS and strong-motion data. *Bulletin of the Seismological Society of America*, *103*(2B), 1336–1347.
- Wei, S., Graves, R., Helmberger, D., Avouac, J.-P., & Jiang, J. (2012). Sources of shaking and flooding during the Tohoku-Oki earthquake: A mixture of rupture styles. *Earth and Planetary Science Letters*, *333*, 91–100.
- Xie, Z., & Cai, Y. (2018). Inverse method for static stress drop and application to the 2011  $M_w$  9.0 Tohoku-Oki earthquake. *Journal of Geophysical Research: Solid Earth*, *123*(4), 2871–2884.
- Yagi, Y., & Fukahata, Y. (2011a). Introduction of uncertainty of green’s function into waveform inversion for seismic source processes. *Geophysical Journal International*, *186*(2), 711–720.
- Yagi, Y., & Fukahata, Y. (2011b). Rupture process of the 2011 Tohoku-Oki earthquake and absolute elastic strain release. *Geophysical Research Letters*, *38*(19).
- Yamanaka, Y., & Kikuchi, M. (2004). Asperity map along the subduction zone in northeastern Japan inferred from regional seismic data. *Journal of Geophysical Research: Solid Earth*, *109*(B7).
- Yamazaki, Y., Cheung, K. F., & Lay, T. (2018). A self-consistent fault slip model for the 2011 Tohoku earthquake and tsunami. *Journal of Geophysical Research: Solid Earth*, *123*(2), 1435–1458.
- Yoffe, E. H. (1951). Lxxv. the moving griffith crack. *The London, Edinburgh, and Dublin Philosophical Magazine and Journal of Science*, *42*(330), 739–750.
- Yokota, Y., Koketsu, K., Fujii, Y., Satake, K., Sakai, S., Shinohara, M., & Kanazawa, T. (2011). Joint inversion of strong motion, teleseismic, geodetic, and tsunami datasets for the rupture process of the 2011 Tohoku earthquake. *Geophysical Research Letters*, *38*(7).
- Yoshida, Y., Ueno, H., Muto, D., & Aoki, S. (2011). Source process of the 2011 off the Pacific coast of Tohoku earthquake with the combination of teleseismic and strong motion data. *Earth, planets and space*, *63*(7), 565–569.
- Yue, H., & Lay, T. (2013). Source rupture models for the  $M_w$  9.0 2011 Tohoku

1557 earthquake from joint inversions of high-rate geodetic and seismic data. *Bul-*  
1558 *letin of the Seismological Society of America*, 103(2B), 1242–1255.

1559 Yue, H., Lay, T., Rivera, L., An, C., Vigny, C., Tong, X., & Báez Soto, J. C. (2014).  
1560 Localized fault slip to the trench in the 2010 maule, chile mw= 8.8 earthquake  
1561 from joint inversion of high-rate gps, teleseismic body waves, insar, campaign  
1562 gps, and tsunami observations. *Journal of Geophysical Research: Solid Earth*,  
1563 119(10), 7786–7804.

1564 Zhou, X., Cambiotti, G., Sun, W., & Sabadini, R. (2014). The coseismic slip dis-  
1565 tribution of a shallow subduction fault constrained by prior information: the  
1566 example of 2011 Tohoku ( $M_w$  9.0) megathrust earthquake. *Geophysical Jour-*  
1567 *nal International*, 199(2), 981–995.

# A quantitative comparison and validation of finite-fault models: The 2011 Tohoku-Oki earthquake

Jeremy Wing Ching Wong<sup>1</sup>, Wenyan Fan<sup>1</sup>, Alice-Agnes Gabriel<sup>1,2</sup>

<sup>1</sup>Scripps Institution of Oceanography, University of California San Diego, La Jolla, CA, USA

<sup>2</sup>Department of Earth and Environmental Sciences, Ludwig-Maximilians-Universität München, Munich ,  
Germany

## Key Points:

- We evaluate 32 finite-fault models of the 2011 Tohoku-Oki earthquake, using realistic slab geometry and varying spatial resolution.
- Models at the 64 km scale agree well with each other, indicating variability stems primarily from small-scale slip features.
- Seismic observations show sensitivity to rupture propagation but not to small-scale slip heterogeneity.

---

Corresponding author: Jeremy Wing Ching Wong, [wcwong@ucsd.edu](mailto:wcwong@ucsd.edu)

## Abstract

Large earthquakes rupture faults over hundreds of kilometers within minutes. Finite-fault models image these processes and provide observational constraints for understanding earthquake physics. However, finite-fault inversions are subject to non-uniqueness and uncertainties. The diverse range of published models for the well-recorded 2011  $M_w$  9.0 Tohoku-Oki earthquake illustrates this issue, and details of its rupture process remain under debate. Here, we comprehensively compare 32 finite-fault models of the Tohoku-Oki earthquake and analyze the sensitivity of four commonly-used observational data types (geodetic, teleseismic, regional seismic-geodetic, and tsunami) to their slip features. We first project all models to a realistic megathrust geometry and a 1-km subfault size. At this scale, we observe low correlation among the models, irrespective of the data type. However, model agreement improves significantly with increasing subfault sizes, implying that their differences primarily stem from small-scale features. We then forward-compute geodetic and seismic synthetics and compare them with observations available during the earthquake. We find that seismic observations are sensitive to rupture propagation, such as the peak-slip rise time. However, neither teleseismic, regional seismic, nor geodetic observations are sensitive to spatial slip features smaller than 64 km. In distinction, the seafloor deformation predicted by all models exhibits poor correlation, indicating sensitivity to small-scale slip features. Our findings suggest that fine-scale slip features cannot be unambiguously resolved by remote or sparse observations, such as the four data types tested in this study. However, better resolution may become achievable from dense offshore instrumentation.

## Plain Language Summary

Large earthquakes often rupture in unexpected ways across extensive areas of geologic faults. Scientists use finite-fault models to resolve these processes in detail. These models use different observations to help us understand earthquakes and plan for future hazard mitigation and risk management. However, these models are not perfect: they are often challenging to resolve, and different models of the same earthquake can show very different results. For example, many different models have been published for the 2011  $M_w$  9.0 Tohoku-Oki earthquake, each showing varying “slip features” of how the megathrust moved during the event. In this study, we compare 32 of these models with each other and with observations in a new and systematic way. The models show coherent features at a scale of 64 km while disagreeing on the smaller, fine-scale details. We find that such fine-scale features cannot be uniquely resolved by the commonly-used remote observations, such as geodetic, regional seismic-geodetic, teleseismic and tsunami data. Our study suggests that to gain a better understanding of large megathrust earthquakes, dense networks of instruments placed directly offshore close to the megathrust are needed for robustly resolving their rupture processes.

## 1 Introduction

Large earthquake rupture can evolve rapidly, propagating hundreds of kilometers in complex ways (Ammon et al., 2005; Ide et al., 2011; Simons et al., 2011). Imaging earthquake rupture processes is vital for understanding earthquake physics and the associated hazards (Tinti, Spudich, & Cocco, 2005; Uchida & Bürgmann, 2021). Finite-fault models characterize the spatiotemporal slip distributions of large earthquakes (Ide, 2007), and these models can be developed using a range of datasets and inversion methods (Hartzell & Heaton, 1983; Ide, 2007; Ji et al., 2002; Jia et al., 2023; S. Minson et al., 2013; Yagi & Fukahata, 2011a). However, finite-fault inversion is often parameterized as an ill-conditioned problem with a large number of unknowns and a simplified, assumed fault configuration (e.g., Fan et al., 2014; Ide, 2007). Moreover, unknown 3D Earth structure leads to inaccurate Green’s functions, further hampering the robustness of finite-fault models (Beresnev,

2003; Gallovič et al., 2015; Wald & Graves, 2001). Dense, near-field geophysical observations can offer critical constraints that help resolve finite-fault models with high fidelity (e.g. Asano & Iwata, 2016; Scognamiglio et al., 2018; Tinti et al., 2016). However, many earthquakes occur in remote regions where observations are scarce, such as in subduction zones. Finite-fault models often significantly differ from each other for the same earthquake (e.g., Mai et al., 2007; Razafindrakoto et al., 2015; Shearer & Bürgmann, 2010; K. Wang et al., 2020), and quantitatively comparing and differentiating these models remains challenging (e.g., Lay, 2018; Mai et al., 2016; K. Wang et al., 2018).

The 2011  $M_w$  9.0 Tohoku-Oki earthquake is one of the best-observed megathrust earthquakes (Lay, 2018). The earthquake ruptured approximately 400 km along-strike and 220 km along-dip offshore the northern Honshu area in Japan (Kodaira et al., 2020). The event was well recorded by a dense and diverse set of observations, including on-shore geodetic data (Sagiya, 2004), offshore acoustic-GNSS (e.g., Kido et al., 2011; M. Sato et al., 2011) and pressure gauge data (e.g., Hino et al., 2011; Y. Ito et al., 2011; Maeda et al., 2011a), regional and global seismic data (e.g., Okada et al., 2004), and tsunami (e.g., Maeda et al., 2011a; Mungov et al., 2013) and seafloor mapping data (Fujiwara et al., 2011; Kodaira et al., 2012). These datasets facilitate the development of many finite-fault models of the Tohoku-Oki earthquake (Sun et al., 2017). However, these models exhibit significant differences in their slip distributions (Lay, 2018; Razafindrakoto et al., 2015). For example, maximum slip estimates at the trench range from 0 m to 80 m for an along-dip cross-section through the hypocenter of 45 published models (Sun et al., 2017). Similar variability exists along the strike direction, particularly regarding the northern rupture extent beyond 39.5°N, which leaves the source of the Sanriku region tsunami a topic under debate (Du et al., 2021; Kodaira et al., 2020; Mori et al., 2011). The discrepancies among the finite-fault models of the Tohoku-Oki earthquake have given rise to several unresolved questions, including the tsunami sources and variability in megathrust and off-fault rheologies (Kodaira et al., 2020; Lay, 2018; Ma, 2023; Sun et al., 2017; Tajima et al., 2013; Uchida & Bürgmann, 2021).

The remainder of this paper is structured as follows. In Section 2, we describe the 32 published finite fault models analyzed in this study and introduce a new reparameterization framework to unify their model parameters for systematic comparison. The model comparison in Section 3 quantitatively identifies their coherent and unique features at varying spatial scales. We quantify the sensitivity of geodetic, teleseismic, regional seismic-geodetic, and tsunami data to the variability in the finite-fault models in Section 4. We discuss controlling factors of model variability and implications of our study as well as future opportunities in Section 5.

## 2 Finite-fault Models of the 2011 Tohoku-Oki Earthquake

We analyze 32 finite-fault slip models of the 2011 Tohoku-Oki earthquake (Figure 1; Text S1). The models have been obtained using various inversion techniques and Green’s functions, which result from the fault parameterization and the Earth’s structure. The finite-fault models are inverted from a wide range of datasets and exhibit a wide range of slip features (Figure 2). Here, we focus on the final slip distribution of each model because a large portion of the models are static. While we do not systematically compare available slip rate histories, we use them to investigate their impact on teleseismic and regional seismo-geodetic observations when available (Sections 4.2.3 and 4.3). We classify the models into five groups based on the datasets used (Figure 1 and 2).

The geodetic finite-fault group (in the following, labeled as “G”) includes nine models that describe the static slip distributions of the Tohoku-Oki earthquake (Diao et al., 2012; Hashima et al., 2016; Iinuma et al., 2012; T. Ito et al., 2011; Pollitz et al., 2011; C. Wang et al., 2012; R. Wang et al., 2013; Xie & Cai, 2018; Zhou et al., 2014). These models are inferred from geodetic measurements, including both onshore and offshore



displacement acquisitions. The regional seismic finite-fault group (“R”) comprises four models (Lee et al., 2011; Suzuki et al., 2011; Wei et al., 2012; Yue & Lay, 2013), which were developed from data of onshore strong ground motion, broadband, and high-rate GNSS (Global Navigation Satellite System) stations. The teleseismic finite-fault group (“S”) contains six models (Ammon et al., 2011; Goldberg et al., 2022; Hayes, 2011; Ide et al., 2011; Kubo & Kakehi, 2013; Yagi & Fukahata, 2011b), primarily derived from teleseismic body waves and surface waves recorded at stations located within the 30° to 90° epicentral distance range. The tsunami finite-fault group (“T”) includes eight models (Fujii et al., 2011; Gusman et al., 2012; Hooper et al., 2013; Kubota et al., 2022; Romano et al., 2014; Satake et al., 2013; Saito et al., 2011; Simons et al., 2011), which are based on tsunami data from near-source pressure gauges, tide gauges, and open-ocean buoys. Six T models are obtained using geodetic data as well, but without using seismic data. Lastly, the joint tsunami seismic and geodetic finite-fault group (“J”) includes five models (Bletery et al., 2014; Melgar & Bock, 2015; S. E. Minson et al., 2014; Yokota et al., 2011; Yamazaki et al., 2018). Models in this last group are required to incorporate geodetic, seismic (regional and/or teleseismic), and tsunami datasets.

## 2.1 Unifying Model Parameterization for Quantitative Comparison

We design a unifying framework to consistently reparameterize the models, ensuring that they share the same geometric and subfault configuration. This unifying procedure allows a quantitative and systematic comparison. We first project the finite-fault models onto the subduction interface using the Slab2.0 model to provide a realistic fault plane geometry (Hayes et al., 2018). Our projection method preserves the seismic potency of each subfault, which is defined as slip times rupture area. We align the shallowest subfault extents of each finite-fault model with the location of the Japan Trench (GEBCO, 2023; Hayes et al., 2018), which is situated approximately 7.65 km below the sea surface. We then project the depth-shifted models onto the subduction interface along the strike-depth plane, as defined by the Slab2.0 model (Hayes et al., 2018), but extending it to the Japan Trench (Figure 3b).

The Slab2.0 model maps the megathrust interface from 10 km to 150 km depth, omitting the shallowest near-trench geometry. Considering that the Tohoku-Oki earthquake likely ruptured all the way to the trench (Lay, 2018; Uchida & Bürgmann, 2021), we here extend the Slab2.0 megathrust to the trench assuming a shallow megathrust dipping angle of 10°. This extension is guided by the near-trench seismic reflection surveys (Y. Ito et al., 2011; Tsuji et al., 2011). We shift the Slab2.0 megathrust geometry to be 0.5 km shallower for a smooth connection with the shallow extension to the trench. This 0.5 km depth shift falls well within the depth uncertainty of the Slab2.0 model (Hayes et al., 2018).

We densify the projected models to a grid with uniformly spaced points, set 1 km apart, following the scheme outlined in Tinti, Fukuyama, et al. (2005). We use a cubic spline interpolation to densify each model to 16 times the original number of subfaults, with four times each along-dip and along-strike direction (Figure 3c). This cubic spline interpolation process assures spatial smoothness without preserving the seismic potency distribution. Therefore, we calculate the sum of the interpolated seismic potency within the area of each original subfault and compare it with that of the original slip distribution to compute the potency ratio per subfault with the ideal ratio as 1. We then use the potency ratio per subfault to scale the original slip for each subfault. We iterate the interpolation with the scaled original slip until the discrepancy in seismic potency between the original and interpolated models falls below a 10% threshold, which typically takes 2–3 iterations. This iterative procedure effectively preserves the seismic potency of the original models while ensuring spatial smoothness in the interpolated models. Without the iterative steps, applying the potency ratio to the interpolated models may result in artificially sharp edges in the upscaled slip distribution due to the coarse param-



eterizations of the original models. We apply this densifying procedure to both the along-strike and along-dip slip to preserve the original rake at each subfault. Finally, we linearly map the densified model to a set of grid points spaced 1 km apart horizontally, and their depths are defined by the megathrust geometry (Figure 3d). We apply this projection-upscaling procedure to all 32 models, leading to a collection of uniformly parameterized models that our following analyses are based on (Figure S1).

Our projection scheme differs from the one outlined in Brown et al. (2015) (hereafter referred to as the Brown method). The Brown method linearly interpolates a finite-fault slip distribution onto a set of dense grids that overlaps with the original finite-fault area, and extrapolates the slip towards the trench using values from the nearest neighbors. In contrast, our projection method adjusts the original subfault locations to align with the realistic megathrust geometry and trench location and interpolates the slip values accordingly (Figure S1). It is important to note that both projection methods could distort the original slip distribution. For example, the Brown method could result in a 20% increase in potency when projecting the planar G7 model onto the Slab 2.0 geometry, whereas our method causes a 2% potency difference compared to the original model (Figure S5). Additionally, the Brown method maps the downdip limit of the original G7 model from 25 km to 38 km due to the increased dipping angle of the megathrust at depth (Hayes, 2018; Figure S5).

Therefore, the projection choice should be guided by the goal of the analysis. The Brown method prioritizes preserving the original fault location in latitude and longitude, whereas our projection emphasizes the megathrust geometry and subfault depth (Figure S5). The emphasis on realistic geometry is important because of our focus on evaluating data sensitivity including the static deformation comparison (Section 4.1). Differences in near-trench geometry, including depth, dip angle, and planar geometry, could lead to varying and even contrasting crustal deformation patterns (K. Wang et al., 2018). As an example, we compare the onshore and offshore crustal deformation using both projection methods using the 3D velocity structure Green’s function in Figure S6. Because of the extrapolated slip towards the trench, the projected model obtained using the Brown method would lead to a greater overestimation of horizontal displacement compared to the offshore observations (Figure S6). We find that both projection methods perform equally well for most models with 3D geometry (Figure S7). Specifically, both methods can preserve the pattern differences among the models, albeit at varying levels. Therefore, our approach is adequate for identifying the variability in the finite-fault models.

## 2.2 General Features of the Finite-fault Models

The megathrust in the Japan subduction zone extends along the strike from the Ibaraki region to the Sanriku-Oki region. This area can be divided into three main sections along-strike: the northern Sanriku-Oki region (ZN), the central Miyagi-Oki region (ZC), and the southern Ibaraki-Fukushima-Oki region (ZS). Following this geographic along-strike division, we further segment these three sections into six zones, using a depth of 20 km as an along-dip boundary (Figure 4). The 32 finite-fault models exhibit disagreement with respect to their exact rupture extents within these regions. We consider that a respective zone was ruptured during the Tohoku-Oki earthquake if it has  $\geq 10$  m slip.

We summarize the characteristics of each projected slip model according to this six-zone division in Table 1 and indicate the zones for each slip model in Figure S1. During the last 1,500 years, three  $M \geq 8$  earthquakes occurred prior to the 2011 Tohoku-Oki earthquake in the same region. These include the 869 Jyogan  $M$  8.3 earthquake in the central Miyagi-Oki region, and the 1896 Meiji Sanriku  $M$  8.5 tsunami earthquake in the northern Sanriku-Oki region (Tanioka & Satake, 1996; Imai, 2015) (ZN1, Figure 4). However, no major earthquake with  $M$  8 or larger has been documented in the southern sec-

tion (Satake, 2015) (ZS1, Figure 4). The Tohoku-Oki earthquake was located in the central shallow zone (ZC1, Figure 4) and might have ruptured more than one section or zone. Approximately one-third of the models, including a joint inversion model, J5, show an extended shallow rupture in the Sanriku-Oki region (ZN1, Figure 4d). If true, the Tohoku-Oki earthquake may have re-ruptured the slip area of the 1896 Meiji tsunami earthquake, which may explain the exceptionally high tsunami heights of up to 30 m near the  $39.5^\circ$  coast and the large tsunami runup extending up to 10 km inland (Mori et al., 2011). However, this ZN1-slip feature is not present in all models. In addition, five out of the 32 models suggest that the Tohoku-Oki earthquake penetrated a deeper portion of the megathrust in the Sanriku region (ZN2; Table 1).

All the projected finite-fault models suggest that the Tohoku-Oki earthquake ruptured the central shallow part of the Japan trench megathrust (Figure S1), specifically in the Miyagi-Oki region (ZC1), at a depth of less than 20 km. Bathymetric surveys and acoustic ranging conducted before and after the earthquake identified a horizontal trenchward seafloor displacement of more than 50 m at  $38^\circ\text{N}$  (Y. Ito et al., 2011; Kodaira et al., 2012), providing definitive evidence of significant slip near the trench in the central section. However, the models differ significantly regarding the down-dip rupture extent, with around three-quarters of models indicating deep slip beyond the 20 km depth in the Miyagi-Oki region. Furthermore, the location of the peak slip varies from model to model, with 18 models placing the largest slip at the trench (e.g., G4 and T8 in Figure 4) and 14 models locating the maximum slip away from the trench (e.g., models R3 and J5 in Figure 2). These discrepancies imply contrasting rupture mechanisms and/or variations in the material properties of the very shallow part of the Japan subduction zone (Sun et al., 2017; Ulrich et al., 2022). For example, the role of the shallowest megathrust during the earthquake’s rupture remains debated. The large and shallow slip challenges the previous paradigm that the near-trench rheology would prohibit large slips due to velocity-strengthening fault friction and weak impeding sediments (Kozdon & Dunham, 2013).

The southern extent of the Tohoku-Oki earthquake rupture in the Ibaraki-Fukushima-Oki region remains ambiguous. For example, Bassett et al. (2016) and Liu and Zhao (2018) argued that an altered forearc structure might have controlled the frictional behavior of the megathrust, thus effectively limiting the rupture extent to the shallow Ibaraki-Oki region. In this scenario, the forearc structure at the shallow southern section (ZS1) acts as a barrier to halt southern rupture. However, approximately one-third of the models locate significantly large slip in ZS1, such as model R3 in Figure 4b. Moreover, about one-fourth of the models suggest deeper rupture in the southern section (ZS2; Table 1) in a potentially disconnected secondary slip patch triggered by the main slip in ZC1 (e.g., G4 in Figure 4a).

We derive a median slip model (M) by taking the median slip value at the along-dip and along-strike directions of the 32 finite-fault models at each subfault (Figure 5). The median model has a simple slip distribution with a smooth, circular patch up-dip of the hypocenter (ZC1). The lateral extent of the slip is predominantly confined between  $37^\circ$  to  $39^\circ$  along the strike direction. Regarding the dip direction, the model suggests significant slip extending to the trench, although the maximum slip, valued at 38.0 m, occurs approximately 5 km away from the trench (Figure 5).

The standard deviation of the 32 collected slip distributions highlights the variability among the finite-fault models (Figure 5). The standard deviation peaks at more than 20 m near the trench in ZC1, suggesting that the shallow slip of the Tohoku-Oki earthquake is poorly resolved. Depending on the inversion strategies, some models have likely tapered the slip towards the trench. Therefore, we categorize the models into two groups based on the near-trench slip (Figure 1) and compute their standard deviations separately. We find that the respective standard deviations within each of the two groups remain greater than 15 m near the trench, indicating variations in either the peak-slip

location or the peak-slip amplitude at the trench (Figure 5). The standard deviation distributions and the relative standard deviation (defined as standard deviation over median slip) also suggest widespread slip uncertainties—greater than 2.5 m and 100% median slip—in the northern region up to 40° north, southern region, and down-dip regions up to 60 km depth (Figure 5b and Figure 5d), although the major slip area in the median model has low relative standard deviation (Figure 5d).

### 3 Model Comparison

All finite-fault models suggest large near-trench slip in ZC1 (Figure S1), where a large slip deficit had been estimated prior to the Tohoku-oki earthquake (Hashimoto et al., 2012; Loveless & Meade, 2011). This slip feature is the most consistent attribute among the models, with primary differences arising in secondary features, such as slip distributions in zones away from ZC1 (Lay, 2018). Within zone ZC1, model differences manifest as peak slip locations or variations in the heterogeneity of the slip distributions (Sun et al., 2017). We caution that peak slip may not be well resolved in these finite-fault models due to varying fault parameterization and varying selected Earth structural models (Lay, 2018; K. Wang et al., 2018).

The models obtained using single data types have different limitations, mainly reflecting their sensitivities to offshore slip and network configurations (Lay, 2018; Uchida & Bürgmann, 2021). For example, geodetic models tend to have smooth slip distributions with their peak slip patch located near the hypocentral region (K. Wang et al., 2018). Models using tsunami data may be influenced by spurious seafloor deformation and secondary sources, including inelastic off-fault deformation and possible submarine landslides (Du et al., 2021; Kodaira et al., 2021; Uchida & Bürgmann, 2021; K. Wang et al., 2018). However, tsunami data has an advantage over onshore observations due to its sensitivity to slip near the trench (Lay, 2018; Kodaira et al., 2021). Differential bathymetry and near-trench turbidities can directly constrain the occurrence and amplitude of the near-trench slip, and post-earthquake surveys suggest that the main coseismic slip was limited to the south of 39.2° (Ikehara et al., 2016; Kodaira et al., 2020, 2021). Models obtained from joint inversions using multiple datasets may best represent the various observations of the Tohoku-Oki earthquake (Lay, 2018; Uchida & Bürgmann, 2021). However, the slip distributions of the joint-inversion models are significantly more complex than those of other models. These complexities may be affected by incomplete isolation of the coseismic signals, inaccurate assumptions about signal sources, and the strategies of combining different geophysical datasets (Lay, 2018; K. Wang et al., 2018).

Razafindrakoto et al. (2015) qualitatively compared the overall variability of 21 finite-fault models by computing multi-dimensional scaling statistics, including a grey-scale matrix. Their statistics show large variability among the models, likely reflecting the different underlying dataset types (Razafindrakoto et al., 2015). Specifically, their grey-scale matrix suggests that models obtained using tsunami data are more variable when compared to models developed using other data types (Razafindrakoto et al., 2015). Since their model comparison is drawn from statistical metrics, it is challenging to delineate specific slip features, leaving the spatial differences of the slip distributions unclear. Sun et al. (2017) focused on the near-trench slip characteristics of 45 finite-fault models and compared an along-depth slip profile at 38°N. Their comparison identified a high level of variability among the models (Sun et al., 2017).

In this section, we design a new model-comparison framework to quantitatively extract coherent and unique slip features of the finite-fault models at varying length scales. We also quantify the model variability of the five model groups by examining the wavelength power-spectral densities of their respective median models. Without certainty about the actual rupture process of the Tohoku-Oki earthquake, we consider all models equally feasible since they can explain their respective datasets; we do not rank the models.

### 3.1 Slip Heterogeneity

To investigate variability in smaller-scale heterogeneity of the finite-fault models, we compute the spatial power spectra of each slip distribution. We apply a 2D Fourier transform to obtain a 2D power spectral density. By performing a circular mean over the wave number range ( $k = \sqrt{k_s^2 + k_d^2}$ ,  $k_s$  and  $k_d$  are the along-strike and along-dip wave numbers), we derive a 1D power spectral density of each slip distribution (Goda et al., 2014; Mai & Beroza, 2002). We then compute the respective median spectra for the five model groups. We use these median spectra to evaluate the variations in slip heterogeneity associated with each data type (Figure 6). Their decay rates are related to the smoothness of the slip distributions and reflect the relative heterogeneity in slip distributions at different spatial scales (Mai & Beroza, 2002).

The power spectra density of the slip models show that the spectra variability increases with the wave number, suggesting an increase in model complexities with smaller features (Figure 6). The model spectra show good agreement in the wavelength range below  $1/80 \text{ km}^{-1}$ , which reflects that all models have a significant slip patch approximately 80 km in dimension. However, we find systematic differences in the spectra for different groups in the wave number range of  $1/80$  to  $1/10 \text{ km}^{-1}$  (Figure 6). This variability in spectra results in different spectrum decay rates of the five groups, ranging from -2.1 to -3.0. The tsunami and joint-inversion groups have decay rates around -2.2, indicating that these models are enriched in heterogeneous small-scale features, such as more than one major slip patch or sporadic near-trench slip (Figure 2). In contrast, smooth models, such as those from the geodesy and regional-seismic data groups, are characterized by faster spectra decays with corresponding rates around -3.0 (Figure 6). Models developed from teleseismic data have decay rates of approximately -2.7, reflecting their one or two major smooth patches with few secondary features. Within each group the variability of the spectra varies among different groups, indicating inconsistent model features even when using the same data type.

### 3.2 Model Correlation at Multiple Scales

We quantitatively evaluate the similarity between models by computing a correlation coefficient for each pair of models. This correlation coefficient is the inner dot product of two normalized slip-vector fields, which is the sum of each vector dot product. A slip-vector includes the along-strike and along-dip slip values, and a slip-vector field characterizes the final slip distribution of a finite-fault model. We define the correlation-coefficient  $R_{ij}$ , similar to a Pearson correlation, as:

$$R_{ij} = \frac{\langle \Phi_i, \Phi_j \rangle}{\sqrt{\langle \Phi_i, \Phi_i \rangle \langle \Phi_j, \Phi_j \rangle}} \quad (1)$$

where  $i$  and  $j$  are model indices, and  $\Phi_i$  and  $\Phi_j$  are the corresponding slip models with the unified parameterization configuration. The resulting correlation-coefficient  $R_{ij}$  ranges from -1 to 1: a coefficient of 1 indicates that the two slip-vector fields share an identical spatial pattern, although their absolute values may differ; a coefficient of 0 indicates no correlation between the slip-vectors.

Our unified models all have a subfault size of 1 km, and the model correlation-coefficients range from 0.61 to 0.95 (Figure 7) with an average and median value of 0.79 and 0.79, respectively. This broad range of values indicates clear differences in the slip distribution among the models. Generally, the geodetic group (G) shows the highest coherence among their finite-fault models compared to other groups, with an average and median correlation value of 0.83 and 0.81, respectively. Most of these models consist of a smooth, single slip patch located at the up-dip area near the hypocenter, such as models G3, G5, and G6 (Figure 2), which leads to very high inter-model correlation. Model G2, however, significantly differs from other geodetic models with an average correlation value

of 0.73 with other models. The model suggests a southern slip patch at the up-dip hypocenter region in zone ZC1. The regional seismic group (R) shows high coherence among their finite-fault models compared to other groups. In comparison, the teleseismic group (S) shows a broad range of correlation values, generally lower than those of groups G and R (Figure 2b). Teleseismic models show large variations in secondary slip features, such as the extended slip in different zones.

Intriguingly, models developed using tsunami data, both T and J groups, show considerable variability within their respective groups and when compared to models of other groups. These models comprise a more heterogeneous slip distribution with complex slip features in their distribution and values, causing the observed low correlation values. We find that the median model, M, highly correlates with all other models, with a median correlation value of 0.89. This high correlation reflects that the main feature of the median model—the slip in ZC1—is captured by all models. The results also suggest that the dominant slip area likely centers around a single slip patch in ZC1, since more complex slip features of the models do not impact the correlation values very much.

Our 1-km model parameterization is much smaller than the typical subfault sizes used in finite-fault inversion (Ide, 2007). Subfault dimensions are often set to be around 16, 32, and 64 km for geodetic, seismic, and tsunami finite-fault inversions, respectively (e.g. Inuma et al., 2012; Wei et al., 2012; Satake et al., 2013). Therefore, we downscale the slip models to increase the subfault sizes from 1 km to 16, 32, and 64 km and then compare the variability of slip features at different length scales (Figure 8). We apply a 2D discrete wavelet transform to the slip distributions using the Daubechies’ first wavelet (Daubechies, 1990). The wavelet transform allows us to isolate slip features at varying spatial scales by filtering out higher-order wavelets (Figure 8). For example, inversely transforming a low-pass filtered wavelet spectrum results in a lower-resolution slip distribution. This wavelet transform process is similar to an image compression technique using Daubechies’ first wavelet group (Daubechies, 1990). Importantly, our downscaling process preserves the overall moment, moment centroid location, and spatial distribution of the slip features at the selected wavelength scale.

We apply the downscaling procedure to each 1 km subfault-size model to 16, 32, and 64 km subfault sizes, and process the slip distributions of the along-strike and along-dip directions separately (Figure S2–S4). The 64 km length scale approximates the wavelength of a 10 s period crustal P wave at subduction zones, and the displacements of these 10 s period P waves are commonly used in teleseismic finite-fault inversions (e.g. Ammon et al., 2005; Kubo & Kakehi, 2013; Yue et al., 2014). As an example, Figure 8 shows the slip distribution of model S3 and the median model at scales of 1, 16, 32, and 64 km. The original S3 model consists of two major along-strike slip patches shallower than 20 km, along with complex small-scale patches at around 40 km depth. These deeper patches have spatial scales of less than 32 km, and the 64 km scale model primarily retains the dominant, large-scale shallow slip features. Thus, our wavelet-based downscaling procedure effectively removes the small length-scale features of the finite-fault models.

The correlation coefficients between the models increase as the subfault size increases, confirming that the model variability primarily originates from small-scale features (Figure 9a–c). At the 64 km scale, the median and average correlation-coefficients are 0.89 and 0.88, respectively. This coherent pattern is present in all model pairs, regardless of the datasets used (Figure 9c). Much like at the 1-km scale, all models show a high correlation with the median model at larger scales (Figure 9d). Our results reveal a coherent pattern emerging among all the projected models: a primary slip patch that occurred up-dip of the hypocenter around 10 km depth during the Tohoku-Oki earthquake. However, the model features are inconsistent at the 16 and 32 km length scales, either in their locations or amplitudes. The correlation results from 1 km to 16 km scales largely remain the same (Figure 7,9), indicating that the original model resolutions were limited to around 16 km.



## 4 Model Validation

Previous model-comparison studies primarily focused on identifying coherent and unique slip features (e.g., Ide, 2007; Razafindrakoto et al., 2015; K. Wang et al., 2018, 2020). Here, we systematically examine the sensitivity of four commonly-used datasets to the variability in the finite-fault models (Figures 10–16), including geodetic (Section 4.1), teleseismic (Section 4.2), regional seismic-geodetic (Section 4.3), and tsunami data (Section 4.4). We compute synthetics for all models using the same Green’s functions. Then, we compare the synthetics with observations using the correlation-coefficient and variance-reduction metrics. We test the models not only by comparing their respective data types used in obtaining the models but also by inspecting the fit to datasets not included in their finite-fault inversions.

Our comparison evaluates both the data sensitivity to model variability and the data capability to resolve smaller-scale features. We examine the data sensitivity to the slip features identified in Section 3, including the contrasting rupture extent in different zones. Additionally, we compare synthetics with observations, as well as with each other, using slip distributions at varying scales.

### 4.1 Onshore and Offshore Geodetic Data

We test the geodetic data type using both onshore and offshore static-displacement measurements. We compute the synthetic static displacements for each site using Green’s functions from Hori et al. (2021), applied to models at the 16, 32, and 64 km spatial scales. These Green’s functions are numerically computed using a 3D velocity structural model and realistic topography at approximately 1 km resolution of the Japan region. Specifically, we compute the synthetics for the onshore GEONET network, which includes 365 stations, and the eight offshore GNSS-A sites (Table S1; M. Sato et al., 2011; Kido et al., 2011). Additionally, we examine vertical displacement data recorded by six pressure gauges operated by Tohoku University (Hino et al., 2011; Y. Ito et al., 2011) and the University of Tokyo (Maeda et al., 2011b). Our primary focus are the correlation-coefficients between the synthetics and observations instead of the variance reduction metric. The variance reduction metric is strongly influenced by synthetic amplitudes, which depend on the assumed velocity models and the finite-fault parameterization. For example, using a 3D velocity structure to compute synthetics from models obtained using 1D structures may reduce the overall amplitudes (K. Wang et al., 2018). The correlation-coefficient, on the other hand, evaluates the coherence between synthetic and observed displacement fields and is better suited to compare slip distributions with large spatial heterogeneities. However, the variance reduction metric can be a useful tool for differentiating models as long as the models are resolved using the same Green’s function for an objective comparison (e.g., Figure S8).

We find that neither the onshore nor the offshore geodetic observations can distinguish between the slip models at the same scale (Figure 10). For example, the four models in Figure 10 at the 16 km scale, including the median model (M), can all explain the observed displacement fields well, with correlation-coefficients greater than 0.91 between their synthetics and the observations. The median model has a simple distribution with only one slip patch in ZC1 (Figure 10d), while the other three models have distinct, incoherent features, such as model R3 ruptures in ZS1 (Figure 10e), model J5 ruptures in ZN1 (Figure 10f), and model S3 ruptures in ZC2 (Figure 10a), respectively. For the onshore stations, the limited data resolution likely results from the 150 km distance between the epicenter of the offshore earthquake and the nearest coastal station of the GEONET network. Even for models with significant down-dip slip in ZC2, the coastal GEONET stations remain too far to resolve the down-dip slip features conclusively due to the increasing depth of the megathrust (Figure S9).

The offshore geodetic network, consisting of GNSS-A and pressure gauge stations, cannot resolve the differences in the slip distributions or the peak-slip locations (Figures 10h, S9–S10). For example, models G3 to G6 can all generate synthetics with correlation-coefficients  $\geq 0.97$ . However, some models locate the peak slip near the trench (G4), whereas others place the peak slip around the hypocenter (G3, G5, and G6). Additionally, secondary slip features, such as slip in ZS1 and ZN1, do not impact the offshore synthetics significantly. The median model and model J5 can explain the offshore displacements equally well, while model J5 is remarkably more heterogeneous than the median model. The limited resolution of the offshore geodetic network is likely due to the fact that most of its stations are located in the central Miyagi-Oki section. Only 13 stations were deployed in this 150 km by 150 km area prior to the earthquake. This offshore network configuration determines that the offshore observations were primarily controlled by the slip directly beneath these stations. Given that all projected models coherently resolve a large slip patch in ZC1, they can all reasonably explain the offshore observations. We emphasize that the location of the offshore geodetic network covered the center of the Tohoku-Oki earthquake rupture area, playing a critical role in resolving the largest slip patch, although its sparse configuration limited its capability in resolving secondary slip features.

We find negligible differences in the geodetic synthetics among the same models at the 16, 32, and 64 km scales. The correlation values between the observations and the synthetics remain consistently high ( $> 0.90$ ) for all models across all scales, for both onshore and offshore geodetic data (Figure 10). These results suggest that the resolution of the geodetic dataset is likely lower than 64 km for the offshore slip distribution and that the data cannot differentiate slip features at smaller scales. For example, the synthetic onshore-geodetic static displacements from model S3 show no differences across the three scales (Figure 10a–c, synthetics in red and observations in black). The offshore synthetics show similar patterns, suggesting marginal resolution differences across scales, even though all models inverted from geodetic datasets included part or all of the offshore data and their original models have subfault sizes much smaller than the 64 km scale.

We compute the variance reductions for the finite-fault models with respect to the geodetic datasets (Figure S8). The variance reduction metric shows a higher sensitivity to slip distribution variability than the correlation coefficient. Most of the models have  $\geq 80\%$  variance reduction, with the exception of four models. The variance reduction pattern of the onshore geodetic data shows a similar pattern as the model correlation with the median model (Figure 9d). This suggests that onshore geodetic data can generally well-resolve slip features at the 64 km spatial scale. In addition, there is a difference in variance reduction for offshore data between the 32 and 64 km scales for most models. However, these differences in variance reduction are negligible when comparing the same models at the 16 and 32 km scales. These results show that the amplitudes of offshore displacement under the present conditions are sensitive to localized slip features, suggesting that the offshore geodetic data might have higher spatial resolution than 64 km when evaluated using the variance reduction metric.

## 4.2 Teleseismic Data

Teleseismic waves are one of the most commonly used observations to invert finite-fault models of large earthquakes (e.g., Ji et al., 2002; Yagi & Fukahata, 2011a; Okuwaki et al., 2020). They have relatively simple waveforms and can effectively characterize the temporal evolution of earthquake rupture processes (Okuwaki & Fan, 2022). Different from computing geodetic synthetics, both the slip distribution and slip-rate functions are required for synthesizing teleseismic waveforms. Slip-rate functions characterize the temporal moment release for each individual subfault (Ide, 2007). To focus on comparing the slip distribution variability, we first test, validate, and identify a slip-rate func-



tion type. We assume a single-time-window slip-rate function with a uniform duration for all subfaults. We test a range of slip-rate functions, such as the cosine and Yoffe functions, and then apply the best-performing one to all models to compute teleseismic synthetics. The best-performing slip-rate function is defined as the one resulting in the highest variance reduction in fitting teleseismic P waves. With this replaced uniform slip-rate function, our comparison focuses on the impact of the slip distribution variability. The slip-rate function is paired with the peak-slip-rate time (PSRT) distribution from model S3 to synthesize teleseismic seismic waves, including both body and surface waves. The peak-slip-rate time distribution of model S3 is used because the model is obtained using the single-time window method and inverted from both body waves and surface waves. We justify the procedure in Sections 4.2.1–4.2.3.

We compute teleseismic synthetic displacement waveforms using Instaseis (van Driel et al., 2015). This method uses pre-computed Green’s function databases, calculated using the anisotropic version of the Preliminary Reference Earth Model (PREM) and the AxiSEM method up to 2 s period band (Dziewonski & Anderson, 1981; Nissen-Meyer et al., 2014). The teleseismic synthetics are compared with three-component broadband records at 40 stations from the II and IU networks, located within an epicentral range of 30° to 90° and covering all azimuths (Figure 11a; see Open Research for details). We remove the instrument response from the observations, integrate velocity waveforms into displacement waveforms, and decimate the data to a 1 Hz sampling rate. Both the observations and synthetics are filtered using a 4<sup>th</sup>-order Butterworth band-pass filter to the appropriate period band before the comparison: body waves are filtered in the 10–150 s period band and surface waves are filtered in the 100–200 s period band. We compare the windowed body waves from -20 to 230 s relative to their PREM-predicted arrival times and surface waves from 500s to 3300 s relative to the Tohoku-Oki earthquake origin time. These frequency ranges are comparable to the teleseismic analysis used in the S models, as well as in teleseismic finite-fault models of the  $M_w$  8.8 Maule earthquake and the  $M_w$  9.1 Sumatra earthquake (e.g. Ammon et al., 2005; Kubo & Kakehi, 2013; Yue et al., 2014). Before comparing the waveforms, we cross-correlate the synthetics with the observations and apply an empirical time correction to account for the arrival time uncertainty due to the 3D Earth structure. We adopt the same correlation value metric to compare the waveforms and use the median correlation value for each wave type as a representative metric to compare the finite-fault models.

#### 4.2.1 Geometric Effects

We explore and validate the effects of fault geometry on teleseismic synthetics. We use model S3 as an example and compare the synthetics obtained from the original multi-planar fault configuration and the projected S3 model onto a realistic megathrust geometry. The projected model has the same number of subfaults as the original model, and the slip-rate functions of the subfaults remain the same. The synthetics from both models are nearly identical, leading to almost the same correlation coefficients of 0.90 with the observations. For example, the P wave synthetics (blue) using the realistic megathrust geometry, those from the original configuration (red), and the observed P waves (black) share a high resemblance, as illustrated in Figure S17. We conclude that the projection scheme does not significantly impact the teleseismic synthetics (Table S2). This exercise validates the idealized planer parameterization in most finite-fault models of the Tohoku-Oki earthquake. The results suggest that the 2011 Tohoku-Oki teleseismic waves are not very sensitive to geometry changes, likely due to that the majority of the observations are located far away from the nodal planes with down-going rays (Figure S14). We expect insignificant geometric effects on geodetic observations as well because all the models can explain the observed offsets equally well with high correlation values (Figure 10).

#### 4.2.2 Slip-rate Function Effects

The original model S3 uses a cosine function as its slip-rate function, with rise times varying from 6 to 24 s and durations ranging from 12 to 48 s. We replace these original slip-rate functions of the projected S3 model with a regularized Yoffe function (Tinti, Fukuyama, et al., 2005; Yoffe, 1951), characterized by a rise time of 16 s and a duration of 40 s for all subfaults to compute teleseismic synthetics. The rest of the finite-fault parameters remain the same to isolate the effects of a chosen slip-rate function. We select the regularized Yoffe function as the slip-rate function because it is compatible and consistent with the traction and slip evolution of the dynamic propagation of earthquake ruptures (Tinti, Spudich, & Cocco, 2005). The varying rise time and decay rates of the Yoffe function resemble the results from both dynamic simulations and laboratory experiments (Ohnaka & Yamashita, 1989; Tinti, Spudich, & Cocco, 2005).

The two sets of synthetics are nearly identical, and they both can satisfactorily explain the observations (Figure S18). The synthetics obtained using the replaced slip-rate function have fewer high-frequency signals compared to the synthetics using the original model (Figure S18), likely due to the absence of rise-time variations. Nonetheless, the model adopting the replaced slip-rate function can fit the observed seismograms with a median correlation coefficient of 0.84 for P waves (Table S2). Similarly, the SH and SV waves with the uniform slip-rate function can fit the observed seismograms with a median correlation of 0.77 and 0.81. These findings validate our proposed strategy of computing teleseismic synthetics.

We explore a range of slip-rate functions, including cosine, triangular, and different Yoffe slip-rate functions with durations of 40 and 55 s (Text S2; Figure S16). The teleseismic synthetics are insensitive to these variations, and the median correlation coefficients are all greater than 0.82 for the P waves (Table S2). Furthermore, we test varying durations for the suite of slip-rate functions and find that the slip-rate duration does not significantly impact the synthetic amplitudes as long as the duration is less than 40 s for the given subfault parameterization (Figure S18 and S20). For longer durations, the associated synthetic body waves have lower amplitudes than those using slip-rate functions with shorter durations (Figure S21). With the same spatial configuration, the variation in duration relates to the variation in the apparent rupture-front propagation, the effects of which will be evaluated in the next Section 4.2.3. Overall, the results confirm that the chosen regularized Yoffe function, with a rise time of 16 s and a duration of 40 s, can effectively represent the slip-rate functions for computing and comparing teleseismic synthetics from the set of finite-fault models.

#### 4.2.3 Rupture Propagation Effects

The earthquake rupture propagation significantly impacts teleseismic synthetics (Figure S19). To evaluate this effect, we vary the rupture propagation parameters to compute the onset times of each slip-rate function and corresponding teleseismic synthetics and keep the remaining finite-fault setup the same as the original model S3. We first assume a constant rupture velocity, resulting in a circular rupture front as shown in Figure S14c. With an assumed rupture speed of 2 km/s, the synthetic P waves cannot explain the observed waveforms between 30 to 80 s (Figure S19), and the median correlation value drops to 0.65 for P waves (Table S2). We then assume a slower speed of 1.5 km/s for the first 100 km of rupture propagation and a rupture speed of 2 km/s for the remaining rupture process, following finite-fault inversion schemes used in some of the teleseismic models (e.g., Ammon et al., 2011; Lay et al., 2011; Shao et al., 2011). Teleseismic synthetics obtained using this two-step rupture propagation cannot explain the observations either, resulting in a median correlation value of 0.65 for P waves (Figure S19).

In our experiment in Section 4.2.2, we use a single, regularized Yoffe function constrained by the S3 onset time distribution for computing teleseismic synthetics. Here,

we align the onset times of the slip-rate functions with the peak-slip-rate times (PSRT) in model S3 for each subfault. The associated synthetics are nearly identical to those from the original S3 model, with correlation-coefficient differences less than 0.02 (Table S2). The PSRT configuration improves the data fitting to the observed waveforms more than the original onset time configuration when using the uniform, single slip-rate function approach (Figure S18). Specifically, the PSRT synthetics can produce the high-frequency waveforms that is missing in the onset-time synthetics (Figure S18).

We validate our approach using slip distributions and peak-slip-rate times from other finite-fault models. To test the effects of different PSRT distributions, we also apply the PSRT approach to models S6 and J3 using their respective distributions (Figure S23). This analysis yields satisfactory P-wave data fitting with correlation coefficients of 0.75 and 0.75 for the two models (Figure S24), respectively, while synthetics from their original models have correlation coefficients of 0.71 and 0.73 with the observations, respectively. We then use the S3 PSRT and slip distributions from models S6 and J3 at the 16 km scale to generate teleseismic synthetics (Figure S22). The synthetics can explain the observations with correlation coefficients of 0.77 and 0.76 (Table S2), which are around 0.05 different from those of the model S3 synthetics at the same scale (Table S2). This validation demonstrates that the model S3 PSRT distribution can be used to pair with other slip distributions to compute teleseismic synthetics. Therefore, we use the model S3 PSRT distribution and the selected single Yoffe slip-rate function to compute teleseismic synthetics for all 32 finite-fault models. We note that our analysis does not consider complex rupture propagation effects, such as multiple slip episodes inferred from multiple time-window slip inversion (Lee et al., 2011; Melgar & Bock, 2015; Yue & Lay, 2013) or in dynamic rupture scenario simulations informed from local strong ground motions (Galvez et al., 2016, 2020).

#### 4.2.4 Sensitivity of Teleseismic Data to Finite-fault Model Variation

We compute teleseismic synthetic waveforms using the final slip distributions at the 16, 32, and 64 km scales of all models. We employ the same procedure, using the model S3 PSRT distribution and a regularized Yoffe slip-rate function with a rise time of 16 s and a duration of 40 s, to compute the synthetic waveforms. When generating teleseismic synthetics with spatial scales greater than 16 km, the 32 or 64 km size subfault are divided into 16 km subfaults and each 16 km subfault has the same slip as the 32 or 64 km size subfault. We then use the same slip-rate and PRST distribution with this slip distribution to generate synthetic waveforms. The synthetics include both body and surface waves. As an example, Figure 11 shows the resulting synthetic teleseismic waveforms from 16 km scale models at the IL.BRVK, IU.COR, and IU.HNR stations, representing azimuths of  $312^\circ$ ,  $51^\circ$ , and  $158^\circ$ , respectively. Figure S11 and S12 show the resulting synthetic teleseismic waveforms from 32 km and 64 km scale models. For a quantitative comparison, we compute correlation coefficients between the synthetics and the observed waveforms for five wave types from each model, including the P, SH, SV, Rayleigh, and Love waves (Figure 12).

We find that none of the five types of teleseismic waveforms is sensitive to variations in the slip distribution (Figure 11c). Synthetic seismograms for the same stations are highly coherent with each other (red lines in Figure 11c,d). For example, Figure 11c shows body wave synthetics from all 32 finite-fault models and the median model at the 16 km scale at stations IL.BRVK, IU.COR, and IU.HNR, which are nearly identical to each other. These synthetics can all satisfactorily explain the body wave phases, such as fitting the complex P wave phases correctly. It is worth noting that these synthetics can achieve comparable misfit reductions (waveform fittings) to other teleseismic finite-fault inversion studies (e.g. Kubo & Kakehi, 2013; Yoshida et al., 2011). The S wave synthetics have similar correlation coefficients with those of P waves (Figure 12), and the two phases do not show distinctive sensitivities. Similarly, the surface wave synthetics

from different models are coherent with each other and can all explain the observations (Figure 11d and 12). These synthetic surface waves tend to have higher amplitudes than real observations, likely due to our simplistic 1D Green’s functions. In addition, we also find that the associated moment-rate functions of the models share a similar function shape (Figure 11b). We further compare the teleseismic synthetics with 32 and 64 km scales in Figure S2 and S3 and observe similar waveform fits. The synthetics of the five types of teleseismic waves show minor variations with different slip models. Our results reveal that with the same temporal evolution of the rupture propagation, variations in the slip distributions do not significantly impact the moment-rate function or teleseismic synthetics.

We further quantify the sensitivity of teleseismic waves to the same slip models at the 16, 32, and 64 km scales. For each model, we compute the synthetics using three different length scales and correlate the synthetics with the observations to examine their sensitivities (Figure 12). We find little difference in the synthetic waveforms for different scales, and they all correlate well with the observations. For example, the P wave synthetics have consistent correlation values around 0.70–0.80 for the same models at all scales. Similarly, the S waves and surface waves cannot resolve slip models at finer scales either (Figure 11). These results indicate that teleseismic finite-fault models likely have a spatial resolution of around 64 km for the Tohoku-Oki earthquake.

### 4.3 Regional Seismic and Geodetic Data

The 2011 Tohoku-Oki earthquake was recorded by densely distributed regional strong ground motion seismic and high-rate geodetic stations. Using regional seismic and geodetic data often led to finite-fault models with a higher degree of rupture complexity, including multiple rupture episodes near the hypocenter (e.g., Lee et al., 2011; Melgar et al., 2013; Bletery et al., 2014). We follow the same setup as used in Section 4.2 to compute the regional seismic and geodetic synthetics and evaluate the sensitivity of the regional data to rupture propagation and slip distribution variations. We focus on 30 high-rate GNSS time series (Figure 13) from the GEONET network of the Geospatial Information Authority (GSI) of Japan and 25 K-NET and KiK-net three-component strong motion stations (Figure 14) from the National Research Institute for Earth Science and Disaster Prevention (NIED) data center. All stations are located within 350 km of the epicenter of the 2011 Tohoku-Oki earthquake.

We first validate our projection method by comparing the synthetics resulting from the original and projected model J4 (Supplementary Text S3). We find that the original and projected synthetics agree well when using the J4 original slip-rate functions, with the strong ground motion comparison in Figure S35 and high-rate GNSS comparison in Figure S39. This exercise validates the projection procedure for examining the two regional data types.

To compare to high-rate GNSS data, we focus on horizontal components and low-pass filter the GNSS time series at 10 seconds. We compute high-rate GNSS synthetics following the same procedure as for obtaining the teleseismic synthetics (see Supplementary Text S3). We use the regularized Yoffe slip-rate function and the model S3 PSRT distribution (Section 4.2). This procedure is applied to each of the 33 slip models at the 16, 32, and 64 km scales, respectively (e.g., Figure 13). The high-rate GNSS synthetics from different models share similar waveforms but have different amplitudes, including different static offsets. The amplitudes of the synthetic static offsets, here using the Instaseis method with a 1D velocity model (van Driel et al., 2015), are comparable to the results computed using the 3D Green’s function in Section 4.1. For example, Figures S38 and S39 illustrate the agreement between the 1D and 3D synthetic offsets as well as between the observed and synthetic offsets for model J4. Figure S40 compares the variance reduction for static offsets at the 30 GNSS stations for all models at 16, 32,

and 64 km scales using 1D and 3D synthetics. We find that the variance reduction metrics are different for the 33 models, although the correlation values are largely comparable.

The static-offset differences between synthetics from the 33 models are highlighted in Figure 13. These synthetics correlate well with the observations with correlation coefficients exceeding 0.9 on average. However, when their amplitudes are normalized, the high-rate GNSS synthetics are almost identical (Figure S41). This result indicates that the high-rate GNSS data may not be able to distinguish the small-scale spatial variability among the slip models. The amplitude differences primarily result from the variations in the total seismic moment and in slip in the down-dip regions (e.g., ZC2). Models with larger moments lead to higher static offsets in the synthetics (Figure S9). We note that the similarity between the normalized synthetics stems from using the same set of slip rate functions and PSRT distribution.

We find that regional strong ground motion data may be more sensitive to the details of earthquake rupture propagation than other regional observations. The coastal strong ground motion records have complex waveforms, and the vertical seismograms cannot be easily explained by the assumed, simplified model. In the 10-to-100-second period band, the original model J4 that includes re-rupturing episodes near the hypocenter can explain the three-component displacement records at the 25 strong motion stations. The corresponding vertical synthetics have an average correlation value of 0.86 with the observations (Figure S35). In contrast, the assumed, simplified model using the J4 slip distribution, the S3 rupture propagation without re-activation, and the regularized Yoffe slip-rate functions leads to an average correlation value of 0.65 between the associated synthetics and vertical observations (Figure S36). In distinction, the horizontal component strong motion data can be explained by the assumed, simplified model with an average correlation coefficient of 0.7, including stations MYGH03, MYGH08, and FK031 that are close to the earthquake epicenter (Figure 14).

To isolate the sensitivity of strong ground motions to the slip distribution variability, we compute three-component synthetics (10-to-100-second period band) using the same simplified rupture propagation and the slip distributions of the 33 models at the 16, 32, and 64 km scales (e.g., Figure 14, Figure S43 and Figure S44), and then compare the synthetics with those from the median model (M). At the same spatial scales, the three-component synthetics have similar waveforms to those from the median model (Figure 14d). For example, models J3 and J4 have distinct slip complexities (Figure S3 and Figure S4), but they generate similar synthetic waveforms. Additionally, the horizontal synthetics can match the observed displacement waveforms in the same period band. We find that the same slip models at 16, 32, and 64 km scales result in similar synthetic waveforms, with correlation values exceeding 0.9 on average (Figure 14d, Figure S36 and S37). These synthetic waveform tests indicate that the strong-ground motion records are less sensitive to small-scale variability in the slip models (Figure 14d).

Our analysis implies that strong motion stations within 200 km of the 2011 Tohoku-Oki earthquake are likely most valuable in resolving both the earthquake rupture propagation and slip distribution. When comparing the synthetics with observations at different distances, we find that the sensitivity of regional strong motion records decreases with increasing epicentral distance (Figure 15). The observations can be well explained by the synthetics obtained assuming the simplified rupture propagation model once the epicentral distance is larger than 300 km, with their correlation coefficients greater than 0.7 on average, including the vertical components. These waveforms are less complex, comparable to those of teleseismic observations (Figure 14). In contrast, waveforms at stations within 200 km epicentral distance are complex and are challenging to model even when multiple rupture episodes are permitted, such as in the original model J4. While this model is obtained using the regional seismic observation and the multi-time-window method, its synthetic waveforms have an average correlation value of 0.71 for the ver-



tical component observations in comparison to a value of 0.95 for the east component (Figure S35).

#### 4.4 Tsunamigenic Seafloor Uplift

The Tohoku-Oki earthquake generated a devastating and far-reaching tsunami across the Pacific Ocean. Tsunami data has a unique sensitivity to seafloor displacement, and the data recorded by offshore bottom-pressure gauges, Global Positioning System (GPS) wave gauges, and DART buoys are commonly used to invert for seafloor uplift models, which are then used to invert for earthquake slip distributions (e.g., M. Sato et al., 2011; Maeda et al., 2011a; Saito et al., 2011; Hossen et al., 2015; Dettmer et al., 2016; Jiang & Simons, 2016). This two-step procedure decouples the observed tsunami data from the assumed fault geometry and Earth structures, allowing the inverted seafloor displacement to be validated by other independent geophysical observations (Fujiwara et al., 2011; Kodaira et al., 2012).

We take advantage of a published seafloor uplift model obtained using tsunami data (Jiang & Simons, 2016) and compute synthetics from the collection of slip models to compare with the smoothed uplift model of Jiang and Simons (2016). This model is obtained by inverting data from ocean bottom pressure gauges, seafloor cable pressure gauges and GPS gauges, and three open ocean DART tsunami meters. We use the smooth version of the seafloor uplift model (referred to as model SJS hereinafter) because of its reported lower uncertainty. This model shows a broad uplift region at the major slip area shown in the median model, albeit with a more heterogeneous spatial pattern (Figure 16a). Using the procedure outlined in Section 4.1, we compute the vertical seafloor displacement at the same set of model grid points as in Jiang and Simons (2016). The displacements are obtained using the same Green's functions from Hori et al. (2021) as we used for computing the onshore and offshore geodetic synthetics. We then compare the seafloor uplift synthetics with model SJS by calculating their correlation-coefficients. We apply the comparison procedure to finite-fault models at the 16, 32, and 64 km scales for all 32 models and the median model.

The seafloor-uplift synthetics show clear differences among the finite-fault models, suggesting that seafloor uplift observations can distinguish their major features. For example, seafloor-uplift synthetics from five models in Figure 16 at the 16 km scale have large variations, reflecting the variations in their corresponding slip distributions (Figures 16 and 2). In addition, models at different spatial scales would cause different seafloor-uplift fields, indicating that this type of data may have a spatial resolution of 32 km for the 2011 Tohoku-Oki earthquake, such as the model J5 example in Figure 16. However, seafloor-uplift fields cannot distinguish the secondary features of the slip models, such as the contrasting shallow and deep rupture patches in the southern section of models R3 and G4, respectively (Figures 4 and 16). The southern secondary slips of both models exceed 10 m. However, the corresponding seafloor uplifts are less than 2 m, an uplift amplitude within the absolute uncertainty range of model SJS (Jiang & Simons, 2016).

Despite the seafloor-uplift synthetics showing a clear distinction among different slip models, the synthetics do not correlate well with model SJS, with an average correlation-coefficient of 0.6. These low correlation-coefficients stem from the variability of the finite-fault models and may also reflect significant uncertainties in the tsunami-inferred seafloor uplift (Jiang & Simons, 2016). The variations in synthetics lead to a large range of corresponding correlation coefficients comparable to the variations in the slip models. Our synthetic analyses also indicate that a well-resolved seafloor uplift field has the potential to determine finite-fault slip distributions at a 32 km scale, a higher resolution than those of the teleseismic or geodetic datasets.



## 5 Discussion

### 5.1 What Controls the Finite-fault Model Variability?

We quantitatively compare the collection of finite-fault models for the Tohoku-Oki earthquake and find that they share a consistent feature regarding the location of the largest slip patch, updip of the hypocenter in the Miyagi-Oki shallow region (ZC1). At a spatial scale of 64 km, these models have an average correlation coefficient of 0.88. We generate a static net slip median model that effectively captures this coherent slip feature, with correlation-coefficients  $\geq 0.80$  compared with other models at all spatial scales, from 1 to 64 km (Figure 9d). Furthermore, the median model does not have secondary features in other zones, and its 10 m slip contour only extends 220 km along the strike direction. Our data validation analyses show that the median model can explain the on-shore and offshore geodetic observations (Figure 10). The model can also explain teleseismic observations when paired with an appropriate PSRT distribution (Figure 11–16). The excellent performance of the median model results from the averaging procedure, which can reduce both model-induced and data-induced errors (S. Minson et al., 2013). The averaging procedure is particularly effective when a large set of models obtained from a diverse set of datasets is available (Twardzik et al., 2012), as the Green’s functions linearly connect the model to the data.

Our model comparisons reveal considerable variability in secondary slip features among the models. Specifically, slip features with spatial extents less than 64 km are distinctive across different models. We find that the degree of variability seems to correlate with the types of data used in developing the models. Most models in groups R and S are characterized by one or two large slip patches in ZC1 without significant secondary features. This characteristic is reflected in the model correlation-coefficient histograms in Figure 7b, which display smaller spreads than other groups. Models in group G can vary greatly, leading to two separate subgroups, as shown in Figure 7b. Models in group T are highly heterogeneous, and their secondary features do not agree with each other, leading to nearly uniform correlation-coefficient distributions within the group and with other groups (Figure 7b). Models in group J are inverted from a variety of datasets, but they all have included tsunami and seismic data. These models show the least coherence within their group or compared to models of other groups (Figure 7b). As shown in Section 4, the available geodetic and seismic observations can constrain the models to approximately a 64 km scale, while the tsunami data might provide sensitivity at a spatial scale of 32 km. This discrepancy in sensitivity may contribute to the observed complexities in the models developed using tsunami data, which is also reflected in the power spectra of the slip models in Figure 6.

The rupture extent of the models differs among the five groups. The G, R and S groups have an average along-strike extent of 250 km for the 10 m slip contour, whereas the rest of the groups show rupture extents up to 300 km for the same slip contour range along the strike direction. The extended slip areas are shown as secondary slip features in models from the T, and J groups. The limited sensitivity of geodetic, regional seismic and teleseismic data to these small-scale features may account for these differences. However, secondary slip features in the T, and J group models disagree, and no consistent rupture extent can be extracted from these models, even within the same model group. Even though tsunami observations may have higher sensitivities to smaller slip patches, the inconsistent model features cannot support the notion that they are superior to those from the geodetic, regional seismic, or teleseismic data. Joint inversion of multiple datasets may balance the complementary sensitivities of different datasets to resolve more accurate finite-fault models. However, the localized, small-scale features in the J models are notably different from those of models from other groups, casting doubt on their reliability in capturing small-scale features.

The sensitivity of tsunami data to small-scale features likely results from the slow propagation speed of tsunamis. Assuming a tsunami wave speed of 200 m/s, a 32 km separation of slip patches would lead to an 1800-second separation in the recorded tsunami waves for an instantaneous rupture scenario. This temporal separation in the record would allow the tsunami data to record small-scale slip features. However, due to the space-time trade-offs for large earthquakes, the number and azimuth distribution of tsunami observations have critical controls in determining the seafloor displacement, which could cause model disparities when the observations are sparse.

In addition, the inversion of tsunami data often involves multiple steps, which include translating the recorded tsunamis into seafloor deformations, followed by inverting slip at the megathrust interface using the deformation estimates. For example, Hossen et al. (2015) and Dettmer et al. (2016) demonstrate that tsunami dispersion effects and accounting for source kinematics may lead to differences in the imaged seafloor uplift, notably in the northern region with extended uplift near the trench. Other timing discrepancies in the tsunami far-field may stem from solid Earth elasticity and ocean water compressibility (Tsai et al., 2013). Differences in model setup, effectively different Green's functions, have strong controls in the seafloor deformation response, consequently resulting in discrepancies in the inverted slip distributions. K. Wang et al. (2018) underscores the influence of model assumption in the slip models, and the poorly constrained near-trench fault geometry and bathymetry would lead to large uncertainties in the modeled seafloor deformation.

Another potential factor that may cause the large variability in models obtained using tsunami data is the possible existence of unaccounted secondary sources, such as submarine landslides, localized off-fault deformation, or splay fault slip, which can amplify coseismic seafloor displacements and contribute to generating tsunamis (Y. Ito et al., 2011; Ide et al., 2011; Tsuji et al., 2011; Ma & Nie, 2019; van Zelst et al., 2022; Biemiller et al., 2023; Ma, 2023). The collection of finite-fault models assumes that all geophysical signals are solely stemming from earthquake slip across the megathrust. If submarine landslides or other events occurred during or shortly after coseismic rupture, they may bias the inferred slip models. In this case, strong additional sources would yield coherent secondary slip features in the models derived from the tsunami data. However, our analyses show that the T and J groups contain the least coherent models at small scales. This observation does not appear to confirm the secondary source hypothesis.

In addition to the data types, finite-fault inversion methods have a strong impact on the resulting models. For example, the collection of models shows pronounced differences in slip distribution near the trench. Some models feature tapered slips near the trench, potentially due to no-slip boundary conditions employed during the inversion. The peak-slip location is influenced by boundary conditions. For example, Zhou et al. (2014) demonstrated that the peak-slip location would shift away from the trench if a no-slip boundary condition is imposed during the inversion. For example, models T1 and S3 demonstrate strong taper slips to zero near the trench. Conversely, a free-slip boundary condition would lead to the peak-slip location being placed near the trench, including models G4 and G7 (e.g., Figure 1). Inversion techniques also influence the model variability (Figure 2). Particularly, models from full Bayesian methods without employing smoothness or spatial correlation priors are more heterogeneous, such as models T1 and J2 in Figure 2, and averaging ensemble models does not equal to a smoothness prior (D. S. Sato et al., 2022; Yagi & Fukahata, 2011b; Zhou et al., 2014).

The finite-fault model configuration, such as the fault geometry and subfault parameterization, and the adopted velocity structures directly impact the model variability (K. Wang et al., 2018). Our analysis assumes a fixed fault geometry from Slab2.0 and uses a 1D velocity structure to compute Green's function. This procedure allows us to explore the data sensitivity to different slip distributions but does not examine model-induced uncertainties, which may have contributed to the model variability (e.g., Bletery

et al., 2015; Funning et al., 2014; K. Wang et al., 2018; Ragon et al., 2018; Halló & Gallovič, 2020; Agata et al., 2021).

## 5.2 What Does the Variability Imply?

The exact rupture extent of the Tohoku-Oki earthquake has both scientific and societal implications, particularly the extent and amplitude of potential secondary slip features in the northern and southern sections. Based on the rupture extents of historical earthquakes, the Japan subduction zone was estimated to be capable of generating earthquakes of a maximum magnitude of 8.2 prior to the Tohoku-oki earthquake (Uchida & Bürgmann, 2021). Ten of the 32 finite-fault models suggest that the Tohoku-oki earthquake ruptured into zone ZN1 in the Sanriku-Oki region, which may have hosted the large tsunamigenic 1611 M8.5 Sanriku earthquake (Kawakatsu & Seno, 1983; Imai, 2015). Rupture in ZN1 has important implications for our understanding of the recurrence pattern of large earthquakes in the region. In the southern section, contrasting frictional and material behaviors of the upper plate may act as rupture barriers and limit the rupture extent to the shallow Ibraki-Oki region (ZS1) (e.g. Bassett et al., 2016; Liu & Zhao, 2018). Subducted seamounts leading to a rough subduction interface at around 36°N may also terminate the southern rupture (K. Wang & Bilek, 2014). However, 7 out of 32 finite-fault models show extended southern extended deep rupture (ZS2), and 11 finite-fault models show extended shallow rupture in the southern section (ZS1). The varying southern deep extended rupture may also penetrate the three 1936, 1937, and 1978 M7 or above Fukushima Shioya-Oki earthquake rupture areas (Abe, 1977; Yamanaka & Kikuchi, 2004; Simons et al., 2011; Nakata et al., 2016). Given the variability and uncertainty of the finite-fault models, and a lack of certainty of the mechanics of how earthquakes arrest (e.g., Kammer et al., 2015; Galis et al., 2017), physical controls of megathrust earthquake rupture extents are yet to be confirmed in the Japan subduction zone and globally.

The scale and distribution of slip heterogeneity may reflect fault-zone heterogeneities, including in the pre-earthquake stress distribution, fault frictional properties, fault geometry and roughness, pore fluid pressure or fault zone materials (Bassett & Watts, 2015; Gallovič et al., 2019; Moore et al., 2015; Madden et al., 2022; Tinti et al., 2021; K. Wang & Bilek, 2014). The observed slip complexities in the suite of models, if true, suggest that the seismogenic zone composes of a wide range of heterogeneity with spatial scales reaching tens of kilometers. Specifically, the J models suggest highly complex slip behavior in the hypocentral and near trench regions, which would require either very high initial stress build-up, strong co-seismic weakening, or other mechanisms to sustain the nucleation and dynamic rupture propagation (e.g., Goldsby & Tullis, 2011; Di Toro et al., 2011; Viesca & Garagash, 2015). However, we show that these small features cannot be confidently confirmed by the commonly used datasets. Future physics-based dynamic rupture or seismic cycling simulations are needed to explore these features in a self-consistent way.

## 5.3 How to Better Evaluate Finite-Fault Models?

Even though the collection of models suggests a variety of slip distributions, their moment-release distributions may bear a higher resemblance with each other (Lay et al., 2011). Slip distributions are impacted by the Green's functions used in the finite-fault inversion, and there are trade-offs between the assumed velocity structure and the final slip distributions (Gallovič et al., 2015). The moment-release distribution is a composite model that includes both the slip distribution and the local velocity structures, and it is better resolved in finite-fault inversions. Lay et al. (2011) compared two contrasting slip distributions, one obtained with and the other without shallow, weak sediments (a low shear modulus layer) near the trench. The model obtained with a low shear modulus layer has a significantly larger slip near the trench, an effect confirmed in 3D megathrust dynamic rupture simulations (Sallarès & Ranero, 2019; Ulrich et al., 2022). How-

ever, the moment-release distributions of the two models are almost identical. Comparisons based on the moment-release distributions may lead to more consistent interpretations of the rupture process. However, such comparisons would require detailed documentation of not only the finite-fault models but also the associated Green's functions and near-source velocity structures.

Our investigation of both the teleseismic and regional seismic synthetics shows that the spatial complexity in the final slip distribution does not significantly impact the waveform fitting (Figures 12 and 14). However, the temporal evolution of the rupture front plays a critical role in explaining the data, and it cannot be approximated as a smooth propagation with one or two rupture speeds for the Tohoku-Oki earthquake. Specifically, we find that both regional seismic and teleseismic observations are highly sensitive to the peak-slip-rate-time distribution. We find that the peak-slip-rate-time distributions from different kinematic models agree on major slip episodes when using similar teleseismic datasets. For example, Figures S14 and S15 show that peak-slip-rate-time from models S3, S6, and J3 can explain the teleseismic observations equally well. These peak-slip-rate-time distributions can also be represented as slip-rate snapshots in kinematic finite-fault models, and Gallovič and Ampuero (2015) reported similar findings: finite-fault models developed using seismic data agree well on their spatiotemporal evolution, even when the final slip distributions are distinctively different. Additionally, regional seismic observations, particularly the vertical component of the strong motion records of the 2011 Tohoku-Oki earthquake, are also sensitive to the slip-rate functions. A simplified rupture propagation model with a single-time-window slip-rate function is insufficient to reproduce the observed strong motion waveforms.

#### 5.4 Future Opportunities

Our seafloor uplift synthetics suggest that the seafloor displacement field can resolve megathrust slip distributions at a spatial scale of 32 km. The resolution can discern detailed slip patterns, which can provide critical insights into rupture dynamics and faulting conditions. Although the offshore geodetic measurements during the Tohoku-Oki earthquake can provide the most accurate displacement measurements, their sparse distribution limits their resolutions to less than 64 km.

The Seafloor Observation Network for Earthquakes and Tsunamis along the Japan Trench (S-net) has the potential to resolve future megathrust earthquakes in great detail (Nishikawa et al., 2019). The S-net was developed after the Tohoku-Oki earthquake and it covers the entire Japan subduction zone with 150 colocated pressure gauges and accelerograms with a nominal inter-station interval between 30 and 60 km (Mochizuki et al., 2018). It is a cabled network and transmits data back to onshore in real-time. The network configuration suggests a high sensitivity to megathrust slip distributions. We conduct a synthetic analysis following the procedure outlined in Section 4.1 to compute static displacements at each S-net station. Specifically, we calculate the vertical uplift synthetics using all slip models at different scales and compare the synthetics to those from the median model at the corresponding scales. The correlation coefficients of the synthetics show the sensitivity of S-net data to variations in slip features relative to the median model.

We find that S-net can distinguish variability in the slip distributions (Figure 17). The seafloor uplift synthetics in Figure 17 show clear differences among six example models at the 16 km scale. The synthetics can directly contour slip areas with slips of 5 m or above. This resolution can accurately resolve secondary slip features that do not significantly impact the geodetic or teleseismic synthetics. The synthetics vary for the same model at different scales (e.g., Figure 17), suggesting a possible resolving ability of 16 km. This resolution results from both the dense spatial coverage and the uplift amplitude sensitivity of the instruments. Our synthetic experiment shows that large-scale, dense off-

shore networks are critical to constraining megathrust slips and mitigating the associated hazards.

We find that teleseismic data are highly sensitive to the spatiotemporal rupture process, such as the peak-slip-rate-time distribution. However, the data seems to have limited resolvability for small-scale slip features. This apparently paradoxical sensitivity is likely due to the fact that the observed teleseismic displacement P-wave waveforms are dominated by signals in the 20–30 s period band. In this case, the characteristic wavelength of the waveforms would be around 120–180 km, and such long wavelengths limit the data resolution. Therefore, higher frequency teleseismic observations may better constrain the spatial-temporal evolution of megathrust earthquakes. Specifically, velocity P-wave waveforms have higher frequency signals than displacement records, and they may potentially resolve the small-scale slip features at higher resolutions (Yagi & Fukahata, 2011b). To explore this hypothesis, we conduct a similar teleseismic validation exercise using velocity waveforms at the same set of stations (Figures S23-S24 and Text S3). We find that the synthetics do not correlate with the teleseismic velocity records as well as the displacement records, suggesting a possible higher sensitivity to variations in the finite-fault models. Similarly, we find that regional strong motion seismic records are sensitive to the earthquake rupture propagation, and exploiting these observations, particularly observations within 200 km epicentral distance may yield finite-fault models with an improved resolution.

## 6 Conclusion

We quantitatively compare and validate 32 finite-fault models of the 2011 Tohoku-Oki earthquake. We first design a reparameterization framework to unify the models using a realistic megathrust geometry while preserving potency distribution at a 1 km scale. We then downscale the models to 16, 32, and 64 km scales to compare their coherent and unique features. We find that the models agree well at the 64 km scale but do not agree on small-scale features, either regarding their locations or amplitudes. All unified models suggest that the Tohoku-Oki earthquake ruptured the updip megathrust near the hypocenter in the Miyagi-Oki region, and large slip occurred near or at the trench. This coherent feature is reflected in the median model, obtained by averaging the collection of models. We examine the sensitivity of the commonly used geodetic, teleseismic, regional seismic and geodetic, and tsunami seafloor uplift datasets to the variability in the finite-fault models. Our results suggest that geodetic, regional seismic, and teleseismic data have a spatial resolution of 64 km for the final slip distribution, while the tsunami data might have a higher sensitivity to slip features at 32 km scales. We find that both regional seismic and teleseismic observations are highly sensitive to the earthquake rupture process. However, teleseismic data are less sensitive to the slip-rate functions at each subfault. We calculate synthetic vertical uplifts at the S-net offshore in Japan, and the results suggest that the network can resolve megathrust earthquake slip distribution at a high spatial resolution of 16 km. Our results show that near-field and uniformly gridded dense offshore instrumentation networks are crucial for resolving complex earthquake rupture processes and assessing their associated hazards.

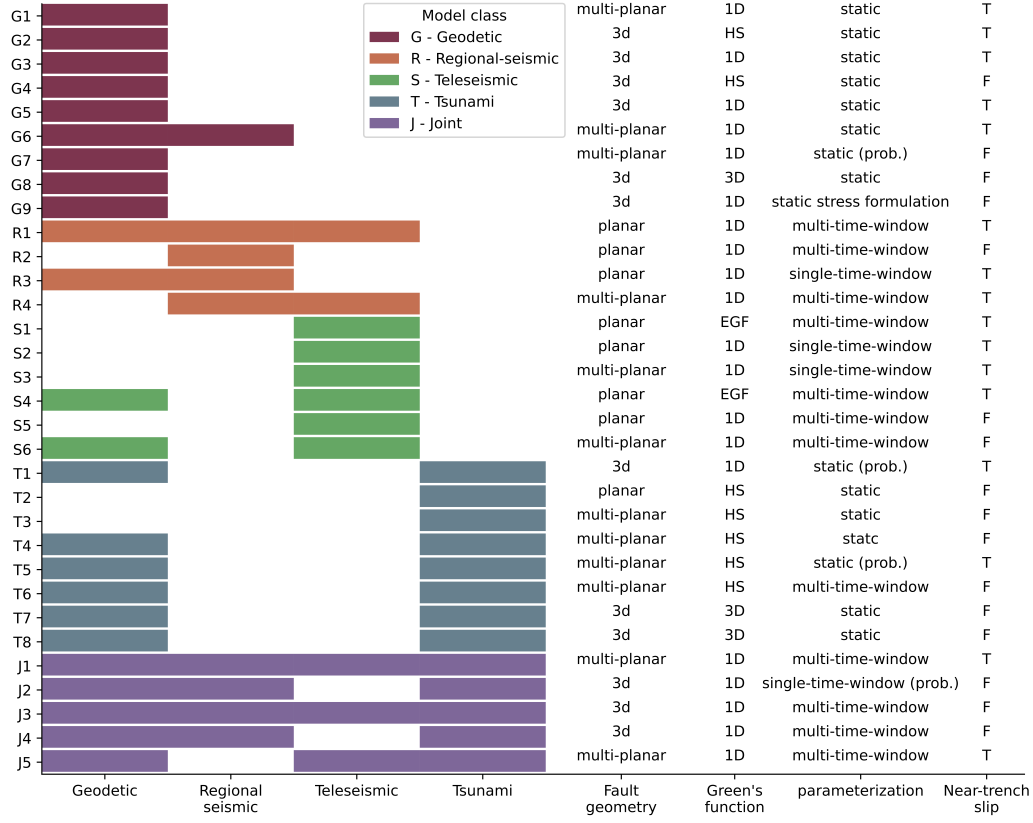


**Figure 1.** Thirty-two finite fault models used in our analysis, arranged by dataset type and publication date (see Text S1 for details). Color blocks in the left-four columns indicate datasets used to obtain each finite fault model with the color indicating the five model groups. Right-four columns describe the fault geometry, Green's function (HS: halfspace model, 1D: one-dimensional velocity model, 3D: three-dimensional velocity model, EGF: empirical Green's function), parameterization used and near-trench slip features (T: tapered slip, F: free slip to trench) of each finite fault model, respectively.



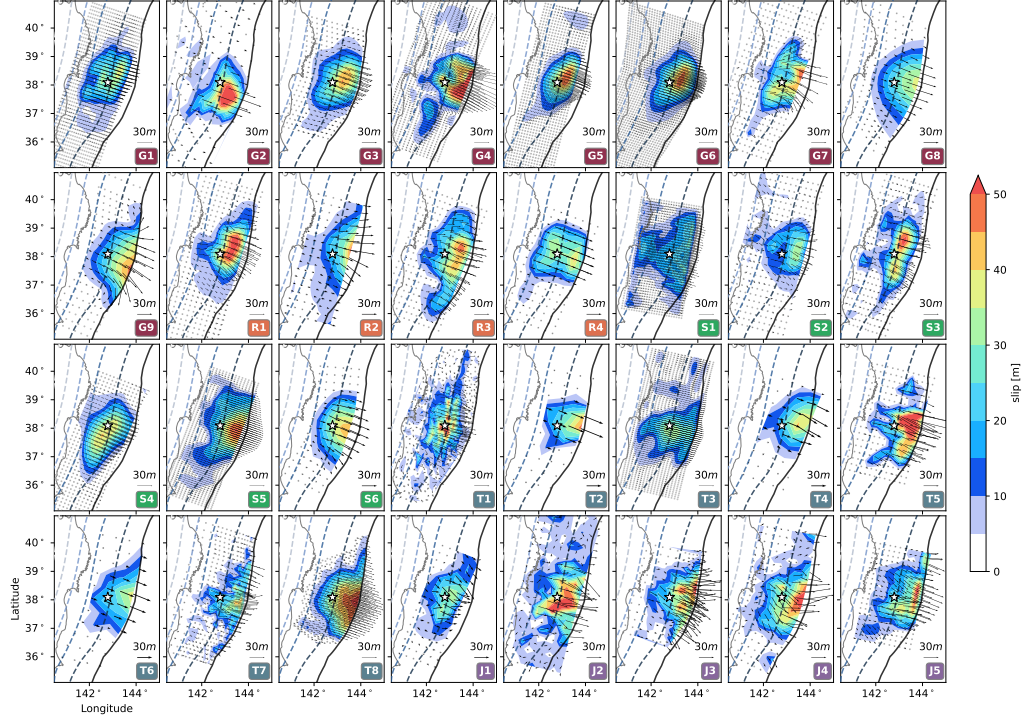


**Figure 2.** Slip distributions of the 32 finite fault models. Slip distributions and slip directions are shown as color contours and vectors, respectively. Grey dots indicate the centers of each model’s subfaults. USGS hypocenter location is shown as a white star. Slab2.0 megathrust geometry from Hayes et al. (2018) is shown as dotted contours with a 20 km depth interval. Japan trench is shown as a black solid line and the Japanese coastline is shown as a grey solid line. All model acronyms are defined in Figure 1 and detailed in Text S1.

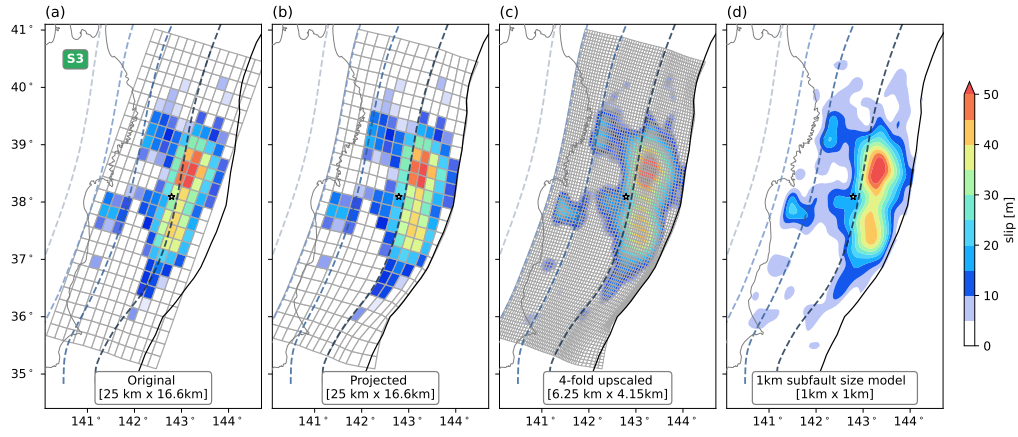


**Figure 3.** Illustration of the upscaling and projection scheme for an exemplary finite-fault model, S3. (a) Original slip distribution and subfault parameterization of the planar fault geometry. (b) Projected model using the slab 2.0 megathrust geometry. (c) Up-scaled slip distribution with densified subfault along dip and along strike four times respectively. (d) Final projected and up-scaled slip distribution at a 1 km spatial scale. Numbers on the legend indicate the subfault size.

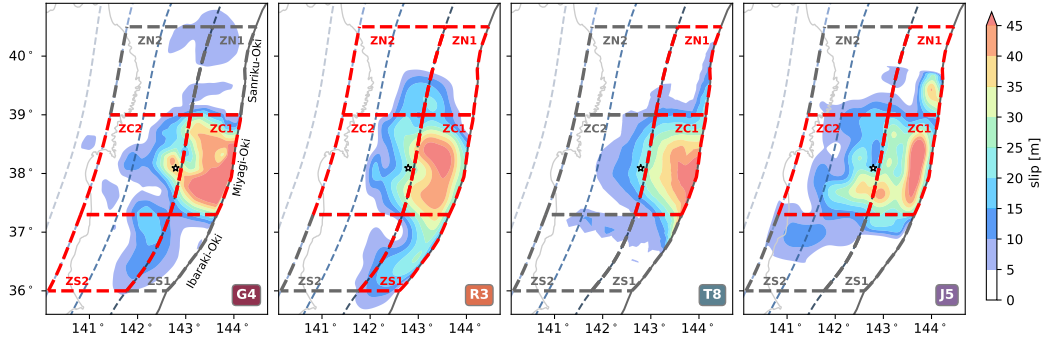


**Figure 4.** Division of the Japan megathrust into six zones and zone categorizations of four example finite-fault models. Zones with  $\geq 10$  m slip features are highlighted using red dashed contours. Table 1 summarizes the models with respect to their major slip features in each associated zone.

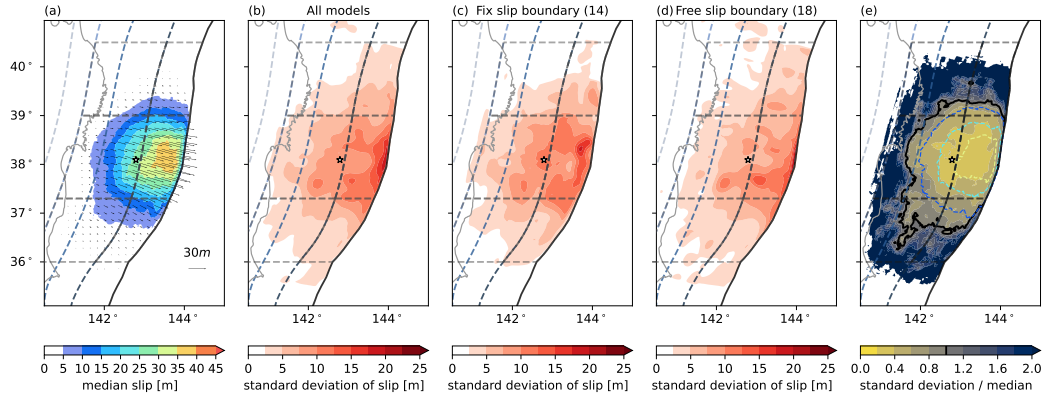


**Figure 5.** Median and standard deviations of the 32 finite-fault models. (a) Median model slip distribution at 1 km spatial scale. (b) Standard deviation of slip distribution for all models. (c) Standard deviation of slip distribution for models with tapered slip towards the trench. (d) Standard deviation of slip distribution for models with a free-slip boundary condition at the trench. Number of models included in the groups are shown in subtitle parentheses. (e) Standard deviation over median of the slip distributions. Solid black line delineates the region below 1. Colored dotted lines indicate a 10m contour of the median slip distribution. Artifacts in the standard deviation distributions are due to the original coarse fault parameterization of the finite-fault models. Grey dotted lines indicate the zones listed in Figure 4. Similar averaging finite-fault models approach are also applied in K. Wang et al. (2018) .

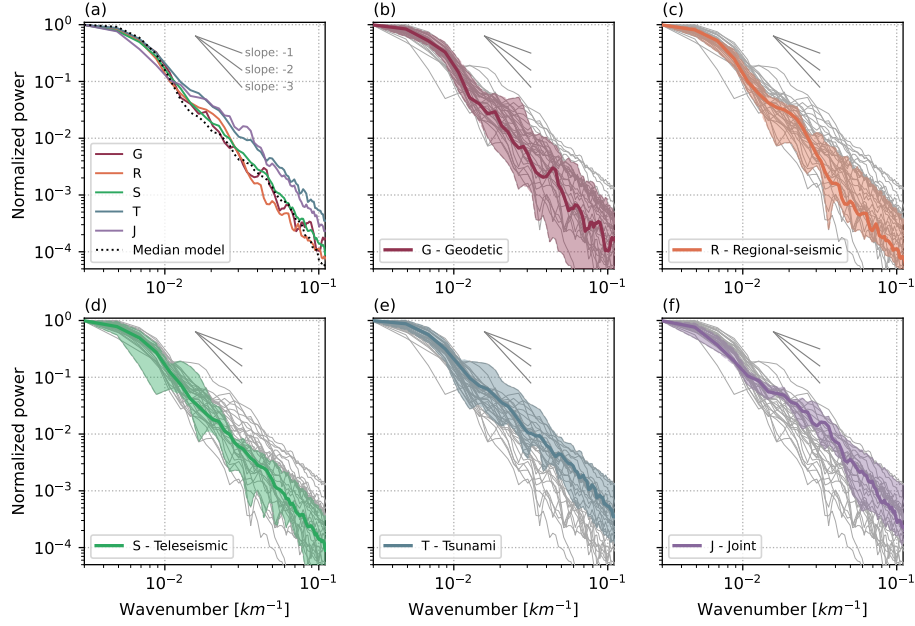


**Figure 6.** Normalized wavenumber ( $k$ ) power spectra of the 32 finite-fault models and the median model. (a) Color solid lines are the respective median spectra of each five model groups and the grey dotted line is the spectrum of the median model (Figure 5). Power spectra of the (b) geodetic group, (c) regional seismic group, (d) teleseismic group, (e) tsunami group and (f) joint-inversion group. Color-shaded areas are the range of the minimum and maximum respective spectra of the models in each group. Solid colored line is the median spectra of each model group. Grey lines represent the spectra of all 33 slip models. Decay rates of the models range from -2.0 to -4.0, with -3.0 for the geodetic group median, -3.0 for the regional-seismic group median, -2.8 for the teleseismic group median, -2.3 for the tsunami group median, and -2.1 for the joint-inversion group median.

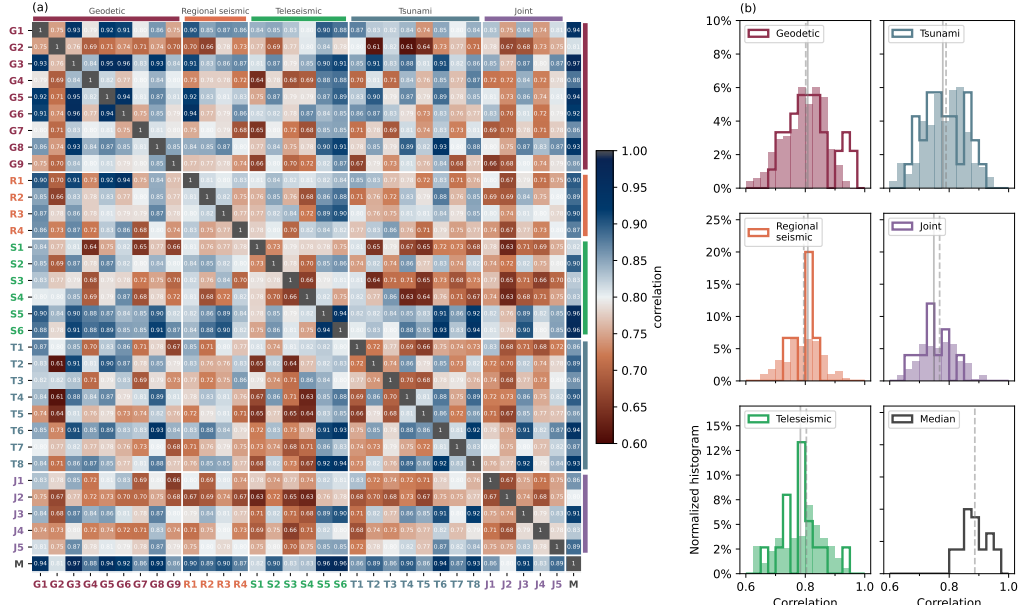


**Figure 7.** Correlation coefficients for finite-fault models at a 1 km scale. (a) Correlation coefficients matrix of the 32 finite-fault models and the median model, with each entry representing the correlation coefficient between two respective models. Background color of each entry indicates the correlation coefficient value. Matrix rows follow the same sorting order as in Figure 1 with the last row added+ for the median model (M). (b) Correlation coefficient histograms of the five model groups and the median model: solid lines show the correlation coefficient distribution of models within the group; filled histograms show the correlation coefficient distribution of models with other model groups. Light grey solid lines indicate the median value of the correlation coefficients within the respective group and dashed grey lines indicate the median value of the correlation coefficients with other model groups. Median model histogram shows its correlation with the 32 finite-fault models. Median values of the correlation coefficients within the groups: Geodetic (G), 0.81; Regional seismic (R), 0.81; Teleseismic (S), 0.78; Tsunami (T), 0.78; Joint (J): 0.75. Median value of the correlation coefficients with the median model is 0.89.



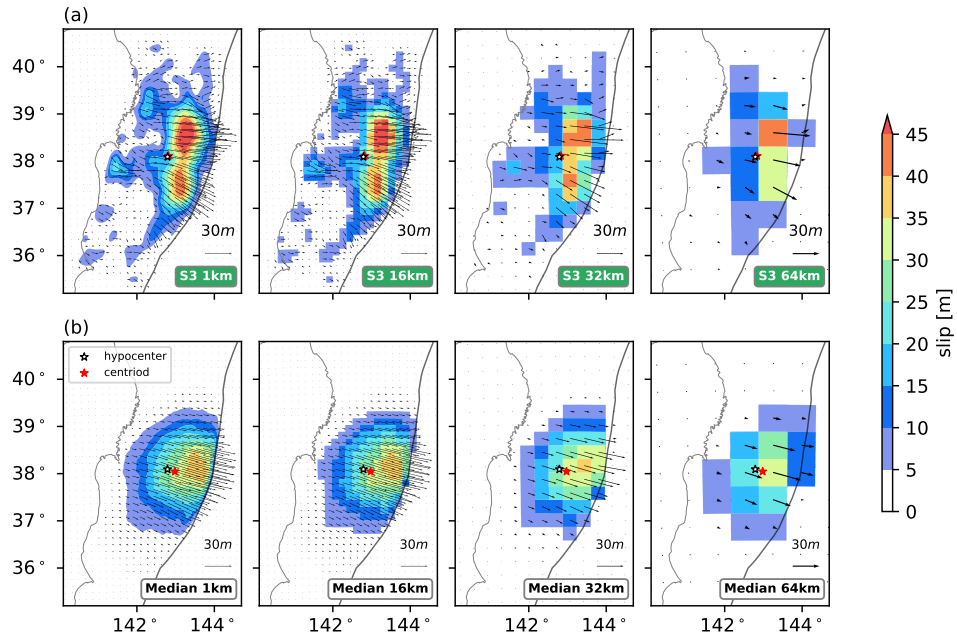


**Figure 8.** Example slip models at the 1, 16, 32, and 64 km spatial scales. (a) Model S3 at the four spatial scales. (b) Median model at the four spatial scales. Models at larger spatial scales lose fine-scale features, but the centroid locations are preserved. Hypocenter and centroid locations are indicated as white and red stars, respectively.

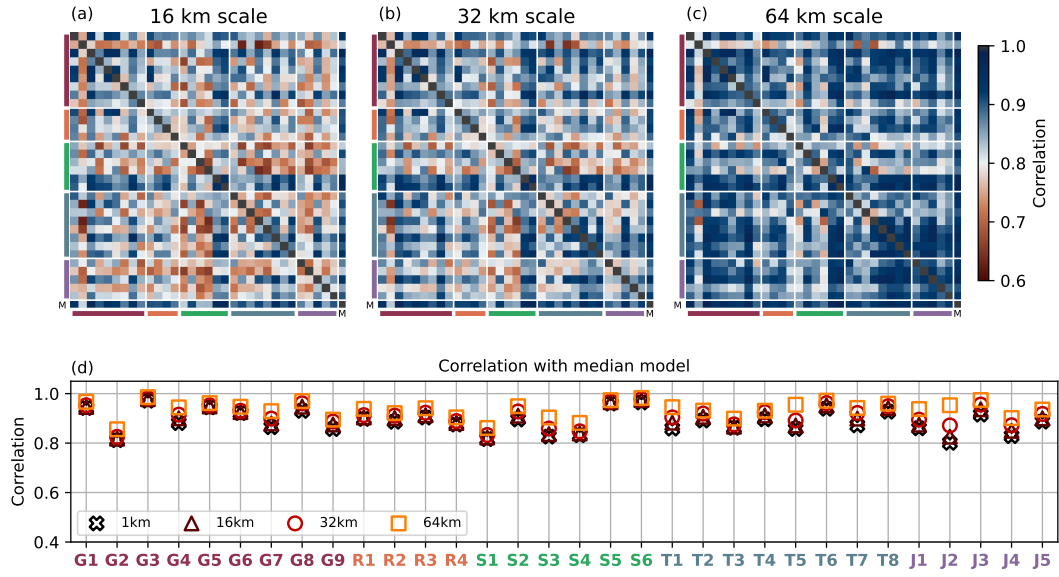


**Figure 9.** Correlation coefficients of models at the (a) 16, (b) 32, and (c) 64 km scales. Legends are similar to that in Figure 7. (d) Correlation coefficients of the 32 models with the median model at the 1, 16, 32, and 64 km scales. Median and standard deviation of models at the 16, 32, and 64 km scales are 0.81 and 0.07, 0.84 and 0.06, and 0.89 and 0.05, respectively.

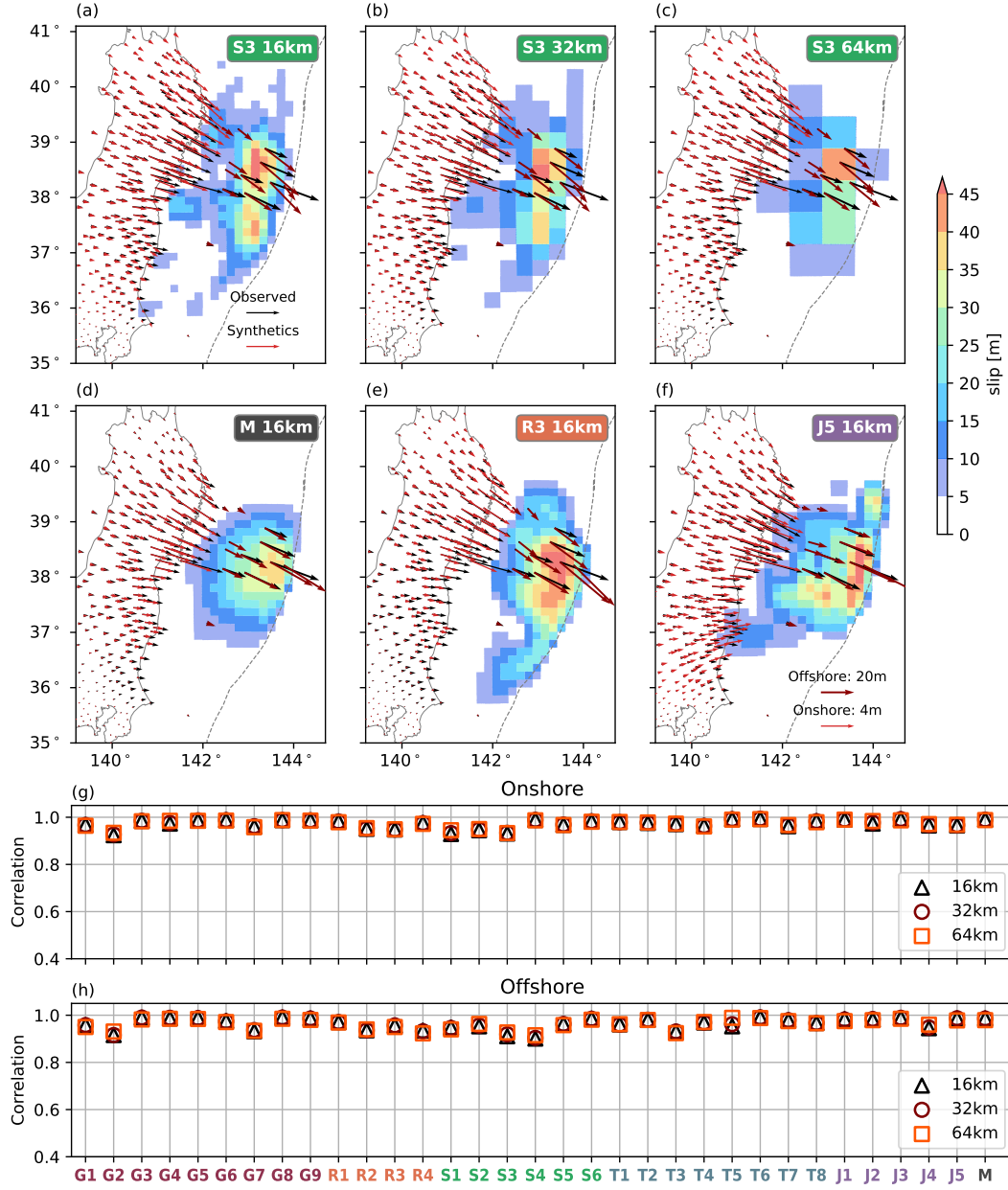


**Figure 10.** Onshore and offshore horizontal geodetic displacement observations (black arrows) and synthetics (red arrows), and their correlation coefficient values. (a)–(c) synthetic (black) and observed (red) horizontal geodetic displacements of model S3 at the 16 (a), 32 (b), and 64 km (c) scales. (d)–(f) Geodetic synthetics and observations of model M (d), R3 (e), J5 (f) at the 16 km scale. (g) Correlation coefficient values between the onshore geodetic synthetics and observations at the 16, 32, and 64 km scales. (h) Correlation coefficient values between the offshore geodetic synthetics and observations at the 16, 32, and 64 km scales.

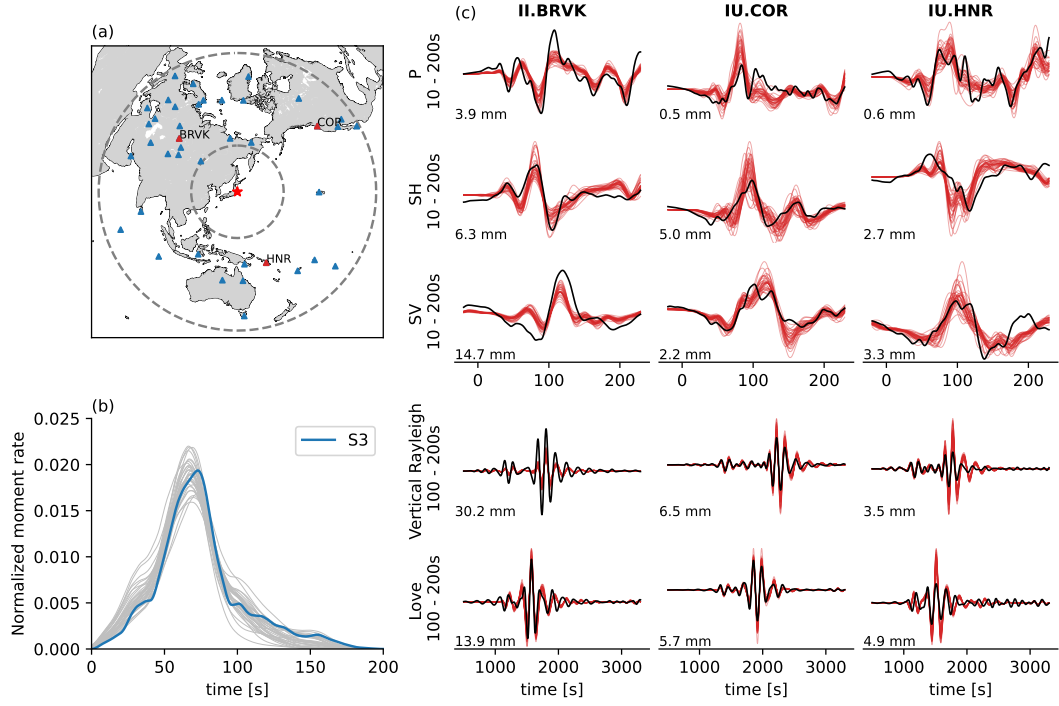


**Figure 11.** Comparison of teleseismic observations and synthetics at 16 km slip model scale. (a) Map view of 40 II and IU stations used in the analysis. Red triangles are the stations in (c). Dotted circles show epicentral distances of 30° and 90°, respectively. (b) Normalized moment rate functions of the original S3 model (blue), the 32 unified finite-fault models, and median model (grey). (c) Synthetic and observed teleseismic waveforms. Black lines are the observed waveforms; red lines are the synthetic waveforms from the 32 finite-fault models and the median model. Five rows are P wave, SH wave, SV wave, Rayleigh wave, and Love wave, respectively. Amplitudes of the observed waveforms are labeled at the lower-left corner of each waveform plot.

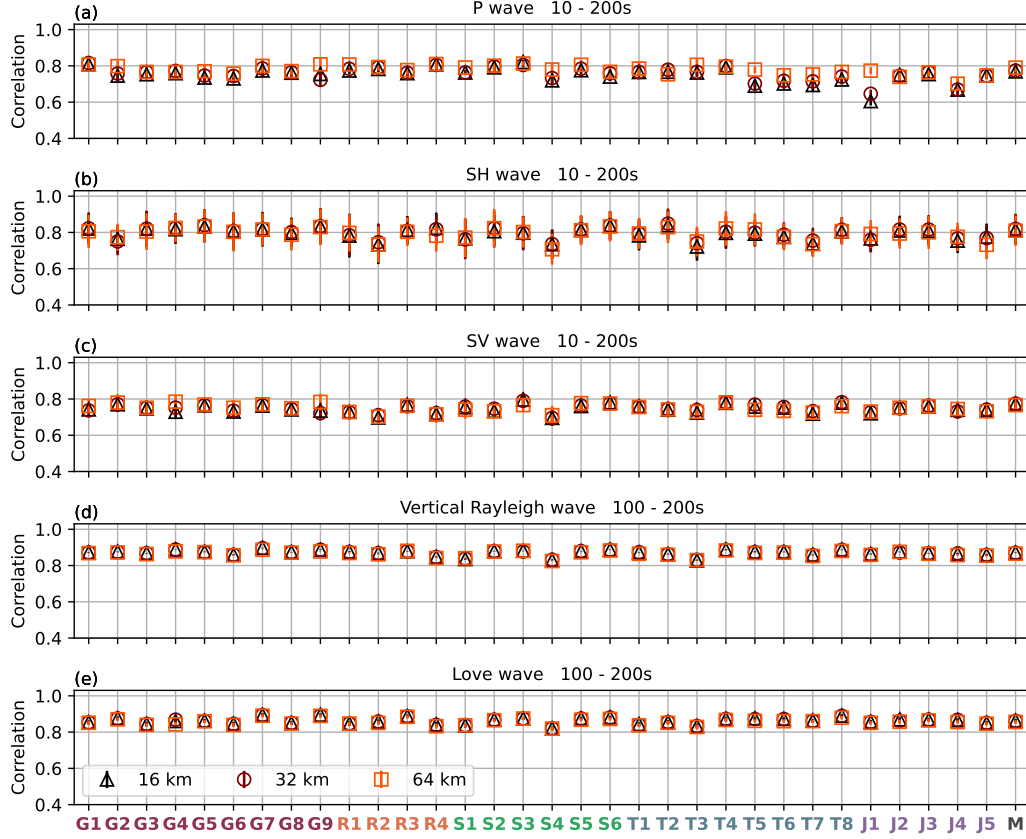


**Figure 12.** Correlation coefficient values between the teleseismic observations and synthetics at the 16, 32, and 64 km scales. (a) P wave. (b) SH wave. (c) SV wave. (d) Rayleigh wave. (e) Love wave. Median correlation values between the synthetic and observed teleseismic waveforms at the 40 teleseismic stations are taken as the characteristic correlation coefficient values for each model. Three markers indicate the characteristic median values for models at the 16, 32, and 64 km scales. Error bars represent the associated standard deviation of correlation coefficient values of the 40 stations.

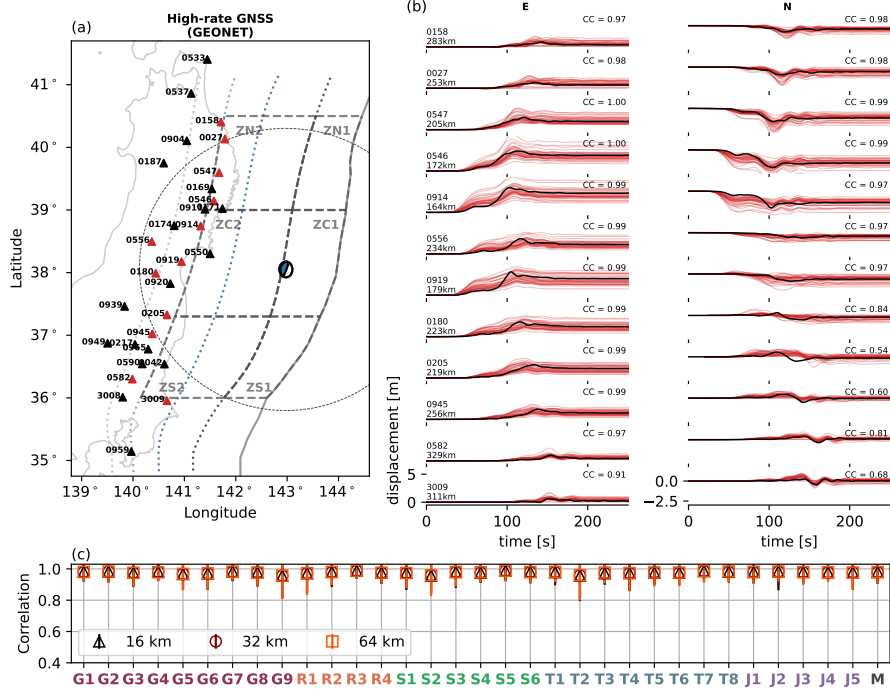


**Figure 13.** Comparison of high-rate GNSS observations and synthetics at 16 km slip model scale. (a) Map view of the GEONET stations used in the study. Red triangles are the stations in (b). Beach-ball focal mechanism represents the centroid location of the median model. Dotted circles show the centroid distance of 250 km (b) Synthetics and observed waveforms. Black lines are the observed waveforms; Red lines are the synthetics from the 32 finite-fault models and the median model at the 16 km scale. (c) Correlation coefficient values between the observations and synthetics at the 16, 32, and 64 km scale. Markers indicate the median correlation values of all stations, with an error bar indicating the associated standard deviation.



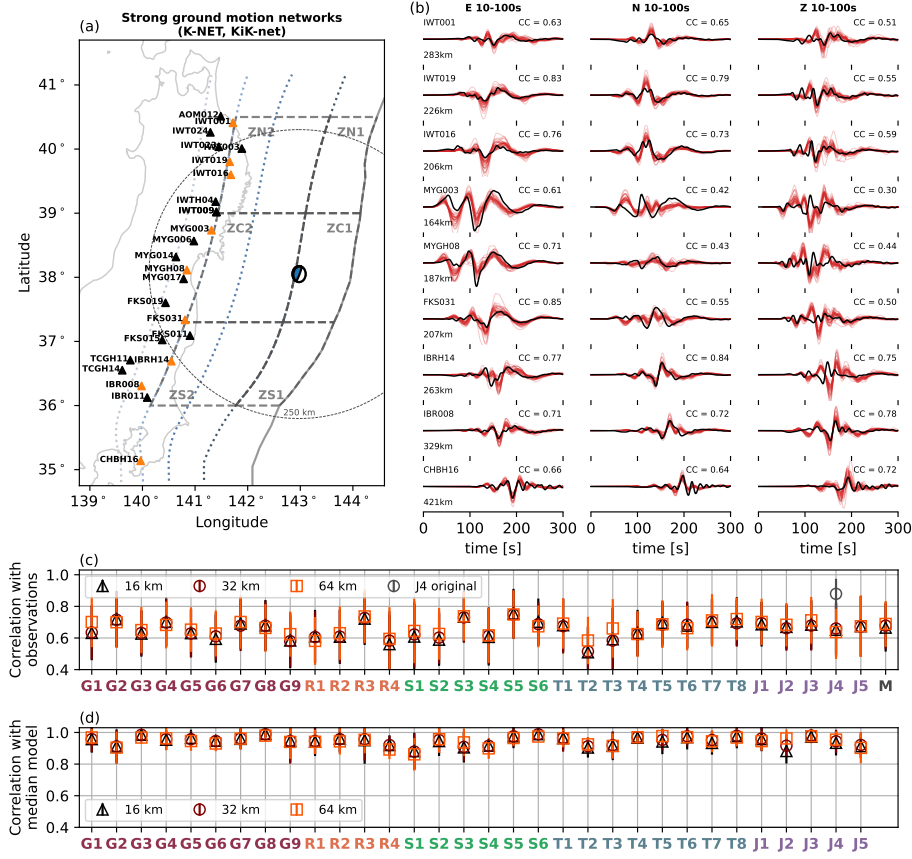


**Figure 14.** Comparison of regional strong-ground motion records (displacement) with synthetics at 16 km slip model scale. (a) Map view of the strong-ground motion stations used in the study. Red triangles are the stations in (b). The beachball focal mechanism represents the centroid location of the median model. Dotted circles show the centroid distance of 250 km (b) Synthetics and observed waveforms. Black lines are the observed waveforms; Red lines are the synthetics from the 32 finite-fault models and the median model at 16 km scale. (c) Correlation coefficient between the observations and synthetics at the 16, 32, and 64 km scale. (d) Correlation coefficients between the median synthetics and all models at 16, 32 and 64 km scale. Markers indicate the median correlation values of all stations, with an error bar indicating the associated standard deviation.

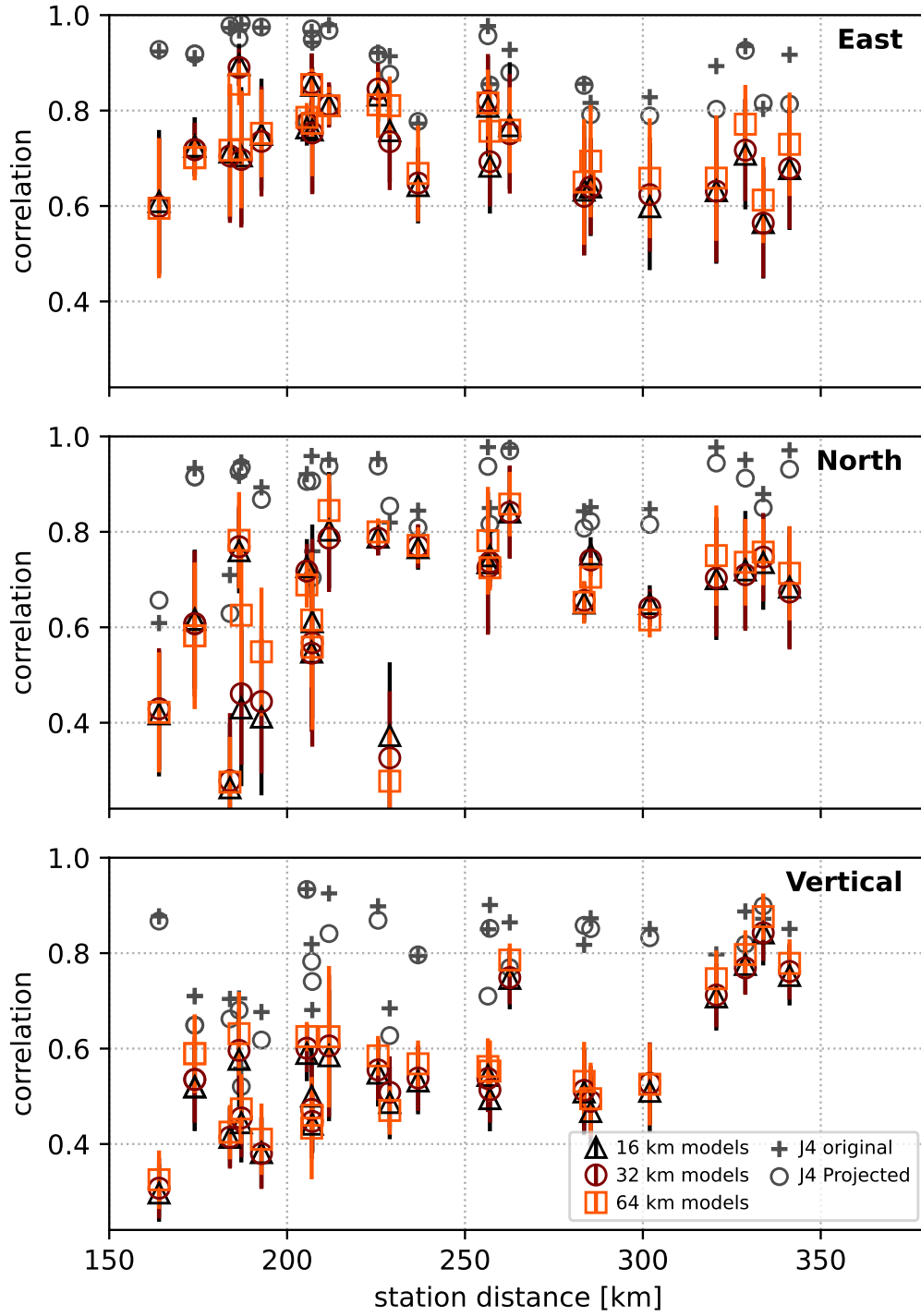


**Figure 15.** Strong ground motion synthetics correlation with respect to station distance. Synthetics correlation at (a) East component, (b) north component, and (c) vertical component. Colored error bars represent the median value and standard deviation of the correlation coefficient of all 33 model synthetics at each station. Cross and circle grey scatters are the correlation coefficients of the J4 model original synthetics and projected geometry synthetics.

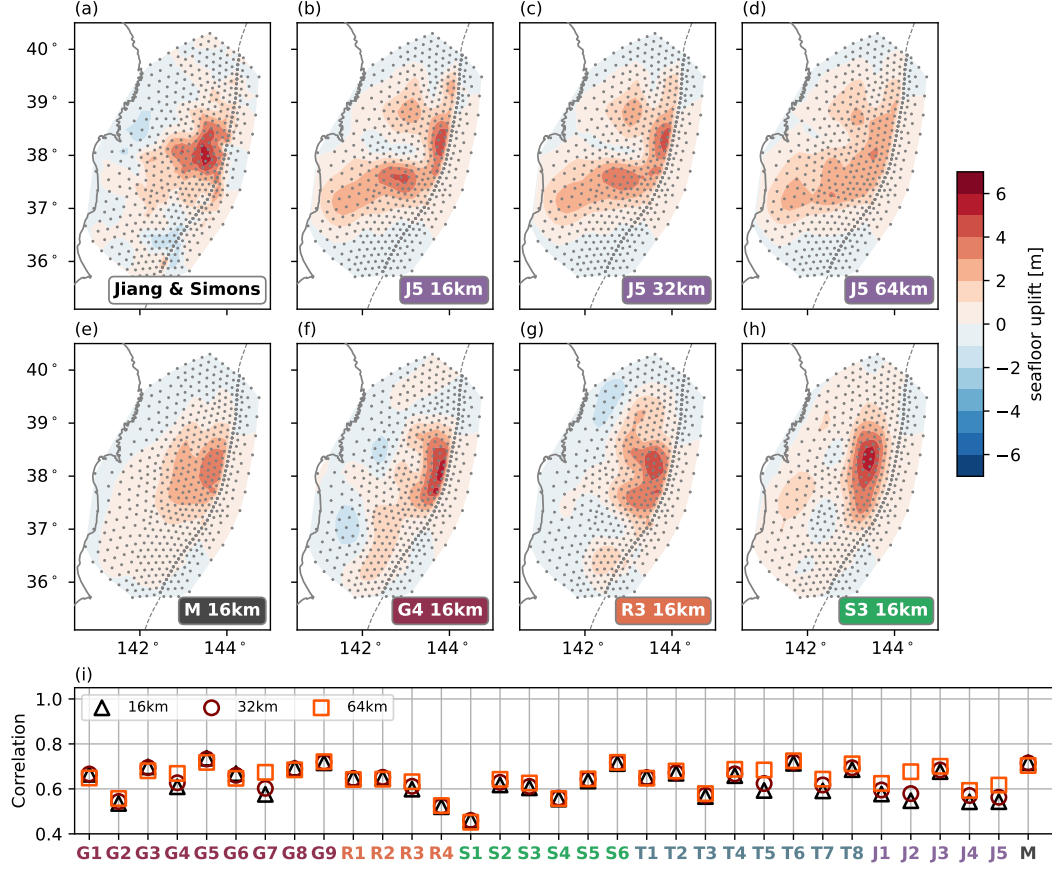


**Figure 16.** Seafloor uplift model of Jiang and Simons (2016) (model SJS), seafloor uplift synthetics from the finite-fault models, and their correlation coefficient values between the synthetics with model SJS. Grey dots show the modeled grid points. (a) Model SJS. (b)–(d) Synthetic seafloor uplift of model J5 model at the 16 (b), 32 (c), and 64 km (d) scales, respectively. (e)–(h) Synthetic seafloor uplift of the median slip model, models G5, R4, and S3 at a 16 km scale. (i) Correlation coefficient values between model SJS and synthetics of the 32 finite-fault models and the median model at the 16, 32, and 64 km scales.

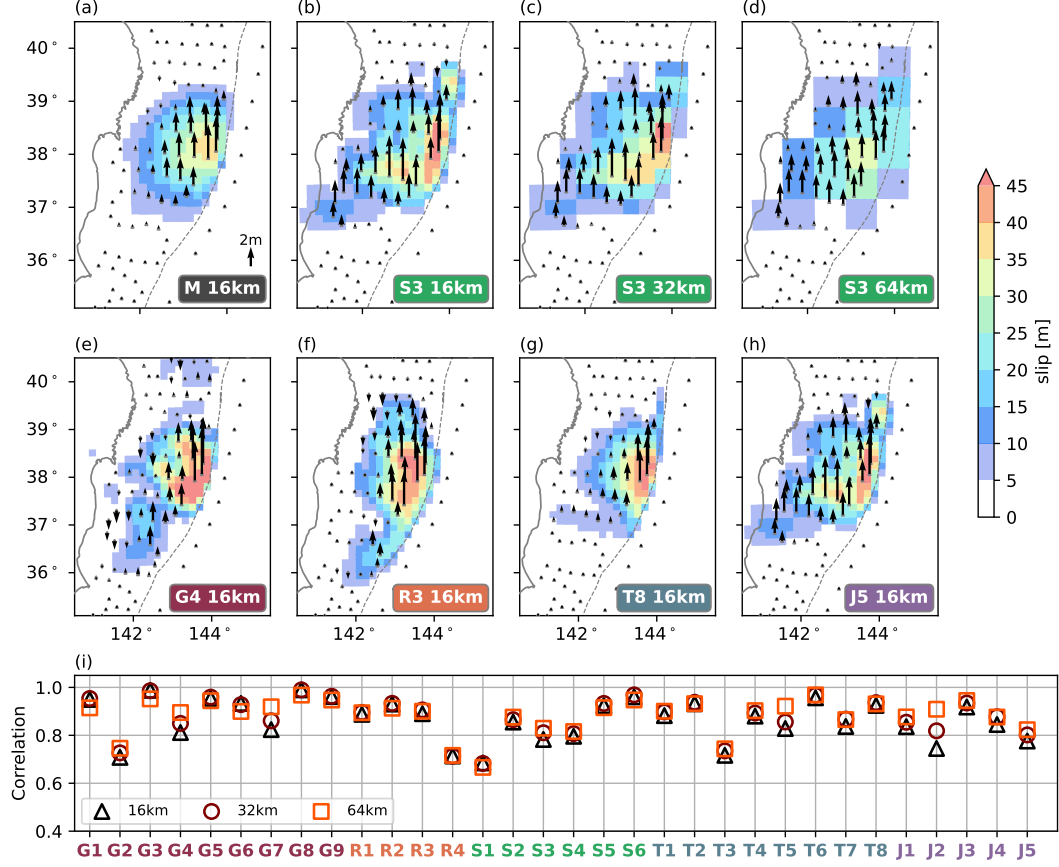


**Figure 17.** S-net seafloor uplift synthetics and their correlation coefficient values with the synthetics of the median model. S-net stations are shown as grey dots (Mochizuki et al., 2018). (a) Synthetic coseismic seafloor uplifts of the median slip model at the 16 km scale. (b)–(d) Synthetics seafloor uplifts of model S3 at the 16, 32, and 64 km scales. (e)–(h) Synthetics seafloor uplifts of models G5, R4, T8, and S3 at the 16 km scale. (i) Correlation coefficient values between synthetics of the median model and the 32 finite-fault models at the 16, 32, and 64 km scales.

**Table 1.** Finite-fault model features in rupture zones

Zone (counts)	Models
ZN1: Sanriku - shallow (10)	R1, R2, R3, T5, T6, T8, J1, J2, J4, J5
ZN2: Sanriku - deep (4)	G7, R4, S3, T1
ZC1: Miyagi - shallow (32)	All models
ZC2: Miyagi - deep (26)	G1, G2, G4, G6, G7, R1, R3, R4, S1, S2, S3, S4, S5, S6, T1, T2, T3, T5, T6, T7, T8, J1, J2, J3, J4, J5
ZS1: Ibaraki-Fukushima - shallow (11)	G9, R1, R3, S3, T1, T5, T7, T8, J2, J3, J4
ZS2: Ibaraki-Fukushima - deep (7)	G4, R5, S2, S4, T1, T5, J2

## 7 Open Research

The 32 finite-fault models are retrieved from a subset of Sun et al. (2017) collected models, the SRCMOD database (Mai & Thingbaijam, 2014), online datasets shared with referenced papers, and from authors sharing them directly. The GEONET GNSS data was provided by the Geospatial Information Authority (GSI) (Sagiya, 2004). We compared the teleseismic synthetics with the teleseismic data obtained from the Federation of Digital Seismic Networks (FDSN) through the Incorporated Research Institutions for Seismology (IRIS). Figures are generated with the python Matplotlib package (Hunter, 2007). We use SimModeler of the Simmetrix Simulation Modeling Suite to create the geometry of the slab interface. We use Python throughout the analysis (Van Rossum & Drake Jr, 1995). The median slip model is shared as Data Set S1.

The Green’s function library for subduction zones are provided by Hori et al. (2021), which was created by JAMSTEC’s own modification of a computer program under development by Earthquake Research Institute, The University of Tokyo. The library includes data modified from Japan Integrated Velocity Structure Model version 1 (JIVSM) (Koketsu et al., 2009, 2012) and the Earth Gravitational Model 2008 (Pavlis et al., 2012).

## Acknowledgments

We thank Editor Satoshi Ide, the Associate Editor, Kelin Wang, and an anonymous reviewer for helpful comments. We thank Tianhaozhe Sun, Shiann-Jong Lee, Quentin Bletery, Akinori Hashima, and Thorsten Becker for sharing their Tohoku-Oki earthquake finite-fault models and Yuji Yagi and Ryo Okuwaki for insightful discussions. We thank Dorian Golriz and Yehuda Bock for sharing the processed GEONET data. The project was supported by NSF grants EAR-2143413 and EAR-2121568. AAG acknowledges additional support from NASA (grant No. 80NSSC20K0495), NSF (grants EAR-2225286, OAC-2139536, OAC-2311208), the European Union’s Horizon 2020 Research and Innovation Programme (grant No. 852992), Horizon Europe (grant No. 101093038, 101058129, and 101058518) and the Southern California Earthquake Center (SCEC awards 22135, 23121). Computing resources were provided by the Institute of Geophysics of LMU Munich (Oeser et al., 2006).

## References

- Abe, K. (1977). Tectonic implications of the large shioya-Oki earthquakes of 1938. *Tectonophysics*, 41(4), 269–289.
- Agata, R., Kasahara, A., & Yagi, Y. (2021). A bayesian inference framework for fault slip distributions based on ensemble modelling of the uncertainty of underground structure: with a focus on uncertain fault dip. *Geophysical Journal International*, 225(2), 1392–1411.

- Ammon, C. J., Ji, C., Thio, H.-K., Robinson, D., Ni, S., Hjorleifsdottir, V., . . . others (2005). Rupture process of the 2004 sumatra-andaman earthquake. *science*, 308(5725), 1133–1139.
- Ammon, C. J., Lay, T., Kanamori, H., & Cleveland, M. (2011). A rupture model of the 2011 off the Pacific coast of Tohoku earthquake. *Earth, Planets and Space*, 63(7), 693–696.
- Asano, K., & Iwata, T. (2016). Source rupture processes of the foreshock and mainshock in the 2016 Kumamoto earthquake sequence estimated from the kinematic waveform inversion of strong motion data. *Earth, Planets and Space*, 68(1), 1–11.
- Bassett, D., Sandwell, D. T., Fialko, Y., & Watts, A. B. (2016). Upper-plate controls on co-seismic slip in the 2011 magnitude 9.0 Tohoku-Oki earthquake. *Nature*, 531(7592), 92–96.
- Bassett, D., & Watts, A. B. (2015). Gravity anomalies, crustal structure, and seismicity at subduction zones: 1. seafloor roughness and subducting relief. *Geochemistry, Geophysics, Geosystems*, 16(5), 1508–1540.
- Beresnev, I. A. (2003). Uncertainties in finite-fault slip inversions: to what extent to believe?(a critical review). *Bulletin of the Seismological Society of America*, 93(6), 2445–2458.
- Biemiller, J., Gabriel, A.-A., & Ulrich, T. (2023). Dueling dynamics of low-angle normal fault rupture with splay faulting and off-fault damage. *Nature Communications*, 14(1), 2352.
- Bletery, Q., Sladen, A., Delouis, B., & Mattéo, L. (2015). Quantification of tsunami bathymetry effect on finite fault slip inversion. *Pure and Applied Geophysics*, 172, 3655–3670.
- Bletery, Q., Sladen, A., Delouis, B., Vallée, M., Nocquet, J.-M., Rolland, L., & Jiang, J. (2014). A detailed source model for the  $M_w$  9.0 Tohoku-Oki earthquake reconciling geodesy, seismology, and tsunami records. *Journal of Geophysical Research: Solid Earth*, 119(10), 7636–7653.
- Brown, L., Wang, K., & Sun, T. (2015). Static stress drop in the  $M_w$  9 Tohoku-Oki earthquake: Heterogeneous distribution and low average value. *Geophysical Research Letters*, 42(24), 10–595.
- Daubechies, I. (1990). The wavelet transform, time-frequency localization and signal analysis. *IEEE transactions on information theory*, 36(5), 961–1005.
- Dettmer, J., Hawkins, R., Cummins, P. R., Hossen, J., Sambridge, M., Hino, R., & Inazu, D. (2016). Tsunami source uncertainty estimation: The 2011 Japan tsunami. *Journal of Geophysical Research: Solid Earth*, 121(6), 4483–4505.
- Diao, F., Xiong, X., & Zheng, Y. (2012). Static slip model of the m w 9.0 Tohoku (Japan) earthquake: Results from joint inversion of terrestrial GPS data and seafloor GPS/acoustic data. *Chinese Science Bulletin*, 57, 1990–1997.
- Di Toro, G., Han, R., Hirose, T., De Paola, N., Nielsen, S., Mizoguchi, K., . . . Shimamoto, T. (2011). Fault lubrication during earthquakes. *Nature*, 471(7339), 494–498.
- Du, Y., Ma, S., Kubota, T., & Saito, T. (2021). Impulsive tsunami and large runup along the sanriku coast of Japan produced by an inelastic wedge deformation model. *Journal of Geophysical Research: Solid Earth*, 126(8), e2021JB022098.
- Dziewonski, A. M., & Anderson, D. L. (1981). Preliminary reference earth model. *Physics of the earth and planetary interiors*, 25(4), 297–356.
- Fan, W., Shearer, P. M., & Gerstoft, P. (2014). Kinematic earthquake rupture inversion in the frequency domain. *Geophysical Journal International*, 199(2), 1138–1160.
- Fujii, Y., Satake, K., Sakai, S., Shinohara, M., & Kanazawa, T. (2011). Tsunami source of the 2011 off the Pacific coast of Tohoku earthquake. *Earth, planets and space*, 63(7), 815–820.
- Fujiwara, T., Kodaira, S., No, T., Kaiho, Y., Takahashi, N., & Kaneda, Y. (2011).



- The 2011 Tohoku-Oki earthquake: Displacement reaching the trench axis. *Science*, 334(6060), 1240–1240.
- Funning, G. J., Fukahata, Y., Yagi, Y., & Parsons, B. (2014). A method for the joint inversion of geodetic and seismic waveform data using abic: application to the 1997 manyi, tibet, earthquake. *Geophysical Journal International*, 196(3), 1564–1579.
- Galis, M., Ampuero, J. P., Mai, P. M., & Cappa, F. (2017). Induced seismicity provides insight into why earthquake ruptures stop. *Science advances*, 3(12), eaap7528.
- Gallovič, F., & Ampuero, J.-P. (2015). A new strategy to compare inverted rupture models exploiting the eigenstructure of the inverse problem. *Seismological Research Letters*, 86(6), 1679–1689.
- Gallovič, F., Imperatori, W., & Mai, P. M. (2015). Effects of three-dimensional crustal structure and smoothing constraint on earthquake slip inversions: Case study of the  $M_w$ 6.3 2009 L’Aquila earthquake. *Journal of Geophysical Research: Solid Earth*, 120(1), 428–449.
- Gallovič, F., Valentová, L., Ampuero, J.-P., & Gabriel, A.-A. (2019). Bayesian dynamic finite-fault inversion: 2. application to the 2016  $M_w$  6.2 amatrice, italy, earthquake. *Journal of Geophysical Research: Solid Earth*, 124(7), 6970–6988.
- Galvez, P., Dalguer, L. A., Ampuero, J.-P., & Giardini, D. (2016). Rupture reactivation during the 2011 m w 9.0 Tohoku earthquake: Dynamic rupture and ground-motion simulations. *Bulletin of the Seismological Society of America*, 106(3), 819–831.
- Galvez, P., Petukhin, A., Irikura, K., & Somerville, P. (2020). Dynamic source model for the 2011 Tohoku earthquake in a wide period range combining slip reactivation with the short-period ground motion generation process. *Pure and Applied Geophysics*, 177, 2143–2161.
- GEBCO. (2023). *Gebco 2023 grid* [dataset]. doi: 10.5285/f98b053b-0cbc-6c23-e053-6c86abc0af7b
- Goda, K., Mai, P. M., Yasuda, T., & Mori, N. (2014). Sensitivity of tsunami wave profiles and inundation simulations to earthquake slip and fault geometry for the 2011 Tohoku earthquake. *Earth, Planets and Space*, 66, 1–20.
- Goldberg, D., Barnhart, W., & Crowell, B. (2022). Regional and teleseismic observations for finite-fault product. *US Geol. Surv. Data Release*.
- Goldsby, D. L., & Tullis, T. E. (2011). Flash heating leads to low frictional strength of crustal rocks at earthquake slip rates. *Science*, 334(6053), 216–218.
- Gusman, A. R., Tanioka, Y., Sakai, S., & Tsushima, H. (2012). Source model of the great 2011 Tohoku earthquake estimated from tsunami waveforms and crustal deformation data. *Earth and Planetary Science Letters*, 341, 234–242.
- Halló, M., & Gallovič, F. (2020). Bayesian self-adapting fault slip inversion with green’s functions uncertainty and application on the 2016 mw7. 1 kumamoto earthquake. *Journal of Geophysical Research: Solid Earth*, 125(3), e2019JB018703.
- Hartzell, S. H., & Heaton, T. H. (1983). Inversion of strong ground motion and teleseismic waveform data for the fault rupture history of the 1979 Imperial Valley, California, earthquake. *Bulletin of the Seismological Society of America*, 73(6A), 1553–1583.
- Hashima, A., Becker, T. W., Freed, A. M., Sato, H., & Okaya, D. A. (2016). Co-seismic deformation due to the 2011 Tohoku-Oki earthquake: influence of 3-D elastic structure around Japan. *Earth, Planets and Space*, 68(1), 1–15.
- Hashimoto, C., Noda, A., & Matsuura, M. (2012). The m w 9.0 northeast Japan earthquake: total rupture of a basement asperity. *Geophysical Journal International*, 189(1), 1–5.
- Hayes, G. P. (2011, 09). Rapid source characterization of the 2011  $M_w$  9.0 off the Pacific coast of Tohoku earthquake. *Earth, Planets and Space*, 63(7), 529–534.

- Hayes, G. P., Moore, G. L., Portner, D. E., Hearne, M., Flamme, H., Furtney, M., & Smoczyk, G. M. (2018). Slab2, a comprehensive subduction zone geometry model. *Science*, *362*(6410), 58–61.
- Hino, R., Ito, Y., Suzuki, K., Suzuki, S., Inazu, D., Inuma, T., ... Kaneda, Y. (2011). Foreshocks and mainshock of the 2011 Tohoku earthquake observed by ocean bottom seismic/geodetic monitoring. In *AGU Fall Meeting Abstracts*.
- Hooper, A., Pietrzak, J., Simons, W., Cui, H., Riva, R., Naeije, M., ... Socquet, A. (2013). Importance of horizontal seafloor motion on tsunami height for the 2011  $M_w=9.0$  Tohoku-Oki earthquake. *Earth and Planetary Science Letters*, *361*, 469–479.
- Hori, T., Agata, R., Ichimura, T., Fujita, K., Yamaguchi, T., & Inuma, T. (2021). High-fidelity elastic green's functions for subduction zone models consistent with the global standard geodetic reference system. *Earth, Planets and Space*, *73*.
- Hossen, M. J., Cummins, P. R., Dettmer, J., & Baba, T. (2015). Tsunami waveform inversion for sea surface displacement following the 2011 Tohoku earthquake: Importance of dispersion and source kinematics. *Journal of Geophysical Research: Solid Earth*, *120*(9), 6452–6473.
- Hunter, J. D. (2007). Matplotlib: A 2d graphics environment. *Computing in Science & Engineering*, *9*(3), 90–95. doi: 10.1109/MCSE.2007.55
- Ide, S. (2007). Slip inversion. *Earthquake seismology*, *4*, 193–223.
- Ide, S., Baltay, A., & Beroza, G. C. (2011). Shallow dynamic overshoot and energetic deep rupture in the 2011  $M_w$  9.0 Tohoku-Oki earthquake. *Science*, *332*(6036), 1426–1429.
- Inuma, T., Hino, R., Kido, M., Inazu, D., Osada, Y., Ito, Y., ... others (2012). Co-seismic slip distribution of the 2011 off the Pacific Coast of Tohoku earthquake ( $M9.0$ ) refined by means of seafloor geodetic data. *Journal of Geophysical Research: Solid Earth*, *117*(B7).
- Ikehara, K., Kanamatsu, T., Nagahashi, Y., Strasser, M., Fink, H., Usami, K., ... Wefer, G. (2016). Documenting large earthquakes similar to the 2011 Tohoku-Oki earthquake from sediments deposited in the Japan trench over the past 1500 years. *Earth and Planetary Science Letters*, *445*, 48–56.
- Imai, K. (2015). Paleo tsunami source estimation by using combination optimization algorithm—Case study of the 1611 Keicho earthquake tsunami. *Tohoku Journal of Natural Disaster Science*, *51*, 139.
- Ito, T., Ozawa, K., Watanabe, T., & Sagiya, T. (2011). Slip distribution of the 2011 off the Pacific coast of Tohoku earthquake inferred from geodetic data. *Earth, planets and space*, *63*(7), 627–630.
- Ito, Y., Tsuji, T., Osada, Y., Kido, M., Inazu, D., Hayashi, Y., ... Fujimoto, H. (2011). Frontal wedge deformation near the source region of the 2011 Tohoku-Oki earthquake. *Geophysical Research Letters*, *38*(7).
- Ji, C., Wald, D. J., & Helmberger, D. V. (2002). Source description of the 1999 Hector Mine, California, earthquake, part i: Wavelet domain inversion theory and resolution analysis. *Bulletin of the Seismological Society of America*, *92*(4), 1192–1207.
- Jia, Z., Jin, Z., Marchandon, M., Ulrich, T., Gabriel, A.-A., Fan, W., ... others (2023). The complex dynamics of the 2023 kahramanmaraş, turkey, m w 7.8-7.7 earthquake doublet. *Science*, *381*(6661), 985–990.
- Jiang, J., & Simons, M. (2016). Probabilistic imaging of tsunamigenic seafloor deformation during the 2011 Tohoku-Oki earthquake. *Journal of Geophysical Research: Solid Earth*, *121*(12), 9050–9076.
- Kammer, D. S., Radiguet, M., Ampuero, J.-P., & Molinari, J.-F. (2015). Linear elastic fracture mechanics predicts the propagation distance of frictional slip. *Tribology letters*, *57*, 1–10.
- Kawakatsu, H., & Seno, T. (1983). Triple seismic zone and the regional variation

- of seismicity along the northern Honshu arc. *Journal of Geophysical research: Solid Earth*, 88(B5), 4215–4230.
- Kido, M., Osada, Y., Fujimoto, H., Hino, R., & Ito, Y. (2011). Trench-normal variation in observed seafloor displacements associated with the 2011 Tohoku-Oki earthquake. *Geophysical Research Letters*, 38(24).
- Kodaira, S., Fujiwara, T., Fujie, G., Nakamura, Y., & Kanamatsu, T. (2020). Large coseismic slip to the trench during the 2011 Tohoku-Oki earthquake. *Annual Review of Earth and Planetary Sciences*, 48, 321–343.
- Kodaira, S., Iinuma, T., & Imai, K. (2021). Investigating a tsunamigenic megathrust earthquake in the Japan trench. *Science*, 371(6534), eabe1169.
- Kodaira, S., No, T., Nakamura, Y., Fujiwara, T., Kaiho, Y., Miura, S., . . . Taira, A. (2012). Coseismic fault rupture at the trench axis during the 2011 Tohoku-Oki earthquake. *Nature Geoscience*, 5(9), 646–650.
- Koketsu, K., Miyake, H., & Suzuki, H. (2012). Japan integrated velocity structure model version 1. In *Proceedings of the 15th world conference on earthquake engineering* (Vol. 1, p. 4).
- Koketsu, K., Miyake, H., Tanaka, Y., et al. (2009). A proposal for a standard procedure of modeling 3-d velocity structures and its application to the Tokyo metropolitan area, Japan. *Tectonophysics*, 472(1-4), 290–300.
- Kozdon, J. E., & Dunham, E. M. (2013). Rupture to the trench: Dynamic rupture simulations of the 11 March 2011 Tohoku earthquake. *Bulletin of the Seismological Society of America*, 103(2B), 1275–1289.
- Kubo, H., & Kakehi, Y. (2013). Source process of the 2011 Tohoku earthquake estimated from the joint inversion of teleseismic body waves and geodetic data including seafloor observation data: source model with enhanced reliability by using objectively determined inversion settings. *Bulletin of the Seismological Society of America*, 103(2B), 1195–1220.
- Kubota, T., Saito, T., & Hino, R. (2022). A new mechanical perspective on a shallow megathrust near-trench slip from the high-resolution fault model of the 2011 Tohoku-Oki earthquake. *Progress in Earth and Planetary Science*, 9(1), 1–19.
- Lay, T. (2018). A review of the rupture characteristics of the 2011 Tohoku-Oki  $M_w$  9.1 earthquake. *Tectonophysics*, 733, 4–36.
- Lay, T., Ammon, C. J., Kanamori, H., Xue, L., & Kim, M. J. (2011, 09). Possible large near-trench slip during the 2011  $M_w$  9.0 off the Pacific coast of Tohoku earthquake. *Earth, Planets and Space (Online)*, 63(7), 687–692.
- Lee, S.-J., Huang, B.-S., Ando, M., Chiu, H.-C., & Wang, J.-H. (2011). Evidence of large scale repeating slip during the 2011 Tohoku-Oki earthquake. *Geophysical Research Letters*, 38(19).
- Liu, X., & Zhao, D. (2018). Upper and lower plate controls on the great 2011 Tohoku-Oki earthquake. *Science advances*, 4(6), eaat4396.
- Loveless, J. P., & Meade, B. J. (2011). Spatial correlation of interseismic coupling and coseismic rupture extent of the 2011  $M_w$  = 9.0 Tohoku-Oki earthquake. *Geophysical Research Letters*, 38(17).
- Ma, S. (2023). Wedge plasticity and a minimalist dynamic rupture model for the 2011  $M_w$  9.1 Tohoku-Oki earthquake and tsunami. *Tectonophysics*, 869, 230146.
- Ma, S., & Nie, S. (2019). Dynamic wedge failure and along-arc variations of tsunamigenesis in the Japan trench margin. *Geophysical Research Letters*, 46(15), 8782–8790.
- Madden, E. H., Ulrich, T., & Gabriel, A.-A. (2022). The state of pore fluid pressure and 3-D megathrust earthquake dynamics. *Journal of Geophysical Research: Solid Earth*, 127(4), e2021JB023382.
- Maeda, T., Furumura, T., Sakai, S., & Shinohara, M. (2011a). Significant tsunami observed at ocean-bottom pressure gauges during the 2011 off the Pacific coast

- of Tohoku earthquake. *Earth, Planets and Space*, 63, 803–808.
- Maeda, T., Furumura, T., Sakai, S., & Shinohara, M. (2011b, 09). Significant tsunami observed at ocean-bottom pressure gauges during the 2011 off the Pacific coast of Tohoku earthquake. *Earth, Planets and Space (Online)*, 63(7), 803–808.
- Mai, P. M., & Beroza, G. C. (2002). A spatial random field model to characterize complexity in earthquake slip. *Journal of Geophysical Research: Solid Earth*, 107(B11), ESE–10.
- Mai, P. M., Burjanek, J., Delouis, B., Festa, G., Francois-Holden, C., Monelli, D., ... Zahradnik, J. (2007). Earthquake source inversion blindtest: Initial results and further developments. In *AGU Fall Meeting Abstracts* (Vol. 2007, pp. S53C–08).
- Mai, P. M., Schorlemmer, D., Page, M., Ampuero, J.-P., Asano, K., Causse, M., ... others (2016). The earthquake-source inversion validation (SIV) project. *Seismological Research Letters*, 87(3), 690–708.
- Mai, P. M., & Thingbaijam, K. (2014). SRCMOD: An online database of finite-fault rupture models. *Seismological Research Letters*, 85(6), 1348–1357.
- Melgar, D., & Bock, Y. (2015). Kinematic earthquake source inversion and tsunami runup prediction with regional geophysical data. *Journal of Geophysical Research: Solid Earth*, 120(5), 3324–3349.
- Melgar, D., Crowell, B. W., Bock, Y., & Haase, J. S. (2013). Rapid modeling of the 2011  $M_w$  9.0 Tohoku-Oki earthquake with seismogeodesy. *Geophysical Research Letters*, 40(12), 2963–2968.
- Minson, S., Simons, M., & Beck, J. (2013). Bayesian inversion for finite fault earthquake source models i—theory and algorithm. *Geophysical Journal International*, 194(3), 1701–1726.
- Minson, S. E., Simons, M., Beck, J., Ortega, F., Jiang, J., Owen, S., ... Sladen, A. (2014). Bayesian inversion for finite fault earthquake source models—ii: the 2011 great Tohoku-Oki, Japan earthquake. *Geophysical Journal International*, 198(2), 922–940.
- Mochizuki, M., Uehira, K., Kanazawa, T., Kunugi, T., Shiomi, K., Aoi, S., ... others (2018). S-net project: Performance of a large-scale seafloor observation network for preventing and reducing seismic and tsunami disasters. In *2018 OCEANS-MTS/IEEE Kobe Techno-Oceans (OTO)* (pp. 1–4).
- Moore, J. C., Plank, T. A., Chester, F. M., Polissar, P. J., & Savage, H. M. (2015). Sediment provenance and controls on slip propagation: Lessons learned from the 2011 Tohoku and other great earthquakes of the subducting northwest Pacific plate. *Geosphere*, 11(3), 533–541.
- Mori, N., Takahashi, T., Yasuda, T., & Yanagisawa, H. (2011). Survey of 2011 Tohoku earthquake tsunami inundation and run-up. *Geophysical research letters*, 38(7).
- Mungov, G., Eblé, M., & Bouchard, R. (2013). DART® tsunameter retrospective and real-time data: A reflection on 10 years of processing in support of tsunami research and operations. *Pure and Applied Geophysics*, 170, 1369–1384.
- Nakata, R., Hori, T., Hyodo, M., & Ariyoshi, K. (2016). Possible scenarios for occurrence of  $M \sim 7$  interplate earthquakes prior to and following the 2011 Tohoku-Oki earthquake based on numerical simulation. *Scientific reports*, 6(1), 25704.
- Nishikawa, T., Matsuzawa, T., Ohta, K., Uchida, N., Nishimura, T., & Ide, S. (2019). The slow earthquake spectrum in the Japan trench illuminated by the S-net seafloor observatories. *Science*, 365(6455), 808–813.
- Nissen-Meyer, T., van Driel, M., Stähler, S. C., Hosseini, K., Hempel, S., Auer, L., ... Fournier, A. (2014). AxiSEM: broadband 3-D seismic wavefields in axisymmetric media. *Solid Earth*, 5(1), 425–445.

- Oeser, J., Bunge, H.-P., & Mohr, M. (2006). Cluster design in the earth sciences tethys. In M. Gerndt & D. Kranzlmüller (Eds.), *High-performance computing and communications* (pp. 31–40). Springer Berlin Heidelberg.
- Ohnaka, M., & Yamashita, T. (1989). A cohesive zone model for dynamic shear faulting based on experimentally inferred constitutive relation and strong motion source parameters. *Journal of Geophysical Research: Solid Earth*, 94(B4), 4089–4104.
- Okada, Y., Kasahara, K., Hori, S., Obara, K., Sekiguchi, S., Fujiwara, H., & Yamamoto, A. (2004). Recent progress of seismic observation networks in Japan—Hi-net, F-net, K-Net and KiK-net. *Earth, Planets and Space*, 56, xv–xxviii.
- Okuwaki, R., & Fan, W. (2022). Oblique convergence causes both thrust and strike-slip ruptures during the 2021 M 7.2 Haiti earthquake. *Geophysical Research Letters*, 49(2), e2021GL096373.
- Okuwaki, R., Hirano, S., Yagi, Y., & Shimizu, K. (2020). Inchworm-like source evolution through a geometrically complex fault fueled persistent supershear rupture during the 2018 Palu Indonesia earthquake. *Earth and Planetary Science Letters*, 547, 116449.
- Pavlis, N. K., Holmes, S. A., Kenyon, S. C., & Factor, J. K. (2012). The development and evaluation of the earth gravitational model 2008 (egm2008). *Journal of geophysical research: solid earth*, 117(B4).
- Pollitz, F. F., Bürgmann, R., & Banerjee, P. (2011). Geodetic slip model of the 2011 M9.0 Tohoku earthquake. *Geophysical Research Letters*, 38(7).
- Ragon, T., Sladen, A., & Simons, M. (2018). Accounting for uncertain fault geometry in earthquake source inversions—i: theory and simplified application. *Geophysical Journal International*, 214(2), 1174–1190.
- Razafindrakoto, H. N., Mai, P. M., Genton, M. G., Zhang, L., & Thingbaijam, K. K. (2015). Quantifying variability in earthquake rupture models using multidimensional scaling: Application to the 2011 Tohoku earthquake. *Geophysical Journal International*, 202(1), 17–40.
- Romano, F., Trasatti, E., Lorito, S., Piromallo, C., Piatanesi, A., Ito, Y., ... Cocco, M. (2014). Structural control on the Tohoku earthquake rupture process investigated by 3d FEM, tsunami and geodetic data. *Scientific reports*, 4(1), 1–11.
- Sagiya, T. (2004). A decade of geonet: 1994–2003 the continuous GPS observation in Japan and its impact on earthquake studies. *Earth, planets and space*, 56(8), xxix–xli.
- Saito, T., Ito, Y., Inazu, D., & Hino, R. (2011). Tsunami source of the 2011 Tohoku-Oki earthquake, Japan: Inversion analysis based on dispersive tsunami simulations. *Geophysical Research Letters*, 38(7).
- Sallarès, V., & Ranero, C. R. (2019). Upper-plate rigidity determines depth-varying rupture behaviour of megathrust earthquakes. *Nature*, 576(7785), 96–101.
- Satake, K. (2015). Geological and historical evidence of irregular recurrent earthquakes in Japan. *Philosophical Transactions of the Royal Society A: Mathematical, Physical and Engineering Sciences*, 373(2053), 20140375.
- Satake, K., Fujii, Y., Harada, T., & Namegaya, Y. (2013). Time and space distribution of coseismic slip of the 2011 Tohoku earthquake as inferred from tsunami waveform data. *Bulletin of the seismological society of America*, 103(2B), 1473–1492.
- Sato, D. S., Fukahata, Y., & Nozue, Y. (2022). Appropriate reduction of the posterior distribution in fully bayesian inversions. *Geophysical Journal International*, 231(2), 950–981.
- Sato, M., Ishikawa, T., Ujihara, N., Yoshida, S., Fujita, M., Mochizuki, M., & Asada, A. (2011). Displacement above the hypocenter of the 2011 Tohoku-Oki earthquake. *Science*, 332(6036), 1395–1395.



- Scognamiglio, L., Tinti, E., Casarotti, E., Pucci, S., Villani, F., Cocco, M., ... Dreger, D. (2018). Complex fault geometry and rupture dynamics of the  $M_w$  6.5, 30 october 2016, Central Italy earthquake. *Journal of Geophysical Research: Solid Earth*, *123*(4), 2943–2964.
- Shao, G., Li, X., Ji, C., & Maeda, T. (2011). Focal mechanism and slip history of the 2011  $M_w$  9.1 off the Pacific coast of Tohoku earthquake, constrained with teleseismic body and surface waves. *Earth, planets and space*, *63*(7), 559–564.
- Shearer, P., & Bürgmann, R. (2010). Lessons learned from the 2004 sumatra-andaman megathrust rupture. *Annual Review of Earth and Planetary Sciences*, *38*, 103–131.
- Simons, M., Minson, S. E., Sladen, A., Ortega, F., Jiang, J., Owen, S. E., ... others (2011). The 2011 magnitude 9.0 Tohoku-Oki earthquake: Mosaicking the megathrust from seconds to centuries. *science*, *332*(6036), 1421–1425.
- Sun, T., Wang, K., Fujiwara, T., Kodaira, S., & He, J. (2017). Large fault slip peaking at trench in the 2011 Tohoku-Oki earthquake. *Nature communications*, *8*(1), 14044.
- Suzuki, W., Aoi, S., Sekiguchi, H., & Kunugi, T. (2011). Rupture process of the 2011 Tohoku-Oki mega-thrust earthquake ( $M_0$  0) inverted from strong-motion data. *Geophysical Research Letters*, *38*(7).
- Tajima, F., Mori, J., & Kennett, B. L. (2013). A review of the 2011 Tohoku-Oki earthquake ( $M_w$  9.0): Large-scale rupture across heterogeneous plate coupling. *Tectonophysics*, *586*, 15–34.
- Tanioka, Y., & Sataka, K. (1996). Fault parameters of the 1896 sanriku tsunami earthquake estimated from tsunami numerical modeling. *Geophysical research letters*, *23*(13), 1549–1552.
- Tinti, E., Casarotti, E., Ulrich, T., Taufiqurrahman, T., Li, D., & Gabriel, A.-A. (2021). Constraining families of dynamic models using geological, geodetic and strong ground motion data: The  $M_w$  6.5, october 30th, 2016, norcia earthquake, italy. *Earth and Planetary Science Letters*, *576*, 117237.
- Tinti, E., Fukuyama, E., Piatanesi, A., & Cocco, M. (2005). A kinematic source-time function compatible with earthquake dynamics. *Bulletin of the Seismological Society of America*, *95*(4), 1211–1223.
- Tinti, E., Scognamiglio, L., Michelini, A., & Cocco, M. (2016). Slip heterogeneity and directivity of the  $M_l$  6.0, 2016, Amatrice earthquake estimated with rapid finite-fault inversion. *Geophysical Research Letters*, *43*(20), 10–745.
- Tinti, E., Spudich, P., & Cocco, M. (2005). Earthquake fracture energy inferred from kinematic rupture models on extended faults. *Journal of Geophysical Research: Solid Earth*, *110*(B12).
- Tsai, V. C., Ampuero, J.-P., Kanamori, H., & Stevenson, D. J. (2013). Estimating the effect of earth elasticity and variable water density on tsunami speeds. *Geophysical Research Letters*, *40*(3), 492–496.
- Tsuji, T., Ito, Y., Kido, M., Osada, Y., Fujimoto, H., Ashi, J., ... Matsuoka, T. (2011). Potential tsunamigenic faults of the 2011 off the Pacific coast of Tohoku earthquake. *Earth, planets and space*, *63*, 831–834.
- Twardzik, C., Madariaga, R., Das, S., & Custódio, S. (2012). Robust features of the source process for the 2004 parkfield, california, earthquake from strong-motion seismograms. *Geophysical Journal International*, *191*(3), 1245–1254.
- Uchida, N., & Bürgmann, R. (2021). A decade of lessons learned from the 2011 Tohoku-Oki earthquake. *Reviews of Geophysics*, *59*(2), e2020RG000713.
- Ulrich, T., Gabriel, A.-A., & Madden, E. H. (2022). Stress, rigidity and sediment strength control megathrust earthquake and tsunami dynamics. *Nature Geoscience*, *15*(1), 67–73.
- van Driel, M., Krischer, L., Stähler, S. C., Hosseini, K., & Nissen-Meyer, T. (2015). Instaseis: Instant global seismograms based on a broadband waveform database. *Solid Earth*, *6*(2), 701–717.



- Van Rossum, G., & Drake Jr, F. L. (1995). *Python tutorial* (Vol. 620). Centrum voor Wiskunde en Informatica Amsterdam, The Netherlands.
- van Zelst, I., Rannabauer, L., Gabriel, A.-A., & van Dinther, Y. (2022). Earthquake rupture on multiple splay faults and its effect on tsunamis. *Journal of Geophysical Research: Solid Earth*, *127*(8), e2022JB024300.
- Viesca, R. C., & Garagash, D. I. (2015). Ubiquitous weakening of faults due to thermal pressurization. *Nature Geoscience*, *8*(11), 875–879.
- Wald, D. J., & Graves, R. W. (2001). Resolution analysis of finite fault source inversion using one-and three-dimensional green’s functions: 2. combining seismic and geodetic data. *Journal of Geophysical Research: Solid Earth*, *106*(B5), 8767–8788.
- Wang, C., Ding, X., Shan, X., Zhang, L., & Jiang, M. (2012). Slip distribution of the 2011 Tohoku earthquake derived from joint inversion of GPS, InSAR and seafloor GPS/acoustic measurements. *Journal of Asian Earth Sciences*, *57*, 128–136.
- Wang, K., & Bilek, S. L. (2014). Invited review paper: Fault creep caused by subduction of rough seafloor relief. *Tectonophysics*, *610*, 1–24.
- Wang, K., Dreger, D. S., Tinti, E., Bürgmann, R., & Taira, T. (2020). Rupture process of the 2019 Ridgecrest, California  $M_w$  6.4 foreshock and  $M_w$  7.1 earthquake constrained by seismic and geodetic data. *Bulletin of the Seismological Society of America*, *110*(4), 1603–1626.
- Wang, K., Sun, T., Brown, L., Hino, R., Tomita, F., Kido, M., . . . Fujiwara, T. (2018). Learning from crustal deformation associated with the m9 2011 tohoku-oki earthquake. *Geosphere*, *14*(2), 552–571.
- Wang, R., Parolai, S., Ge, M., Jin, M., Walter, T. R., & Zschau, J. (2013). The 2011  $M_w$  9.0 Tohoku earthquake: Comparison of GPS and strong-motion data. *Bulletin of the Seismological Society of America*, *103*(2B), 1336–1347.
- Wei, S., Graves, R., Helmberger, D., Avouac, J.-P., & Jiang, J. (2012). Sources of shaking and flooding during the Tohoku-Oki earthquake: A mixture of rupture styles. *Earth and Planetary Science Letters*, *333*, 91–100.
- Xie, Z., & Cai, Y. (2018). Inverse method for static stress drop and application to the 2011  $M_w$  9.0 Tohoku-Oki earthquake. *Journal of Geophysical Research: Solid Earth*, *123*(4), 2871–2884.
- Yagi, Y., & Fukahata, Y. (2011a). Introduction of uncertainty of green’s function into waveform inversion for seismic source processes. *Geophysical Journal International*, *186*(2), 711–720.
- Yagi, Y., & Fukahata, Y. (2011b). Rupture process of the 2011 Tohoku-Oki earthquake and absolute elastic strain release. *Geophysical Research Letters*, *38*(19).
- Yamanaka, Y., & Kikuchi, M. (2004). Asperity map along the subduction zone in northeastern Japan inferred from regional seismic data. *Journal of Geophysical Research: Solid Earth*, *109*(B7).
- Yamazaki, Y., Cheung, K. F., & Lay, T. (2018). A self-consistent fault slip model for the 2011 Tohoku earthquake and tsunami. *Journal of Geophysical Research: Solid Earth*, *123*(2), 1435–1458.
- Yoffe, E. H. (1951). Lxxv. the moving griffith crack. *The London, Edinburgh, and Dublin Philosophical Magazine and Journal of Science*, *42*(330), 739–750.
- Yokota, Y., Koketsu, K., Fujii, Y., Satake, K., Sakai, S., Shinohara, M., & Kanazawa, T. (2011). Joint inversion of strong motion, teleseismic, geodetic, and tsunami datasets for the rupture process of the 2011 Tohoku earthquake. *Geophysical Research Letters*, *38*(7).
- Yoshida, Y., Ueno, H., Muto, D., & Aoki, S. (2011). Source process of the 2011 off the Pacific coast of Tohoku earthquake with the combination of teleseismic and strong motion data. *Earth, planets and space*, *63*(7), 565–569.
- Yue, H., & Lay, T. (2013). Source rupture models for the  $M_w$  9.0 2011 Tohoku

- 1557 earthquake from joint inversions of high-rate geodetic and seismic data. *Bul-*  
1558 *letin of the Seismological Society of America*, 103(2B), 1242–1255.
- 1559 Yue, H., Lay, T., Rivera, L., An, C., Vigny, C., Tong, X., & Báez Soto, J. C. (2014).  
1560 Localized fault slip to the trench in the 2010 maule, chile mw= 8.8 earthquake  
1561 from joint inversion of high-rate gps, teleseismic body waves, insar, campaign  
1562 gps, and tsunami observations. *Journal of Geophysical Research: Solid Earth*,  
1563 119(10), 7786–7804.
- 1564 Zhou, X., Cambiotti, G., Sun, W., & Sabadini, R. (2014). The coseismic slip dis-  
1565 tribution of a shallow subduction fault constrained by prior information: the  
1566 example of 2011 Tohoku ( $M_w$  9.0) megathrust earthquake. *Geophysical Jour-*  
1567 *nal International*, 199(2), 981–995.

1 **Supporting Information for “A quantitative comparison**  
2 **and validation of finite-fault models: The 2011**  
3 **Tohoku-Oki earthquake”**

4 **Jeremy Wing Ching Wong<sup>1</sup>, Wenyan Fan<sup>1</sup>, Alice-Agnes Gabriel<sup>1,2</sup>**

5 <sup>1</sup>Scripps Institution of Oceanography, University of California San Diego, La Jolla, CA, USA

6 <sup>2</sup>Department of Earth and Environmental Sciences, Ludwig-Maximilians-Universität München, Munich ,  
7 Germany

8 **Supplementary Contents**

- 9 1. Text S1–S3  
10 2. Table S1–S3  
11 3. Figures S1–S43

---

Corresponding author: Jeremy Wing Ching Wong, [wcwong@ucsd.edu](mailto:wcwong@ucsd.edu)

## Text S1: Overview of the 32 Finite-fault Slip Models

Model G1 is from Pollitz et al. (2011), which is obtained using geodetic measurements. The total moment of the model is  $4.1 \times 10^{22}$  N·m, equivalent to a  $M_w$  9.01 earthquake. The model includes a total of 5151 subfaults, with 101 and 51 subfaults along the strike and dip directions, respectively. Each subfault has an area of  $7 \times 4.5$  km<sup>2</sup>. The model is parameterized as three planar faults with strike and dip as 195° and 10°, 195° and 14°, and 195° and 22° at the depth ranges of 3–21, 21–39, and 39–57 km. The rake angles of all subfaults are fixed at 90°. The model composes of two major slip patches located updip and downdip of the hypocenter in zones ZC1 and ZC2, with peak slip away from the trench.

Model G2 is from Ito et al. (2011), which is obtained using geodetic measurements. The total moment of the model is  $4.1 \times 10^{22}$  N·m, equivalent to a  $M_w$  9.01 earthquake. The model includes a total of 525 subfaults, with 35 and 15 subfaults along the strike and dip directions, respectively. Each subfault has a varying area. The model is parameterized as a non-planar fault. The model composes of a single slip patch at the updip area in zone ZC1. The major slip patch is slightly south of the hypocenter, located between 37°N to 38°N.

Model G3 is from Diao et al. (2012), which is obtained using geodetic measurements. The total moment of the model is  $2.3 \times 10^{22}$  N·m, equivalent to a  $M_w$  8.84 earthquake. The model includes a total of 288 subfaults, with 24 and 12 subfaults along the strike and dip directions, respectively. Each subfault has an area of  $20 \times 20$  km<sup>2</sup>. The model is parameterized as a non-planar fault. The model composes of a single smooth slip patch in zone ZC1.

Model G4 is from Iinuma et al. (2012), which is obtained using geodetic measurements. The total moment of the model is  $4.0 \times 10^{22}$  N·m, equivalent to a  $M_w$  9.00 earthquake. The model includes a total of 806 subfaults, with 31 and 13 subfaults along the strike and dip directions, respectively. Each subfault is represented by bi-cubic B-spines with 20 km intervals. The model is parameterized as a non-planar fault. The model has the largest slip at the trench and extended along strike slip patch. The model consists of a secondary slip patch extending to the southern deeper region in zone S2.

Model G5 is from C. Wang et al. (2012), which is obtained using geodetic measurements and InSAR measurements. The total moment of the model is  $3.2 \times 10^{22}$  N·m, equivalent to a  $M_w$  8.94 earthquake. The model includes a total of 1080 subfaults, with 60 and 18 subfaults along the strike and dip directions, respectively. Each subfault has an area of  $11.7 \times 11.1$  km<sup>2</sup>. The model is parameterized as a varying dip angle fault with a striking angle of 195°. The model has a single slip patch at the updip of the hypocenter in zone ZC1 with peak slip away from the trench.

Model G6 is from R. Wang et al. (2013), which is obtained from geodetic measurements and displacement from integrated strong ground motion waveforms. The total moment of the model is  $2.9 \times 10^{22}$  N·m, equivalent to a  $M_w$  8.91 earthquake. The model includes 1920 subfaults with 64 subfaults along strike and 30 subfaults along dip. Each subfaults has a size of  $10 \times 10$  km<sup>2</sup>. The model is parameterized as a non-planar fault. The model composes of a single slip patch at the updip of the hypocenter in zone ZC1 with peak slip away from the trench.

Model G7 is from Zhou et al. (2014), which is obtained from probabilistic inversion of geodetic data. The total moment of the model is  $3.8 \times 10^{22}$  N·m, equivalent to a  $M_w$  8.99 earthquake. The model includes 350 subfaults with 25 subfaults along the strike and 14 subfaults along the dip. Each subfault has a size of  $25 \times 18$  km<sup>2</sup>. The model is parameterized as a varying dipping angle fault with a striking angle of 201. The model has a horse-shoe-shaped slip patch surrounding the hypocenter with peak slip at the trench in zones ZC1 and ZC1.

Model G8 is from Hashima et al. (2016), which is obtained from geodetic measurements. The total moment of the model is  $4.0 \times 10^{22}$  N·m, equivalent to a  $M_w$  9.00 earthquake. The model includes 256 subfaults with 32 along-strike subfaults and eight along-dip subfaults. Each subfaults has a varying subfault area. The model is parameterized as a non-planar fault. The rake angles of all subfaults are fixed with the incoming plate direction. The model has a board and smooth slip patch with slip peaking at the trench at the updip area of the hypocenter in zone ZC1.

Model G9 is from Xie and Cai (2018), which applies stress inversion formulation for slip distribution from geodetic measurements. The total moment of the model is  $4.5 \times 10^{22}$  N·m, equivalent to a  $M_w$  9.04 earthquake. The model includes 140 subfaults with 20 along-strike subfaults and seven along-dip subfaults. Each subfaults has a  $25 \text{ km} \times 25 \text{ km}$  subfault area. The model is parameterized as a non-planar fault. The model has a board and smooth slip patch with slip peaking at the trench in zone ZC1, with a slightly wider rupture than other geodetic models.

Model R1 is from Lee et al. (2011), which is obtained by inverting regional velocity waveform integrated from strong ground motion records (0.01 - 0.2 Hz), teleseismic P waves (0.005 - 0.2 Hz) and geodetic measurements. The total moment of the model is  $3.7 \times 10^{22}$  N·m, equivalent to a  $M_w$  8.98 earthquake. The model includes 396 subfaults with 33 along-strike subfaults and 12 along-dip subfaults. Each subfaults has a  $20 \times 20 \text{ km}^2$  subfault area. The model is parameterized as a planar fault with strike and dip as  $195^\circ$  and  $14^\circ$ , respectively. The model shows a single smooth, slightly elongated slip patch at the updip in zone ZC1 and towards the north of the hypocenter with peak slip away from the trench in zone N1.

Model R2 is from Suzuki et al. (2011), which is obtained by inverting regional velocity waveform integrated from accelerograms strong ground motion records (0.01 - 0.125 Hz). The total moment of the model is  $4.4 \times 10^{22}$  N·m, equivalent to a  $M_w$  9.03 earthquake. The model includes 119 subfaults with 17 along-strike subfaults and seven along-dip subfaults. Each subfaults has a  $30 \times 30 \text{ km}^2$  subfault area. The model is parameterized as a planar fault with strike and dip as  $195^\circ$  and  $13^\circ$ . The model shows a single smooth, expanded, increasing slip from the hypocenter region to the trench in zone ZC1. The expanded slip reaches beyond  $39^\circ\text{N}$  in zone ZN1.

Model R3 is from Wei et al. (2012), which is obtained by inverting strong ground motion records, high-rate GPS (0 - 0.25 Hz) and geodetic measurements. The total moment of the model is  $5.3 \times 10^{22}$  N·m, equivalent to a  $M_w$  9.08 earthquake. The model includes 273 subfaults with 21 along-strike subfaults and 13 along-dip subfaults. Each subfault has an area of  $25 \times 20 \text{ km}^2$ . The model is parameterized as a planar fault with strike and dip as  $201^\circ$  and  $10^\circ$ . The model shows a major slip patch in zone ZC1, with peak slip located away from the trench. Significant shallow slip extends to the southern ZS1 region, reaching  $36^\circ\text{N}$ .

Model R4 is from Yue and Lay (2013), which is obtained by inverting high-rate geodetic data and teleseismic data. The total moment of the model is  $4.2 \times 10^{22}$  N·m, equivalent to a  $M_w$  9.02 earthquake. The model includes 120 subfaults with 15 along strike subfaults and 8 along dip subfaults. Each subfaults has a size of  $30 \times 30 \text{ km}^2$ . The model is parameterized as a dip-varying planar fault with the strike as  $202^\circ$ . The slip distribution is characterized by two major slip patches, with one located at the updip of the hypocenter in zone ZC1 and a similar one located at the down dip of the hypocenter in zone ZC1.

Model S1 is from Ide et al. (2011), which is inverted slip distribution from vertical broadband seismograms with a high-pass filter above 200 s using the empirical Green's function method. The total moment of the model is  $4.5 \times 10^{22}$  N·m, equivalent to a  $M_w$  9.04 earthquake. The model includes 231 subfaults with 21 along-strike subfaults and

11 along-dip subfaults. Each subfaults consist of bilinear spline basis functions with 10 km node separation. The model is parameterized as a planar fault with strike and dip as 190 and 15.3. The model has a widespread slip distribution from the downdip at around 50 km depth to the trench in zone ZC1 and ZC1. The near trench slip extends from 39.5°N to 36.5°S.

Model S2 is from Hayes (2011), which is the initial USGS model inverted from teleseismic body waves of P, SH with a period range of 1 to 200 s and surface waves in a period range of 200 to 500 s. The total moment of the model is  $4.9 \times 10^{22}$  N·m, equivalent to a  $M_w$  9.06 earthquake. The model includes 325 subfaults with 25 along strike subfaults and 13 along dip subfaults. Each subfault has an area of  $25 \times 20$  km<sup>2</sup>. The model is parameterized as a planar fault with strike and dip as 194° and 10°. The model shows a major slip patch at the updip of the hypocenter in zone ZC1 and a secondary slip patch at the down-dip of the hypocenter in zone ZC1.

Model S3 is from the revised USGS finite-fault model of the Tohoku-oki earthquake, with the last update in 2018 (Goldberg et al., 2022). The model is inverted from teleseismic body waves of P, SH with a period range of 1 to 200 s and surface waves in the period range of 200 to 500 s. The total moment of the model is  $4.8 \times 10^{22}$  N·m, equivalent to a  $M_w$  9.05 earthquake. The model has 325 subfaults, with 25 along strike subfaults and 13 along dip subfaults. The model is parameterized as a varying strike planar fault with strike and dip as 198 and 8, 198 and 15, and 198 and 21 at the depth ranges of 3–15, 15–33, and 33–52 km. The model shows a distinctive two major slip patch with one at the north of the hypocenter and one at the south of the hypocenter. The overall slip distribution is elongated along the strike with two minor deeper slip patches at the down-dip and north of the hypocenter in zone ZC1, reaching 50 km.

Model S4 is from Ammon et al. (2011), which is obtained by inverting teleseismic P waves with relative source time function inverted from Rayleigh waves and high-rate GPS recordings (lowpass 30s). The total moment of the model is  $3.6 \times 10^{22}$  N·m, equivalent to a  $M_w$  8.98 earthquake. The model has 560 subfaults, with 50 along strike subfaults and 14 along dip subfaults. Each subfault has a size of  $15 \times 15$  km<sup>2</sup>. The model is parameterized as a planar fault with strike and dip as 202° and 12°. The model shows a large smooth single-slip patch with peak slip extending from the hypocenter to the south of the hypocenter, located in the zone ZC1 and ZC1.

Model S5 is from Yagi and Fukahata (2011), which is obtained by inverting teleseismic P waves in velocity with a period of 2.6 to 100 s. The total moment of the model is  $5.7 \times 10^{22}$  N·m, equivalent to a  $M_w$  9.10 earthquake. The model has 250 subfaults with 25 along strike subfaults and 10 along dip subfaults. Each subfaults has a size of  $10 \times 10$  km<sup>2</sup>. The model is parameterized as a planar fault with strike and dip as 200° and 12°. The rake angles of all subfaults are fixed at 90°. The model shows a major slip patch at the updip of the hypocenter, with the peak slip extending towards the trench in zone ZC1. Slip extends towards the south and deeper region in zone S2.

Model S6 is from Kubo and Kakehi (2013), which is obtained by inverting teleseismic P waves with a period of 10 to 100 s. The total moment of the model is  $3.4 \times 10^{22}$  N·m, equivalent to a  $M_w$  8.95 earthquake. The model has 108 subfaults with 18 along strike subfaults and six along dip subfaults. Each subfaults has a varying size. The model is parameterized as multiple planar faults with strike and dip 185° and 7°, 197.5° and 11°, and 210° and 23° along strike. The model shows a very smooth slip patch with peak slip at the updip of the hypocenter reaching the trench in zone ZC1.

Model T1 is from Simons et al. (2011), which is obtained by inverting tsunami and geodetic data. The total moment of the model is  $7.8 \times 10^{22}$  N·m, equivalent to a  $M_w$  9.19 earthquake. The model has 419 subfaults with varying subfault sizes. The model is parameterized as a curved geometry triangulated by the subfaults. The model shows



an elongated slip patch along the strike of the hypocenter in zones N1, ZC1 and ZC1. The elongated slip extends from  $40^\circ$  north to  $37^\circ$  N. The model also shows a high level of heterogeneity with many smaller slip patches.

Model T2 is from Fujii et al. (2011), which is obtained by inverting the tsunami data. The total moment of the model is  $3.8 \times 10^{22}$  N·m, equivalent to a  $M_w$  8.99 earthquake. The model has 40 subfaults, with ten along strike subfaults and four along dip subfaults. Each subfault has a size of  $50 \times 50$  km<sup>2</sup>. The model is parameterized as a planar fault with strike and dip as  $193^\circ$  and  $14^\circ$ . The rake angles of all subfaults are fixed at  $81^\circ$ . The model shows a single and concentrated slip patch at the updip hypocenter region with slip increases towards the trench in zone ZC1.

Model T3 is from Saito et al. (2011), which is obtained by inverting the tsunami data. The total moment of the model is  $3.8 \times 10^{22}$  N·m, equivalent to a  $M_w$  8.99 earthquake. The model has 130 grid nodes, with 13 nodes along the strike and 10 nodes along the dip. Each node is represented by a Gaussian basis function. The model is parameterized as a varying dip fault with a strike of  $193^\circ$ . The model shows a major slip asperity at the hypocenter region and extended slip towards the trench in zone ZC1.

Model T4 is from Gusman et al. (2012), which is obtained by inverting tsunami and geodetic data. The total moment of the model is  $5.1 \times 10^{22}$  N·m, equivalent to a  $M_w$  9.07 earthquake. The model has 45 subfaults with nine along strike and five along dip subfaults. Each subfault has a size of  $50 \times 40$  km<sup>2</sup>. The model is parameterized as a varying dip fault with a strike of  $202^\circ$ . The model shows a smooth single slip patch at the updip of the hypocenter with significant slip at the trench in zone ZC1.

Model T5 is from Hooper et al. (2013), which is obtained by inverting tsunami and geodetic data. The total moment of the model is  $4.0 \times 10^{22}$  N·m, equivalent to a  $M_w$  9.00 earthquake. The model has 234 subfaults with 18 along strike subfaults and 13 along dip subfaults. Each subfault has a size of  $25 \times 20$  km<sup>2</sup>. The model is parameterized as a dip varying fault with a strike of  $194^\circ$ . The model has a major slip patch at the updip of the hypocenter in zone ZC1. Narrow and elongated slip features from 20 km to 40 km extend near the hypocenter and towards the south of the hypocenter. A northern minor slip patch at the depth of 12 km in zone ZN1 also appears in the slip distribution.

Model T6 is from Satake et al. (2013), which is obtained by inverting tsunami and geodetic data. The total moment of the model is  $4.2 \times 10^{22}$  N·m, equivalent to a  $M_w$  9.02 earthquake. The model has 55 subfaults, with 11 along strike subfaults and five along dip sub faults. Each subfault has a size of  $50 \times 50$  km<sup>2</sup>. The model is parameterized as a dip-varying planar fault with a strike of  $193^\circ$ . The model shows a smooth large expanding slip patch in the updip of the hypocenter with increasing slip toward the trench in zone ZC1.

Model T7 is from Romano et al. (2014), which is obtained by inverting tsunami and geodetic data. The total moment of the model is  $5.7 \times 10^{22}$  N·m, equivalent to a  $M_w$  9.10 earthquake. The model has 398 subfaults. The model is parameterized as a curved fault with the subfaults subdivided into patches of variable size:  $24$  km  $\times$   $14$  km,  $24$  km  $\times$   $24$  km,  $35 \times 35$  km<sup>2</sup> at depth ranges of 2-15, 15-40, 40-60 km. The model shows a similar overall slip structure as model G6 with a large expanding slip patch in the updip of the hypocenter with increasing slip toward the trench in zone ZC1. The model shows a high level of slip heterogeneity with many small slip patches.

Model T8 is from Kubota et al. (2022), which is obtained by inverting Tsunami and geodetic data. The total moment of the model is  $5.1 \times 10^{22}$  N·m, equivalent to a  $M_w$  9.07 earthquake. The model has 434 subfaults triangulating the 3D fault surface, with the length of each side of the triangle about 10 km. The model shows a smooth large

slip patch at the updip of the hypocenter with increasing slip towards the trench in zone ZC1. The model shows near trench slip at the northern section in zone ZN1 reaching 39.5°N.

Model J1 is from Yokota et al. (2011), which is jointly inverted from geodetic, strong ground motion (0.01 - 0.1 Hz), teleseismic P wave (0.002 - 0.25 Hz) and tsunami observations. The total moment of the model is  $4.2 \times 10^{22}$  N·m, equivalent to a  $M_w$  9.02 earthquake. The model has 96 subfaults, with 16 along strike subfaults and five along dip subfaults. Each subfault has a size of  $30 \times 30$  km<sup>2</sup>. A varying dip fault geometry is used with a strike angle of 200°. The model shows a concentrated slip at the hypocenter along the 20 km depth in zones ZC1 and ZC1. The slip extends to the north, reaching 39.5°N.

Model J2 is from Minson et al. (2014), which is jointly inverted from the tsunami and high-rate GPS data (0.005 - 0.1 Hz). The total moment of the model is  $5.3 \times 10^{22}$  N·m, equivalent to a  $M_w$  9.08 earthquake. The model has 219 subfaults, with 24 along strike subfaults and nine along dip subfaults. Each subfault has a size of around  $30 \times 30$  km<sup>2</sup>. The model is parameterized as a varying dip fault with a strike of 194°. The model shows a major slip patch at the hypocenter in zones ZC1 and ZC1. Extensive near trench slip was also imaged by the model extending from 39°N to 37°N. The model also shows a higher level of slip heterogeneity with patches of slip across the major slip area and other parts of the fault.

Model J3 is from Bletery et al. (2014), which is obtained by inverting the geodetic, high-rate geodetic (0.01 - 0.08 Hz), strong ground motion (double-integrated to displacement and filtered between 0.01 and 0.08 Hz), teleseismic P (1.25-100 s) and SH waves (2.5-100 s) and tsunami data. The total moment of the model is  $3.5 \times 10^{22}$  N·m, equivalent to a  $M_w$  8.96 earthquake. The model has 187 subfaults with varying subfault sizes. The model is parameterized as a curved fault. The model shows a patchy shallow slip distribution with most slip confined at the updip of the hypocenter region in zone ZC1. The near trench slip extends from 37°N to 39.3°N.

Model J4 is from Melgar and Bock (2015), which is obtained by inverting the collocated seismogendetic recordings and tsunami data. The total moment of the model is  $5.5 \times 10^{22}$  N·m, equivalent to a  $M_w$  9.09 earthquake. The model has 189 subfaults, with 21 along strike subfaults and nine along dip subfaults. Each subfault has a size of  $25 \times 25$  km<sup>2</sup>. The model is parameterized as a curved fault. The model shows a major slip patch at the updip of the hypocenter with a confined large slip at the shallowest 10 km section of the fault in zone ZC1. Small near trench slip patches also appear in 40°N and 36°N.

J4 model uses 20 colocated seismo-geodetic stations to invert the slip distribution. The displacement and velocity data are filtered between 0 and 0.5 Hz to match their greens function. However, they discovered that the coherence greatly depleted for wave period shorter than 7-8 seconds.

Model J5 is from Yamazaki et al. (2018), which is iteratively inverted from the geodetic, teleseismic and tsunami data. The total moment of the model is  $4.0 \times 10^{22}$  N·m, equivalent to a  $M_w$  9.00 earthquake. The model has 240 subfaults with 20 along strike subfaults and 12 along dip subfaults. Each subfault has a size of  $20 \times 20$  km<sup>2</sup>. The model is parameterized as a varying dip fault. The model shows a major L shape slip patch at the updip of the hypocenter with a confined large slip at the shallowest 10 km section of the fault and extended slip to 20 km dip at the south of the hypocenter in zone ZC1. Secondary features of the slip include a near trench slip at 39.5 °N in zone ZN1 and slip reaching 40 km depth at 37 °N in zone S2.

## Text S2: Teleseismic Displacement Waveforms Sensitivity Analysis

We compute teleseismic synthetic waveforms using the single-time window method with an assumed slip-rate function. We systematically compare synthetics from different slip-rate functions with varying duration. We use cosine, triangular, and regularized Yoffe functions to compute the synthetics (Figure S16). We pair the slip-rate functions with the same peak-slip-rate-time distribution from model S3 model for a consistent comparison. The comparison with the observations is summarized in Table S2.

We find that the teleseismic synthetics are insensitive to the shape and duration of the slip-rate functions. The synthetics are highly similar to the observations, with a median  $\geq 0.82$  correlation coefficient for all slip-rate functions. Figure S20 compares the synthetics with Yoffe, cosine and triangle functions, all having the same rise-time of 16 s and duration of around 32 s. The synthetics show negligible differences, suggesting that teleseismic waveforms are insensitive to the shape of the slip-rate function, given similar rise-time and duration.

We further compare the teleseismic data sensitivity to the decay rate and duration of the slip-rate function. We apply the Yoffe function with the same-rise time but with extended durations (40, 28, and 55 s), as shown in Figure S16. The synthetics show highly similar shapes with varying amplitudes (Figure S21). Particularly, the synthetics of the Yoffe function with varying duration show the same peak and trough timing in the synthetic waveforms. Hence, teleseismic waveforms seem to have limited sensitivity to the variation of the Yoffe function, confirming that our method with regularized Yoffe function for all models can effectively describe the slip-rate function for computing the teleseismic synthetics.

We further examine the rupture propagation effects on the teleseismic waveforms. We compare and validate different models' peak-slip-rate-time (PSRT) distributions, which describe the rupture front evolution of the respective models. We use three different slip models: Models S3, S6, and J5, all of which use teleseismic waveforms to invert slip distributions. Model S3 uses the single-time window method to describe the slip-rate evolution, while models S6 and J5 use the multi-time window method. We extract the PSRT of each projected model and map it to the model S3 slip distribution at the 16 km scale. We use the uniform regularized Yoffe function for each subfault and align it with the peak-slip-rate time accordingly.

The three PSRT distributions agree on major slip episodes but show varying complexity (Figure S23). Models S3 and J3 show a relatively smooth and regular expansion in the first 50 s, followed by a complex and irregular pattern for the rest of the rupture, associated with the major slip patch in ZC1. In contrast, model S6 shows a consistently smooth PSRT evolution. This smooth evolution continues through the major rupture area but with an increasing rupture speed. All three models show similar peak-slip-rate timing in the major slip patch. They suggest that the peak-slip-rate time for the major slip patch ranges from 40–80 s.

Synthetics using the S6 and J3 PSRT distributions show satisfactory fitting with the observed seismograms (Figure S24), with both synthetics reaching a correlation coefficient of 0.75. Comparatively, we compute the synthetics of models S6 and S3 using a uniform Yoffe function aligned with their peak-slip-rate time, respectively. The resulting synthetics have correlation coefficients with the observations of 0.71 for model S6 and 0.73 for model J3. The slight decrease in correlation results from our simplification of the complex slip-rate function from the multi-time-window method. Nevertheless, our comparison validates that the teleseismic waveforms are sensitive to the rupture propagation effects, and the peak-slip-rate time distribution of model S3 is effective in describing the slip-rate evolution.

### Text S3: Teleseismic Velocity Sensitivity Analysis

Our teleseismic data validation test in Section 4.2 shows that teleseismic displacement data are insensitive to the small-scale slip features. The displacement synthetics of the body waves have a dominant period of 20–30 s, which corresponds to a 90–120 km wavelength (Figure 11). We further test the sensitivity of teleseismic velocity waveforms, which contain more higher-frequency signals than the displacement waveforms, with a dominant period of around 15 s for the body waves. We follow the same procedure in Section 4.2.

We find that the teleseismic velocity waveforms have additional sensitivity to the fault geometry as compared to the displacement waveforms (Figure S26). We investigate the slip-rate function effects on the teleseismic velocity waveforms following the same procedure in Section 4.2.2. Our tests show that the velocity records have limited sensitivity to the slip-rate function (Figures S29 and S30). We explore the rupture propagation effects on the teleseismic velocity waveforms. We compare the slip-rate onset time alignment with the original S3 model onset time, peak-slip-rate time, and constant rupture velocity. We find that rupture propagation has a strong impact on the teleseismic velocity synthetics. Figure S29 shows synthetics using the original onset time alignment and a uniform Yoffe slip-rate function, resulting in a correlation of 0.52, while the original projected model has a correlation of 0.76. The synthetics using the PSRT alignment and a uniform Yoffe slip-rate function fit the observed waveforms, with a correlation of 0.71 (Figure S28). Similar to the displacement waveforms, both the constant rupture speed and two-step rupture speed failed to produce reasonable waveform fits (Figure S28).

We also apply the PSRT approach using the PSRT distributions from models S6 and J3. Following the same procedure in Section 4.2.3, we compute the teleseismic velocity synthetics using the S3 slip distribution and the PRST distributions from models S6 and J3. Both sets of synthetics can fit the long-period waveforms but not the short-period signals (Figure S32). We compute synthetics using the PSRT from model S3 and the slip distributions from models S6 and J3. The synthetics are similar to those from the S3 slip distribution.

We follow the same procedure and compute teleseismic synthetics velocity waveforms using the final slip distributions at the 16, 32, and 64 km scales for all models. Figure S33 shows teleseismic body-wave velocity synthetics for all models at a 16 km scale. The synthetics fit the first-order features of the teleseismic velocity observations. For example, the synthetics show accurate peaks and troughs for SH and SV waves at station BRVK. However, synthetics variations are more significant in the teleseismic velocity waveforms than the displacement waveforms. Synthetics SH waves from different slip models show contrasting waveform shapes around 50–150 s from S wave arrivals at both stations COR and HNR. The variations in velocity waveforms suggest a possible higher sensitivity for secondary slip features. We compute the correlation coefficients of the synthetic body waves with the observations. The velocity seismic synthetics of all models at three scales show a lower correlation ranges from 0.5 to 0.7, with the SH synthetics slightly better than P and SV synthetics. However, it is worth noting that the correlation value of the velocity waveforms is also compatible with typical inversion results (e.g. Melgar & Bock, 2015).

## Text S4: High-rate GNSS and Strong-Ground Motion Sensitivity Analysis

We compute the High-rate GNSS and strong ground motion synthetics following the same procedure of Section 4.2 Teleseismic Data analysis. The synthetics are computed using the open-source software *Instaseis* (van Driel et al., 2015). This method uses pre-computed Green’s function databases, calculated using the anisotropic version of the Preliminary Reference Earth Model (PREM) and the *AxiSEM* method up to 2 s period band (Dziewonski & Anderson, 1981; Nissen-Meyer et al., 2014). Green’s function is convoluted with the source time function either with the original finite-fault models or the unified source-time function, with the same Yoffee-slip rate function aligned with the S3 peak-slip-rate time.

The synthetics are compared with the strong-ground motion records and the horizontal high-rate GNSS record. The strong ground motion records are doubled-integrated into displacement and band-passed between 10-100s, while the high-rate GNSS records are lowpass-filtered at 10 seconds. The frequency range is compatible with the regional seismic and joint-inversion models’ data processing procedure.

To validate the geometric effects of the projection, we compare the synthetics from the original J4 finite-fault model and the projected J4 finite-fault model. We use the original multi-time-window method to compute the synthetics. Figure S35 compares the differences between the two models. Both sets of synthetics demonstrate high similar waveforms, suggesting the projected fault geometry can reproduce the observed regional seismic records.

Similarly, we compare the original and projected J4 finite-fault models synthetics with the high-rate GNSS records (Figure S38). Both synthetics show overlapping waveforms with the observations. In addition, we compare the synthetics with the static offset computed by 3D Green’s function in Section 4.1, as shown by the dashed grey lines in Figure S38. All synthetics including the original J4 model, and projected J4 model show consistency with the observations and the deformation by 3D velocity structure Green’s function.

**Table S1.** Offshore geodetic stations

Station	Longitude	Latitude	Depth [km]	Eastward displace- ment [m]	Northward displace- ment [m]	Vertical displace- ment [m]
GJT3	143.483	38.273	3.281	29.500	-11.000	3.734
GJT4	142.833	38.407	1.445	14.000	-5.000	3.500
MYGI	142.917	38.084	1.700	22.100	-10.400	3.100
MYGW	142.433	38.153	1.100	14.300	-5.100	-0.800
FUKU	142.083	37.166	1.200	4.400	-1.700	0.900
KAMS	143.263	38.636	2.200	21.100	-8.900	1.500
KAMN	143.363	38.887	2.300	13.800	-5.800	1.600
CHOS	141.670	35.500	1.600	0.950	-0.950	0.400
TJT1	143.796	38.209	5.758	N.A.	N.A.	5.093
P02	142.502	38.500	1.100	N.A.	N.A.	-0.801
P06	142.584	38.634	1.250	N.A.	N.A.	-0.975
TM1	142.780	39.236	1.500	N.A.	N.A.	-0.800
TM2	142.446	39.256	1.000	N.A.	N.A.	-0.300



**Table S2.** Summary of teleseismic P wave displacement synthetics performance on changing geometry, subfault size, slip-rate, and rupture front time-alignment.

Slip model	subfault <sup>a</sup>	slip-rate <sup>b</sup>	slip-rate alignment <sup>c</sup>	P wave correlation <sup>d</sup>	P wave variance reduction <sup>d</sup>	Figure <sup>e</sup>
S3	original	original	original	0.90 (0.01)	80% (5%)	FigS17
S3 projected	original	original	original	0.89 (0.01)	68% (28%)	FigS17
S3 projected	original	Yoffe16(40)	original	0.84 (0.01)	65% (15%)	FigS18
S3 projected	original	Yoffe16(40)	S3 PSRT	0.88 (0.01)	74% (9%)	FigS18
S3 projected	original	original	Vr 2.0 km/s	0.65 (0.01)	27% (30%)	FigS19
S3 projected	original	original	Vr 1.5 & 2.0 km/s	0.65 (0.01)	31% (12%)	FigS19
S3 projected	original	Cosine16	S3 PSRT	0.88 (0.01)	71% (18%)	FigS20
S3 projected	original	Tri 16	S3 PSRT	0.88 (0.01)	74% (11%)	FigS20
S3 projected	original	Yoffe16(48)	S3 PSRT	0.85 (0.01)	71% (5%)	FigS21
S3 projected	original	Yoffe16(55)	S3 PSRT	0.82 (0.01)	66% (2)	FigS21
S3 projected	16 km	Yoffe16(40)	S3 PSRT	0.82 (0.01)	63% (17%)	FigS22
S6 projected	16 km	Yoffe16(40)	S3 PSRT	0.77 (0.03)	47% (36%)	FigS22
J3 projected	16 km	Yoffe16(40)	S3 PRST	0.76 (0.02)	48% (17%)	FigS22
G4 projected	16 km	Yoffe16(40)	S3 PSRT	0.76 (0.04)	50% (24%)	FigS25
R3 projected	16 km	Yoffe16(40)	S3 PRST	0.75 (0.04)	48% (73%)	FigS25
S3 projected	16 km	Yoffe16(40)	S6 PSRT	0.75 (0.03)	49% (41%)	FigS24
S3 projected	16 km	Yoffe16(40)	J3 PSRT	0.75 (0.02)	54% (18%)	FigS24

<sup>a</sup> subfault size of the finite fault model, original S3 model subfault size is 25 km  $\times$  16.6 km<sup>b</sup> Yoffe16(): Yoffe function with rise time 16s with duration in parentheses; Cosine16: Cosine function with rise time 16; Tri16: Triangle function with rise time 16. The slip-rate functions are shown in Figure S16<sup>c</sup> Vr km/s - Rupture onset by constant rupture speed; Rupture onset - follow model rupture onset time; PSRT - peak slip rate time (Figure S15 and Figure S23).<sup>d</sup> median (standard deviation)<sup>e</sup> supplementary figure showing the synthetics and observed waveforms comparison

**Table S3.** Summary of teleseismic P wave velocity synthetics performance on changing geometry, subfault size, slip-rate, and rupture front time-alignment.

Slip model	subfault <sup>a</sup>	slip-rate <sup>b</sup>	slip-rate alignment <sup>c</sup>	P wave correlation <sup>d</sup>	P wave variance reduction <sup>d</sup>	Figure <sup>e</sup>
S3	original	original	original	0.81 (0.01)	55% (25%)	FigS26
S3 projected	original	original	original	0.76 (0.01)	44% (65)	FigS26
S3 projected	original	Yoffe16(40)	original	0.52 (0.02)	20% (1%)	FigS27
S3 projected	original	Yoffe16(40)	S3 PSRT	0.71 (0.02)	50% (8%)	FigS27
S3 projected	original	original	Vr 2.0 km/s	0.48 (0.01)	21% (2%)	FigS28
S3 projected	original	original	Vr 1.5 & 2.0 km/s	0.54 (0.01)	22% (24%)	FigS28
S3 projected	original	Cosine16	S3 PSRT	0.74 (0.02)	52% (21%)	FigS29
S3 projected	original	Tri 16	S3 PSRT	0.72 (0.02)	50% (8%)	FigS29
S3 projected	original	Yoffe16(48)	S3 PSRT	0.68 (0.02)	45% (4%)	FigS30
S3 projected	original	Yoffe16(55)	S3 PSRT	0.67 (0.02)	42% (3)	FigS30
S3 projected	16 km	Yoffe16(40)	S3 PSRT	0.62 (0.01)	32% (11%)	FigS31
S6 projected	16 km	Yoffe16(40)	S3 PSRT	0.53 (0.02)	15% (19%)	FigS31
J3 projected	16 km	Yoffe16(40)	S3 PSRT	0.56 (0.03)	23% (16%)	FigS31
S3 projected	16 km	Yoffe16(40)	S6 PSRT	0.58 (0.02)	32% (13%)	FigS32
S3 projected	16 km	Yoffe16(40)	J3 PSRT	0.55 (0.02)	28% (13%)	FigS32

<sup>a</sup> subfault size of the finite fault model, original S3 model subfault size is 25 km × 16.6 km<sup>b</sup> Yoffe16(): Yoffe function with rise time 16s with duration in parentheses; Cosine16: Cosine function with rise time 16; Tri 16: Triangle function with rise time 16. The slip-rate functions are shown in Figure S16<sup>c</sup> Vr km/s - Rupture onset by constant rupture speed; Rupture onset - follow model rupture onset time; PSRT - peak slip rate time (Figure S15 and Figure S23).<sup>d</sup> median (standard deviation)<sup>e</sup> supplementary figure showing the synthetics and observed waveforms comparison

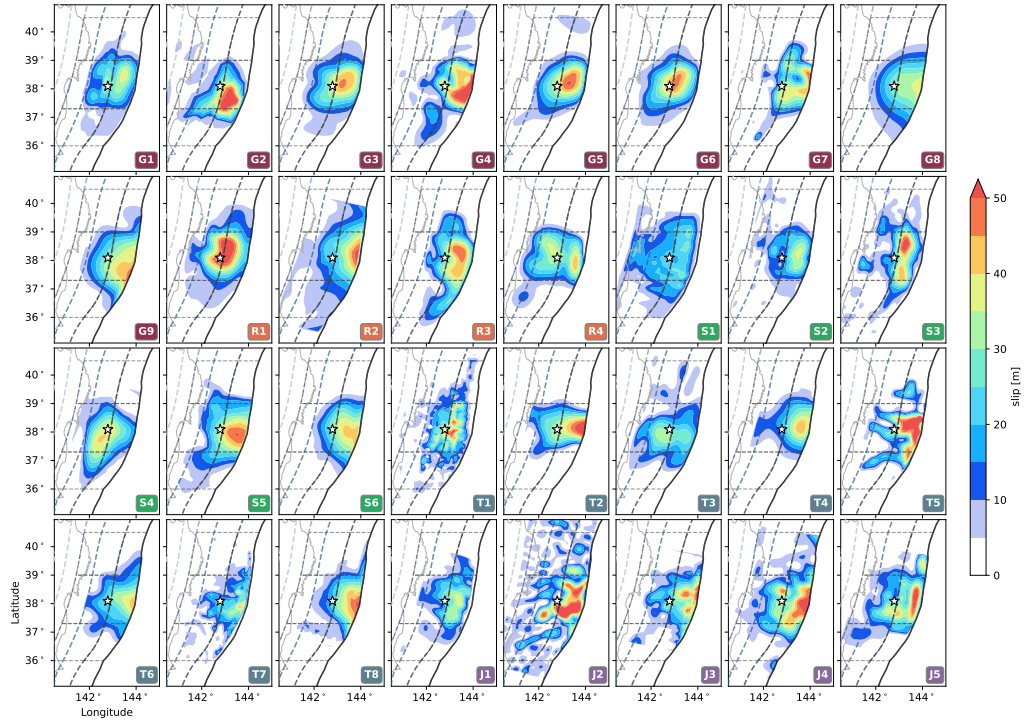


**Figure S1.** Slip distribution of the 32 re-parameterized finite fault models with 1 km subfault size. Slip distribution are shown as color contours. All model acronyms are defined in Figure 1 and detailed in Text S1. Grey lines indicate the six zones listed in Figure 4.

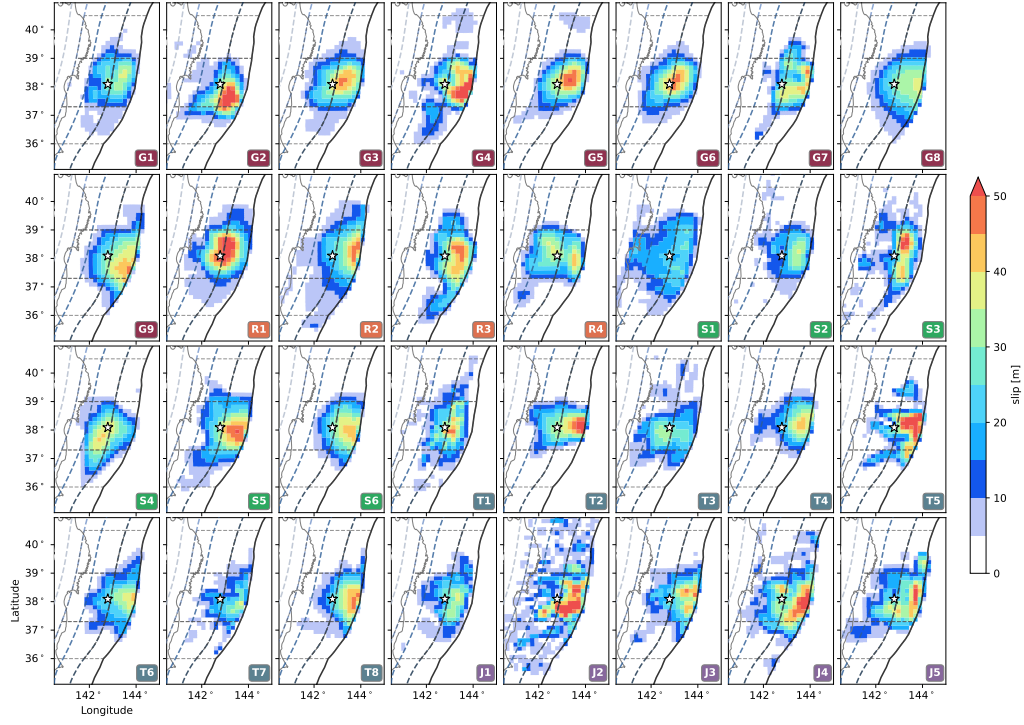


**Figure S2.** Slip distribution of the 32 re-parameterized finite fault models with 16 km sub-fault size. Same plotting style as Figure S1. Slip distributions are shown as color contours. All model acronyms are defined in Figure 1 and detailed in Text S1.

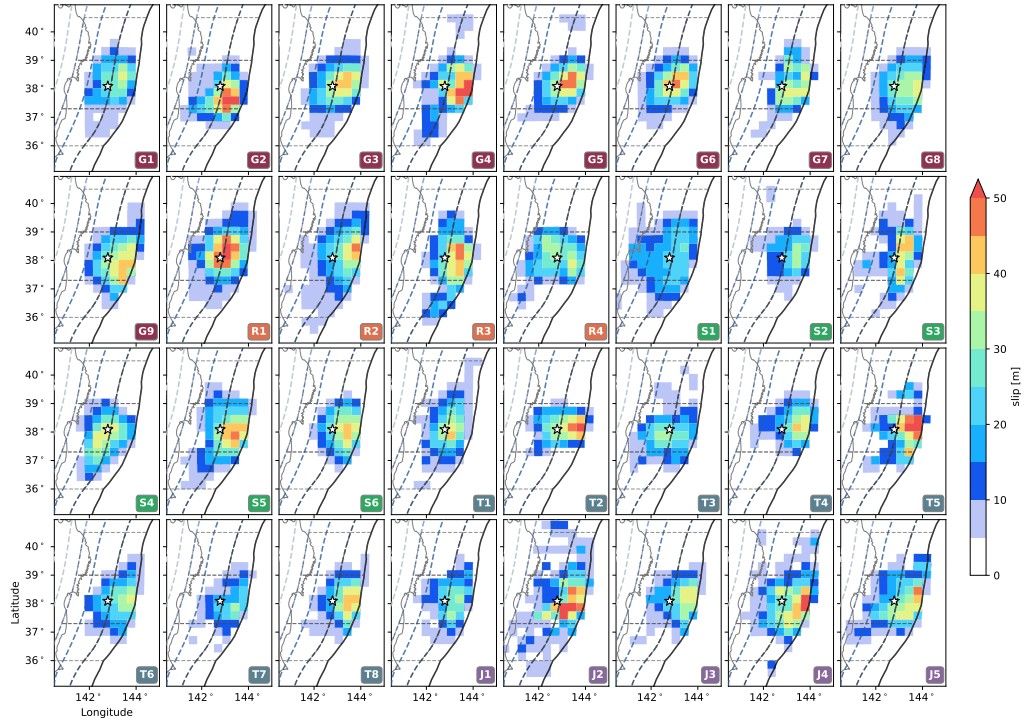


**Figure S3.** Slip distribution of the 32 re-parameterized finite fault models with 32 km sub-fault size. Same plotting style as Figure S1. Slip distributions are shown as color contours. All model acronyms are defined in Figure 1 and detailed in Text S1.

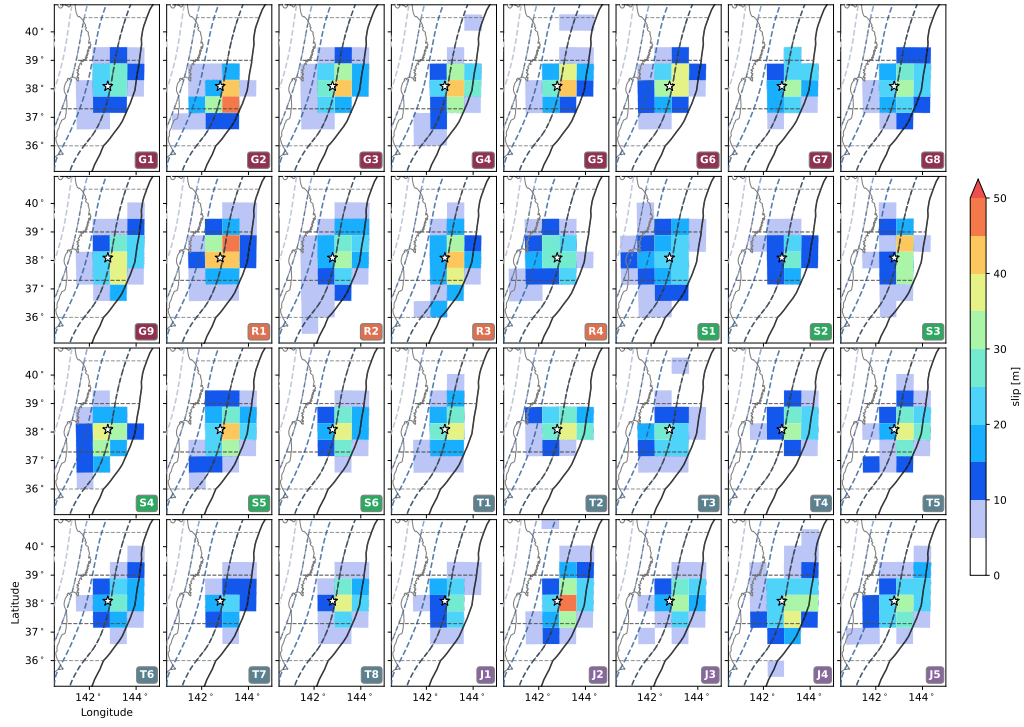


**Figure S4.** Slip distribution of the 32 re-parameterized finite fault models with 64 km sub-fault size. Same plotting style as Figure S1. Slip distributions are shown as color contours. All model acronyms are defined in Figure 1 and detailed in Text S1.



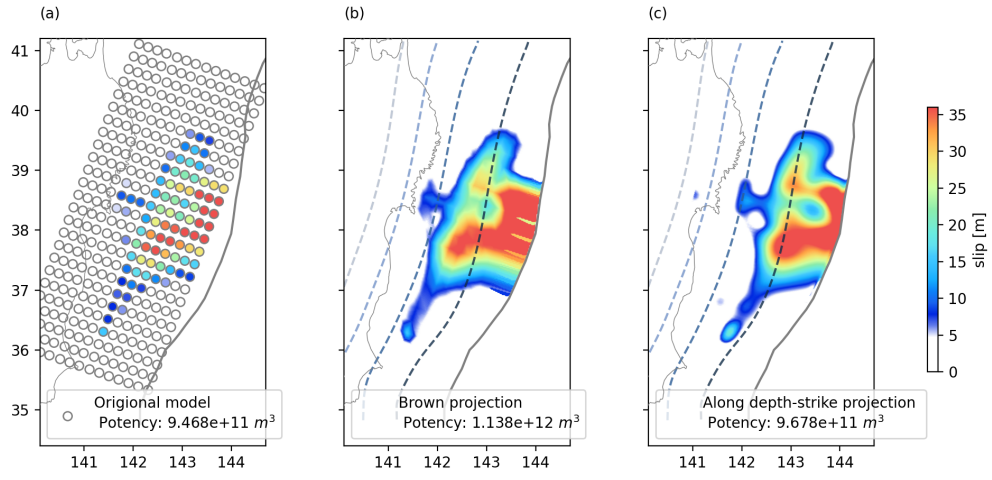


**Figure S5.** Comparison of (a) the original G7 model (Zhou et al., 2014), (b) the projected model using the Brown method, and (c) the projection method of this study. Inset indicates the total potency, defined as the slip times the subfault area. Solid line delineates the trench location. Dashed lines indicate the Slab 2.0 model with a 20 km depth interval.

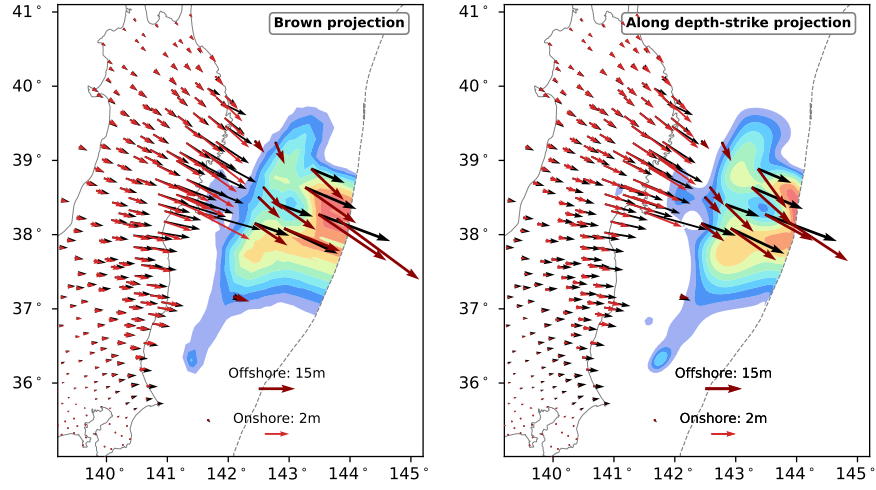


**Figure S6.** Comparison of the onshore and offshore horizontal displacements by (a) the projected model using the Brown method, and (b) the projection method of this study. Black and red arrows are the observations and synthetics respectively. Dotted line indicates the trench line. Color-filled contour shows the projected slip distribution.

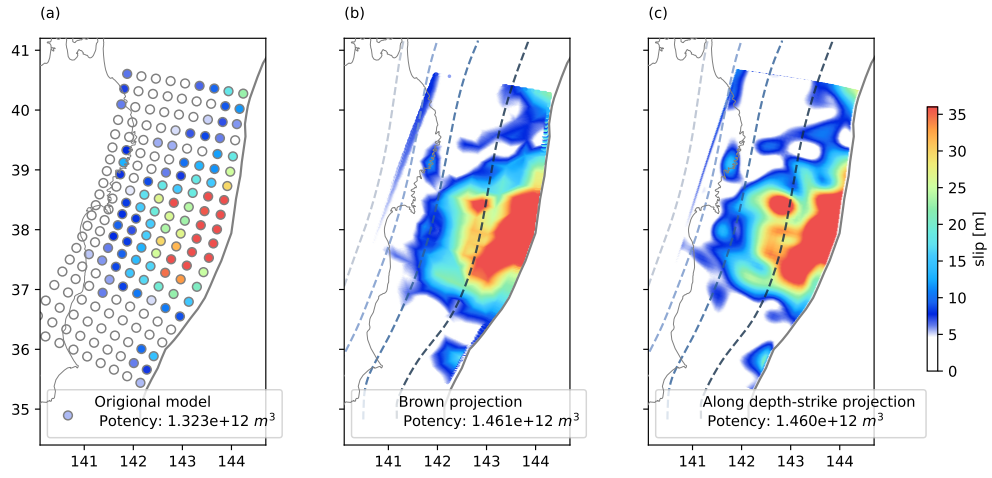


**Figure S7.** Comparison of (a) the original J4 model (Melgar & Bock, 2015), (b) the projected model using the Brown method, and (c) the projection method of the study. Inset indicates the total potency, defined as the slip times the subfault area. Solid line delineates the trench location. Dashed lines indicate the Slab 2.0 model with a 20 km depth interval. The J4 model was obtained using the Slab 1.0 geometry.

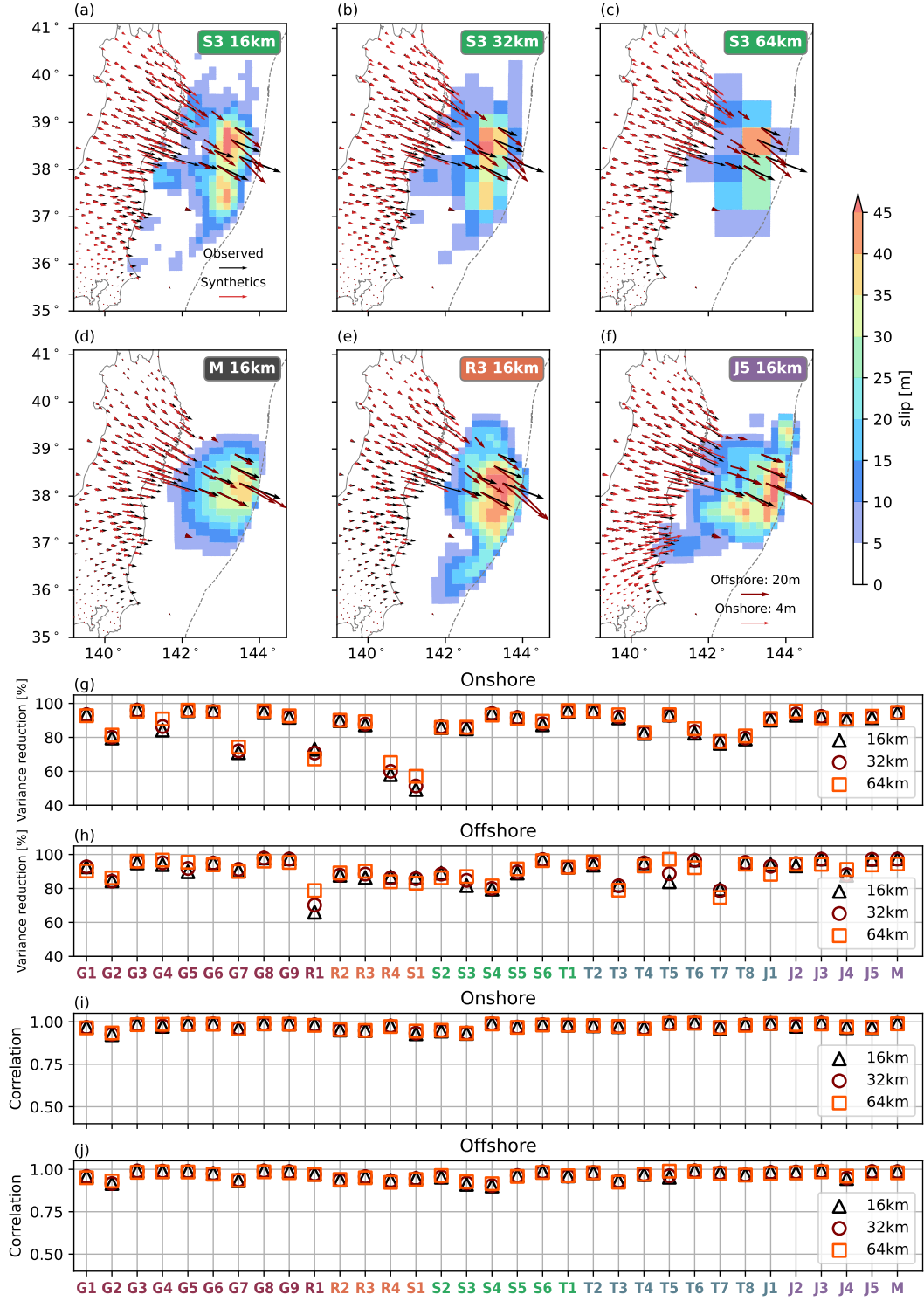


**Figure S8.** Onshore and offshore horizontal geodetic displacement observations (red arrows) and synthetics (black arrows), and their correlation and variance reduction values. (a)–(c) synthetic (black) and observed (red) horizontal geodetic displacements of model S3 at the 16 (a), 32 (b), and 64 km (c) scales. (d)–(f) geodetic synthetics and observations of model M (d), R3 (e), J5 (f) at the 16 km scale. (g) variance reduction values between the onshore geodetic synthetics and observations at the 16, 32, and 64 km scales. (h) variance reduction values between the offshore geodetic synthetics and observations at the 16, 32, and 64 km scales. (i) Correlation coefficients between the onshore geodetic synthetics and observations at the 16, 32, and 64 km scales. (j) Correlation coefficients between the offshore geodetic synthetics and observations at the 16, 32, and 64 km scales.

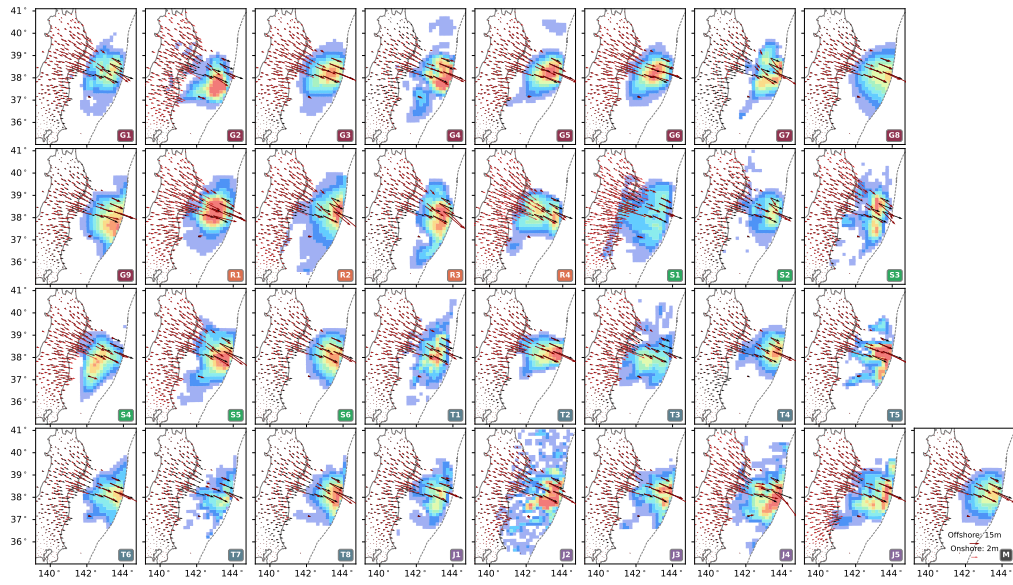


**Figure S9.** Onshore and offshore horizontal geodetic displacement observations (red arrows) and synthetics (black arrows) of all 33 models in 16 km scale.

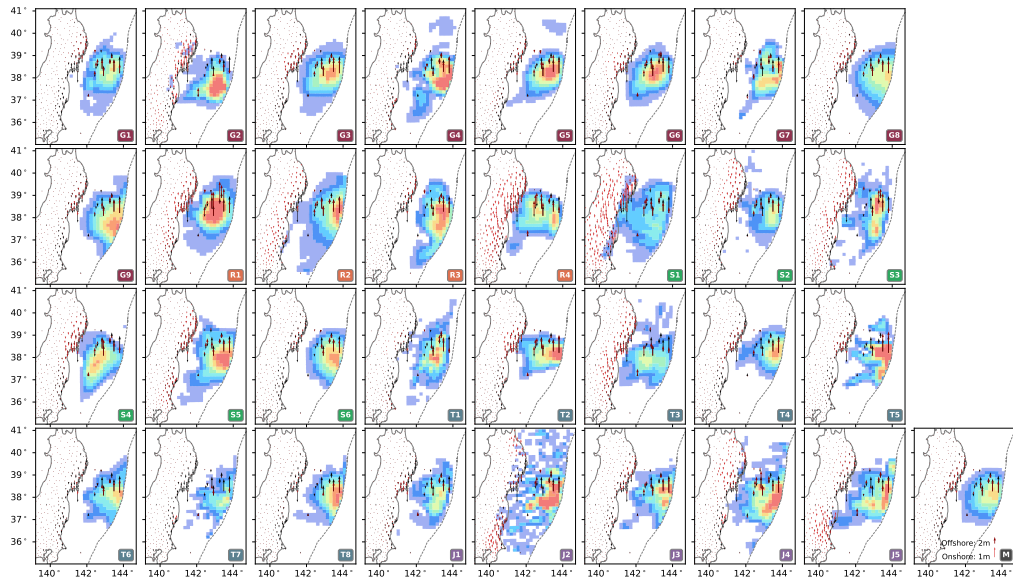


**Figure S10.** Onshore and offshore vertical geodetic displacement observations (red arrows) and synthetics (black arrows) of all 33 models in 16 km scale.



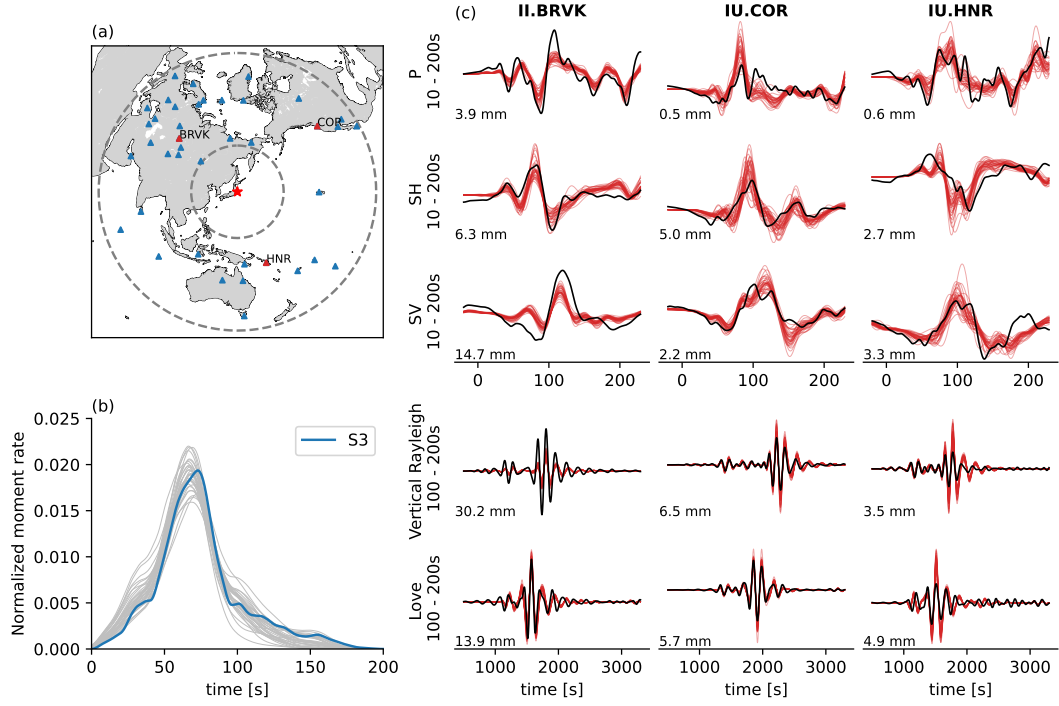


**Figure S11.** Comparison of teleseismic observations and synthetics at 32 km scale. (a) Map view of 40 II and IU stations used in the analysis. Red triangles are the stations in (c). Dotted circles show epicentral distances of  $30^{circ}$  and  $90^{circ}$ , respectively. (b) Normalized moment rate functions of the original S3 model and the other 32 finite-fault models and the median model. (c) Synthetic and observed teleseismic waveforms. Black lines are the observed waveforms; red lines are the synthetic waveforms from the 32 finite-fault models and the median model. Five rows are P wave, SH wave, SV wave, Rayleigh wave, and Love wave, respectively. Amplitudes of the observed waveforms are labeled at the lower-left corner of each waveform plot.

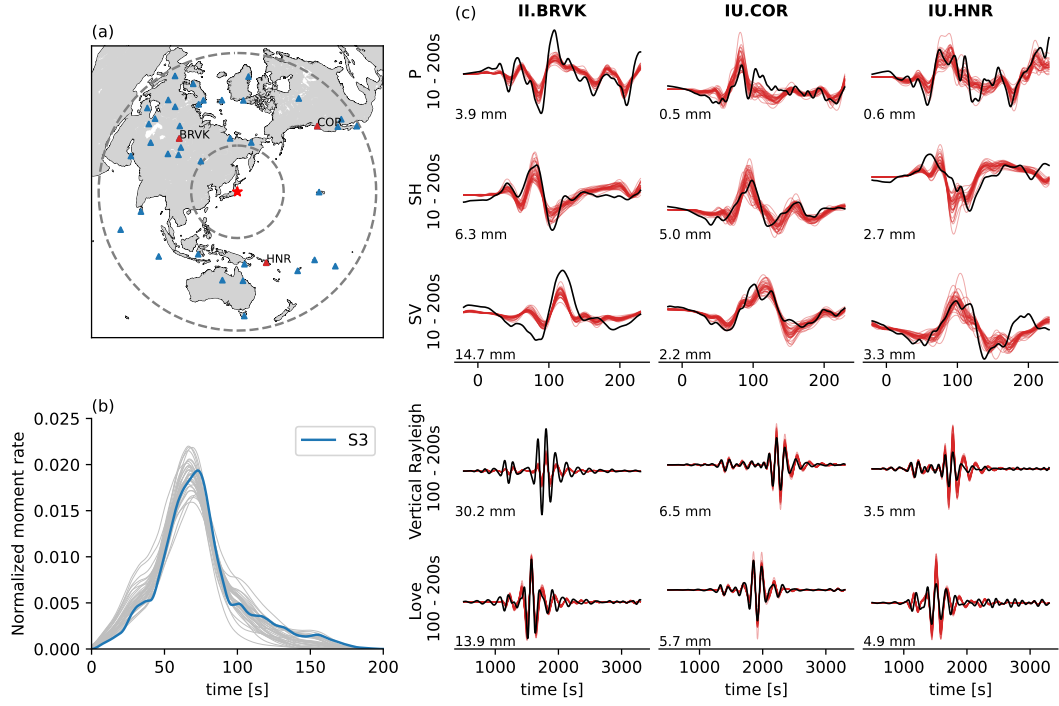


**Figure S12.** Comparison of teleseismic observations and synthetics at a 64 km scale. (a) Map view of 40 II and IU stations used in the analysis. Red triangles are the stations in (c). Dotted circles show epicentral distances of  $30^{circ}$  and  $90^{circ}$ , respectively. (b) Normalized moment rate functions of the original S3 model and the other 32 finite-fault models and the median model. (c) Synthetic and observed teleseismic waveforms. Black lines are the observed waveforms; red lines are the synthetic waveforms from the 32 finite-fault models and the median model. Five rows are P wave, SH wave, SV wave, Rayleigh wave, and Love wave, respectively. Amplitudes of the observed waveforms are labeled at the lower-left corner of each waveform plot.

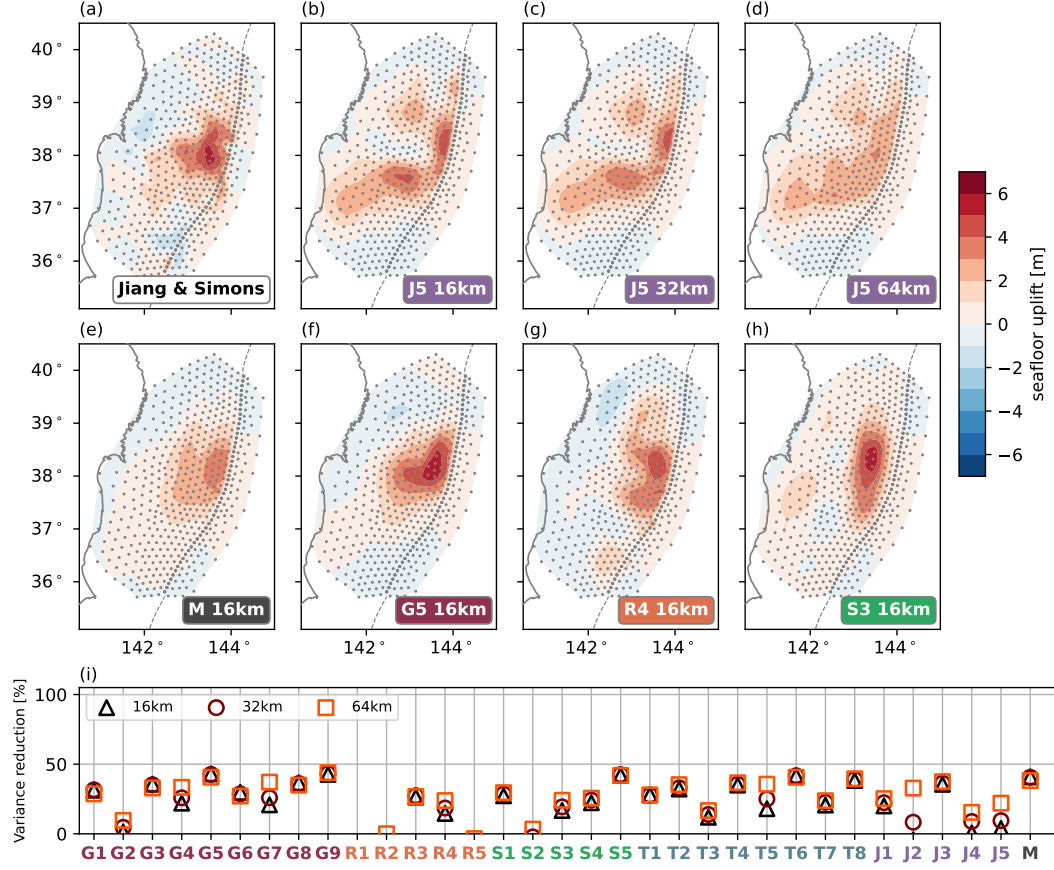


**Figure S13.** Seafloor uplift model of Jiang and Simons (2016) (model SJS), seafloor uplift synthetics from the finite-fault models, and their variance reduction values between the synthetics with model SJS. Grey dots show the modeled grid points. (a) Model SJS. (b)–(d) Synthetic seafloor uplift of model J5 model at the 16 (b), 32 (c), and 64 km (d) scales, respectively. (e)–(h) Synthetic seafloor uplift of the median slip model, models G5, R4, and S3 at a 16 km scale. (i) variance reduction values between model SJS and synthetics of the 32 finite-fault models and the median model at the 16, 32, and 64 km scales.

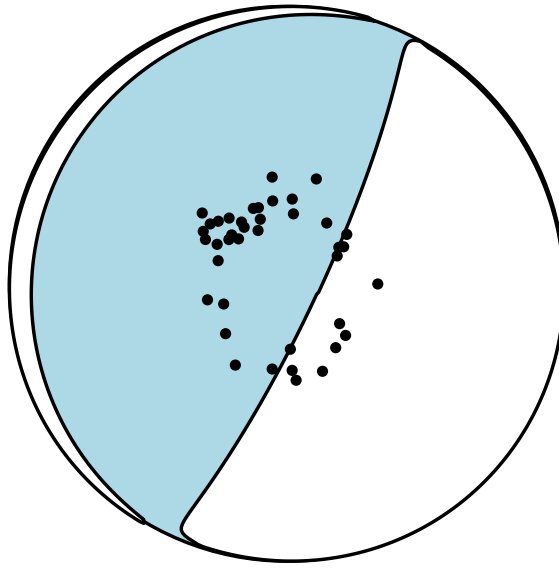


**Figure S14.** Azimuth and takeoff angle of the teleseismic stations used in the analysis with the Tohoku-Oki earthquake moment tensor from GCMT.

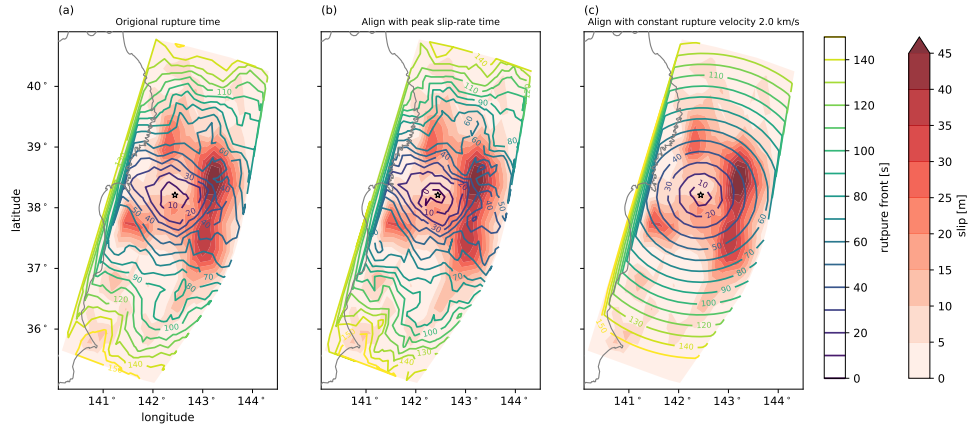


**Figure S15.** Rupture onset time alignment for the teleseismic synthetics. Panel a shows the original rupture onset time of the S3 model. Panel b shows the alignment with the peak-slip-rate time (PSRT) of the S3 model. Panel c shows the alignment with the constant 2.0 m/s rupture velocity.

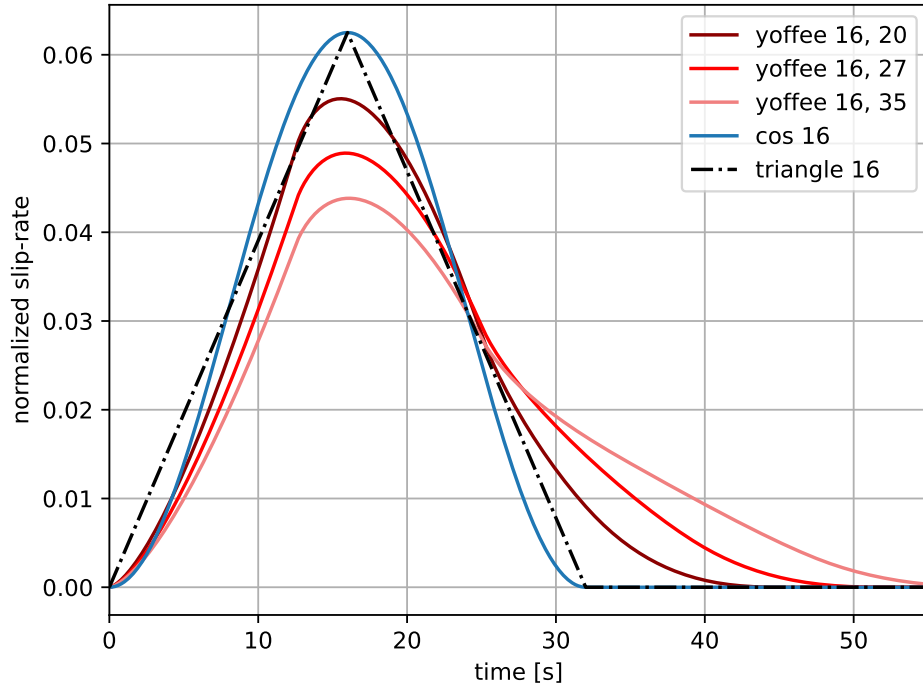


**Figure S16.** Normalized slip-rate functions evaluated in the teleseismic synthetics. Slip-rate functions include three sets of Yoffe slip-rate functions (reds) with the same rise-time of 16 s and varying duration of 40, 48, and 55 s, and a cosine function with a 16 s rise time (blue) and a symmetrical-triangular function with a rise time of 16 s (grey).



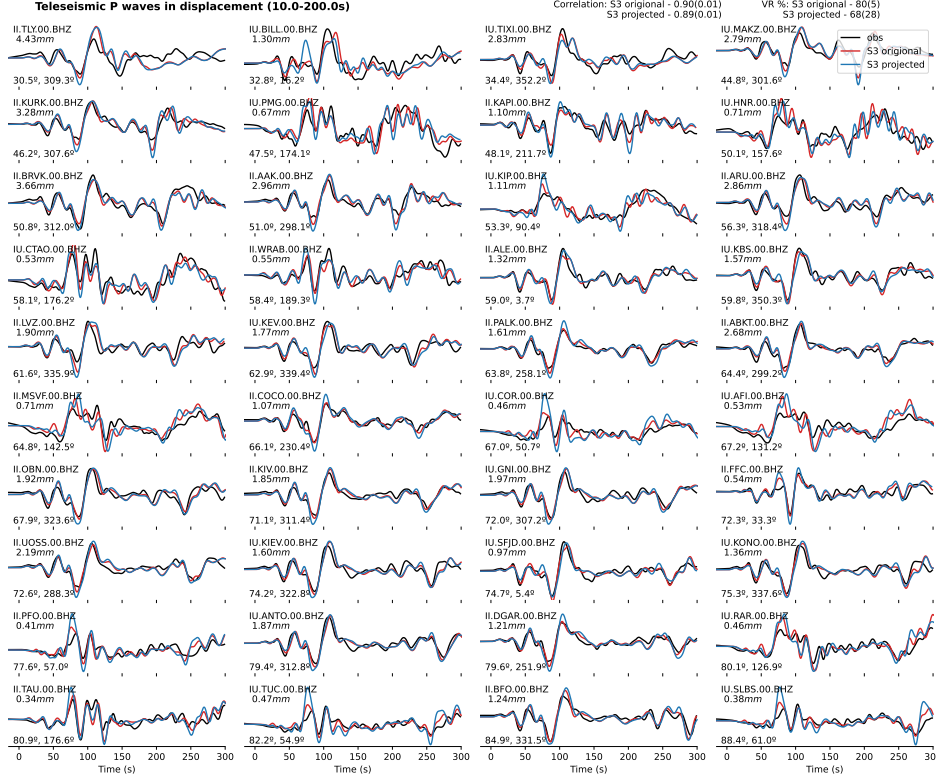


**Figure S17.** Comparison of the Teleseismic P wave on changing fault geometry. P wave synthetics of the S3 original model (red) and S3 projected model (blue) and observations (black) for all 40 stations in Figure 11. The waveform is filtered between 10–200s period and aligned with maximum cross-correlation value. Overall correlation and variance reduction value with the observations are labeled at the top-right corner of the figure. Medians and standard deviations of the correlation value of the original model and projected model synthetics are 0.9 and 0.01, and 0.89 and 0.01, respectively. The median variance reduction of the original model is 80%, and the projected model is 68%, respectively. Distance in degree and back azimuth of the station are shown at the bottom-left corner of each waveform plot. Station trace ID and amplitude are labeled at the upper-left corner of each waveform plot.

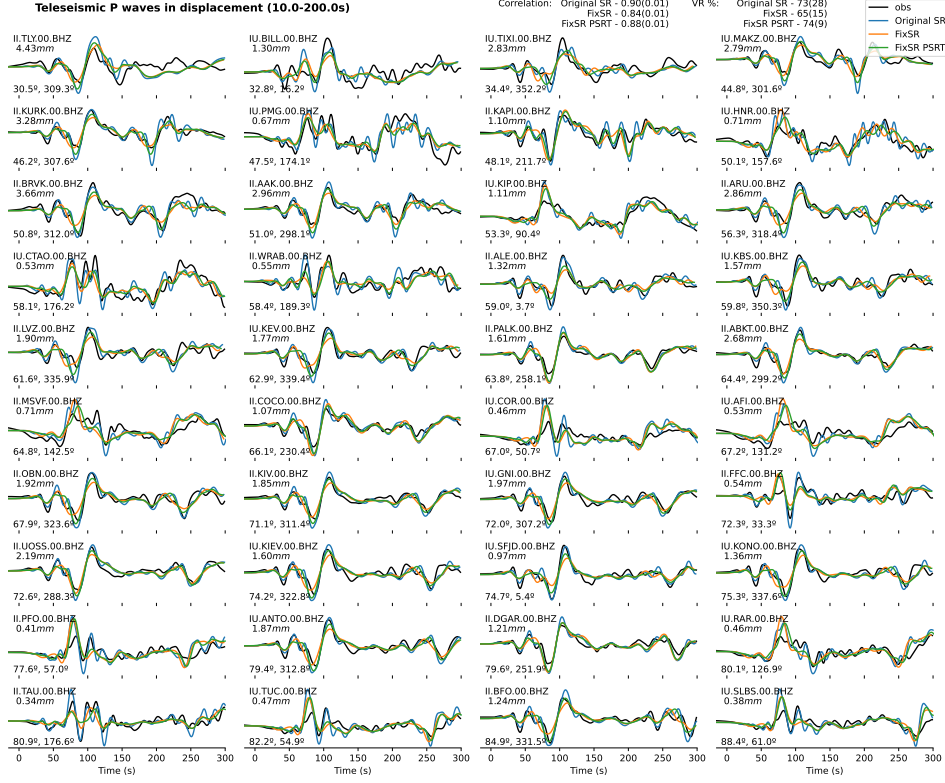


**Figure S18.** Comparison of the Teleseismic P wave on unifying slip rate function with Yoffe function and rupture front alignment. Same plotting as Figure S17. P wave synthetics of the S3 projected model [S3p] (blue), S3 projected unified slip rate model [S3p FixSR](orange), S3 projected unified slip rate model aligned with S3 peak slip rate time [S3p FixSR PSRT](green) and observations (black) of all 40 stations.

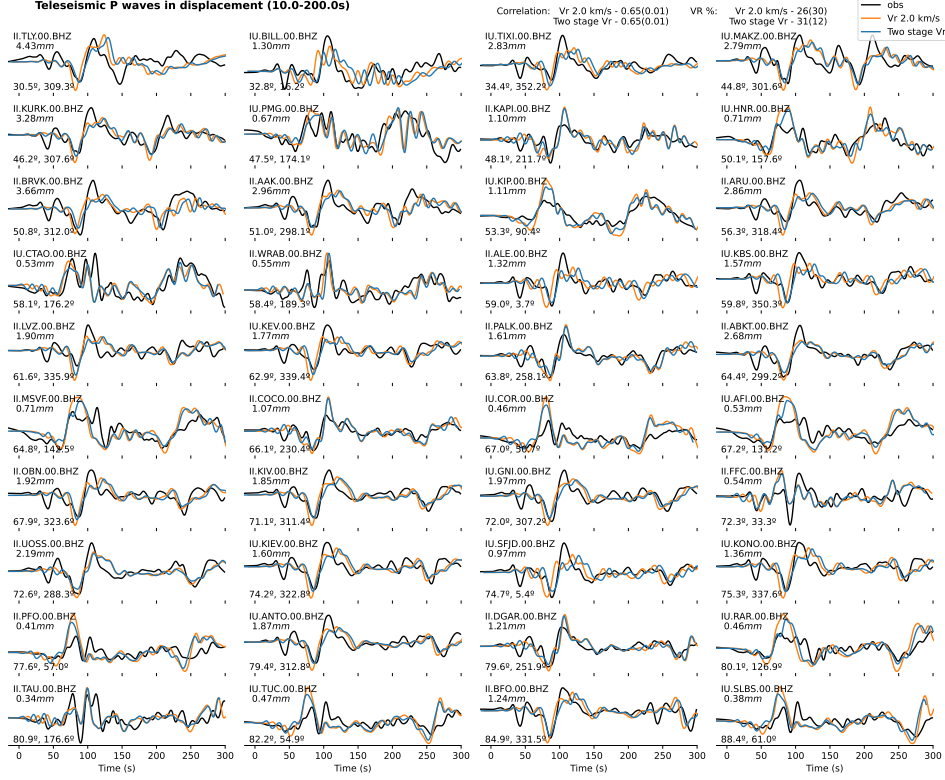


**Figure S19.** Comparison of the Teleseismic P wave on aligning rupture onset with constant rupture velocity. Same plotting as Figure S17. S3 projected with fix 2.0 km/s rupture velocity model [S3p Vr 20km/s](blue), P wave synthetics with two steps 1.5 km/s and 2.0 km/s rupture velocity model [orange] (blue) and observations (black) of all 40 stations.

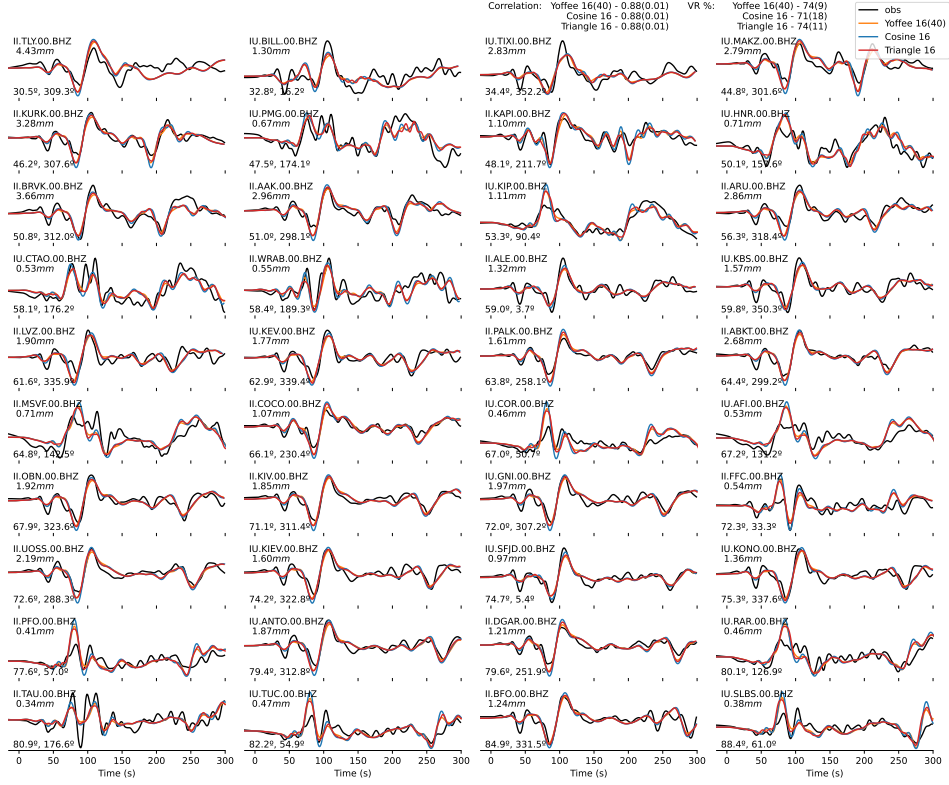


**Figure S20.** Comparison of the Teleseismic P wave with varying slip-rate function. Same plotting as Figure S17. P wave synthetics with Yoffe slip-rate function (orange), synthetics with cosine slip-rate function (blue), synthetics with triangular slip-rate function (red), and observations (black) of all 40 stations.

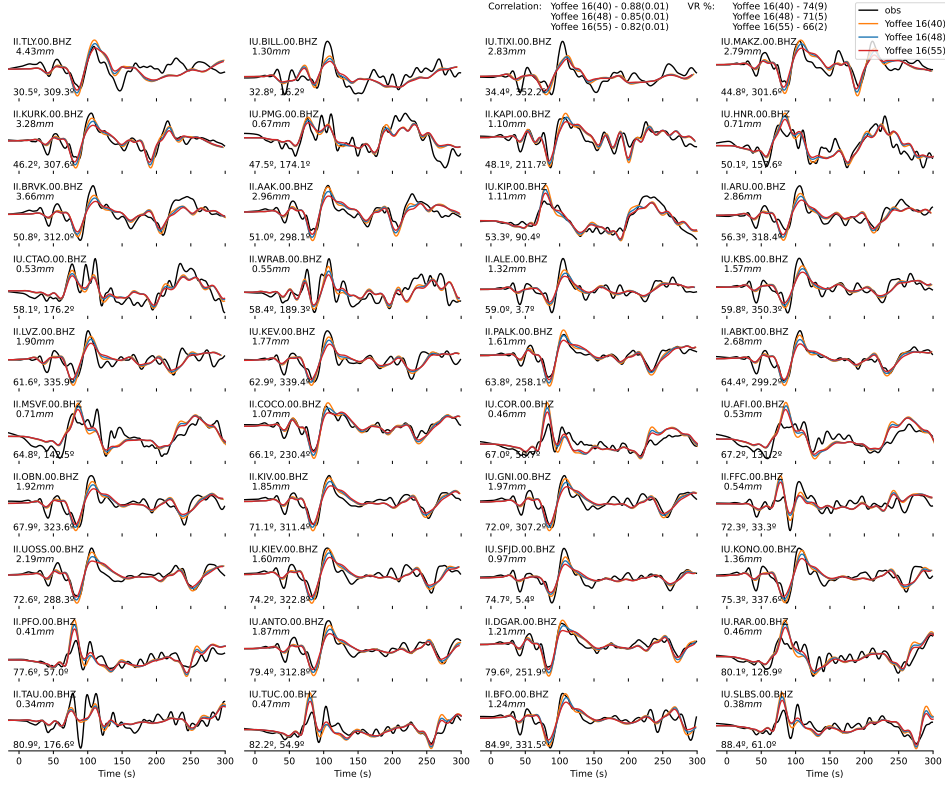


**Figure S21.** Comparison of the Teleseismic P wave with varying Yoffe slip-rate function. Same plotting as Figure S17. P wave synthetics with Yoffe function rise time and duration of 16 and 40 s (orange), synthetic with Yoffe function rise time and duration of 16 and 48s (blue), synthetics with Yoffe function rise time and duration of 16 and 55s (red), and observations (black) of all 40 stations.

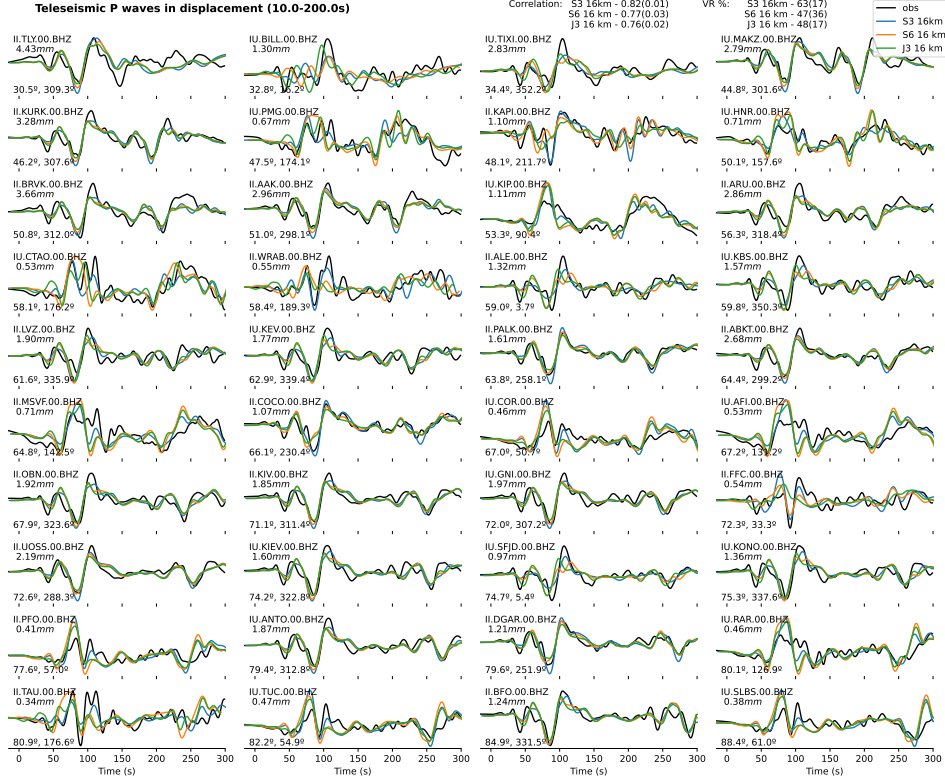


**Figure S22.** Comparison of the Teleseismic P wave with slip model S3, S6 and J3 at 16 km resolution. Same plotting as Figure S17. P wave synthetics of slip model S3 (blue), synthetics of slip model S6 (orange), synthetics of slip model J3 (green), and observations (black) of all 40 stations.



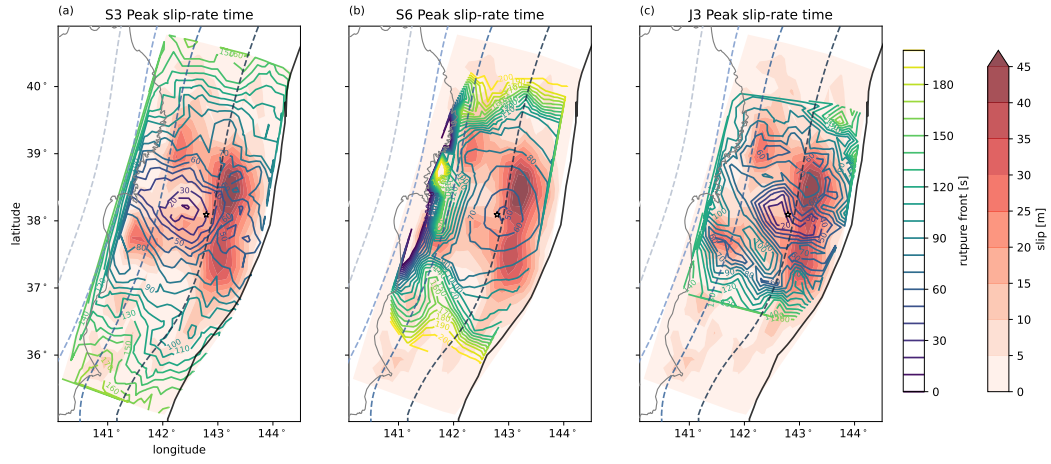


**Figure S23.** Comparing models peak slip-rate time. Color contours show the (a) S3, (b) S6, and (c) J3 models' peak slip-rate time, respectively. Model S3 slip distribution is shown as the color-filled contour. The peak slip-rate time of models S6 and J3 are spatially limited due to the different fault parameterization of these two models. Hypocenters of these models are also shifted due to the projection onto the realistic geometry

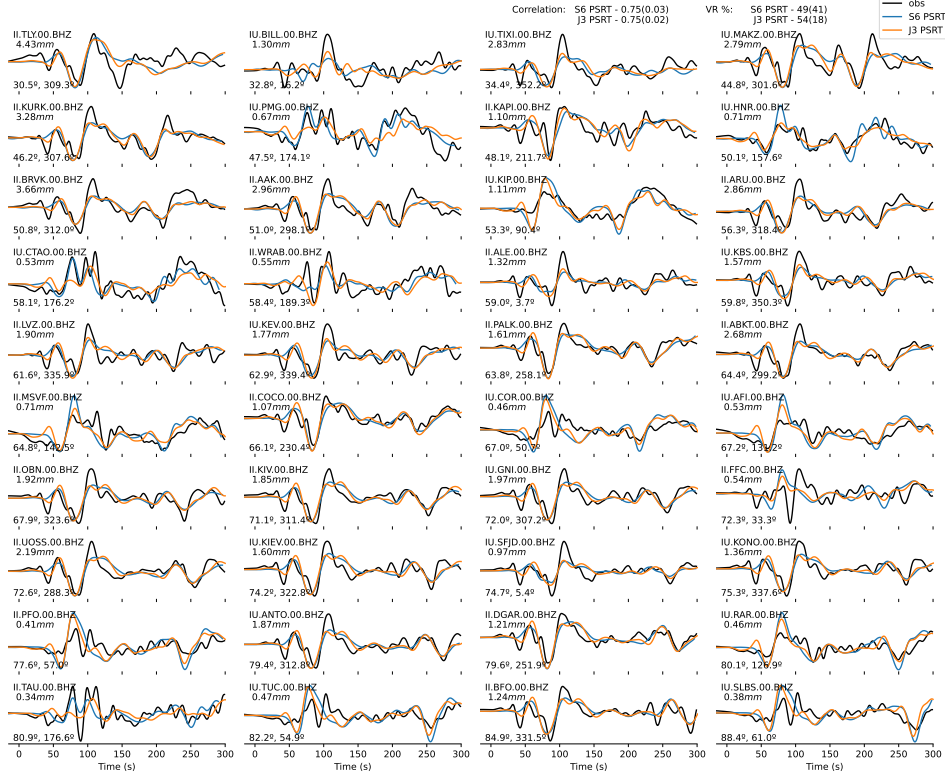


**Figure S24.** Comparison of the Teleseismic P wave with rupture front alignment with the peak-slip-rate time of S6 and J3 models with S3 slip model at 16 km resolution. Same plotting as Figure S17. P wave synthetics with rupture front align with S6 peak-slip-rate time (blue), synthetics with rupture front align with J3 peak-slip-rate time (orange), and observations (black) of all 40 stations.

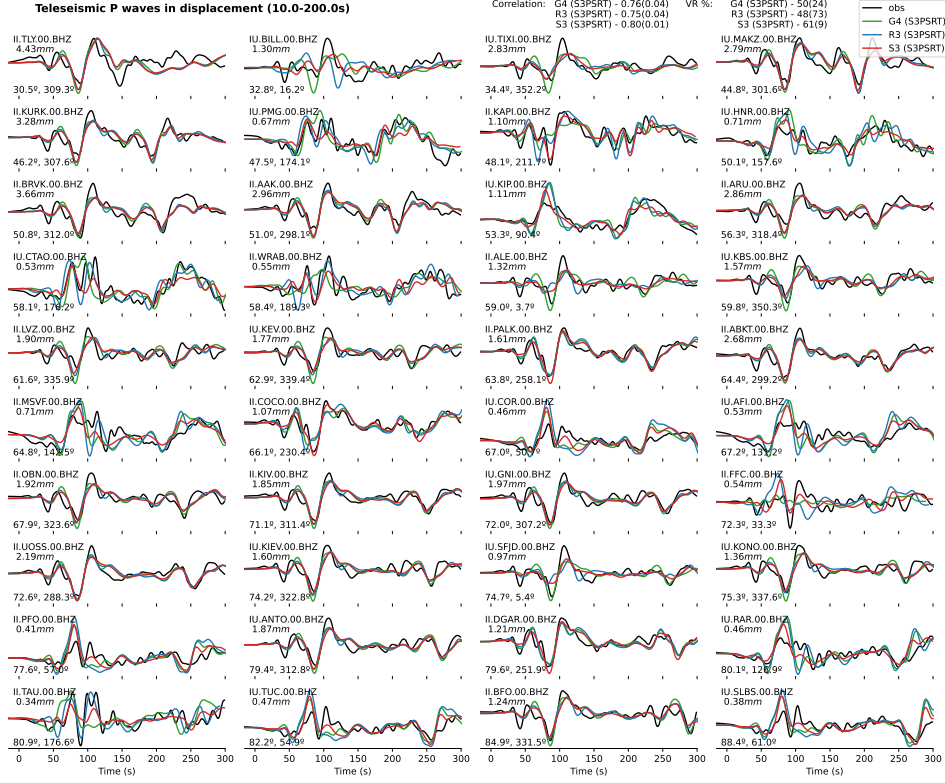


**Figure S25.** Comparison of the Teleseismic P wave with slip model G4, R3 and S3 at 16 km resolution. Same plotting as Figure S17. P wave synthetics with G4 model slip distribution (green), synthetics with R3 model slip distribution (blue), synthetics with S3 model slip distribution (red), and observations (black) of all 40 stations.

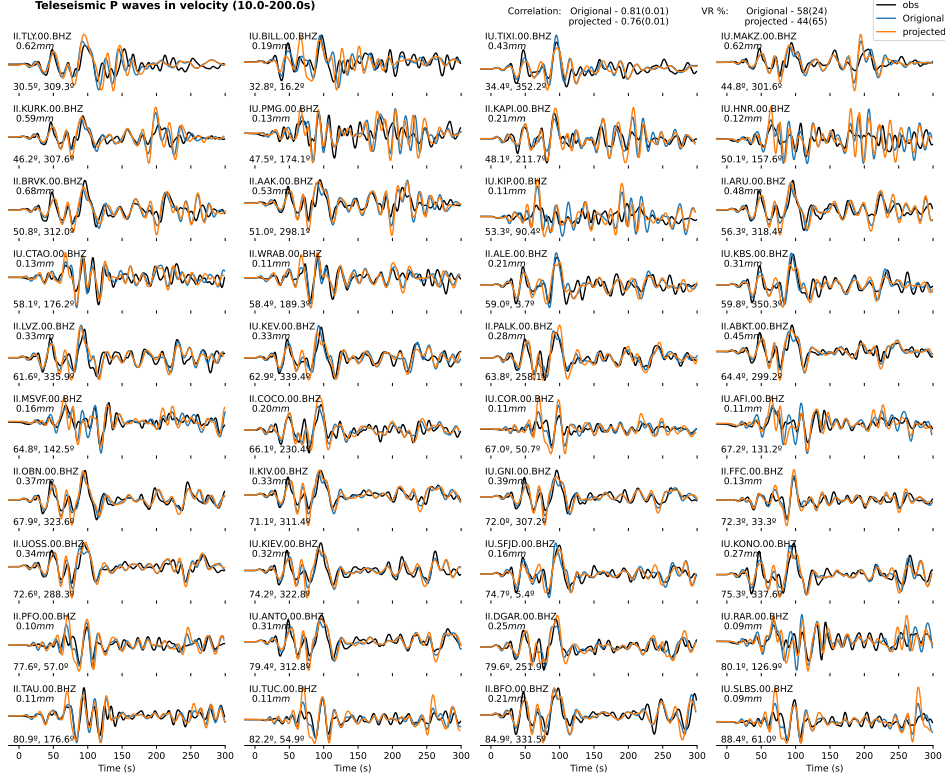


**Figure S26.** Comparison of the Teleseismic velocity P wave with original S3 finite-fault model and projected S3 finite-fault model. Same plotting as Figure S17. P wave synthetics of the original S3 finite-fault model (blue), synthetics of the projected S3 finite-fault model (orange), and observations (black) of all 40 stations.

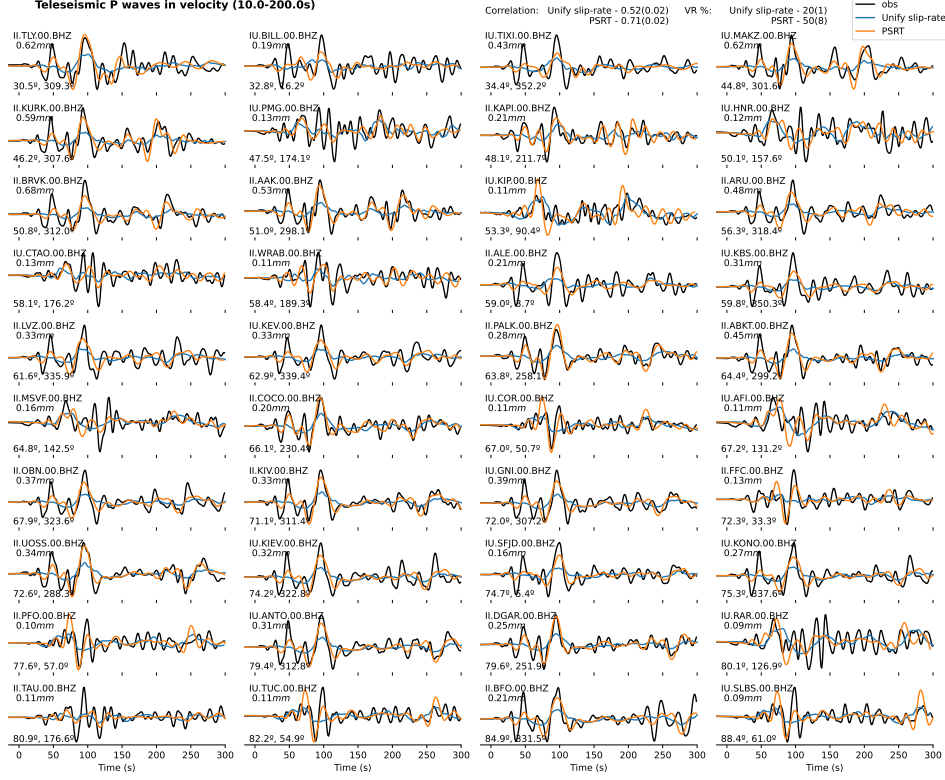


**Figure S27.** Comparison of the Teleseismic velocity P wave with unified slip-rate function with original onset-time alignment and peak-slip-rate time alignment. Same plotting as Figure S17. P wave synthetics of unified slip-rate function with original onset-time alignment (blue), synthetics of unified slip-rate function with peak-slip-rate time alignment (orange), observations (black) of all 40 stations.

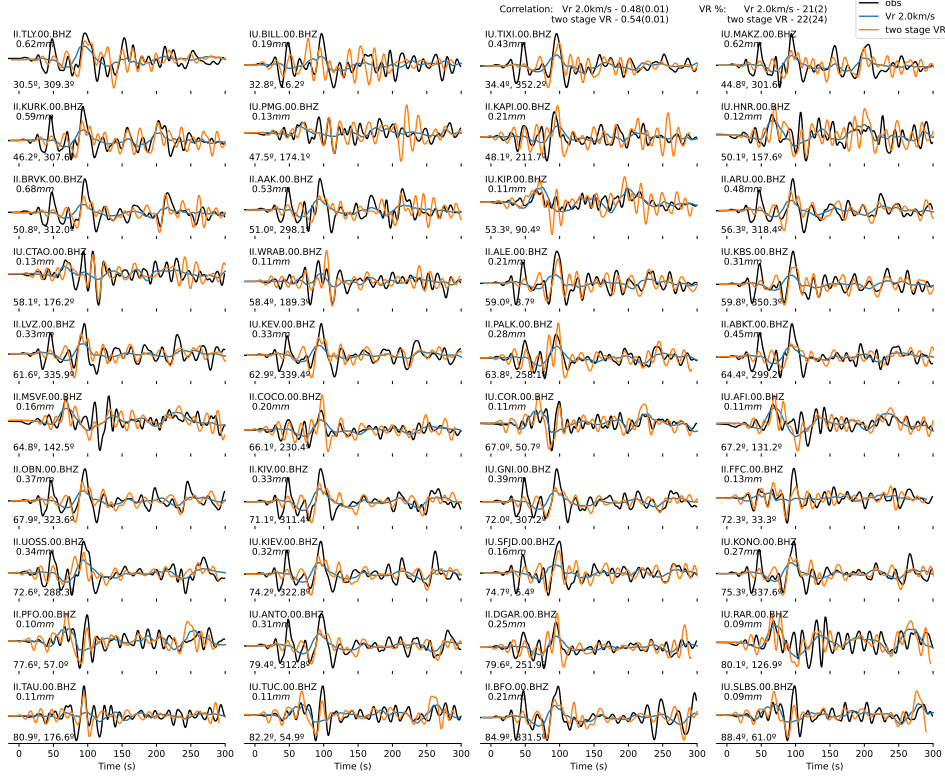


**Figure S28.** Comparison of the Teleseismic velocity P wave with onset-time alignment with constant rupture speed of 2.0 km/s and two-step rupture speed with S3 slip distribution. Same plotting as Figure S17. P wave synthetics of constant rupture speed of 2.0 km/s (blue), synthetics of two-step rupture speed (orange), observations (black) of all 40 stations.

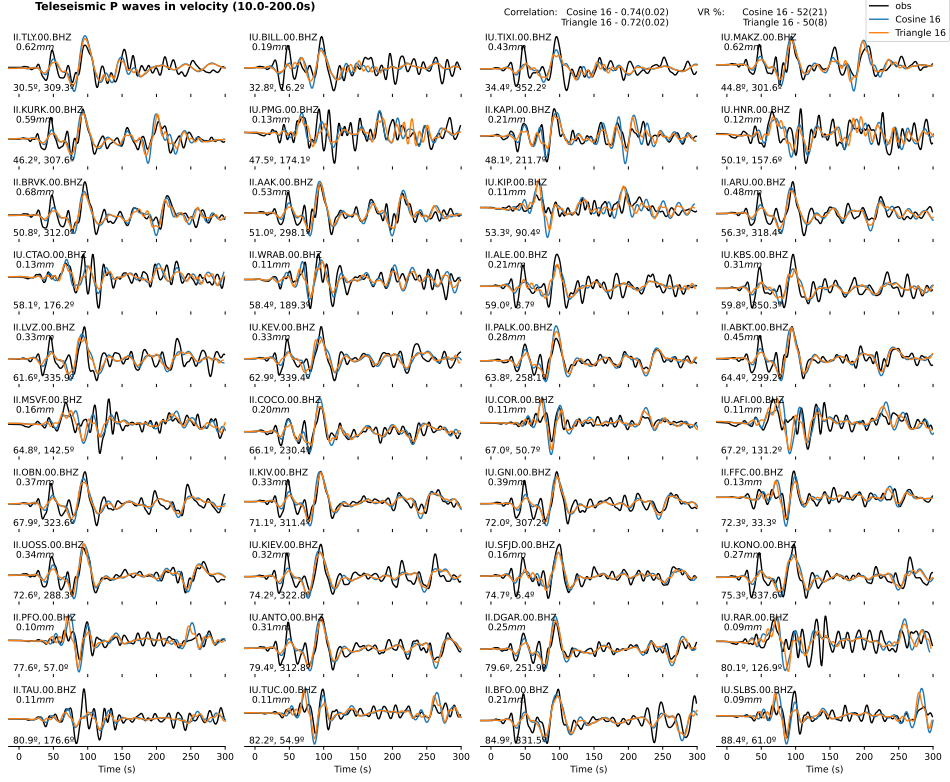


**Figure S29.** Comparison of the Teleseismic velocity P wave with cosine slip-rate function and triangular slip-rate function. Same plotting as Figure S17. P wave synthetics of cosine slip-rate function (blue), synthetics of triangle slip-rate function (orange), observations (black) of all 40 stations.



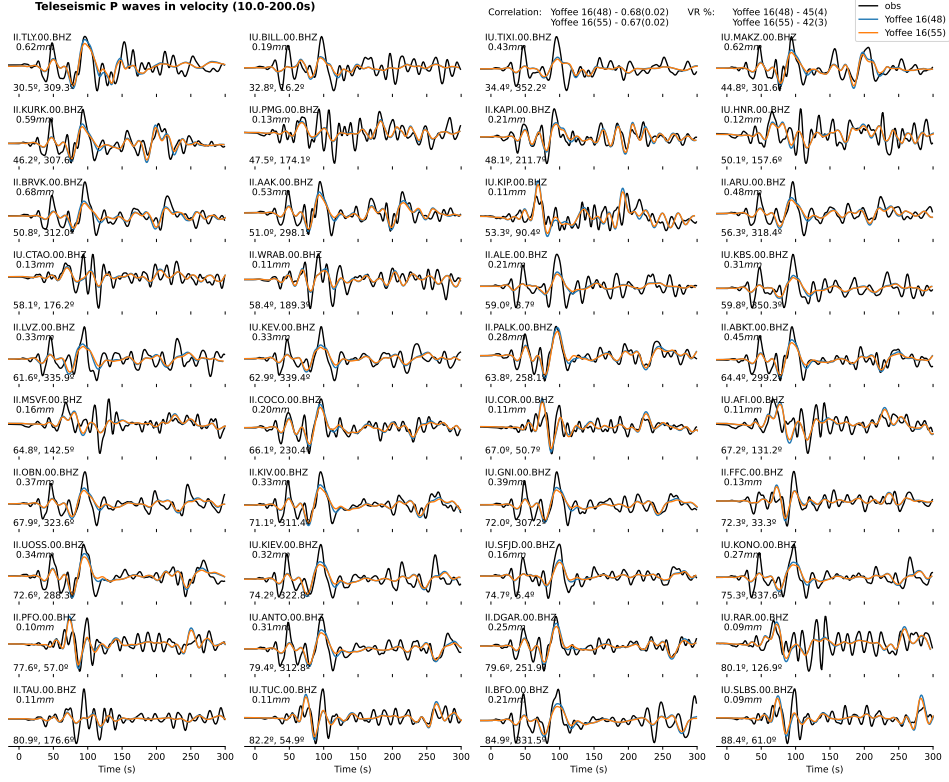


**Figure S30.** Comparison of the Teleseismic velocity P wave with varying Yoffee function. Same plotting as Figure S17. P wave synthetics of the Yoffee function with 48s duration (blue), synthetics of the Yoffee function with 55s duration (orange), and observations (black) of all 40 stations.

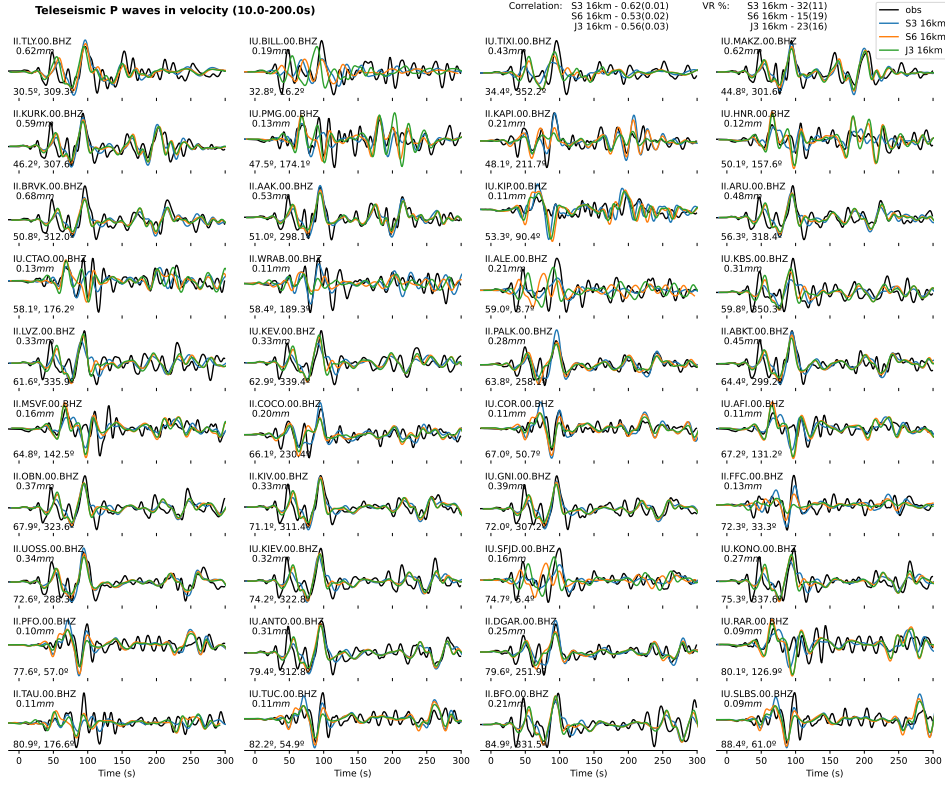


**Figure S31.** Comparison of the Teleseismic velocity P wave with different model slip distribution and S3 model PSRT onset-time alignment. Same plotting as Figure S17. P wave synthetics of S3 slip model (blue), synthetics of S6 slip model (orange), synthetics of J3 slip model (green), and observations (black) of all 40 stations.

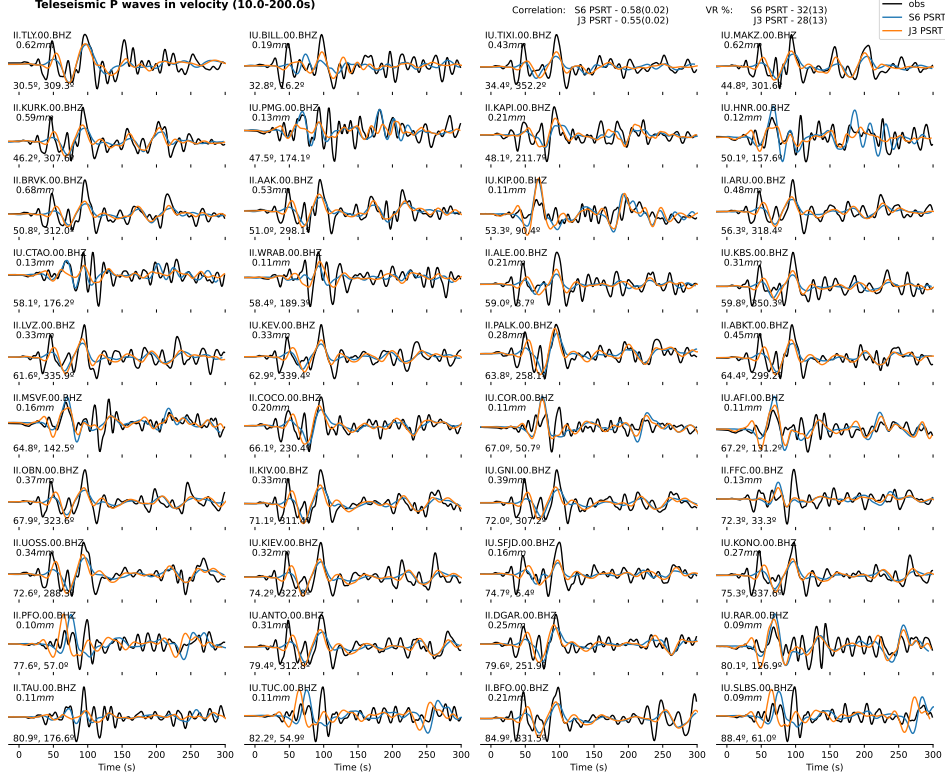


**Figure S32.** Comparison of the Teleseismic velocity P wave with different model PSRT onset-time alignment and S3 model slip distribution. Same plotting as Figure S17. P wave synthetics of S6 model PSRT (blue), synthetics of J3 model PSRT (orange), and observations (black) of all 40 stations.

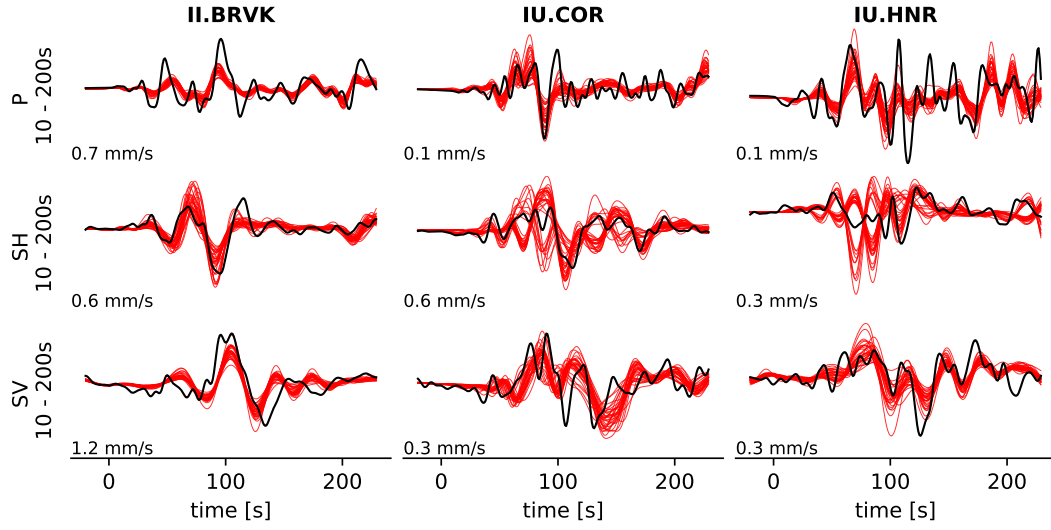


**Figure S33.** Comparison of teleseismic velocity observations and synthetics at a 16 km scale. Synthetic and observed teleseismic waveforms. Black lines are the observed waveforms; red lines are the synthetic waveforms from the 32 finite-fault models and the median model. Three rows are P wave, SH wave and SV wave, respectively. Amplitudes of the observed waveforms are labeled at the lower-left corner of each waveform plot.

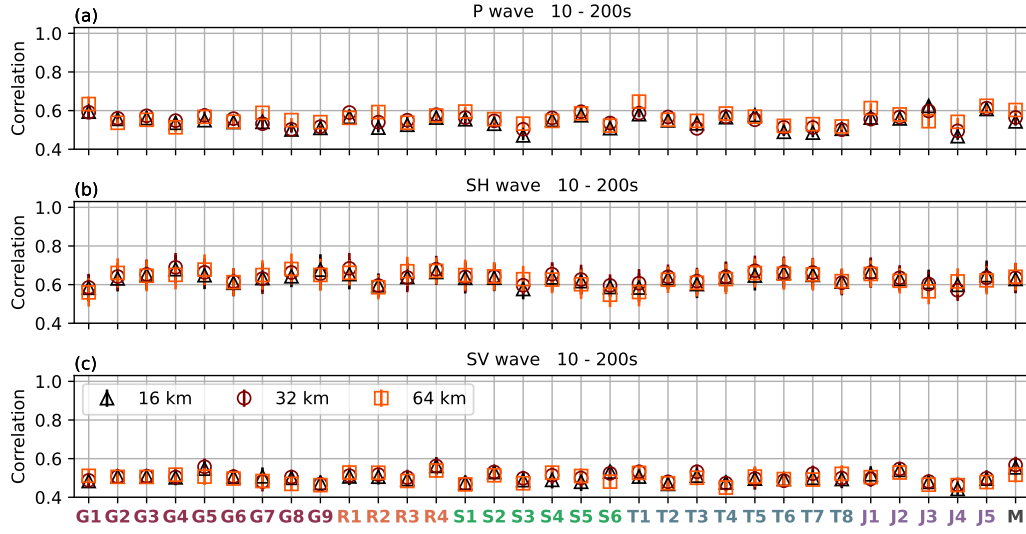


**Figure S34.** Correlation coefficient values between the teleseismic velocity observations and synthetics at the 16, 32, and 64 km scales. (a) P wave. (b) SH wave. (c) SV wave. Median correlation values between the synthetic and observed teleseismic waveforms at the 40 teleseismic stations are taken as the characteristic correlation coefficient values for each model. Three markers indicate the characteristic median values for models at the 16, 32, and 64 km scales. Error bars represent the associated standard deviation of correlation coefficient values of the 40 stations.

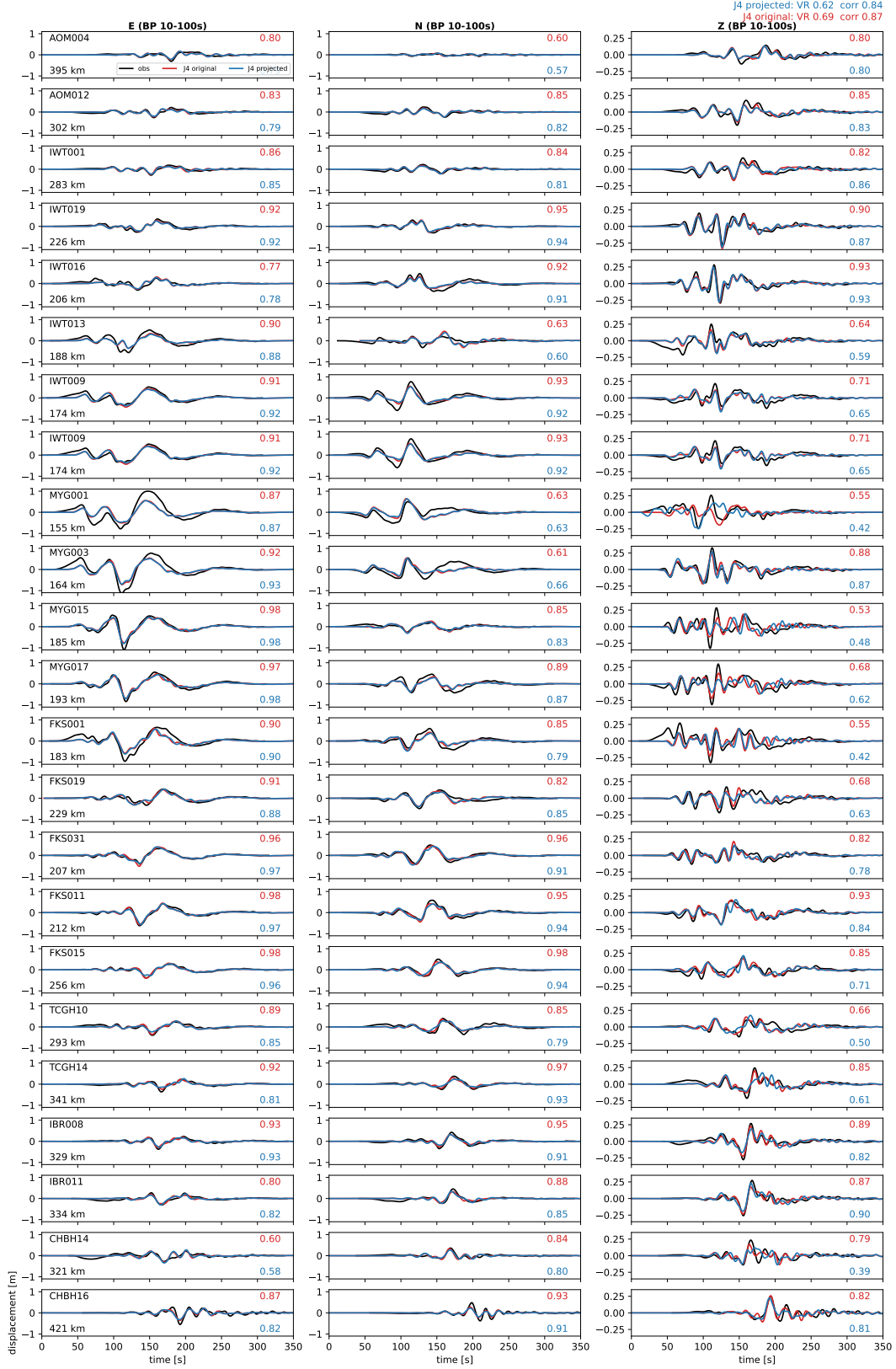


**Figure S35.** Comparison of strong ground motion observations and synthetics of original and projected J4 model. Black lines are the observations. Red lines are the synthetics from J4 original subfault geometry. Blue lines are the synthetics with the projected J4 model. The correlation values of each component are shown on the top right and bottom right of each waveform subplot. Station name and distance from the centroid location are shown in top left and bottom left of each waveform subplot. The overall median variance and the correlation value of the two sets of synthetics are shown at the top right of the figure.

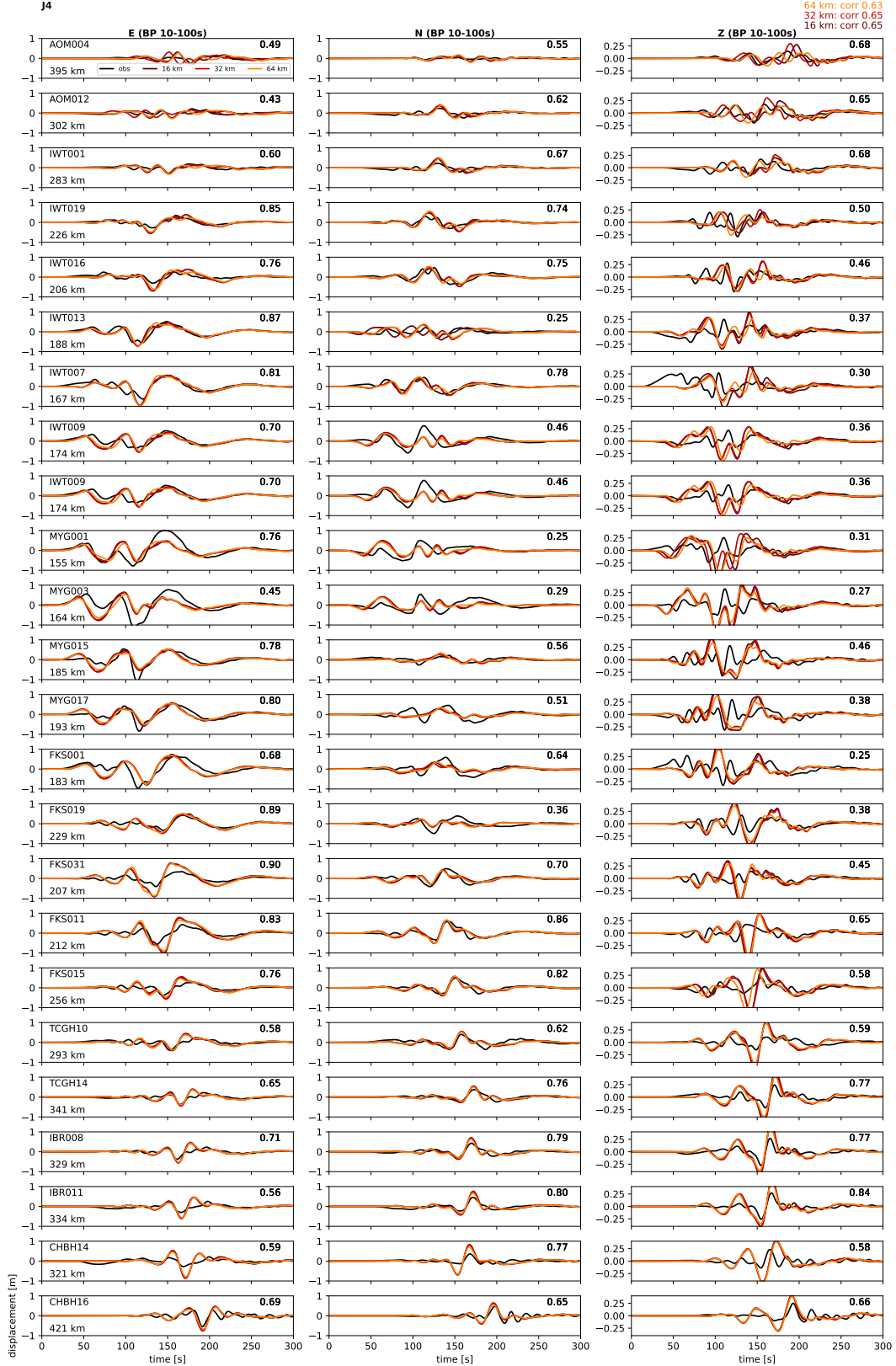


**Figure S36.** Comparison of strong ground motion observations and synthetics of projected and unified slip-rate J4 model at 16, 32 and 64 km scale. Black lines are the observations. Dark red, red, and yellow lines are the J4 synthetics of 16, 32, and 64 km scale, respectively. The correlation values of each component are shown on the top right and bottom right of each waveform subplot. Station name and distance from the centroid location are shown in top left and bottom left of each waveform subplot. The overall median variance and the correlation value of the two sets of synthetics are shown at the top right of the figure.



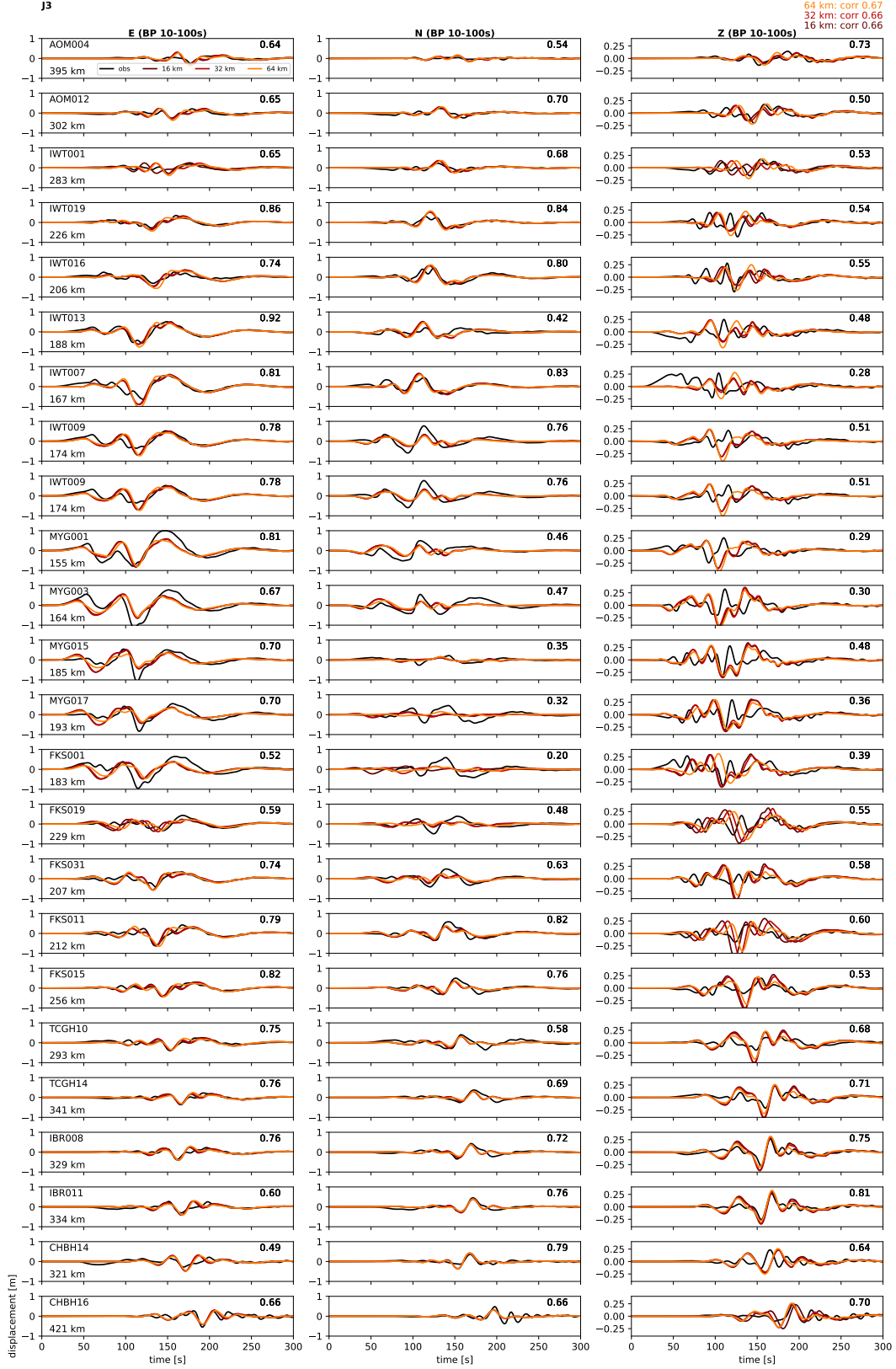


**Figure S37.** Comparison of strong ground motion observations and synthetics of projected and unified slip-rate J3 model at 16, 32 and 64 km scale. Black lines are the observations. Dark red, red, and yellow lines are the J4 synthetics of 16, 32, and 64 km scale, respectively. The correlation values of each component are shown on the top right and bottom right of each waveform subplot. Station name and distance from the centroid location are shown in top left and bottom left of each waveform subplot. The overall median variance and the correlation value of the two sets of synthetics are shown at the top right of the figure.

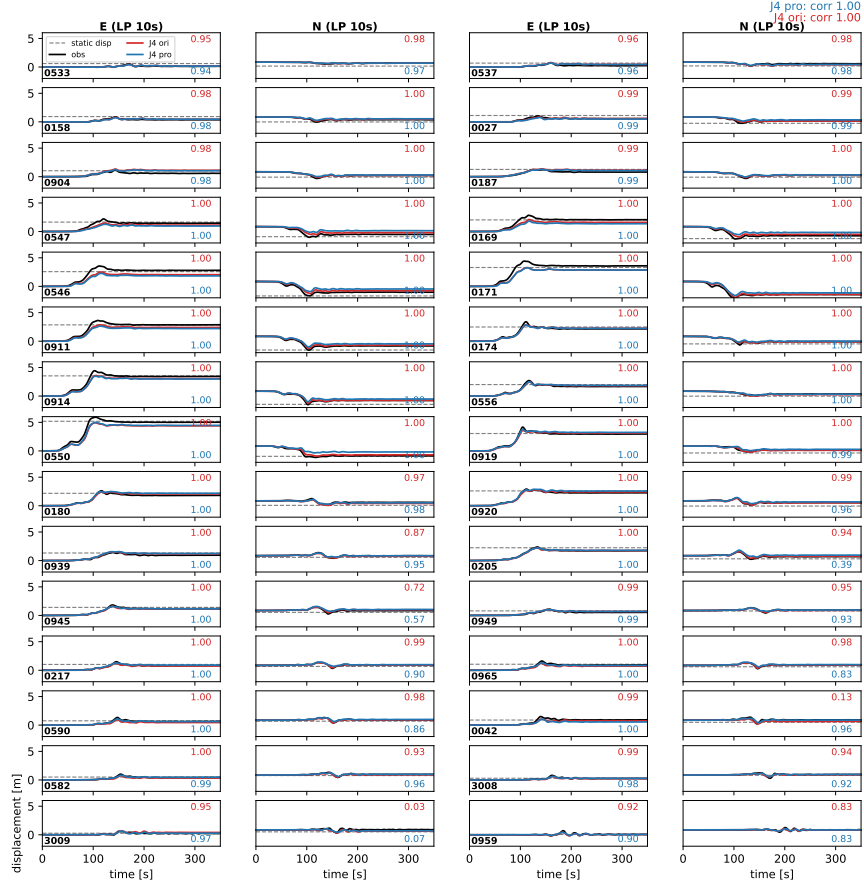


**Figure S38.** Comparison of high rate-GNSS observations and synthetics of original and projected J4 model. Black lines are the observations. Red and blue lines are the J4 synthetics of the original finite-fault model and the projected model. The grey dashed line is the static offset using the 3D velocity structure Green's function. The correlation values of each component are shown on the top right and bottom right of each waveform subplot. Station name and distance from the centroid location are shown in top left and bottom left of each waveform subplot. The overall median variance and the correlation value of the two sets of synthetics are shown at the top right of the figure.

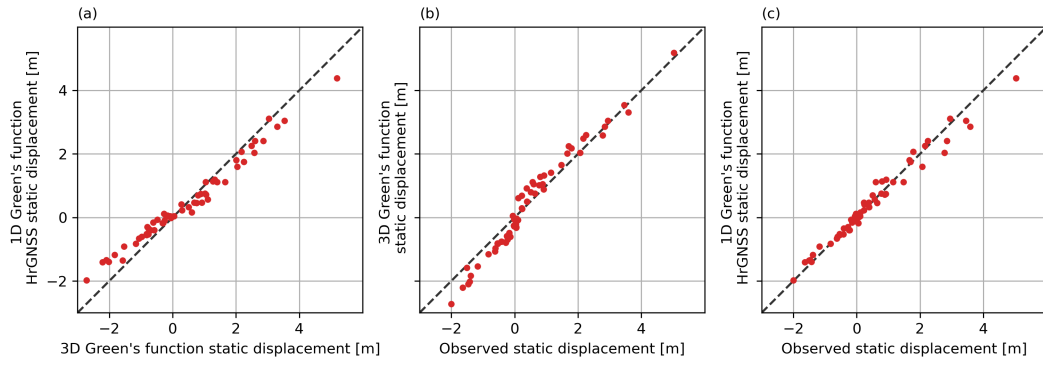


**Figure S39.** Comparison of static offset between Model J4 HrGNSS synthetics using 1D Green's function, Model J4 static offset synthetics using 3D Green's function and observations.

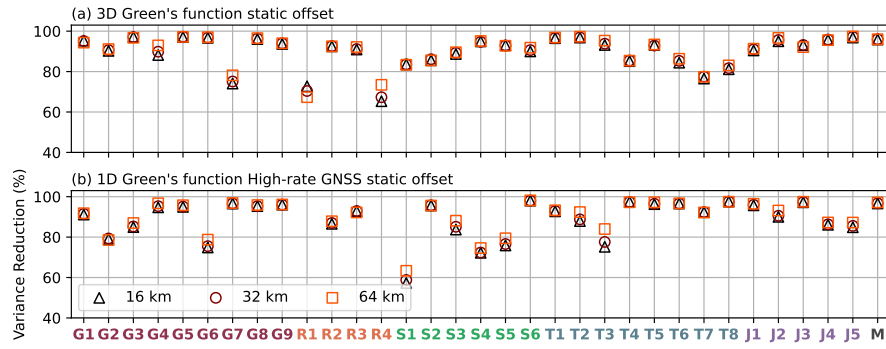


**Figure S40.** Geodetic offset variance reduction comparison with (a) 3D Green's function and (b) 1D Green's function High-rate GNSS static offset with the observations for 33 models at 16, 32, and 64 km scale. Markers indicate the variance reduction of the static offset between the synthetics and the observations.

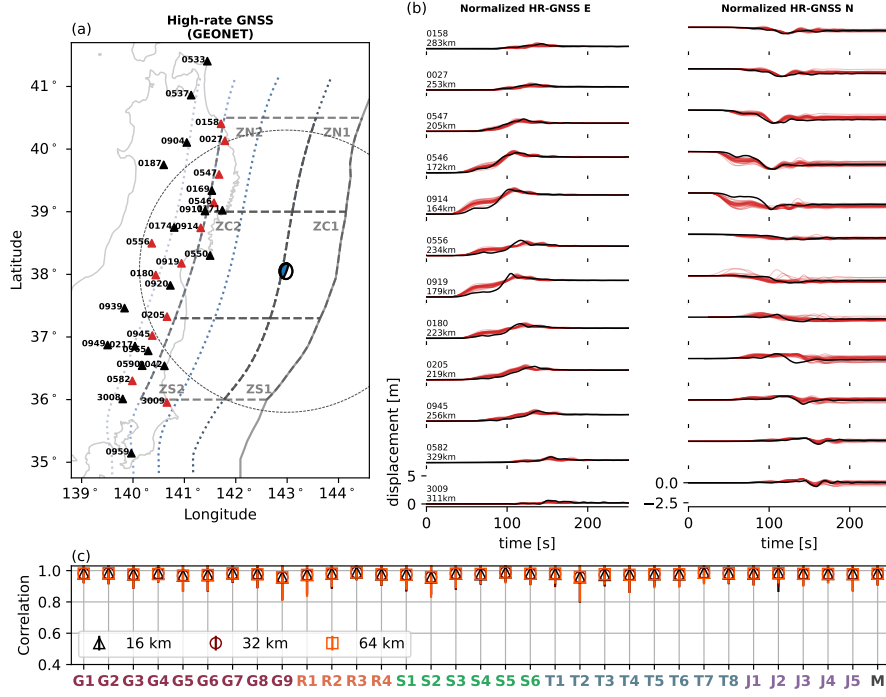


**Figure S41.** Comparison of normalized high-rate GNSS observations and synthetics at 16 km slip model scale. (a) Map view of the GEONET stations used in the study. Red triangles are the stations in (b). Beach-ball focal mechanism represents the centroid location of the median model. Dotted circles show the centroid distance of 250 km. (b) Black lines are the observed waveforms; Red lines are the synthetics from the 32 finite-fault models and the median model at the 16 km scale, with their amplitude normalized with the observed amplitude. (c) Correlation coefficient values between the observations and synthetics at the 16, 32, and 64 km scale. Markers indicate the median correlation values of all stations, with an error bar indicating the associated standard deviation.

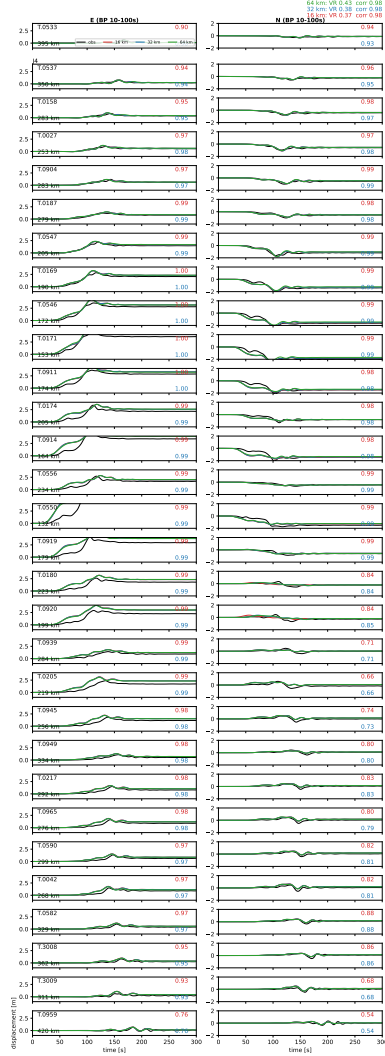


**Figure S42.** Comparison of high rate-GNSS observations and synthetics of projected and unified slip-rate J4 model at 16, 32 and 64 km scale. Black lines are the observations. Dark red, red, and yellow lines are the J4 synthetics of 16, 32, and 64 km scale, respectively. The correlation values of each component are shown on the top right and bottom right of each waveform subplot. Station name and distance from the centroid location are shown in top left and bottom left of each waveform subplot. The overall median variance and the correlation value of the two sets of synthetics are shown at the top right of the figure.

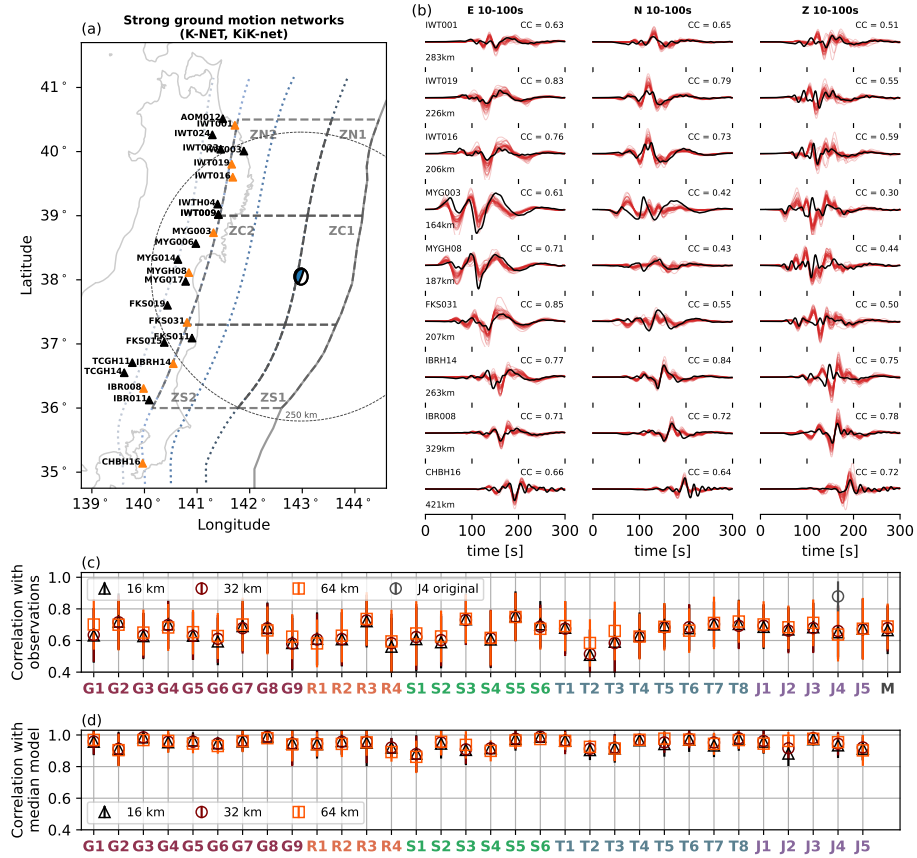


**Figure S43.** Comparison of regional strong-ground motion records (displacement) with synthetics at 32 km slip model scale. Same plotting style with Figure 14.



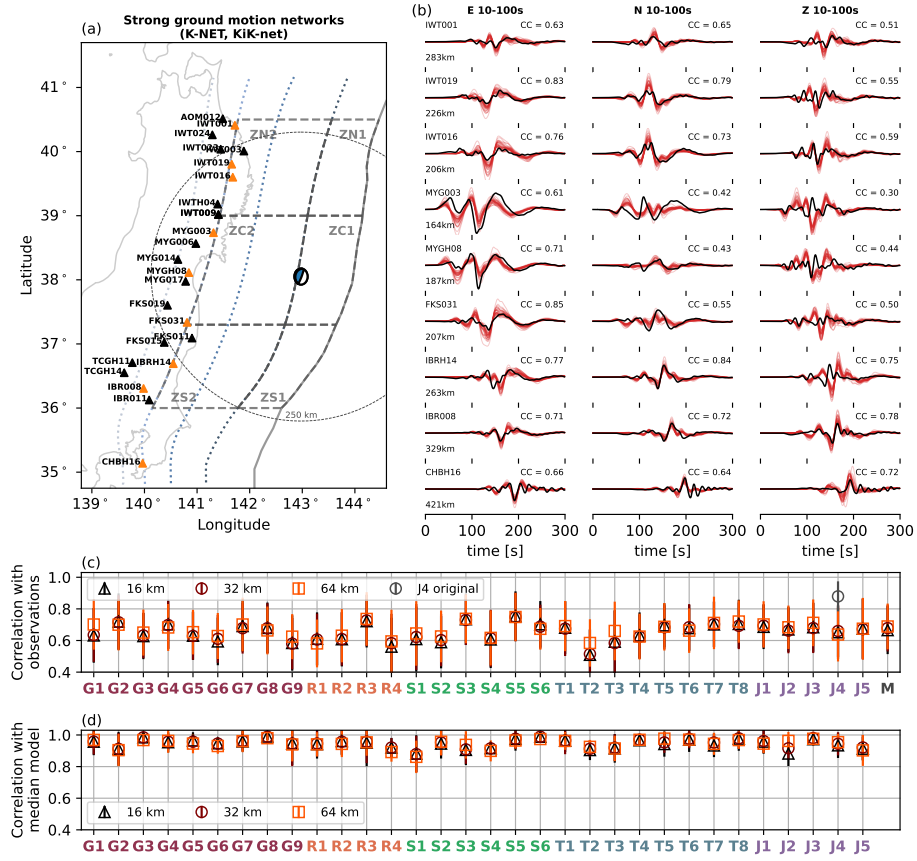


**Figure S44.** Comparison of regional strong-ground motion records (displacement) with synthetics at 64 km slip model scale. Same plotting style with Figure 14.

## References

- Ammon, C. J., Lay, T., Kanamori, H., & Cleveland, M. (2011). A rupture model of the 2011 off the Pacific coast of Tohoku earthquake. *Earth, Planets and Space*, 63(7), 693–696.
- Bletery, Q., Sladen, A., Delouis, B., Vallée, M., Nocquet, J.-M., Rolland, L., & Jiang, J. (2014). A detailed source model for the  $M_w$  9.0 Tohoku-Oki earthquake reconciling geodesy, seismology, and tsunami records. *Journal of Geophysical Research: Solid Earth*, 119(10), 7636–7653.
- Diao, F., Xiong, X., & Zheng, Y. (2012). Static slip model of the  $m_w$  9.0 Tohoku (Japan) earthquake: Results from joint inversion of terrestrial GPS data and seafloor GPS/acoustic data. *Chinese Science Bulletin*, 57, 1990–1997.
- Dziewonski, A. M., & Anderson, D. L. (1981). Preliminary reference earth model. *Physics of the earth and planetary interiors*, 25(4), 297–356.
- Fujii, Y., Satake, K., Sakai, S., Shinohara, M., & Kanazawa, T. (2011). Tsunami source of the 2011 off the Pacific coast of Tohoku earthquake. *Earth, planets and space*, 63(7), 815–820.
- Goldberg, D., Barnhart, W., & Crowell, B. (2022). Regional and teleseismic observations for finite-fault product. *US Geol. Surv. Data Release*.
- Gusman, A. R., Tanioka, Y., Sakai, S., & Tsushima, H. (2012). Source model of the great 2011 Tohoku earthquake estimated from tsunami waveforms and crustal deformation data. *Earth and Planetary Science Letters*, 341, 234–242.
- Hashima, A., Becker, T. W., Freed, A. M., Sato, H., & Okaya, D. A. (2016). Co-seismic deformation due to the 2011 Tohoku-Oki earthquake: influence of 3-D elastic structure around Japan. *Earth, Planets and Space*, 68(1), 1–15.
- Hayes, G. P. (2011, 09). Rapid source characterization of the 2011  $M_w$  9.0 off the Pacific coast of Tohoku earthquake. *Earth, Planets and Space*, 63(7), 529–534.
- Hooper, A., Pietrzak, J., Simons, W., Cui, H., Riva, R., Naeije, M., ... Socquet, A. (2013). Importance of horizontal seafloor motion on tsunami height for the 2011  $M_w$  = 9.0 Tohoku-Oki earthquake. *Earth and Planetary Science Letters*, 361, 469–479.
- Ide, S., Baltay, A., & Beroza, G. C. (2011). Shallow dynamic overshoot and energetic deep rupture in the 2011  $M_w$  9.0 Tohoku-Oki earthquake. *Science*, 332(6036), 1426–1429.
- Inuma, T., Hino, R., Kido, M., Inazu, D., Osada, Y., Ito, Y., ... others (2012). Co-seismic slip distribution of the 2011 off the Pacific Coast of Tohoku earthquake ( $M_9.0$ ) refined by means of seafloor geodetic data. *Journal of Geophysical Research: Solid Earth*, 117(B7).
- Ito, T., Ozawa, K., Watanabe, T., & Sagiya, T. (2011). Slip distribution of the 2011 off the Pacific coast of Tohoku earthquake inferred from geodetic data. *Earth, planets and space*, 63(7), 627–630.
- Jiang, J., & Simons, M. (2016). Probabilistic imaging of tsunamigenic seafloor deformation during the 2011 Tohoku-Oki earthquake. *Journal of Geophysical Research: Solid Earth*, 121(12), 9050–9076.
- Kubo, H., & Kakehi, Y. (2013). Source process of the 2011 Tohoku earthquake estimated from the joint inversion of teleseismic body waves and geodetic data including seafloor observation data: source model with enhanced reliability by using objectively determined inversion settings. *Bulletin of the Seismological Society of America*, 103(2B), 1195–1220.
- Kubota, T., Saito, T., & Hino, R. (2022). A new mechanical perspective on a shallow megathrust near-trench slip from the high-resolution fault model of the 2011 Tohoku-Oki earthquake. *Progress in Earth and Planetary Science*, 9(1), 1–19.
- Lee, S.-J., Huang, B.-S., Ando, M., Chiu, H.-C., & Wang, J.-H. (2011). Evidence of large scale repeating slip during the 2011 Tohoku-Oki earthquake. *Geophysical Research Letters*, 38(19).

- Melgar, D., & Bock, Y. (2015). Kinematic earthquake source inversion and tsunami runup prediction with regional geophysical data. *Journal of Geophysical Research: Solid Earth*, 120(5), 3324–3349.
- Minson, S. E., Simons, M., Beck, J., Ortega, F., Jiang, J., Owen, S., ... Sladen, A. (2014). Bayesian inversion for finite fault earthquake source models—ii: the 2011 great Tohoku-Oki, Japan earthquake. *Geophysical Journal International*, 198(2), 922–940.
- Nissen-Meyer, T., van Driel, M., Stähler, S. C., Hosseini, K., Hempel, S., Auer, L., ... Fournier, A. (2014). AxiSEM: broadband 3-D seismic wavefields in axisymmetric media. *Solid Earth*, 5(1), 425–445.
- Pollitz, F. F., Bürgmann, R., & Banerjee, P. (2011). Geodetic slip model of the 2011 M9.0 Tohoku earthquake. *Geophysical Research Letters*, 38(7).
- Romano, F., Trasatti, E., Lorito, S., Piromallo, C., Piatanesi, A., Ito, Y., ... Cocco, M. (2014). Structural control on the Tohoku earthquake rupture process investigated by 3d FEM, tsunami and geodetic data. *Scientific reports*, 4(1), 1–11.
- Saito, T., Ito, Y., Inazu, D., & Hino, R. (2011). Tsunami source of the 2011 Tohoku-Oki earthquake, Japan: Inversion analysis based on dispersive tsunami simulations. *Geophysical Research Letters*, 38(7).
- Satake, K., Fujii, Y., Harada, T., & Namegaya, Y. (2013). Time and space distribution of coseismic slip of the 2011 Tohoku earthquake as inferred from tsunami waveform data. *Bulletin of the seismological society of America*, 103(2B), 1473–1492.
- Simons, M., Minson, S. E., Sladen, A., Ortega, F., Jiang, J., Owen, S. E., ... others (2011). The 2011 magnitude 9.0 Tohoku-Oki earthquake: Mosaicking the megathrust from seconds to centuries. *science*, 332(6036), 1421–1425.
- Suzuki, W., Aoi, S., Sekiguchi, H., & Kunugi, T. (2011). Rupture process of the 2011 Tohoku-Oki mega-thrust earthquake (M9.0) inverted from strong-motion data. *Geophysical Research Letters*, 38(7).
- van Driel, M., Krischer, L., Stähler, S. C., Hosseini, K., & Nissen-Meyer, T. (2015). Instaseis: Instant global seismograms based on a broadband waveform database. *Solid Earth*, 6(2), 701–717.
- Wang, C., Ding, X., Shan, X., Zhang, L., & Jiang, M. (2012). Slip distribution of the 2011 Tohoku earthquake derived from joint inversion of GPS, InSAR and seafloor GPS/acoustic measurements. *Journal of Asian Earth Sciences*, 57, 128–136.
- Wang, R., Parolai, S., Ge, M., Jin, M., Walter, T. R., & Zschau, J. (2013). The 2011  $M_w$  9.0 Tohoku earthquake: Comparison of GPS and strong-motion data. *Bulletin of the Seismological Society of America*, 103(2B), 1336–1347.
- Wei, S., Graves, R., Helmberger, D., Avouac, J.-P., & Jiang, J. (2012). Sources of shaking and flooding during the Tohoku-Oki earthquake: A mixture of rupture styles. *Earth and Planetary Science Letters*, 333, 91–100.
- Xie, Z., & Cai, Y. (2018). Inverse method for static stress drop and application to the 2011  $M_w$  9.0 Tohoku-Oki earthquake. *Journal of Geophysical Research: Solid Earth*, 123(4), 2871–2884.
- Yagi, Y., & Fukahata, Y. (2011). Rupture process of the 2011 Tohoku-Oki earthquake and absolute elastic strain release. *Geophysical Research Letters*, 38(19).
- Yamazaki, Y., Cheung, K. F., & Lay, T. (2018). A self-consistent fault slip model for the 2011 Tohoku earthquake and tsunami. *Journal of Geophysical Research: Solid Earth*, 123(2), 1435–1458.
- Yokota, Y., Koketsu, K., Fujii, Y., Satake, K., Sakai, S., Shinohara, M., & Kanazawa, T. (2011). Joint inversion of strong motion, teleseismic, geodetic, and tsunami datasets for the rupture process of the 2011 Tohoku earthquake. *Geophysical Research Letters*, 38(7).

- 495 Yue, H., & Lay, T. (2013). Source rupture models for the  $M_w$  9.0 2011 Tohoku  
496 earthquake from joint inversions of high-rate geodetic and seismic data. *Bul-*  
497 *letin of the Seismological Society of America*, 103(2B), 1242–1255.
- 498 Zhou, X., Cambiotti, G., Sun, W., & Sabadini, R. (2014). The coseismic slip dis-  
499 tribution of a shallow subduction fault constrained by prior information: the  
500 example of 2011 Tohoku ( $M_w$  9.0) megathrust earthquake. *Geophysical Jour-*  
501 *nal International*, 199(2), 981–995.